Durham E-Theses

Structure formation in modified gravity cosmologies

BARREIRA, ALEXANDRE,MIGUEL,RODRIGUE

How to cite:

BARREIRA, ALEXANDRE,MIGUEL,RODRIGUE (2015) *Structure formation in modified gravity cosmologies*, Durham theses, Durham University. Available at Durham E-Theses Online: http://etheses.dur.ac.uk/11248/

Use policy

Structure formation in modified gravity cosmologies

Alexandre Miguel Rodrigues Barreira

Abstract

We study linear and nonlinear structure formation in cosmologies where the accelerated expansion is driven by modifications to general relativity (GR). We focus on Galileon and Nonlocal gravity, which are two classes of models that have been attracting much attention. We derive the linearly perturbed model equations and solve them with suitably modified versions of Einstein-Boltzmann codes. We also derive the perturbed equations keeping the relevant nonlinear terms for small scale structure formation, which we solve using N-body codes and semi-analytical techniques that were developed for these models. Using CMB, SNIa and BAO data we find strong evidence for nonzero active neutrino masses ($\Sigma m_\nu \approx 0.6\,\mathrm{eV}$) in all three main branches of covariant Galileon cosmologies, known as the Cubic, Quartic and Quintic models. However, in all branches, the lensing potential does not decay at late times on sub-horizon scales, which contradicts the measured positive sign of the ISW effect, thereby ruling out the Galileon model. The Nonlocal model we study should be able to fit the CMB with similar parameter values as ΛCDM. The N-body simulation results show that the covariant Galileon model admits realistic halo occupation distributions of luminous red galaxies, even for model parameters whose linear growth is noticieably enhanced ($\sigma_8 \approx 1$) relative to ΛCDM. In the Cubic Galileon model the screening mechanism is very efficient on scales $\lesssim 1\mathrm{Mpc}$, but in the Quartic and Quintic sectors, as well as in the Nonlocal model, we identify potential tensions with Solar System bounds. We illustrate that, despite the direct modifications to the lensing potential in the Cubic Galileon and Nonlocal models, cluster masses estimated from lensing remain the same as in GR. The lensing effects produced by cosmic voids found in the simulations of the Cubic Galileon are significanly boosted ($\approx 100\%$) compared to GR, which strongly motivates using voids in tests of gravity. The combination of linear and nonlinear theory results presented here for Galileon and Nonlocal gravity is an example of what it could be done for any serious alternative models to ΛCDM, which will be tested by future experiments.

Structure formation in modified gravity cosmologies

by Alexandre Miguel Rodrigues Barreira

A thesis submitted to the University of Durham
in accordance with the regulations for
admittance to the Degree of Doctor of Philosophy.

Department of Physics
University of Durham
May 2015

Contents

List of Figures

List of Tables

Declaration

The work described in this thesis was developed between the years 2011 and 2015. During this time, the author was a postgraduate research student under the supervision of Dr. Baojiu Li and Prof. Carlton M. Baugh in the Institute for Computational Cosmology and Prof. Silvia Pascoli in the Institute for Particle Physics Phenomenology at the Department of Physics at the University of Durham.

This work has not been submitted for any other degree at the University of Durham or any other University.

The contents in Chapters 2 are based on Ref. [1], Chapter 3 on Refs. [2, 3, 4], Chapter 4 on Ref. [5], Chapter 5 on Refs. [6, 7] and Chapter 6 on Ref. [8], respectively. These references have all been published in peer reviewed journals.

The contents in Chapter 7 are based on the results of Refs. [9, 10]. These papers have been submitted and are currently under review.

All figures shown in this thesis were made by the author, with the exception of Figs. 8.1 and 8.2. These were taken from Refs. [11, 12], respectively, on which the author has also collaborated.

Acknowledgements

First and foremost, I thank Baojiu, Carlton and Silvia for the excellent guidance they provided over these past four years. Thank you all for your patience and enthusiasm whenever I was too pessimistic, for always pushing me to achieve more and for our productive and very enjoyable discussions. I have learned a great deal from interacting with you. It is very safe to say that I could not have asked for a better supervisory team.

Lydia deserves a paragraph just for herself. It always astonished me that, despite being so busy, you always found time whenever I knocked on your door for help with the computer. Your prompt solutions were crucial to develop all the work in this thesis.

Thanks to all my collaborators Marius Cautun, Wojciech Hellwing, Elise Jennings, Lindsay King, Lucas Lombriser, Julian Merten and Ariel Sanchez for their help and contribution to the work in this thesis. It has been a pleasure working with you all.

Thanks to all of my friends and office mates in Durham. Thank you Michelle, Matthieu, Tamsyn, Flora, Violeta, Mathilde, Sownak, Wojtek, Peter, Andrew, Marius, Jascha, Charles, Will, Agnese, Claudia, Alex (I), Pablo, Manolis and Nikos for being so fun to have around. You all know about my pessimist views about Durham (oh! This weather!), but your presence was always an enjoyable aspect of living here. Thank you so much! Many thanks also to Tiago, Alice and Maite, who I met in my first year, but remain very close friends. My college friends Muneer, Josh, Altyn, Iman and Gina have also been there whenever a good time outside of physics was needed.

My friends at home, despite the distance, are also to blame for making sure I was a happier person during my time in Durham. Thank you Martinha, Filipe, Marta, Manuel, Eduardo, Joao Pedro, Esther, Victor, Vitor, Miguel, Oscar, Gonçalo, Tiago, Rui, João, André. Thanks also to the S. L. Benfica football team for making it feel like home during each of those 90 minutes of play.

Finally, but certainly not least, I am deeply thankful to my Mom and Dad and my favourite sister Mariana for their support, not only during the PhD, but during all my life. Thank you for bearing with my bad temper, for being there when I needed the most and for being that massive source of inspiration. Without you, none of this would be possible.

Pelos sacrifícios que fizeste há 26 anos atrás,

é claro que é para ti Mãe !

Chapter 1

Introduction

1.1 The standard ΛCDM model of cosmology

Over the past twenty years or so, a wealth of cosmological observations – ranging from temperature anisotropies in the cosmic microwave background (CMB) [13], to supernovae type Ia (SNIa) light curves [14, 15], baryonic acoustic oscillations (BAO) imprinted in the galaxy distribution [16, 17], galaxy cluster abundances [18, 19], gravitational lensing [20, 21], etc – have established the so-called Λ cold dark matter (ΛCDM) model as the standard theoretical paradigm. This model, which assumes the cosmological principle (statistical homogeneity and isotropy on large scales), can be devided into four main ingredients. These are (i) the standard model of particle physics (SMPP); (ii) cold dark matter (CDM); (iii) a cosmological constant, Λ; and (iv) general relativity (GR) as the theory of gravity. Next, we briefly discuss each of these in turn.

Standard model of particle physics

This corresponds to all stable known particles that are predicted by the SMPP (including their electroweak and strong force interactions) for after matter/antimatter annihilation (the photon era). For cosmological purposes these include photons, neutrinos and baryons.

Photons Most of the photons in the Universe are part of the CMB. The rest are emitted by astrophysical structures such as stars in galaxies and hot gas inside deep gravitational wells. Today, the photon energy density represents only a tiny fraction ($\sim 0.008\%$) of the energy budget in the Universe, with negligible impact on the dynamics of the expansion. Photons were only dominant before the epoch of radiation-matter equality $z \gtrsim 3000$, where z is the cosmological redshift.

Neutrinos Neutrinos are massless particles in the SMPP, but this is known to be wrong after the detection of neutrino flavour oscillations in atmospheric, solar and reactor experiments [22]. These experiments measure $m_2^2 - m_1^2 \approx (7.5 \pm 0.19) \times 10^{-5}$ eV^2 (1σ) and

$|m_3^2 - m_2^2| \approx (2.427 \pm 0.007) \times 10^{-3}$ eV^2 (1σ) [22], where m_1, m_2, m_3 are the masses of the three neutrino eigenstates. Assuming a normal mass ordering ($m_1 < m_2 < m_3$), the data imply $\Sigma m_\nu > 0.06$ eV, whereas for an inverted mass ordering ($m_3 < m_2 < m_1$), $\Sigma m_\nu > 0.1$ eV, where Σm_ν is the value of the summed neutrino masses. Currently, the upper bound from terrestrial experiments is $\Sigma m_\nu < 6.6$ eV [23, 24].

Baryons The rest of the particles in the Universe (mostly in the form of atomic nuclei and electrons) are referred to as the *baryons* [1]. Baryons exist today in stars inside galaxies and also in diffuse gas inside galaxy groups and clusters. Before the epoch of recombination, baryons could not collapse gravitationally due to the nonnegligible pressure of the photons, to which baryons were coupled. During this time, the competition between photon pressure and gravity produced baryonic accoustic oscillations which are inprinted in the temperature anisotropies of the CMB [13] and also on the large scale distribution of galaxies [16, 17].

Cold Dark Matter

The CDM particle does not interact (or interacts only very weakly) electromagnetically and its existence was postulated to explain a number of observational puzzles [25, 26]. Perhaps the most famous of these is related to the flattening of galaxy rotation curves at large radii, which could not be explained solely by the gravitational field originating from the visible components. This led to explanations in which the galaxies are embedded in larger Dark Matter (DM) haloes [27, 28, 29]. In galaxy clusters, measurements of the temperature of X-ray emitting gas, of galaxy velocity dispersion and of lensing distortions induced on the appearence of background galaxies suggested that the potential wells had to be deeper than accounted by the visible matter [30]. Colliding galaxy clusters provide a particularly strong case for DM [31]. In these events, one observes the gas from the two clusters located at same position, but lensing measurements show an offset between the gas and the bulk of the mass of each cluster. The explanation is that the two DM clumps have passed through each other interacting weakly through gravity only, but the gas stayed behind due to the extra electromagnetic forces that it experiences.

Further strong evidence for DM comes from the large scale structure in the Universe.

---

[1]This is actually incorrect as electrons are leptons. However, in the literature the word *baryons* is used to denote electrons as well, which is why we do the same here.

Before recombination, the diffusion of the photon-baryon plasma from hotter (denser) to colder (less dense) regions should have smeared out the small scale density fluctuations that would later collapse gravitationally to form the galaxies we see today. Dark matter does not experience this diffusion damping (also called Silk damping) since it does not couple to photons (at least strongly), and therefore, its potential wells remain unaffected. After recombination, the baryons decouple from the photons and collapse into the existing gravitational potentials of the dark matter, where galaxies will be able to form. This is also why cold versions of dark matter are preferred over massive neutrinos with masses of a few eV, which would be hot dark matter. Massive neutrinos cannot account for the totality of dark matter since their high streaming velocity would also wipe out small scale fluctuations, and hence, prevent structures from forming [32]. However, warm versions of DM (with masses of a few keV) may be allowed by observations and have received substantial attention recenty in cosmology [33].

Results from N-body simulations suggest that the dark matter distribution in the Universe forms a *cosmic web* [34, 35, 36] made up by (i) voids, which are underdense regions; (ii) filaments and (iii) walls, which are, respectively, one and two dimensional structures that typically surround voids; and (iv) knots, which correspond to the locations of intersection of filaments and walls, where the most massive dark matter haloes form.

Cosmological constant, Λ

The extra diming of the light emitted from SNIa [14, 15] compared to that expected in a Universe containing only matter provided the first concrete evidence for the existence of *dark energy* – a mysterious energy source with negative background pressure that is causing the expansion of the Universe to accelerate. In the ΛCDM model, the role of dark energy is played by vacuum energy, which acts as a cosmological constant, Λ. Despite its simplicity, Λ is responsible for, arguably, the most serious shortcomings of ΛCDM. One is known as the *fine tuning* problem and is related to the huge difference between the value of Λ inferred from observations and the much larger figure that is predicted by the SMPP. If one takes the Planck energy scale as the energy cutoff when estimating the zero-point fluctuations of some field, then the discrepancy reaches 120 orders of magnitude. For Λ to be dark energy, then this implies that there must be some unknown and extreme fine-tuning mechanism, which is hard to reconcile with our current knowledge of quantum fields.

The second problem associated with Λ is known as the *coincidence problem*, which asks why we live at the cosmological epoch when the energy densities of matter and Λ are comparable. The ratio of the energy density of nonrelativistic matter to the cosmological constant is given by $\rho_{m0}a^{-3}/\rho_\Lambda$, where ρ_{m0} and ρ_Λ are, respectively, the energy densities of matter and Λ in the Universe today, and a is the cosmological scale factor. For most of the past evolution of the Universe ($a \ll 1$), this ratio is much larger than unity and in the far future ($a \gg 1$), it is much smaller than unity. We happen to live in the narrow slice of time ($a \approx 1$) when the ratio is approximately unity, which is very unlikely. The coincidence problem refers to the question "Why is this the case?" [2].

General Relativity

The theory of gravity in the ΛCDM model is Einstein's theory of General Relativity (GR). This theory is in remarkably good agreement with a wealth of precision tests performed in the Solar system (SS) [40]. These include the classical tests of gravitational redshift, the lensing of the light from background stars by the Sun and the anomalous perihelion of Mercury, as well as other tests such as the Shapiro time-delay effect measured by the Cassini spacecraft and Lunar laser ranging experiments which meausure the rate of change of the gravitational strength in the SS. Outside of the SS, GR is also in good agreement with the tests that involve changes in the orbital period of binary pulsars due to the emission of gravitational waves. All these tests, however, only probe length scales that are much smaller than those relevant for cosmology. This therefore motivates research on the obser-vational signatures that alternative gravity models can leave on cosmological observables. These investigations form the basis of this thesis.

1.1.1 Key equations

In the ΛCDM model, the spacetime is described by the Friedmann-Roberston-Walker line element

$$\mathrm{d}s^2 = (1 + 2\Psi)\,\mathrm{d}t^2 - a(t)^2\,(1 - 2\Phi)\,\gamma_{ij}\mathrm{d}x^i\mathrm{d}x^j, \tag{1.1}$$

---

[2]Since the coincidence problem is linked to our existence as cosmological observers, there have been at-tempts to solve this problem using anthropic considerations [37, 38, 39]. The argument is that, for instance, life as we know it could only appear after the first galaxies, stars and planets have formed, and therefore we are living soon after the time the Universe became habitable, which would not be that much of a "coincidence".

where $\gamma_{ij} = \text{diag}\,[1, 1, 1]$ is the spatial sector of the metric (which here, and througout this thesis is always taken to be flat), and Ψ and Φ are the two gravitational potentials (the line element is written in the Newtonian gauge considering only scalar perturbations). At the background level ($\Phi = \Psi = 0$) one has the two Friedmann equations

$$3\left(\frac{\dot{a}}{a}\right)^2 \equiv 3H^2 = 8\pi G\bar{\rho}, \tag{1.2}$$

$$\frac{\ddot{a}}{a} = -\frac{4\pi G}{3}\left[\bar{\rho} + 3\bar{p}\right], \tag{1.3}$$

and the conservation equation

$$\dot{\bar{\rho}} + 3H\left(\bar{\rho} + \bar{p}\right) = 0, \tag{1.4}$$

where H is the Hubble expansion rate and $\bar{\rho}$ and $\bar{p}$ are the background density and pressure associated with all the energy species in the model, e.g. $\bar{\rho} = \bar{\rho}_{r0}a^{-4} + \bar{\rho}_{m0}a^{-3} + \bar{\rho}_{\nu0}f_\nu(a) + \bar{\rho}_\Lambda$, where the subscripts r, m, ν and Λ denote radiation, matter (baryons + CDM), massive neutrinos and Λ (the function f encapsulates the time dependence of the neutrino component which cannot be given by a single power law). The subscript 0 denotes the values at the present day, $a = 1$, and a dot denotes a physical time derivative. Equation (1.3) tells us that for the expansion to accelerate ($\ddot{a} > 0$), the Universe must be dominated by an energy component for which $w = \bar{p}/\bar{\rho} < -1/3$, where w is called the equation of state parameter. The cosmological constant is characterized by $w_\Lambda = -1$.

On sub-horizon scales, the geodesic equation for matter particles results in

$$\dot{v}^i + Hv^i = -\frac{1}{a}\nabla^i\Psi, \tag{1.5}$$

where $v^i = a\dot{x}^i$ is the i-th component of the peculiar velocity of the matter particles and the gravitational potentials can be given by the Poisson equation

$$\nabla^2\Phi = 4\pi G\delta\rho \tag{1.6}$$

$$\Phi = \Psi, \tag{1.7}$$

where $\delta\rho = \rho - \bar{\rho}$ is the density perturbation.

1.2   Beyond ΛCDM with modified gravity

The main focus of this thesis is on models that go beyond ΛCDM by exploring modifications to the general relativistic gravitational law. Research on modified gravity in cosmol-

ogy is now a well established and active field on both the theoretical [41, 42, 43] and observational [44, 45, 46] levels. There are two main reasons for this. The first is related to the fact that GR has not been tested on scales larger than the SS, as commented on above. This means that one makes a huge extrapolation of the regime of validity of the theory when using it (as it is common) in cosmological studies. The gravitational law should, therefore, be put to test on larger scales, and *modified gravity* models help to design such observational tests: by understanding the typical observational inprints of alternative gravity scenarios one learns about the observables that have the potential to uncover any departures from GR. The second reason is that these models can also be used to explain the accelerated expansion of the Universe without an explicit Λ term, thereby providing further motivation for their study [3].

Before proceding, we note that a stronger case for modified gravity studies can perhaps be made by noting that GR is a classical theory without a well-defined quantum limit. This suggests that GR should be modified in the high curvature regime (small distance scales), if one wishes to construct a viable quantum field theory. Although cosmology represents the other end of the curvature spectrum (large distance scales), it is not unreasonable to believe that an eventual quantum field theory of gravity that differs from GR on small scales, should also differ from it on cosmological ones.

---

[3]It is important to stress, however, that modified gravity does not explain the fine tuning problem of Λ. Nevertheless, the problem gets relaxed since, if there is now an alternative explanation for dark energy, then the value of Λ can be cancelled exactly, which is easier to motivate (e.g., by some symmetry principle or scenarios of degravitation of Λ [47, 48]) than a case of extreme fine tuning.

1.2.1 Modified gravity: the broad picture

Below we show the actions of some well known examples of cosmological models,

$$S = \int d^4x\sqrt{-g}\left[\frac{\mathcal{R}}{16\pi G} + \mathcal{L}_m + \frac{\Lambda}{8\pi G}\right], \tag{1.8}$$

$$S = \int d^4x\sqrt{-g}\left[\frac{\mathcal{R}}{16\pi G} + \mathcal{L}_m + \frac{1}{2}\nabla^\mu\varphi\nabla_\mu\varphi + V(\varphi)\right], \tag{1.9}$$

$$S = \int d^4x\sqrt{-g}\left[\frac{\mathcal{R}}{16\pi G} + \mathcal{L}_m\left(A(\varphi), g_{\mu\nu}\right) + \frac{1}{2}\nabla^\mu\varphi\nabla_\mu\varphi + V(\varphi)\right], \tag{1.10}$$

$$S = \int d^4x\sqrt{-g}\left[\frac{\mathcal{R}}{16\pi G} + \mathcal{L}_m + f(\mathcal{R})\right], \tag{1.11}$$

$$S = \int d^4x\sqrt{-g}\left[\frac{\mathcal{R}}{16\pi G} + \mathcal{L}_m + \nabla^\mu\varphi\nabla_\mu\varphi\left(\frac{c_2}{2} + \frac{c_3}{2\mathcal{M}^3}\Box\varphi\right)\right], \tag{1.12}$$

$$S = \int d^4x\sqrt{-g}\left[\frac{\mathcal{R}}{16\pi G} + \mathcal{L}_m\left(A(\varphi), g_{\mu\nu}\right) + K\left(\nabla_\mu\varphi\nabla^\mu\varphi\right)\right], \tag{1.13}$$

$$S = \int d^4x\sqrt{-g}\left[\frac{\mathcal{R}}{16\pi G} + \mathcal{L}_m + f\left(\Box^{-n}\mathcal{R}\right)\right], \tag{1.14}$$

$$S = \int d^4x\sqrt{-g}\left[\frac{\mathcal{R}}{16\pi G} + \mathcal{L}_m\right] + \int d^5x^{(5)}\sqrt{g^{(5)}}\left[\frac{\mathcal{R}^{(5)}}{16\pi G^{(5)}}\right], \tag{1.15}$$

where g is the determinant of the metric $g_{\mu\nu}$, $\mathcal{L}_m$ is the Lagrangian density that describes the SMPP and dark matter, $\mathcal{R}$ is the Ricci curvature scalar and G is Newton's constant. This list is not meant to cover all known theoretical models and we use it here simply to illustrate some key ideas. Reference [42] presents a very thorough review of these and many more modified gravity models in cosmology.

The above equations make it apparent that there is a common structure for these models. They all contain (i) the Einstein-Hilbert term, $\frac{\mathcal{R}}{16\pi G}$, which gives rise to the Einstein tensor, $G_{\mu\nu}$, in the metric field equations; (ii) $\mathcal{L}_m$, which is used to define the energy-momentum tensor, $T^m_{\mu\nu}$, in the metric field equations; and (iii) additional terms that modify the standard Einstein metric field equations and which are designed to explain the acceleration of the expansion of the Universe.

Equation (1.8) is the standard ΛCDM model. Models with the action of Eq. (1.9) are known as *quintessence* models [49]. In these models, the cosmological constant is replaced by a scalar field that does not couple to matter and whose equation of state, $w_\varphi = p_\varphi/\rho_\varphi$, is given by

$$w = \frac{\dot{\varphi}^2/2 - V(\varphi)}{\dot{\varphi}^2/2 + V(\varphi)}, \tag{1.16}$$

where p_φ and ρ_φ are, respectively, the background pressure and energy density of φ. If the scalar field rolls slowly down its potential, $\dot\varphi/2 \ll V(\varphi)$, then $w_\varphi \approx -1$. The model of Eq. (1.10) generalizes the quintessence model by allowing the scalar field to conformally couple to matter, i.e., $\mathcal{L}_m$ depends on a function $A(\varphi)$ that governs the physics of the coupling. It is possible to show that, for appropriately chosen forms of $A(\varphi)$, these coupled scalar field scenarios [50, 51] are mathematically equivalent to $f(R)$ models [52, 53, 54], whose action is given by Eq. (1.11) (see e.g. Refs. [51, 55] for an illustration of this equivalence). In crude terms, this equivalence can be described as follows. In the coupled scalar field models, gravity is as in GR and a *fifth force* arises via an explicit interaction between the scalar field and the matter fields (this is called the Einstein frame). In this interpretation, Eqs. (1.6) and (1.7) remain unchanged, but an extra term appears on the right-hand side of Eq. (1.5). On the other hand, in $f(R)$ models, it is the Poisson equation, Eq. (1.6), that acquires extra terms, while the geodesic equation is only changed indirectly via the modified potential (this is called the Jordan frame). Nevertheless, the trajectories of matter particles end up being the same, regardless of which frame one works in[4]. In this thesis, we use the term fifth force to denote any modification to the force law of GR, interpreted either in the Einstein or Jordan frames.

At this point, it is interesting to comment on one aspect related to the naturalness of modified gravity scenarios. Quintessence models are generally portrayed as the simplest alternative to Λ as the dark energy. This is in the sense that these models modify only the expansion rate of the Universe, without introducing any fifth force effects. However, from a theoretical point of view, if one introduces a scalar field into a model, then one could expect it to couple to the remaining matter degrees of freedom. That is, standard quintessence models need to include an explanation for a vanishing coupling strength. These models are therefore somewhat less natural when compared to coupled quintessence models, whose phenomenology is equivalent to modified gravity. In this way, fifth force effects can be regarded as quite a natural consequence of models that go beyond ΛCDM.

The model of Eq. (1.12) is called the Cubic Galileon, which is a special case of the more

---

[4]Note, however, that certain physical processes can be different in between these two frames and therefore care must be taken when interpreting the observations. For instance, in the Einstein frame, the scalar field can induce a time variation of the mass of the matter particles, which must be taken into account when analysing supernovae light curves at different redshift. This shows that these two frames are actually not completely equivalent.

general Covariant Galileon model [56, 57]. The action of this model has no free functions. The starting point for its derivation is the requirement that the theory remains invariant under Galilean shifts, $\partial_\mu \varphi \rightarrow \partial_\mu \varphi + b_\mu$ (where b_μ is a constant four-vector), in flat spacetime. In this model, the acceleration and the modifications to gravity are driven by the nonlinear coupling of the derivatives of the scalar field. A substantial part of this thesis will be devoted to the study of the Galileon model.

The action of Eq. (1.13) is similar to the coupled quintessence model, Eq. (1.10), but the scalar Lagrangian density is given by a nonlinear function of the scalar kinetic term, $\nabla^\mu \varphi \nabla_\mu \varphi / 2$. These models are called K-mouflage [58, 59, 60] models, and recent work on them by the author will be mentioned briefly in this thesis (cf. Chapter 8).

Models whose action can be cast in the form of Eq. (1.14) are called Nonlocal gravity models [61, 62, 63]. In this case, one replaces Λ by a function of the inverse of a derivative operator (like the d'Alembertian $\Box$) acting on some curvature tensor. The meaning of the inverse of a differential operator is essentially an integral, which is a nonlocal operation (hence the name). Nonlocal gravity models are also studied in detail in this thesis.

Finally, Eq. (1.15) shows the action of the Dvali-Gabadadze-Porrati (DGP) model [64]. This is a braneworld model, in which the matter fields are confined to a four-dimensional brane embedded in a five-dimensional bulk spacetime. Gravity can propagate in both the brane and in the extra dimension (in the action, the supercripts $^{(5)}$ mean that a quantity is associated with the bulk). The quantity $r_c = G^{(5)}/G^{(4)}$, is a model parameter known as the *crossover scale*, which determines the distance scale on the brane above which the gravitational effects from the fifth dimension become important. This model is characterized by two branches of solutions. One of them is called the *normal branch*, which contains fifth force effects, but requires an explicit dark energy term to be added to the four-dimensional part of the action. The more appealing *self-accelerating branch* does not require an additional dark energy field to explain the acceleration on the brane, but is plagued by ghost instabilities (degrees of freedom whose energy is unbounded from below) [65, 66, 67, 68]. The *self-accelerating branch* is also ruled out by the CMB and SNIa data [69].

Although there is always some theoretical reasoning behind the forms proposed for the dark energy terms in Eqs. (1.8 - 1.15), the reality is that their motivation always lies on somewhat shaky ground (and this includes the ΛCDM model). In this thesis, we shall not worry too much about the reasoning behind the motivation for the models or their more

theoretical details. Instead, the focus will be given to the study of their phenomenology and the impact it has on observations.

1.2.2 The need for screening mechanisms

The idea of modifying the gravitational law on large scales inevitably leads to the question of how such $\mathcal{O}(1)$ modifications can be made compatible with the stringent SS tests. This reconciliation is typically achieved via *screening mechanisms* which dynamically suppress the modifications to gravity in regions like the SS. Currently, there is a variety of screening mechanisms in the literature which include the *chameleon*, *symmetron*, *dilaton*, *Vainshtein* and *K-mouflage* type screenings. In all of these, the implementation of the screening effects relies on the presence of nonlinear terms in the equations of motion, which act to suppress the size of the fifth force in regions where some criterion is met. This criterion typically involves the size of the gravitational potential or of its derivatives, which tend to be higher on smaller length scales than on larger scales[5].

We note in passing that another way to reconcile the SS tests with sizeable fifth force effects in cosmology is to confine the fifth force to act only within the *dark sector* of the Universe, i.e., an interaction that would only affect dark energy and dark matter [50]. In this way, baryons would be unaffected and the SS contraints could be met. In this thesis, we focus only on models where the modifications to gravity are felt universally by all matter species.

Below, we briefly describe how different types of screening mechanisms operate. We shall be very schematic in the discussion and refer the reader to the cited literature for the details (see also [41, 43] for reviews).

Chameleon Screening

The chameleon screening mechanism operates in models such as coupled quintessence, Eq. (1.10) (as well as $f(R)$, Eq. (1.11), via the conformal equivalence that exists between

---

[5]In the literature, one often encounters this criterion being described as the amplitude of the matter density fluctuations. This is done perhaps to make the explanations simpler, but is inaccurate. For instance, the matter density perturbation between the Sun and the Earth is small (compared to that of each object), but one still requires the fifth force to be screened there. A more correct description would be made in terms of the gravitational potential (or its gradients), which can be sizeable even if there is a vacuum between two massive bodies.

these two models [55]). The equation for the scalar field can be written as [70, 71]

$$\frac{1}{r^2}\left(r^2\varphi_{,r}\right)_{,r} = V(\varphi)_{,\varphi} + \rho(r)A(\varphi)_{,\varphi} \equiv V^{\text{eff}}_{,\varphi}, \qquad (1.17)$$

where we have assumed spherical symmetry for simplicity, $_{,r}$ and $_{,\varphi}$ denote partial differentiation w.r.t. the radial coordinate r and the field φ, $\rho(r)$ is the matter density profile and $V^{\text{eff}} = V + \rho A$ is an effective scalar potential that governs the behaviour of φ. The main premise of the mechanism lies in choosing the functional form of the self-interacting potential, $V(\varphi)$, and the coupling function, $A(\varphi)$, in such a way that the scalar field acquires a large mass in the regions of interest. If the mass is sufficiently large, then the distance scale over which the scalar field can mediate a fifth force can be brought down to undetectable values.

For the sake of illustration (which follows closely that used in Refs. [70, 71]), consider a compact spherical object of size R and constant density ρ_{in}, embedded in an ambient density ρ_{out}. One can think of this as a golf ball embedded in the Earth's atmosphere, or the Earth embedded in the Milky Way halo, or the Milky Way halo embedded in the Local Group, etc. The idea now is to choose the functions $V(\varphi)$ and $A(\varphi)$ so that V^{eff} has a minimum at $\varphi = \varphi_{\text{min}}$. The typical choices are $V \propto \varphi^{-n}$ and $A(\varphi) = e^{\beta\varphi/M_{\text{Pl}}}$, where M_{Pl} is the reduced Planck mass, n is a positive integer and $\beta > 0$ measures the strength of the coupling between the scalar field and matter. Then, the value of the scalar field at the minimum of the potential, φ_{min} (defined by $V^{\text{eff}}_{,\varphi}(\varphi_{\text{min}}) = 0$), and the value of its mass squared, $m_\varphi^2 = V^{\text{eff}}_{,\varphi\varphi}(\varphi_{\text{min}})$, become dependent on the value of ρ. In particular, the larger the density ρ, then the smaller the value of φ_{min} and the larger the mass m_φ.

In these models, the fifth force (which appears as an extra term on the right-hand side of Eq. (1.5)) is proportional to $\partial_r \ln A(\varphi) = \beta \partial_r \varphi$. That is, the fifth force is determined by the spatial gradient of the scalar field in the same way that normal gravity is proportional to the spatial gradient of the gravitational potential. Skipping the details of the derivation [70, 71], it can be shown that if

$$\frac{\Delta R}{R} \approx \frac{\varphi_{\text{min,out}} - \varphi_{\text{min,in}}}{6\beta M_{\text{Pl}}\Phi} \equiv \frac{\Delta\varphi}{6\beta M_{\text{Pl}}|\Phi|} \ll 1, \qquad (1.18)$$

then the scalar field profile outside of the spherical overdensity can be approximated as (for $r > R$)

$$\varphi(r) \approx \varphi_{\text{min,out}} - \left(\frac{3\beta}{4\pi M_{\text{Pl}}}\right)\left(\frac{\Delta R}{R}\right)M\frac{e^{-m_{\text{out}}(r-R)}}{r}, \qquad (1.19)$$

where, in the above two equations, $\varphi_{\text{min,in}}$ and $\varphi_{\text{min,out}}$ are, respectively, the values of the field at the minimum of the potential for $\rho = \rho_{\text{in}}$ and $\rho = \rho_{\text{out}}$, m_{out} is the mass of the scalar field for $\rho = \rho_{\text{out}}$, $M = 4\pi\rho_{\text{in}}R^3/3$ is the mass of the spherical object and $\Phi = -GM/R$ is its gravitational potential. Equation (1.19) tells us that the force generated by φ is of the Yukawa type, but that only the matter inside a *thin shell* of width ΔR contributes to it. This is because deeper inside the overdensity, the mass of the scalar field, m_{in}, is large and the spatial dependence of the scalar field becomes exponentially suppressed, $\propto e^{-m_{\text{in}}r}$. Equation (1.19) is valid only if Eq. (1.18) holds, which depends on the ratio between $\Delta\varphi$ and $|\Phi|$. The former is determined by the difference of the minimum of the scalar field in and out of the overdensity, which increases with the density contrast. For fixed density contrast then, the chameleon mechanism works if the gravitational potential of the object is sufficiently deep.

If the condition of Eq. (1.18) is not met, then the scalar field profile is given by

$$\varphi(r) \approx \varphi_{\text{min,out}} - \left(\frac{\beta}{4\pi M_{\text{Pl}}}\right) M \frac{e^{-m_{\text{out}}(r-R)}}{r}, \tag{1.20}$$

in which there are no suppression effects.

Symmetron Screening

The symmetron screening mechanism [72, 73, 74] works similarly to the chameleon case. The effective potential is again $V^{\text{eff}} = V + \rho A$, but now one chooses the functions $V(\varphi)$ and $A(\varphi)$ in such a way that the fifth force is proportional to φ and that for high ρ the effective potential has a minimum at $\varphi = 0$. To illustrate this point one can choose

$$V = -\frac{1}{2}\mu^2\varphi^2 + \frac{\lambda}{4}\varphi^4, \qquad A = 1 + \frac{1}{2\mathcal{M}^2}\varphi^2, \tag{1.21}$$

for which (up to an additive constant)

$$V^{\text{eff}} = V + \rho A = \frac{1}{2}\left(\frac{\rho}{\mathcal{M}^2} - \mu^2\right)\varphi^2 + \frac{\lambda}{4}\varphi^4, \tag{1.22}$$

where μ and $\mathcal{M}$ are two mass scales and λ is a dimensionless self-interacting coupling constant. If $\rho > \mathcal{M}^2\mu^2$, then V^{eff} has a minimum at $\varphi_{\text{min}} = 0$. On the other hand, if $\rho < \mathcal{M}^2\mu^2$, then the potential acquires two minima at $\varphi_{\text{min}} = \pm\mu/\sqrt{\lambda}$. The symmetron mechanism works because in these models the fifth force is proportional to φ: $\partial_r \ln A(\varphi) \propto \varphi \partial_r \varphi$. Hence, deep inside a sufficiently dense object (i.e., $\rho > \mathcal{M}^2\mu^2$), $\varphi = \varphi_{\text{min}} = 0$ and the

scalar field generates no fifth force. However, if the ambient density is such that $\rho < \mathcal{M}^2 \mu^2$, then, at the edge of the dense object, the scalar field must grow to $\varphi = \varphi_{\min} = \mu/\sqrt{\lambda}$. This results in a thin-shell effect similar to that which occurs in the chameleon case. Detailed calculations [73, 74] show that the condition for the thin-shell to develop is given by

$$\frac{\mathcal{M}^2}{6M_{\mathrm{Pl}}^2 \Phi} \ll 1. \tag{1.23}$$

Dilaton screening

Another type of screening that is similar to the above two and that we mention only in passing is the dilaton mechanism [75, 76, 77]. The effective potential $V^{\mathrm{eff}} = V + \rho A$ is now characterized by

$$V \propto e^{-\varphi/M_{\mathrm{Pl}}}, \qquad A = 1 + \frac{\beta}{2M_{\mathrm{Pl}}^2} (\varphi - \varphi_0)^2. \tag{1.24}$$

The idea is to have $\varphi \approx \varphi_0$ in dense regions, and hence, a vanishing fifth force $\partial_r \ln A \propto \beta(\varphi - \varphi_0)\partial_r \varphi \ll 1$. In low density regions, $\varphi \neq \varphi_0$ and the fifth force can become sizeable.

Vainshtein Screening

The Vainshtein screening mechanism [78, 79, 80] operates in models whose equation of motion for the scalar field contains nonlinear second derivative terms. Examples of these include the Galileon and DGP models (cf. Eqs. (1.12) and (1.15)). This mechanism will be studied with greater detail in this thesis (e.g. in Chapters 4 and 5), and so we shall be brief here. Consider a model whose equation of motion can be written as

$$A\left(\frac{\varphi_{,r}}{r}\right)^2 + B\left(\frac{\varphi_{,r}}{r}\right) = C\rho, \tag{1.25}$$

where, for concreteness, we are assuming spherical symmetry, and A, B and C are some time-dependent and model-specific functions. If ρ is small, then the spatial gradient of φ should also be small. In this case, the nonlinear term in Eq. (1.25) can be neglected compared with the other terms and one has that $\varphi_{,r}/r \sim \rho$. Recalling that for normal gravity we have that $\Phi_{,r}/r \sim \rho$, then the ratio of the fifth to the normal gravity force becomes:

$$\frac{F_{\mathrm{5th}}}{F_{\mathrm{GR}}} \sim f(t), \tag{1.26}$$

i.e., a fuction of time alone and not space. On the other hand, when the density gets high, the nonlinear term in Eq. (1.25) dominates, which results in $\varphi_{,r}/r \sim \sqrt{\rho}$. In this case, we have

$$\frac{F_{\mathrm{5th}}}{F_{\mathrm{GR}}} \sim \frac{1}{\sqrt{\rho}} \to 0, \;\; \mathrm{if} \;\; \rho \to \infty, \tag{1.27}$$

and the fifth force is suppressed compared with standard gravity.

K-mouflage Screening

K-mouflage screening [58, 81, 82] operates in models with an action of the form of Eq. (1.14). It can be shown that the ratio of the fifth to normal gravity force in models like these is given by [81, 82]

$$\frac{F_{\mathrm{5th}}}{F_{\mathrm{GR}}} \sim \frac{1}{\mathrm{d}K(\chi)/\mathrm{d}\chi}, \tag{1.28}$$

where $\chi = \nabla_\mu \varphi \nabla^\mu \varphi / 2$. The screening of the fifth force is then realized by tuning the nonlinear function $K(\chi)$ to become sufficiently large in the high-density regions of interest. The K-mouflage screening is at play in models whose equation of motion contains nonlinear first derivative terms. This is similar to the case of Vainshtein screening, except that in the latter the nonlinearity lies in second (not first) derivative terms.

1.2.3 Strategies to constrain modified gravity

Parametrization approach

One approach to constraining modified gravity models consists of parametrizing the modifications to gravity at the level of the equations of motion. For instance, Refs. [83, 84] developed a linear perturbation theory framework that parametrizes the modifications to the metric field equations in a fairly model-independent way. The idea is then to conduct observational constraints on the free functions that enter into the parametrization, and the observational viability of several specific models can be assessed by mapping their equations onto the parametrized framework. To give an example, the relevant equations for structure formation on sub-horizon scales can be written as (see e.g. Refs. [85, 86])

$$\nabla^2 \Phi \;\; = \;\; 4\pi G \left[\frac{G_{\mathrm{eff}}}{G}(a, \vec{r}) \right] \rho, \tag{1.29}$$

$$\frac{\Psi}{\Phi} \;\; = \;\; \eta(a, \vec{r}), \tag{1.30}$$

where $G_{\rm eff}(a, \vec{r})$ encapsulates the deviations from GR in the Poisson equation that governs the dynamical gravitational potential; and $\eta(a, \vec{r})$ quantifies the difference between the two Newtonian potentials. The model-independent nature of the parametrized approach, however, comes at the price that the unspecified time- and space-dependence of the free functions renders them too general to be tightly constrained. Nevertheless, by making simplistic assumptions about the form of the free functions (e.g. that they are scale independent), the parametrized framework can still prove useful in identifying observational tensions. For instance, if some data constrains $G_{\rm eff}(a) \neq 1$ or $\eta(a) \neq 1$, then this might alert us to a tension with ΛCDM. Moreover, the parametrized framework can also be useful in the search for degeneracies that might exist between the free functions. This can be used to determine which data combination can break such degeneracies [87]. Another approach is to describe the free functions in a piecewise manner, in both time and scale, and treat the amplitude of each piece as a free parameter (see e.g. Ref. [88, 89]).

The *effective field theory* (EFT) [90, 91] approach is an example of another framework, in which the parametrization is made at the level of the action instead of the equations of motion (see Refs. [92, 93] for constraint studies with EFT). Other parametrization frameworks include that developed and used by Refs. [94, 95, 96], in which the parametrization of the perturbed equations builds upon the knowledge of the field content in the action, and not its functional form.

The parametrized frameworks described above are generically employed to place fairly model-independent constraints on modified gravity using data that is sensitive to the evolution of linear density fluctuations [97]. However, in the linear regime, the predictions of modified gravity models cannot be explored to their full extent because the scale-dependent effects of the screening mechanisms are not at play in this case. This strongly motivates going beyond linear theory to constrain theories of modified gravity. In the nonlinear regime, however, the majority of the parametrized frameworks becomes less useful because the equations of the models become significantly more complicated. To try to overcome this, in Ref. [98] the authors proposed a way to parametrize the nonlinear regime of models with chameleon/symmetron/dilaton type screening via two functions of time only, which are the mass of the scalar and the coupling function to matter. This parametrization was explored in Refs. [99, 100] using N-body simulations, which being significantly more time consuming than linear perturbation theory calculations prevented the authors from run-

ning more than ≈ 100 simulations. Nevertheless, this is still a remarkable number and allows intuition to be built regarding the physics of the parametrization. However, N-body simulations are still far too slow to be used in statistical explorations of vast parameter spaces. Moreover, the parametrization of Ref. [98] does not cover models with Vainshtein or K-mouflage screening. All in all, to study the nonlinear regime of structure formation, it becomes almost imperative to proceed on a model-by-model basis.

Following a model by model approach in the nonlinear regime

Even within the parameter space of a concrete model, one must still determine which parameter combinations should be the focus of dedicated nonlinear studies. Naturally, these studies should focus on model parameters whose background and linear perturbation evolution are consistent with the CMB, BAO and SNIa observations, which are currently the most robust datasets. This way, in addition to serving as a tool to learn about the phenomenology of the models on nonlinear scales, N-body simulations can also be used to infer their observational viability. Since ΛCDM is in good agreement with the CMB, BAO and SNIa data, one may wonder if this means that any viable modified gravity model should possess a ΛCDM limit in the regime probed by these data. This is often the source of some confusion, and as a result, we believe it is important to clarify this point here. To say that ΛCDM fits the CMB, BAO and SNIa data well is to say that, in a ΛCDM cosmology, there are combinations of the cosmological parameters (such as the matter density and Hubble rate today) which yield a good fit to the data. If an alternative model behaves very closely to ΛCDM, in terms of matching the expansion rate and evolution of linear density fluctuations, then such a model will fit these data with the same goodness-of-fit and with similar parameters as well. On the other hand, if a model does not behave like ΛCDM, then one should not expect the model to fit the data with the same set of cosmological parameters. However, this does not mean that the model is unable to fit the data as well as ΛCDM, simply that the best fit is realised for a different set of parameters[6].

Over the past few years, chameleon models have been extensively studied in the nonlinear regime of structure formation, with the Hu-Sawicki $f(\mathcal{R})$ model being the classic working case [54]. This model admits ΛCDM-like expansion histories, and hence, it fits the BAO and SNIa data as well as the ΛCDM model. The CMB data constrains the model

---

[6]This is precisely what happens in the case of the Galileon model, as we shall see in Chapter 3.

parameter $|f_{\mathcal{R}0}| \lesssim 10^{-2}$ [101, 102], where $f_{\mathcal{R}0}$ is the background value of the scalar degree of freedom today. The smaller the amplitude of this value, the closer the model gets to ΛCDM. One of the strongest bounds on this parameter comes from comparisons of distance indicators in screened and unscreened dwarf galaxies [103] (see also Ref. [104]). If a galaxy is unscreened, then its stars (in this case, cepheids, water masers and tip of the red giant branch stars) behave differently, which affects the distance measurements. Reference [103] reports that this gives $|f_{\mathcal{R}0}| \lesssim 10^{-7}$. The selection of the sample of unscreened dwarfs is based on the results from N-body simulations [105, 106, 107], which show that, for values of $|f_{\mathcal{R}0}| \gtrsim 10^{-7}$, dwarfs in voids are not screened by the low-density environment (they are also not screened by their own potential), and hence, can be used in the above test. This constraint on $f(\mathcal{R})$ improves upon that from the CMB by five orders of magnitude. This highlights the benefits of going beyond linear theory with N-body simulations, particularly when there are screening mechanisms in operation whose efficiency depends on the detailed matter distribution. Other recent nonlinear studies of the Hu-Sawicki model include detailed analyses of the nonlinear and velocity power spectrum [108, 109, 110], studies of halo and subhalo properties [111, 112, 113], cluster abundances [114], redshift space distortions [115], void properties [105, 106, 116, 117], the Integrated Sachs-Wolfe effect in superclusters and supervoids [118], X-ray scaling relations of clusters [119] and Lyman-α forest statistics [120] (see Ref. [121] for a recent review on the observational status of chameleon theories, which includes the Hu-Sawicki $f(R)$ model).

The normal branch of the DGP model has been the representative model to study the Vainshtein screening mechanism on nonlinear scales. The dark energy component that this model requires on the brane is typically tuned to yield exact ΛCDM expansion histories. This model can fit the CMB data with model parameters [122] that still allow for potentially testable predictions in the nonlinear regime. The nonlinear matter and velocity power spectra have been studied in Refs. [123, 124]. Reference [125, 126] used N-body simulations of this model to illustrate how comparisons between dynamical and lensing cluster mass estimates can be a smoking gun of modified gravity (these authors also used the Hu-Sawicki model in their analysis). More recently, Refs. [127, 128] used the normal branch of the DGP model to investigate the dependence of the Vainshtein mechanism on the morphology of the cosmic web.

The nonlinear regime of structure formation was also studied with N-body simulations

in the dilaton [77] and symmetron [129] models. Reference [130] studied the formation and evolution of domain walls in simulations of the symmetron model. Coupled quintessence scenarios with an unscreened coupling to dark matter have been tested against the CMB Planck data in Ref. [97]. These models were simulated in Refs. [131, 132, 133, 134]. Recently, Ref. [135] has investigated the impact of coupled quintessence models on galactic and sub-galactic scales.

In this thesis, we extend the body of work on modified gravity by studying cosmologies with Galileon and Nonlocal gravity, which are two classes of models that have been attracting much attention recently in the theoretical community. In our analysis of these models, our first steps will always involve determining the regions of the parameter space that are consistent with the CMB, BAO and SNIa data. The CMB predictions presented in this thesis for these models were the first to be shown in the literature. Then, armed with the best-fitting parameters, we focus on the model predictions for nonlinear structure formation with the aid of N-body simulations, as well as with some analytical methods assuming spherically symmetric configurations. The study of the nonlinear regime of structure formation in these models had also never been performed prior to the work presented in this thesis. We will see that, indeed, the extra information encoded in the nonlinear regime enriches considerably the phenomenology of Galileon and Nonlocal gravity. Our investigations of these two models will determine not only how much of a serious alternative to ΛCDM they can be, but will also provide insight to develop a number of observational tests that can be used to constrain other theories of modified gravity.

1.3 Thesis outline

The rest of this thesis is organized as follows.

Chapters 2 and 3 are devoted to the predictions of the Galileon model in the linear regime of structure formation. In Chapter 2, we derive the relevant equations and solve them for a fixed number of parameter set combinations. Then, these predictions are confronted with the data from SNIa, BAO and CMB (temperature and lensing potential power spectra) in Chapter 3. By the end of these chapters, we will see that the Galileon model can fit these data with the same goodness-of-fit as ΛCDM, but with substantially different cosmological parameters, such as the total mass of the three active neutrinos Σm_ν. We

shall also identify a major observational tension associated with the sign of the Integrated Sachs-Wolfe (ISW) effect, which is what ends up bringing the observational viability of this model into question.

In Chapter 4, we take a first look at nonlinear structure formation in the Galileon model by analysing its predictions for the spherical collapse of perturbations. In this chapter, we focus on the so-called Quartic and Quintic sectors of the Galileon model. Then, in Chapter 5, we combine the results from N-body simulations and spherical collapse in the Cubic and Quartic Galileons to study the properties of dark matter haloes and build a semi-analytical halo model for the nonlinear matter power spectrum. In this chapter, we also conduct a halo occupation distribution (HOD) analysis to show that these models can match the observed galaxy clustering amplitude on large scales with realistic galaxy distributions. These chapters highlight that the screening mechanism is very efficient in the Cubic Galileon model. In the case of the Quartic Galileon model, it will become apparent that the screening mechanism cannot suppress all modifications to gravity on small scales, which may render this model incompatible with SS tests. It will also become apparent that the higher degree of nonlinearity in the equations of the Quintic Galileon model may imply that the model is unable to provide physically meaningful solutions on small length scales.

Chapter 6 is devoted to the study of the formation of large scale structure in the Nonlocal gravity model of Ref. [136]. We do so by running N-body simulations and analysing the results with the aid of semi-analytical models based on the spherical collapse of perturbations. This model does not have a screening mechanism and we discuss whether or not it is able to comply with the SS bounds. Although we do not perform a formal parameter constraint analysis, this chapter also shows that these models can fit the CMB data.

Chapter 7 focus on the gravitational lensing effects in Cubic Galileon and Nonlocal gravity cosmologies associated with galaxy clusters and cosmic voids. In the first part of the chapter, our main goal is to assess the degree to which the direct modifications to the lensing potential in these models can bias the estimation of cluster masses. We use 19 clusters from the CLASH survey [137] and find that, compared to GR, lensing mass estimates are virtually unaffected by these two gravity models. This is attributed to the strong efficiency of the Vainshtein screening in the Cubic Galileon model and to the rather weak fifth force in the Nonlocal gravity model at the cluster redshifts. In the second part of Chapter 7, we use the results from N-body simulations to measure the effects of the

modified gravity on the density profiles of voids and on their associated lensing signal. We shall see in this chapter that gravitational lensing by voids has the power to be a very good probe of gravity on large scales.

Finally, we summarize our results and outline future research directions in Chapter 8.

Unless otherwise specified, throughout this thesis we use the unit $c = 1$ and metric convention $(+, -, -, -)$. Greek indices run over $0, 1, 2, 3$ and we use $8\pi G = \kappa = M_{\mathrm{Pl}}^{-2}$ interchangeably.

Chapter 2

Linear perturbations in Galileon gravity models

We discussed in the previous chapter that, before undergoing dedicated studies of nonlinear structure formation in modified gravity models, one should first learn about their goodness-of-fit to the data from the CMB, SNIa and BAO. In this chapter, we take the first steps towards using these data to constrain the Covariant Galileon gravity model [56, 57] by studying its linear perturbation theory predictions.

In the Galileon model, the deviations from GR are mediated by a scalar field φ, dubbed the Galileon, whose Lagrangian density is invariant under the Galilean shift symmetry $\partial_\mu \varphi \to \partial_\mu \varphi + b_\mu$ (where b_μ is a constant vector), in flat spacetime. Such a field appears, for instance, as a brane-bending mode in the decoupling limit of the four-dimensional boundary effective action of the DGP braneworld model [64, 138, 139] which was proposed before the Galileon model. However, despite being theoretically appealing, the self-accelerating branch of the DGP model is plagued by the ghost problems (energy states unbounded from below) [65, 66, 67, 68]. Taking the decoupling limit of the DGP model as inspiration, it was shown in Ref. [56] that in four-dimensional Minkowski space there are only five Galilean invariant Lagrangians that lead to second-order field equations, despite containing highly nonlinear derivative self-couplings of the scalar field. The second-order nature of the equations of motion is crucial to avoid the presence of Ostrogradski ghosts [140]. Furthermore, the structure of these five Lagrangians is such that their classical solutions receive no quantum corrections to any loop order in perturbation field theory [141], i.e., the theory is *non-renormalizable*. This means that the theory is an effective field theory whose classical solutions can be trusted up to the energy scale above which a quantum completion of the theory becomes inevitable. In Ref. [57, 142], it was shown how these Lagrangians could be generalised to curved spacetimes. These authors concluded that explicit couplings between the Galileon field derivatives and curvature tensors are needed to keep the equations of motion up to second-order (see Ref. [143] for a recent discussion about how such couplings are not

strictly needed). Such couplings however break the Galilean shift symmetry which is only a symmetry of the model in the limit of flat spacetime. The couplings of the Galileon field to the curvature tensors and to itself in the equations of motion change the way in which particle geodesics responds to the matter distribution, which is why the Galileon model falls under the category of modified gravity.

Since the equations of motion are kept up to second order, it means that the Galileon model is a subclass of the more general Horndeski theory [144, 145, 146]. The Horndeski action is the most general single scalar field action one can write that yields only second order field equations of motion of the metric and scalar fields. Besides the Galileon model, it therefore encompasses simpler cases such as Quintessence (cf. Eq. (1.9)) and $f(R)$ (cf. Eq. (1.11)) models as well as other models which also involve derivative couplings of the scalar field that have recently generated some interest such as Kinetic Gravity Braiding [147, 148, 149], Fab-Four [150, 151, 152, 153, 154], K-mouflage (cf. Eq. (1.14)) and others [155, 156, 157]. An important difference between the Galileon model studied here and some other corners of Horndeski's general theory is that in the Galileon model there are no free functions.

In this chapter, we start by presenting the action and field equations of the Covariant Galileon model. We then derive the fully covariant and gauge invariant linearly perturbed field equations and solve them with a modified version of the CAMB code. We analyse the model predictions for the CMB temperature, CMB lensing and linear matter power spectra, and also for the time evolution of the lensing potential. We do this for a limited number of parameter values to illustrate how the model predictions are obtained. A main goal of this chapter is to build some intuition for the contraint results of Chapter 3.

2.1 The Covariant Galileon model

The action of the covariant uncoupled Galileon model is given by [57]

$$S = \int d^4x \sqrt{-g} \left[\frac{\mathcal{R}}{16\pi G} - \frac{1}{2} \sum_{i=1}^{5} c_i \mathcal{L}_i - \mathcal{L}_m \right], \tag{2.1}$$

with

$$
\begin{aligned}
\mathcal{L}_1 &= M^3 \varphi, \\
\mathcal{L}_2 &= \nabla_\mu \varphi \nabla^\mu \varphi, \\
\mathcal{L}_3 &= \frac{2}{M^3} \Box \varphi \nabla_\mu \varphi \nabla^\mu \varphi, \\
\mathcal{L}_4 &= \frac{1}{M^6} \nabla_\mu \varphi \nabla^\mu \varphi \left[2(\Box \varphi)^2 - 2(\nabla_\mu \nabla_\nu \varphi)(\nabla^\mu \nabla^\nu \varphi) \right. \\
&\quad \left. - R \nabla_\mu \varphi \nabla^\mu \varphi / 2 \right], \\
\mathcal{L}_5 &= \frac{1}{M^9} \nabla_\mu \varphi \nabla^\mu \varphi \left[(\Box \varphi)^3 - 3(\Box \varphi)(\nabla_\mu \nabla_\nu \varphi)(\nabla^\mu \nabla^\nu \varphi) \right. \\
&\quad + 2(\nabla_\mu \nabla^\nu \varphi)(\nabla_\nu \nabla^\rho \varphi)(\nabla_\rho \nabla^\mu \varphi) \\
&\quad \left. - 6(\nabla_\mu \varphi)(\nabla^\mu \nabla^\nu \varphi)(\nabla^\rho \varphi) G_{\nu\rho} \right],
\end{aligned}
\tag{2.2}
$$

where $\mathcal{R}$ is the Ricci curvature scalar, g is the determinant of the metric $g_{\mu\nu}$, and $M^3 \equiv M_{\text{Pl}} H_0^2$ with H_0 being the present-day Hubble expansion rate. The five terms in the Lagrangian density are fixed by the Galilean invariance in a flat spacetime, $\partial_\mu \varphi \to \partial_\mu \varphi + b_\mu$, and c_{1-5} are dimensionless constants. The explicit couplings to the Ricci scalar $\mathcal{R}$ and the Einstein tensor $G_{\mu\nu}$ in $\mathcal{L}_4$ and $\mathcal{L}_5$ break the Galilean symmetry, but are necessary to limit the equations of motion to second-order in field derivatives (and hence free from Ostrogradski ghosts) in spacetimes such as FRW [57] [1]. We set the potential term to zero ($c_1 = 0$), as we are only interested in cases where cosmic acceleration is driven by the kinetic terms of the field. Before proceeding, we note in passing that $\mathcal{L}_4$ and $\mathcal{L}_5$ are associated with some theoretical problems related to the smallness of the energy cutoff below which the theory is valid, as discussed in [56, 158]. In general, in this thesis, we shall always be more concerned about the observational consequences of the models, although such theoretical problems should always be kept in mind.

Besides the terms which appear in the Galileon Lagrangians, $\mathcal{L}_i$, we also consider here a derivative coupling of the form $\mathcal{L}_{coupling} \sim G^{\mu\nu} \nabla_\mu \varphi \nabla_\nu \varphi$, which does not spoil the second-order nature of the equations [159, 160, 161, 162, 163, 164, 165]. Here, for comparison purposes, we follow [159] and add to Eq. (2.1) the Lagrangian density

$$
\mathcal{L}_G = -c_G \frac{M_{\text{Pl}}}{M^3} G^{\mu\nu} \nabla_\mu \varphi \nabla_\nu \varphi,
\tag{2.3}
$$

---

[1]These curvature couplings act as counter terms that cancel the higher derivative terms that arise from the naive promotion of the partial derivatives to covariant ones. However, Ref. [143] has shown that, due to hidden constraints, these curvature couplings are indeed not strictly necessary.

where c_G is a dimensionless constant. The phenomenology of $\mathcal{L}_G$ is only studied in the present chapter, and not anywhere else in this thesis.

The modified Einstein field equations and the Galileon field equation of motion can be obtained by varying the action with respect to $g_{\mu\nu}$ and φ, respectively. Our derivation agrees with those present in the literature [57, 159] although we explicitly write the Riemann tensor in terms of the Ricci and Weyl tensors, whenever it leads to the cancellation of some terms and hence to a slight simplification of the final expressions. The Einstein field equations are given by:

$$G_{\mu\nu} = \kappa \quad \left[T^f_{\mu\nu} + T^{c2}_{\mu\nu} + T^{c3}_{\mu\nu} + T^{c4}_{\mu\nu} + T^{c5}_{\mu\nu} + T^{cG}_{\mu\nu} \right], \tag{2.4}$$

where

$$T^{c_2}_{\mu\nu} = c_2\left[\nabla_\mu\varphi\nabla_\nu\varphi - \frac{1}{2}g_{\mu\nu}\nabla^\alpha\varphi\nabla_\alpha\varphi\right],\tag{2.5}$$

$$T^{c_3}_{\mu\nu} = \frac{c_3}{M^3}\left[2\nabla_\mu\varphi\nabla_\nu\varphi\Box\varphi + 2g_{\mu\nu}\nabla_\alpha\varphi\nabla_\beta\varphi\nabla^\alpha\nabla^\beta\varphi - 4\nabla^\lambda\varphi\nabla_{(\mu}\varphi\nabla_{\nu)}\nabla_\lambda\varphi\right],\tag{2.6}$$

$$T^{c_4}_{\mu\nu} = \frac{c_4}{M^6}g_{\mu\nu}\left[(\Box\varphi)^2\nabla_\lambda\varphi\nabla^\lambda\varphi - \frac{1}{12}R\left(\nabla_\alpha\varphi\nabla^\alpha\varphi\right)^2 + 4\Box\varphi\nabla^\alpha\varphi\nabla^\beta\varphi\nabla_\alpha\nabla_\beta\varphi - 4\nabla_\lambda\nabla_\alpha\varphi\nabla^\lambda\nabla_\beta\varphi\nabla^\alpha\varphi\nabla^\beta\varphi\right.$$
$$\left. - \nabla_\lambda\varphi\nabla^\lambda\varphi\nabla_\alpha\nabla_\beta\varphi\nabla^\alpha\nabla^\beta\varphi - R_{\alpha\beta}\nabla^\alpha\varphi\nabla^\beta\varphi\nabla_\lambda\varphi\nabla^\lambda\varphi\right]$$
$$+ \frac{c_4}{M^6}\left[2(\Box\varphi)^2\nabla_\mu\varphi\nabla_\nu\varphi + 2\nabla_\lambda\varphi\nabla^\lambda\varphi\nabla^\rho\varphi R_{\rho(\mu}\nabla_{\nu)}\varphi - 8\Box\varphi\nabla^\lambda\varphi\nabla_\lambda\nabla_{(\mu}\varphi\nabla_{\nu)}\varphi\right.$$
$$- 2\nabla_\alpha\nabla_\beta\varphi\nabla^\alpha\nabla^\beta\varphi\nabla_\mu\varphi\nabla_\nu\varphi + 8\nabla^\lambda\varphi\nabla_\rho\nabla_\lambda\varphi\nabla^\rho\nabla_{(\mu}\varphi\nabla_{\nu)}\varphi - 2\Box\varphi\nabla_\lambda\varphi\nabla^\lambda\varphi\nabla_\mu\nabla_\nu\varphi$$
$$- 4\nabla_\alpha\nabla_\beta\varphi\nabla^\alpha\nabla^\beta\varphi\nabla_\mu\nabla_\nu\varphi - \frac{2}{3}R\nabla_\lambda\varphi\nabla^\lambda\varphi\nabla_\mu\varphi\nabla_\nu\varphi + \frac{1}{2}R_{\mu\nu}\left(\nabla_\alpha\varphi\nabla^\alpha\varphi\right)^2$$
$$\left. + 2\nabla_\mu\nabla_\alpha\varphi\nabla_\nu\nabla^\alpha\varphi\nabla_\lambda\varphi\nabla^\lambda\varphi + 4\nabla_\mu\nabla_\alpha\varphi\nabla_\nu\nabla_\beta\varphi\nabla^\alpha\varphi\nabla^\beta\varphi + 2\mathcal{W}_{\mu\alpha\nu\beta}\nabla^\alpha\varphi\nabla^\beta\varphi\nabla_\lambda\varphi\nabla^\lambda\varphi\right],\tag{2.7}$$

$$T^{c_5}_{\mu\nu} = \frac{c_5}{M^9}g_{\mu\nu}\left[(\Box\varphi)^3\nabla_\lambda\varphi\nabla^\lambda\varphi + 3(\Box\varphi)^2\nabla^\alpha\nabla^\beta\varphi\nabla_\alpha\varphi\nabla_\beta\varphi - 3\Box\varphi\nabla_\lambda\varphi\nabla^\lambda\varphi\nabla_\alpha\nabla_\beta\varphi\nabla^\alpha\nabla^\beta\varphi\right.$$
$$- 6\Box\varphi\nabla^\alpha\nabla^\beta\varphi\nabla_\alpha\nabla_\lambda\varphi\nabla_\beta\varphi\nabla^\lambda\varphi + 2\nabla_\lambda\varphi\nabla^\lambda\varphi\nabla_\alpha\nabla^\beta\varphi\nabla_\beta\nabla^\gamma\varphi\nabla_\gamma\nabla^\alpha\varphi$$
$$- 3\nabla_\alpha\nabla_\beta\varphi\nabla^\alpha\nabla^\beta\varphi\nabla_\rho\nabla_\sigma\varphi\nabla^\rho\varphi\nabla^\sigma\varphi + 6\nabla_\alpha\nabla_\beta\varphi\nabla^\beta\nabla^\gamma\varphi\nabla_\gamma\nabla_\lambda\varphi\nabla^\alpha\varphi\nabla^\lambda\varphi - R\Box\varphi\left(\nabla_\lambda\varphi\nabla^\lambda\varphi\right)^2$$
$$\left. + \frac{3}{2}R_{\alpha\beta}\nabla^\alpha\nabla^\beta\varphi\left(\nabla_\lambda\varphi\nabla^\lambda\varphi\right)^2 + 3\nabla_\lambda\varphi\nabla^\lambda\varphi\nabla^\alpha\varphi\nabla^\beta\varphi\nabla^\gamma\nabla^\sigma\varphi\mathcal{W}_{\alpha\gamma\beta\sigma}\right]$$
$$+ \frac{c_5}{M^9}\left[(\Box\varphi)^3\nabla_\mu\varphi\nabla_\nu\varphi - 3(\Box\varphi)^2\nabla_\lambda\varphi\nabla^\lambda\varphi\nabla_\mu\nabla_\nu\varphi - 6(\Box\varphi)^2\nabla^\lambda\varphi\nabla_\lambda\nabla_{(\mu}\varphi\nabla_{\nu)}\varphi + 6\Box\varphi\nabla_\lambda\varphi\nabla^\lambda\varphi\nabla_\mu\nabla_\alpha\varphi\nabla_\nu\nabla^\alpha\varphi\right.$$
$$- 6\Box\varphi\nabla_\alpha\nabla_\beta\varphi\nabla^\alpha\varphi\nabla^\beta\varphi\nabla_\mu\nabla_\nu\varphi - 3\Box\varphi\nabla_\alpha\nabla_\beta\varphi\nabla^\alpha\nabla^\beta\varphi\nabla_\mu\varphi\nabla_\nu\varphi + 6\Box\varphi\nabla^\alpha\varphi\nabla^\beta\varphi\nabla_\mu\nabla_\alpha\varphi\nabla_\nu\nabla_\beta\varphi$$
$$+ 12\Box\varphi\nabla_\alpha\varphi\nabla^\alpha\nabla^\beta\varphi\nabla_\beta\nabla_{(\mu}\varphi\nabla_{\nu)}\varphi + 3\nabla_\lambda\varphi\nabla^\lambda\varphi\nabla_\alpha\nabla_\beta\varphi\nabla^\alpha\nabla^\beta\varphi\nabla_\mu\nabla_\nu\varphi - 6\nabla_\lambda\varphi\nabla^\lambda\varphi\nabla^\alpha\nabla^\beta\varphi\nabla_\mu\nabla_\alpha\varphi\nabla_\nu\nabla_\beta\varphi$$
$$+ 6\nabla^\alpha\nabla^\beta\varphi\nabla_\alpha\varphi\nabla_\beta\varphi\nabla_\mu\nabla_\lambda\varphi\nabla_\nu\nabla^\lambda\varphi + 6\nabla^\alpha\nabla^\lambda\varphi\nabla_\beta\nabla_\lambda\varphi\nabla_\alpha\varphi\nabla^\beta\varphi\nabla_\mu\nabla_\nu\varphi + 2\nabla_\alpha\nabla^\beta\varphi\nabla_\beta\nabla^\lambda\varphi\nabla_\lambda\nabla^\alpha\varphi\nabla_\mu\varphi\nabla_\nu\varphi$$
$$+ 6\nabla^\alpha\nabla^\beta\varphi\nabla_\alpha\nabla_\beta\varphi\nabla^\lambda\varphi\nabla_\lambda\nabla_{(\mu}\varphi\nabla_{\nu)}\varphi - 12\nabla^\alpha\varphi\nabla_\alpha\nabla_\beta\varphi\nabla^\beta\nabla^\lambda\varphi\nabla_\lambda\nabla_{(\mu}\varphi\nabla_{\nu)}\varphi$$
$$- 12\nabla_\alpha\varphi\nabla^\alpha\nabla^\lambda\varphi\nabla^\sigma\varphi\nabla_\lambda\nabla_{(\mu}\varphi\nabla_{\nu)}\nabla_\sigma\varphi + \frac{3}{2}\Box\varphi\left(\nabla_\lambda\varphi\nabla^\lambda\varphi\right)^2 R_{\mu\nu} - 3\left(\nabla_\lambda\varphi\nabla^\lambda\varphi\right)^2 R_{\sigma(\mu}\nabla_{\nu)}\nabla^\sigma\varphi$$
$$+ R\left(\nabla_\lambda\varphi\nabla^\lambda\varphi\right)^2\nabla_\mu\nabla_\nu\varphi + 3\Box\varphi\nabla_\lambda\varphi\nabla^\lambda\varphi\nabla^\alpha\varphi\nabla^\beta\varphi\mathcal{W}_{\mu\alpha\nu\beta} - 6\nabla_\lambda\varphi\nabla^\lambda\varphi\nabla^\alpha\varphi\nabla^\beta\nabla^\gamma\varphi\nabla_{(\mu}\varphi\mathcal{W}_{\nu)\beta\alpha\gamma}$$
$$\left. + 6\nabla_\lambda\varphi\nabla^\lambda\varphi\nabla^\alpha\varphi\nabla^\beta\varphi\nabla^\gamma\nabla_{(\mu}\mathcal{W}_{\nu)\alpha\beta\gamma} - 6\nabla_\lambda\varphi\nabla^\lambda\varphi\nabla_\alpha\varphi\nabla^\alpha\nabla_\beta\varphi\nabla_\gamma\varphi\mathcal{W}_{(\mu\nu)}^{\beta\gamma}\right],\tag{2.8}$$

$$T^{c_G}_{\mu\nu} = \frac{M_{\rm Pl}}{M^3}c_G\left[g_{\mu\nu}\left((\Box\varphi)^2 - \nabla_\alpha\nabla_\beta\varphi\nabla^\alpha\nabla^\beta\varphi\right) + 2\nabla_\mu\nabla_\lambda\varphi\nabla_\nu\nabla^\lambda\varphi - 2\Box\varphi\nabla_\mu\nabla_\nu\varphi\right.$$
$$\left. + 2R_{\lambda(\mu}\nabla_{\nu)}\varphi\nabla^\lambda\varphi - R^{\alpha\beta}\nabla_\alpha\varphi\nabla_\beta\varphi g_{\mu\nu} + 2\mathcal{W}_{\alpha\mu\beta\nu}\nabla^\alpha\varphi\nabla^\beta\varphi - \frac{2}{3}R\nabla_\mu\varphi\nabla_\nu\varphi + \frac{1}{6}R\nabla^\lambda\varphi\nabla_\lambda\varphi g_{\mu\nu}\right].\tag{2.9}$$

The Galileon field equation of motion is given by:

$$
\begin{aligned}
0 \;=\;& c_2\Box\varphi + 2\frac{c_3}{M^3}\left[(\Box\varphi)^2 - \nabla^\alpha\nabla^\beta\varphi\nabla_\alpha\nabla_\beta\varphi - R_{\alpha\beta}\nabla^\alpha\varphi\nabla^\beta\varphi\right] \\
&+\frac{c_4}{M^6}\Bigg[2(\Box\varphi)^3 - 6\Box\varphi\nabla_\alpha\nabla_\beta\varphi\nabla^\alpha\nabla^\beta\varphi + 4\nabla_\alpha\nabla_\beta\varphi\nabla^\beta\nabla^\gamma\varphi\nabla_\gamma\nabla^\alpha\varphi - \frac{4}{3}R\nabla^\alpha\varphi\nabla^\beta\varphi\nabla_\alpha\nabla_\beta\varphi \\
&\quad -\frac{5}{3}R\Box\varphi\nabla_\lambda\varphi\nabla^\lambda\varphi + 4R_{\alpha\beta}\nabla^\alpha\nabla^\beta\varphi\nabla_\lambda\varphi\nabla^\lambda\varphi + 4R_{\alpha\beta}\nabla^\alpha\varphi\nabla^\lambda\varphi\nabla^\beta\nabla_\lambda\varphi - 2\Box\varphi R_{\alpha\beta}\nabla^\alpha\varphi\nabla^\beta\varphi \\
&\quad +4\mathcal{W}_{\alpha\beta\lambda\rho}\nabla^\alpha\nabla^\lambda\varphi\nabla^\beta\varphi\nabla^\rho\varphi\Bigg] \\
&+\frac{c_5}{M^9}\Bigg[(\Box\varphi)^4 - 6(\Box\varphi)^2\nabla_\alpha\nabla_\beta\varphi\nabla^\alpha\nabla^\beta\varphi + 3\left(\nabla_\alpha\nabla_\beta\varphi\nabla^\alpha\nabla^\beta\varphi\right)^2 - 6\nabla_\alpha\nabla^\rho\varphi\nabla_\beta\nabla_\rho\varphi\nabla^\alpha\nabla^\lambda\varphi\nabla^\beta\nabla_\lambda\varphi \\
&\quad +8\Box\varphi\nabla_\alpha\nabla^\beta\varphi\nabla_\beta\nabla^\lambda\varphi\nabla_\lambda\nabla^\alpha\varphi + 6\Box\varphi\nabla_\lambda\varphi\nabla^\lambda\varphi R_{\alpha\beta}\nabla^\alpha\nabla^\beta\varphi - 2R(\Box\varphi)^2\nabla_\lambda\varphi\nabla^\lambda\varphi \\
&\quad +\frac{1}{2}RR_{\alpha\beta}\nabla^\alpha\varphi\nabla^\beta\varphi\nabla^\lambda\varphi\nabla_\lambda\varphi - 6R_{\alpha\beta}\nabla^\lambda\varphi\nabla_\lambda\varphi\nabla^\alpha\nabla^\sigma\varphi\nabla^\beta\nabla_\sigma\varphi + 2R\nabla^\lambda\varphi\nabla_\lambda\varphi\nabla^\alpha\nabla^\beta\varphi\nabla_\alpha\nabla_\beta\varphi \\
&\quad -\frac{3}{2}R_{\rho\sigma}R^{\rho\sigma}\left(\nabla_\lambda\varphi\nabla^\lambda\varphi\right)^2 + \frac{1}{4}R^2\left(\nabla_\lambda\varphi\nabla^\lambda\varphi\right)^2 + 6\Box\varphi\mathcal{W}_{\rho\alpha\sigma\beta}\nabla^\rho\nabla^\sigma\varphi\nabla^\alpha\varphi\nabla^\beta\varphi \\
&\quad +12\mathcal{W}_{\rho\alpha\beta\sigma}\nabla^\rho\nabla^\sigma\varphi\nabla^\beta\nabla^\lambda\varphi\nabla^\alpha\varphi\nabla_\lambda\varphi + 3\mathcal{W}_{\rho\alpha\beta\sigma}\nabla^\rho\nabla^\sigma\varphi\nabla^\alpha\nabla^\beta\varphi\nabla^\lambda\varphi\nabla_\lambda\varphi \\
&\quad +6\mathcal{W}_{\alpha\rho\sigma\beta}\nabla^\rho\varphi\nabla^\sigma\varphi\nabla^\alpha\nabla^\lambda\varphi\nabla^\beta\nabla_\lambda\varphi - 3\mathcal{W}_{\alpha\rho\beta\sigma}R^{\rho\sigma}\nabla^\alpha\varphi\nabla^\beta\varphi\nabla^\lambda\varphi\nabla_\lambda\varphi \\
&\quad +\frac{3}{2}R_{\mu\alpha\beta\gamma}R_\nu{}^{\alpha\beta\gamma}\nabla^\mu\varphi\nabla^\nu\varphi\nabla^\lambda\varphi\nabla_\lambda\varphi\Bigg] \\
&+2\frac{M_{\text{Pl}}}{M^3}c_G G_{\alpha\beta}\nabla^\alpha\nabla^\beta\varphi.
\end{aligned}
\tag{2.10}
$$

The equations presented in the literature (e.g. [57, 159]) are related to ours via the following Riemann tensor expansion

$$
\begin{aligned}
R_{\mu\nu\alpha\beta} =\;& \frac{1}{2}\left(g_{\mu\alpha}R_{\nu\beta} + g_{\nu\beta}R_{\mu\alpha} - g_{\mu\beta}R_{\nu\alpha} - g_{\nu\alpha}R_{\mu\beta}\right) \\
&+\mathcal{W}_{\mu\nu\alpha\beta} - \frac{1}{6}R\left(g_{\mu\alpha}g_{\nu\beta} - g_{\mu\beta}g_{\nu\alpha}\right),
\end{aligned}
\tag{2.11}
$$

which cancels some of the terms originally derived in [57]. In Eq. (2.10), we kept only the term proportional to $c_5 R_{\mu\alpha\beta\gamma}R_\nu{}^{\alpha\beta\gamma}$ in terms of the Riemann tensor, as using Eq. (2.11) in this particular case would make the equations longer.

2.2 The perturbation equations

2.2.1 The Perturbed Equations in General Relativity

In this section, we derive the covariant and gauge invariant perturbation equations in Galileon gravity. This will be done in detail below, but first let us outline the main ingredients of $3+1$ decomposition and their application to GR (which is elegantly described in [166]) for ease of later reference.

The main idea of $3 + 1$ decomposition is to make spacetime splits of physical quantities with respect to the 4-velocity u^μ of an observer. The projection tensor $h_{\mu\nu}$ is defined by $h_{\mu\nu} = g_{\mu\nu} - u_\mu u_\nu$ and can be used to obtain covariant tensors which live in 3-dimensional hyperspaces perpendicular to u^μ. For example, the covariant spatial derivative $\hat{\nabla}$ of a tensor field $T^{\beta\cdots\gamma}_{\sigma\cdots\lambda}$ is defined as

$$\hat{\nabla}^\alpha T^{\beta\cdots\gamma}_{\sigma\cdots\lambda} \equiv h^\alpha_\mu h^\beta_\nu \cdots h^\gamma_\kappa h^\rho_\sigma \cdots h^\eta_\lambda \nabla^\mu T^{\nu\cdots\kappa}_{\rho\cdots\eta}. \tag{2.12}$$

The energy-momentum tensor and covariant derivative of the 4-velocity are decomposed, respectively, as

$$T_{\mu\nu} = \pi_{\mu\nu} + 2q_{(\mu}u_{\nu)} + \rho u_\mu u_\nu - p h_{\mu\nu}, \tag{2.13}$$

$$\nabla_\mu u_\nu = \sigma_{\mu\nu} + \varpi_{\mu\nu} + \frac{1}{3}\theta h_{\mu\nu} + u_\mu A_\nu, \tag{2.14}$$

where $\pi_{\mu\nu}$ is the projected symmetric and trace-free (PSTF) anisotropic stress, q_μ is the heat flux vector, p is the isotropic pressure, ρ is the energy density, $\sigma_{\mu\nu}$ is the PSTF shear tensor, $\varpi_{\mu\nu} = \hat{\nabla}_{[\mu}u_{\nu]}$ is the vorticity, $\theta = \nabla^\alpha u_\alpha = 3\dot{a}/a = 3H$ (a is the mean expansion scale factor) is the expansion scalar and $A_\mu = \dot{u}_\mu$; the overdot denotes a time derivative expressed as $\dot{\phi} = u^\alpha \nabla_\alpha \phi$, brackets mean antisymmetrization and parentheses symmetrization. The normalization is such that $u^\alpha u_\alpha = 1$. The quantities $\pi_{\mu\nu}$, q_μ, ρ and p are referred to as dynamical quantities and $\sigma_{\mu\nu}$, $\varpi_{\mu\nu}$, θ and A_μ as kinematical quantities. The dynamical quantities can be obtained from Eq. (2.13) using the relations

$$\rho = T_{\mu\nu}u^\mu u^\nu,$$
$$p = -\frac{1}{3}h^{\mu\nu}T_{\mu\nu},$$
$$q_\mu = h^\nu_\mu u^\rho T_{\nu\rho},$$
$$\pi_{\mu\nu} = h^\rho_\mu h^\tau_\nu T_{\rho\tau} + p h_{\mu\nu}. \tag{2.15}$$

Decomposing the Riemann tensor and making use of Einstein equations, we obtain,

after linearization, five constraint equations [166]:

$$0 = \hat{\nabla}^\alpha \left(\epsilon^{\mu\nu}{}_{\alpha\beta} u^\beta \varpi_{\mu\nu} \right), \tag{2.16}$$

$$\kappa q_\mu = -\frac{2\hat{\nabla}_\mu \theta}{3} + \hat{\nabla}^\nu \sigma_{\mu\nu} + \hat{\nabla}^\nu \varpi_{\mu\nu}, \tag{2.17}$$

$$\mathcal{B}_{\mu\nu} = \left[\hat{\nabla}^\alpha \sigma_{\beta(\mu} + \hat{\nabla}^\alpha \varpi_{\beta(\mu} \right] \epsilon_{\nu)\gamma\alpha}{}^\beta u^\gamma, \tag{2.18}$$

$$\hat{\nabla}^\nu \mathcal{E}_{\mu\nu} = \frac{1}{2}\kappa \left[\hat{\nabla}^\nu \pi_{\mu\nu} + \frac{2}{3}\theta q_\mu + \frac{2}{3}\hat{\nabla}_\mu \rho \right], \tag{2.19}$$

$$\hat{\nabla}^\nu \mathcal{B}_{\mu\nu} = \frac{1}{2}\kappa \left[\hat{\nabla}_\alpha q_\beta + (\rho+p)\varpi_{\alpha\beta} \right] \epsilon_{\mu\nu}{}^{\alpha\beta} u^\nu; \tag{2.20}$$

and five propagation equations:

$$0 = \dot{\theta} + \frac{1}{3}\theta^2 - \hat{\nabla} \cdot A + \frac{\kappa}{2}(\rho + 3p), \tag{2.21}$$

$$0 = \dot{\sigma}_{\mu\nu} + \frac{2}{3}\theta\sigma_{\mu\nu} - \hat{\nabla}_{\langle\mu}A_{\nu\rangle} + \mathcal{E}_{\mu\nu} + \frac{\kappa}{2}\pi_{\mu\nu}, \tag{2.22}$$

$$0 = \dot{\varpi}_{\mu\nu} + \frac{2}{3}\theta\varpi_{\mu\nu} - \hat{\nabla}_{[\mu}A_{\nu]}, \tag{2.23}$$

$$0 = \frac{\kappa}{2}\left[\dot{\pi}_{\mu\nu} + \frac{1}{3}\theta\pi_{\mu\nu} \right] - \frac{\kappa}{2}\left[(\rho+p)\sigma_{\mu\nu} + \hat{\nabla}_{\langle\mu}q_{\nu\rangle} \right]$$
$$- \left[\dot{\mathcal{E}}_{\mu\nu} + \theta\mathcal{E}_{\mu\nu} - \hat{\nabla}^\alpha \mathcal{B}_{\beta(\mu}\epsilon_{\nu)\gamma\alpha}{}^\beta u^\gamma \right], \tag{2.24}$$

$$0 = \dot{\mathcal{B}}_{\mu\nu} + \theta\mathcal{B}_{\mu\nu} + \hat{\nabla}^\alpha \mathcal{E}_{\beta(\mu}\epsilon_{\nu)\gamma\alpha}{}^\beta u^\gamma$$
$$+ \frac{\kappa}{2}\hat{\nabla}^\alpha \pi_{\beta(\mu}\epsilon_{\nu)\gamma\alpha}{}^\beta u^\gamma. \tag{2.25}$$

Here, $\epsilon_{\mu\nu\alpha\beta}$ is the covariant permutation tensor, $\mathcal{E}_{\mu\nu}$ and $\mathcal{B}_{\mu\nu}$ are, respectively, the electric and magnetic parts of the Weyl tensor $\mathcal{W}_{\mu\nu\alpha\beta}$, defined by $\mathcal{E}_{\mu\nu} = u^\alpha u^\beta \mathcal{W}_{\mu\alpha\nu\beta}$ and $\mathcal{B}_{\mu\nu} = -\frac{1}{2}u^\alpha u^\beta \epsilon_{\mu\alpha}{}^{\gamma\delta}\mathcal{W}_{\gamma\delta\nu\beta}$. The angle brackets mean taking the trace-free part of a quantity and $\hat{\nabla} \cdot v = \hat{\nabla}^\alpha v_\alpha$, where v is an arbitrary vector. We note that although there is some level of redundancy in the above equations, one still has enough equations to solve for all the necessary degrees of freedom as we shall see below (we opted to write the redundant equations anyway to maintain the notation of Ref. [166]).

Besides the above equations, it is useful to express the projected Ricci scalar $\hat{R}$ into the hypersurfaces orthogonal to u^μ as

$$\hat{R} = 2\kappa\rho - \frac{2}{3}\theta^2. \tag{2.26}$$

The spatial derivative of the projected Ricci scalar, $\eta_\mu \equiv a\hat{\nabla}_\mu \hat{R}/2$, is given as

$$\eta_\mu = \kappa a\hat{\nabla}_\mu \rho - \frac{2a}{3}\theta\hat{\nabla}_\mu \theta, \tag{2.27}$$

and its propagation equation is given by

$$\dot{\eta}_\mu + \frac{2\theta}{3}\eta_\mu = -\frac{2a\theta}{3}\hat{\nabla}_\mu\hat{\nabla}\cdot A - a\kappa\hat{\nabla}_\mu\hat{\nabla}\cdot q. \tag{2.28}$$

Finally, there are the conservation equations for the energy-momentum tensor:

$$\dot{\rho} + (\rho + p)\theta + \hat{\nabla}\cdot q \ = \ 0, \tag{2.29}$$

$$\dot{q}_\mu + \frac{4}{3}\theta q_\mu + (\rho + p)A_\mu - \hat{\nabla}_\mu p + \hat{\nabla}^\nu\pi_{\mu\nu} \ = \ 0. \tag{2.30}$$

We always consider the case of a spatially-flat Universe and, as a result, the spatial curvature vanishes at the background level. Thus, setting $\hat{R} = 0$ in Eq. (2.26), we obtain the first Friedmann equation

$$\frac{\theta^2}{3} = \kappa\rho. \tag{2.31}$$

Note that at the background level only the zeroth-order terms contribute to the equations. The second Friedmann equation and the energy-conservation equation are obtained by taking the zeroth-order parts of Eqs. (2.21, 2.29), as

$$\dot{\theta} + \frac{1}{3}\theta^2 + \frac{\kappa}{2}(\rho + 3p) \ = \ 0, \tag{2.32}$$

$$\dot{\rho} + (\rho + p)\theta \ = \ 0. \tag{2.33}$$

2.2.2   The Perturbation Quantities in Galileon Gravity

In the effective energy-momentum tensor approach, the field equations Eqs. (2.16 - 2.33) above preserve their forms, but the dynamical quantities ρ, p, q_μ and $\pi_{\mu\nu}$ should be replaced by the effective total ones $\rho^{tot} = \rho^f + \rho^G$, $p^{tot} = p^f + p^G$, $q_\mu^{tot} = q_\mu^f + q_\mu^G$ and $\pi_{\mu\nu}^{tot} = \pi_{\mu\nu}^f + \pi_{\mu\nu}^G$, in which the superscripts ^{G} and ^{f} identify the contributions from the Galileon field and the rest of the matter fluid (including cold dark matter, baryons, photons and neutrinos), respectively. From here on we shall drop the superscript ^{tot} for ease of notation.

Before using Eq. (2.15) to calculate ρ^G, p^G, q_μ^G and $\pi_{\mu\nu}^G$ from the components of the Galileon energy-momentum tensor of Eqs. (2.5-2.9) , we need an explicit expression for the Ricci tensor $R_{\mu\nu}$ in terms of the kinematical quantities. For this, let us expand the symmetric rank-2 tensor $R_{\mu\nu}$ in the following general way

$$R_{\mu\nu} \ = \ \Delta u_\mu u_\nu + \Xi h_{\mu\nu} + 2u_{(\mu}\Upsilon_{\nu)} + \Sigma_{\mu\nu}, \tag{2.34}$$

in which Υ_μ is a four-vector and $\Sigma_{\mu\nu}$ a PSTF rank-2 tensor, both of which live in the 3-dimensional hyperspace perpendicular to the observer's four-velocity ($u^\mu \Upsilon_\mu = u^\mu \Sigma_{\mu\nu} = 0$). Δ and Ξ are scalar quantities. Then, using the modified Einstein field equations

$$R_{\mu\nu} - \frac{1}{2} g_{\mu\nu} R = \kappa T^{tot}_{\mu\nu} = \kappa T^f_{\mu\nu} + \kappa T^G_{\mu\nu}, \tag{2.35}$$

one gets,

$$
\begin{aligned}
\Delta &= \frac{1}{2} \kappa \left(\rho + 3p \right) \\
&= -\left[\dot\theta + \frac{1}{3}\theta^2 - \hat\nabla \cdot A \right], & (2.36) \\
\Xi &= -\frac{1}{2}\kappa \left(\rho - p \right) \\
&= -\frac{1}{3}\left[\dot\theta + \theta^2 + \hat R - \hat\nabla \cdot A \right], & (2.37) \\
\Upsilon_\mu &= \kappa q_\mu \\
&= -\frac{2\hat\nabla_\mu \theta}{3} + \hat\nabla^\nu \sigma_{\mu\nu} + \hat\nabla^\nu \varpi_{\mu\nu}, & (2.38) \\
\Sigma_{\mu\nu} &= \kappa \pi_{\mu\nu} \\
&= -2\left[\dot\sigma_{\mu\nu} + \frac{2}{3}\theta\sigma_{\mu\nu} - \hat\nabla_{\langle\mu} A_{\nu\rangle} + \mathcal{E}_{\mu\nu} \right]. & (2.39)
\end{aligned}
$$

where we have used Eqs. (2.17, 2.21, 2.22, 2.26). Note that the first lines are expressed in terms of total dynamical quantities and the second lines in terms of kinematical quantities.

With the above useful relations and after some tedious but straightforward calculations, the Galileon contribution to the energy-momentum tensor up to first order in perturbed quantities can be identified as

$$
\begin{aligned}
\rho^G &= c_2 \left[\frac{1}{2}\dot\varphi^2 \right] + \frac{c_3}{M^3}\left[2\dot\varphi^3\theta + 2\dot\varphi^2\hat\Box\varphi \right] + \frac{c_4}{M^6}\left[\frac{5}{2}\dot\varphi^4\theta^2 + 4\dot\varphi^3\theta\hat\Box\varphi + \frac{3}{4}\dot\varphi^4\hat R \right] \\
&\quad + \frac{c_5}{M^9}\left[\frac{7}{9}\dot\varphi^5\theta^3 + \frac{5}{3}\dot\varphi^4\theta^2\hat\Box\varphi + \frac{1}{2}\dot\varphi^5\theta\hat R \right] + \frac{M_{\rm Pl}}{M^3}c_G\left[\dot\varphi^2\theta^2 + \frac{4}{3}\dot\varphi\theta\hat\Box\varphi + \frac{1}{2}\dot\varphi^2\hat R \right],
\end{aligned} \tag{2.40}
$$

$$
\begin{aligned}
p^G &= c_2 \left[\frac{1}{2}\dot\varphi^2 \right] + \frac{c_3}{M^3}\left[-2\ddot\varphi\dot\varphi^2 \right] \\
&\quad + \frac{c_4}{M^6}\left[-4\ddot\varphi\dot\varphi^3\theta - \dot\varphi^4\dot\theta - \frac{1}{2}\dot\varphi^4\theta^2 - 4\ddot\varphi\dot\varphi^2\hat\Box\varphi - \frac{4}{9}\dot\varphi^3\theta\hat\Box\varphi + \dot\varphi^4\hat\nabla\cdot A + \frac{1}{12}\dot\varphi^4\hat R \right] \\
&\quad + \frac{c_5}{M^9}\left[-\frac{5}{3}\ddot\varphi\dot\varphi^4\theta^2 - \frac{2}{3}\dot\varphi^5\dot\theta\theta - \frac{2}{9}\dot\varphi^5\theta^3 - \frac{2}{9}\dot\varphi^4\theta^2\hat\Box\varphi - \frac{8}{3}\ddot\varphi\dot\varphi^3\theta\hat\Box\varphi - \frac{1}{2}\ddot\varphi\dot\varphi^4\hat R - \frac{2}{3}\dot\varphi^4\dot\theta\hat\Box\varphi + \frac{2}{3}\dot\varphi^5\theta\hat\nabla\cdot A \right] \\
&\quad + \frac{M_{\rm Pl}}{M^3}c_G\left[-\frac{4}{3}\ddot\varphi\dot\varphi\theta - \frac{2}{3}\dot\varphi^2\dot\theta - \frac{1}{3}\dot\varphi^2\theta^2 + \frac{2}{3}\dot\varphi^2\hat\nabla\cdot A - \frac{4}{3}\ddot\varphi\hat\Box\varphi - \frac{4}{9}\dot\varphi\theta\hat\Box\varphi + \frac{1}{6}\dot\varphi^2\hat R \right],
\end{aligned} \tag{2.41}
$$

$$q_\mu^G = c_2 \left[\dot\varphi \hat\nabla_\mu \varphi \right] + \frac{c_3}{M^3} \left[2\dot\varphi^2 \theta \hat\nabla_\mu \varphi - 2\dot\varphi^2 \hat\nabla_\mu \dot\varphi \right]$$

$$+ \frac{c_4}{M^6} \left[-4\dot\varphi^3 \theta \hat\nabla_\mu \dot\varphi + 2\dot\varphi^3 \theta^2 \hat\nabla_\mu \varphi - \dot\varphi^4 \hat\nabla_\mu \theta + \frac{3}{2} \dot\varphi^4 \hat\nabla^\alpha \sigma_{\mu\alpha} + \frac{3}{2} \dot\varphi^4 \hat\nabla^\alpha \varpi_{\mu\alpha} \right]$$

$$+ \frac{c_5}{M^9} \left[-\frac{5}{3} \dot\varphi^4 \theta^2 \hat\nabla_\mu \dot\varphi + \frac{5}{9} \dot\varphi^4 \theta^3 \hat\nabla_\mu \varphi - \frac{2}{3} \dot\varphi^5 \theta \hat\nabla_\mu \theta + \dot\varphi^5 \theta \hat\nabla^\alpha \sigma_{\mu\alpha} + \dot\varphi^5 \theta \hat\nabla^\alpha \varpi_{\mu\alpha} \right]$$

$$+ \frac{M_{\rm Pl}}{M^3} c_G \left[-\frac{4}{3} \dot\varphi \theta \hat\nabla_\mu \dot\varphi + \frac{2}{3} \dot\varphi \theta^2 \hat\nabla_\mu \varphi - \frac{2}{3} \dot\varphi^2 \hat\nabla_\mu \theta + \dot\varphi^2 \hat\nabla^\alpha \sigma_{\mu\alpha} + \dot\varphi^2 \hat\nabla^\alpha \varpi_{\mu\alpha} \right], \tag{2.42}$$

$$\pi_{\mu\nu}^G = \frac{c_4}{M^6} \left[-\dot\varphi^4 \left(\dot\sigma_{\mu\nu} - \hat\nabla_{\langle\mu} A_{\nu\rangle} - \mathcal{E}_{\mu\nu} \right) - \left(6\ddot\varphi\dot\varphi^2 + \frac{2}{3} \dot\varphi^3 \theta \right) \hat\nabla_{\langle\mu} \hat\nabla_{\nu\rangle} \varphi - \left(6\ddot\varphi\dot\varphi^3 + \frac{4}{3} \dot\varphi^4 \theta \right) \sigma_{\mu\nu} \right]$$

$$+ \frac{c_5}{M^9} \left[- \left(\dot\varphi^5 \dot\theta + \dot\varphi^5 \theta^2 + 6\ddot\varphi\dot\varphi^4 \theta \right) \sigma_{\mu\nu} - \left(\dot\varphi^5 \theta + 3\ddot\varphi\dot\varphi^4 \right) \dot\sigma_{\mu\nu} \right.$$

$$\left. - \left(4\ddot\varphi\dot\varphi^3 \theta + \dot\varphi^4 \dot\theta + \frac{1}{3} \dot\varphi^4 \theta^2 \right) \hat\nabla_{\langle\mu} \hat\nabla_{\nu\rangle} \varphi + \left(\dot\varphi^5 \theta + 3\ddot\varphi\dot\varphi^4 \right) \hat\nabla_{\langle\mu} A_{\nu\rangle} - 6\ddot\varphi\dot\varphi^4 \mathcal{E}_{\mu\nu} \right]$$

$$+ \frac{M_{\rm Pl}}{M^3} c_G \left[- \left(2\ddot\varphi\dot\varphi + \frac{2}{3} \dot\varphi^2 \theta \right) \sigma_{\mu\nu} - \left(\frac{2}{3} \dot\varphi \theta + 2\ddot\varphi \right) \hat\nabla_{\langle\mu} \hat\nabla_{\nu\rangle} \varphi + 2\dot\varphi^2 \mathcal{E}_{\mu\nu} \right], \tag{2.43}$$

in which $\hat\Box \equiv \hat\nabla^\mu \hat\nabla_\mu$.

Following the same procure, the Galileon field equation of motion, Eq. (2.10), is given by

$$0 = c_2 \left[\ddot\varphi + \hat\Box\varphi + \dot\varphi\theta \right] + \frac{c_3}{M^3} \left[4\ddot\varphi\dot\varphi\theta + \frac{8}{3} \dot\varphi\theta\hat\Box\varphi + 4\ddot\varphi\hat\Box\varphi + 2\dot\varphi^2\theta^2 + 2\dot\varphi^2\dot\theta - 2\dot\varphi^2\hat\nabla\cdot A \right]$$

$$+ \frac{c_4}{M^6} \left[6\ddot\varphi\dot\varphi^2\theta^2 + 4\dot\varphi^3\dot\theta\theta + 2\dot\varphi^3\theta^3 + 8\ddot\varphi\dot\varphi\theta\hat\Box\varphi + \frac{26}{9} \dot\varphi^2\theta^2\hat\Box\varphi \right.$$

$$\left. - 4\dot\varphi^3\theta\hat\nabla\cdot A + 4\dot\varphi^2\dot\theta\hat\Box\varphi + 3\ddot\varphi\dot\varphi^2\hat R + \frac{1}{3} \dot\varphi^3\theta\hat R \right]$$

$$+ \frac{c_5}{M^9} \left[\frac{5}{9} \dot\varphi^4\theta^4 + \frac{20}{9} \ddot\varphi\dot\varphi^3\theta^3 + \frac{5}{3} \dot\varphi^4\dot\theta\theta^2 + \frac{8}{9} \dot\varphi^3\theta^3\hat\Box\varphi + \frac{1}{2} \dot\varphi^4\dot\theta\hat R \right.$$

$$\left. + \frac{1}{6} \dot\varphi^4\theta^2\hat R - \frac{5}{3} \dot\varphi^4\theta^2\hat\nabla\cdot A + 4\ddot\varphi\dot\varphi^2\theta^2\hat\Box\varphi + \frac{8}{3} \dot\varphi^3\dot\theta\theta\hat\Box\varphi + 2\ddot\varphi\dot\varphi^3\theta\hat R \right]$$

$$+ \frac{M_{\rm Pl}}{M^3} c_G \left[\frac{2}{3} \ddot\varphi\theta^2 + \frac{4}{3} \dot\theta\hat\Box\varphi + \frac{2}{3} \theta^2\hat\Box\varphi + \frac{4}{3} \dot\varphi\dot\theta\theta + \frac{2}{3} \dot\varphi\theta^3 - \frac{4}{3} \dot\varphi\theta\hat\nabla\cdot A + \ddot\varphi\hat R + \frac{1}{3} \dot\varphi\theta\hat R \right]. \tag{2.44}$$

As a consistency test, we checked that Eqs. (2.40 - 2.43) satisfy the conservation Eqs. (2.29, 2.30).

2.2.3 Perturbed Equations in k-space

For the purpose of the numerical studies presented in this chapter, we need to write the perturbed quantities derived in the last subsection in terms of k-space variables. This is

achieved with the aid of the following harmonic definitions:

$$\hat{\nabla}_\mu \varphi \equiv \sum_k \frac{k}{a} \gamma Q_\mu^k, \quad \hat{\nabla}_\mu \theta \equiv \sum_k \frac{k^2}{a^2} \mathcal{Z} Q_\mu^k,$$

$$A_\mu \equiv \sum_k \frac{k}{a} A Q_\mu^k, \quad \hat{\nabla}_\mu \rho \equiv \sum_k \frac{k}{a} \chi Q_\mu^k,$$

$$\pi_{\mu\nu} \equiv \sum_k \Pi Q_{\mu\nu}^k, \quad \sigma_{\mu\nu} \equiv \sum_k \frac{k}{a} \sigma Q_{\mu\nu}^k,$$

$$\eta_\mu \equiv \sum_k \frac{k^3}{a^2} \eta Q_\mu^k, \quad \mathcal{E}_{\mu\nu} \equiv -\sum_k \frac{k^2}{a^2} \phi Q_{\mu\nu}^k, \tag{2.45}$$

in which Q^k is the eigenfunction of the comoving spatial Laplacian $a^2 \hat{\Box}$ satisfying

$$\hat{\Box} Q^k = \frac{k^2}{a^2} Q^k, \tag{2.46}$$

and Q_μ^k and $Q_{\mu\nu}^k$ are given by $Q_\mu^k = \frac{a}{k} \hat{\nabla}_\mu Q^k$ and by $Q_{\mu\nu}^k = \frac{a}{k} \hat{\nabla}_{\langle\mu} Q_{\nu\rangle}$, respectively.

In terms of these harmonic expansion variables, Eqs. (2.17, 2.19, 2.22, 2.24, 2.27, 2.28) can be rewritten as

$$\frac{2}{3} k^2 (\sigma - \mathcal{Z}) = \kappa q a^2, \tag{2.47}$$

$$k^3 \phi = -\frac{1}{2} \kappa a^2 \left[k(\Pi + \chi) + 3\mathcal{H} q \right], \tag{2.48}$$

$$k(\sigma\prime + \mathcal{H}\sigma) = k^2(\phi + A) - \frac{1}{2} \kappa a^2 \Pi, \tag{2.49}$$

$$k^2(\phi' + \mathcal{H}\phi) = \frac{1}{2} \kappa a^2 \left[k(\rho + p)\sigma + kq - \Pi' - \mathcal{H}\Pi \right], \tag{2.50}$$

$$k^2 \eta = \kappa \chi a^2 - 2k\mathcal{H}\mathcal{Z}, \tag{2.51}$$

$$k\eta\prime = -\kappa q a^2 - 2k\mathcal{H}A, \tag{2.52}$$

respectively, where $\mathcal{H} = a'/a$ and a prime denotes a derivative with respect to conformal time τ ($ad\tau = dt$, with t the physical time). From Eqs. (2.40, 2.42, 2.43) one obtains the k-space variables χ^G, q^G and Π^G

$$
\begin{aligned}
\chi^G =\ & c_2 \frac{1}{a^2} \left(\varphi'\gamma' + \varphi'^2 A \right) + \frac{c_3}{M^3} \frac{1}{a^4} \left(\left[18\varphi'^2\mathcal{H}\gamma' + 18\varphi'^3\mathcal{H}A \right] + k \left[2\varphi'^3 \mathcal{Z} \right] + k^2 \left[2\varphi'^2\gamma \right] \right) \\
& + \frac{c_4}{M^6} \frac{1}{a^6} \left(\left[90\varphi'^3\mathcal{H}^2\gamma' + 90\varphi'^4\mathcal{H}^2 A \right] + k \left[15\varphi'^4\mathcal{H}\mathcal{Z} \right] + k^2 \left[12\varphi'^3\mathcal{H}\gamma + \frac{3}{2}\varphi'^4\eta \right] \right) \\
& + \frac{c_5}{M^9} \frac{1}{a^8} \left(\left[105\varphi'^4\mathcal{H}^3\gamma' + 105\varphi'^5\mathcal{H}^3 A \right] + k \left[21\varphi'^5\mathcal{H}^2 \mathcal{Z} \right] + k^2 \left[15\varphi'^4\mathcal{H}^2\gamma + 3\varphi'^5\mathcal{H}\eta \right] \right) \\
& + \frac{M_{\mathrm{Pl}}}{M^3} c_G \frac{1}{a^4} \left(\left[18\varphi'\mathcal{H}^2\gamma' + 18\varphi'^2\mathcal{H}^2 A \right] + k \left[6\varphi'^2\mathcal{H}\mathcal{Z} \right] + k^2 \left[4\varphi'\mathcal{H}\gamma + \varphi'^2\eta \right] \right),
\end{aligned}
\tag{2.53}
$$

$$
\begin{aligned}
q^G \;=\;& c_2\frac{k}{a^2}\left(\varphi'\gamma\right)+\frac{c_3}{M^3}\frac{k}{a^4}\left(6\varphi'^2\mathcal{H}\gamma-2\varphi'^2\gamma'-2\varphi'^3A\right)\\
&+\frac{c_4}{M^6}\frac{1}{a^6}\left(k\left[-12\varphi'^3\mathcal{H}\gamma'-12\varphi'^4\mathcal{H}A+18\varphi'^3\mathcal{H}^2\gamma\right]+k^2\left[\varphi'^4\sigma-\varphi'^4\mathcal{Z}\right]\right)\\
&+\frac{c_5}{M^9}\frac{1}{a^8}\left(k\left[-15\varphi'^4\mathcal{H}^2\gamma'-15\varphi'^5\mathcal{H}^2A+15\varphi'^4\mathcal{H}^3\gamma\right]+2k^2\left[-\varphi'^5\mathcal{H}\mathcal{Z}+\varphi'^5\mathcal{H}\sigma\right]\right)\\
&+\frac{M_{\rm Pl}}{M^3}c_G\frac{1}{a^4}\left(k\left[-4\varphi'\mathcal{H}\gamma'-4\varphi'^2\mathcal{H}A+6\varphi'\mathcal{H}^2\gamma\right]+\frac{2}{3}k^2\left[\varphi'^2\sigma-\varphi'^2\mathcal{Z}\right]\right),
\end{aligned}\tag{2.54}
$$

$$
\begin{aligned}
\Pi^G \;=\;& \frac{c_4}{M^6}\frac{1}{a^6}\left(k\left[-\varphi'^4\sigma'+3\varphi'^4\mathcal{H}\sigma-6\varphi''\varphi'^3\sigma\right]+k^2\left[4\varphi'^3\mathcal{H}\gamma-6\varphi''\varphi'^2\gamma+\varphi'^4A-\varphi'^4\phi\right]\right)\\
&+\frac{c_5}{M^9}\frac{1}{a^8}\left(k\left[-3\varphi'^5\mathcal{H}'\sigma+12\varphi'^5\mathcal{H}^2\sigma-15\varphi''\varphi'^4\mathcal{H}\sigma-3\varphi''\varphi'^4\sigma'\right]\right.\\
&\qquad\left.+k^2\left[-12\varphi''\varphi'^3\mathcal{H}\gamma+12\varphi'^4\mathcal{H}^2\gamma-3\varphi'^4\mathcal{H}'\gamma+3\varphi''\varphi'^4A+6\varphi''\varphi'^4\phi-6\varphi'^5\mathcal{H}\phi\right]\right)\\
&+\frac{M_{\rm Pl}}{M^3}c_G\frac{1}{a^4}\left(k\left[-2\varphi''\varphi'\sigma\right]-2k^2\left[\varphi''\gamma+\varphi'^2\phi\right]\right).
\end{aligned}\tag{2.55}
$$

Note that the spatial derivative of the isotropic pressure p in k-space is not needed in the CAMB code, which is why we do not write it here. Finally, in k-space, the perturbed Galileon field equation of motion, Eq. (2.44), reads

$$
\begin{aligned}
0 \;=\;& \frac{c_2}{a^3}\left(k\left[\gamma''+2\gamma'\mathcal{H}+\varphi'A'+\varphi'\mathcal{H}A+2\varphi''A\right]+k^2\varphi'\mathcal{Z}+k^3\gamma\right)\\
&+\frac{c_3}{M^3}\frac{1}{a^5}\left(k\left[12\gamma''\varphi'\mathcal{H}+12\varphi'^2\mathcal{H}A'-18\varphi'^2\mathcal{H}^2A+36\varphi''\varphi'\mathcal{H}A+12\varphi''\mathcal{H}\gamma'+12\varphi'\mathcal{H}'\gamma'+18\varphi'^2\mathcal{H}'A\right]\right.\\
&\qquad\left.+k^2\left[6\varphi'^2\mathcal{H}\mathcal{Z}+2\varphi'^2\mathcal{Z}'+4\varphi''\varphi'\mathcal{Z}\right]+k^3\left[4\varphi'\mathcal{H}\gamma-2\varphi'^2A+4\varphi''\gamma\right]\right)\\
&+\frac{c_4}{M^6}\frac{1}{a^7}\left(k\left[54\varphi'^2\mathcal{H}^2\gamma''-108\varphi'^2\mathcal{H}^3\gamma'+54\varphi'^3\mathcal{H}^2A'-198\varphi'^3\mathcal{H}^3A+216\varphi''\varphi'^2\mathcal{H}^2A+108\varphi''\varphi'\mathcal{H}^2\gamma'\right.\right.\\
&\qquad\left.+108\varphi'^2\mathcal{H}\mathcal{H}'\gamma'+144\varphi'^3\mathcal{H}\mathcal{H}'A\right]+k^2\left[-6\varphi'^3\mathcal{H}^2\mathcal{Z}+36\varphi''\varphi'^2\mathcal{H}\mathcal{Z}+12\varphi'^3\mathcal{H}'\mathcal{Z}+12\varphi'^3\mathcal{H}\mathcal{Z}'\right]\\
&\qquad\left.+k^3\left[-10\varphi'^2\mathcal{H}^2\gamma-12\varphi'^3\mathcal{H}A-4\varphi'^3\mathcal{H}\eta+24\varphi''\varphi'\mathcal{H}\gamma+12\varphi'^2\mathcal{H}'\gamma+6\varphi''\varphi'^2\eta\right]\right)\\
&+\frac{c_5}{M^9}\frac{1}{a^9}\left(k\left[-240\varphi'^3\mathcal{H}^4\gamma'-345\varphi'^4\mathcal{H}^4A+60\varphi'^3\mathcal{H}^3\gamma''+60\varphi'^4\mathcal{H}^3A'+300\varphi''\varphi'^3\mathcal{H}^3A+180\varphi''\varphi'^2\mathcal{H}^3\gamma'\right.\right.\\
&\qquad\left.+180\varphi'^3\mathcal{H}^2\mathcal{H}'\gamma'+225\varphi'^4\mathcal{H}^2\mathcal{H}'A\right]+k^2\left[-45\varphi'^4\mathcal{H}^3\mathcal{Z}+60\varphi''\varphi'^3\mathcal{H}^2\mathcal{Z}+15\varphi'^4\mathcal{H}^2\mathcal{Z}'+30\varphi'^4\mathcal{H}\mathcal{H}'\mathcal{Z}\right]\\
&\qquad\left.+k^3\left[-36\varphi'^3\mathcal{H}^3\gamma-12\varphi'^4\mathcal{H}^2\eta-15\varphi'^4\mathcal{H}^2A+3\varphi'^4\mathcal{H}'\eta+36\varphi''\varphi'^2\mathcal{H}^2\gamma+24\varphi'^3\mathcal{H}\mathcal{H}'\gamma+12\varphi''\varphi'^3\mathcal{H}\eta\right]\right)\\
&+\frac{M_{\rm Pl}}{M^3}\frac{c_G}{a^5}\left(k\left[6\mathcal{H}^2\gamma''+6\varphi'\mathcal{H}^2A'-18\varphi'\mathcal{H}^3A+12\varphi''\mathcal{H}^2A+12\mathcal{H}\mathcal{H}'\gamma'+24\varphi'\mathcal{H}\mathcal{H}'A\right]\right.\\
&\qquad\left.+k^2\left[6\varphi'\mathcal{H}^2\mathcal{Z}+4\varphi''\mathcal{H}\mathcal{Z}+4\varphi'\mathcal{H}\mathcal{Z}'+4\varphi'\mathcal{H}'\mathcal{Z}\right]+k^3\left[2\mathcal{H}^2\gamma-4\varphi'\mathcal{H}A+4\mathcal{H}'\gamma+2\varphi''\eta\right]\right).
\end{aligned}\tag{2.56}
$$

As another consistency test, we have checked that the conservation Eqs. (2.29, 2.30) in k-space,

$$
\chi'+(k\mathcal{Z}-3\mathcal{H}A)(\rho+p)+3\mathcal{H}(\chi+\chi^p)+kq \;=\; 0,\tag{2.57}
$$

$$
q'+4\mathcal{H}q+(\rho+p)kA-k\chi^p+\frac{2}{3}k\Pi \;=\; 0,\tag{2.58}
$$

are satisfied by the k-space perturbed expressions derived above.

Synchronous and Newtonian Gauge Equations

Here, we present the recipe to write the CGI perturbation equations in the synchronous and in the newtonian gauge [167].

The perturbed Friedmann-Robertson-Walker line element in the synchronous gauge is written as

$$ds^2{}_S = a^2(\tau) \left[d\tau^2 - (\delta_{ij} + h_{ij}^S)dx^i dx^j \right]. \tag{2.59}$$

Latin indices run over 1, 2 and 3, δ_{ij} is the delta function and the spatial perturbed metric $h_{ij}^S \equiv h_{ij}^S(\mathbf{x}, \tau)$ is given by

$$h_{ij}^S = \int d^3k \, e^{i\mathbf{kx}} \quad \left[\hat{k}_i \hat{k}_j h^S(\mathbf{k}, \tau) + 6 \left(\hat{k}_i \hat{k}_j - \frac{1}{3}\delta_{ij} \right) \eta^S(\mathbf{k}, \tau) \right], \tag{2.60}$$

where a superscript ^{S} denotes quantities in the synchronous gauge, $\mathbf{x}$ is the spatial position vector and $\hat{k} = \mathbf{k}/k$ is the unit vector mode in the $\mathbf{k}$-direction. The CGI and the synchronous gauge quantities are related by means of the following relations

$$
\begin{aligned}
\phi &= \frac{1}{4k^2} \left[6\eta''^S + h''^S \right] - \frac{1}{4}\eta^S, \\
A &= 0, \\
\eta &= -2\eta^S, \\
\mathcal{Z} &= \frac{h'^S}{2k}, \\
\sigma &= \frac{1}{2k} \left(6\eta'^S + h'^S \right).
\end{aligned}
\tag{2.61}
$$

The line element in the Newtonian (also known as longitudinal) gauge is diagonal, described by two scalar potentials Ψ and Φ, and reads

$$ds_N^2 = a^2(\tau) \left[(1 + 2\Psi)d\tau^2 - (1 - 2\Phi)dx^i dx_i \right]. \tag{2.62}$$

Written in this way, the perturbed line element is only applicable to the study of the scalar modes of the metric perturbations. The two potentials are related to the Weyl potential ϕ as

$$
\begin{aligned}
\Psi &= \phi - \frac{1}{2}\left(\frac{a}{k}\right)^2 \kappa\Pi, \\
\Phi &= \phi + \frac{1}{2}\left(\frac{a}{k}\right)^2 \kappa\Pi,
\end{aligned}
\tag{2.63}
$$

and the other CGI quantities are given by

$$
\begin{aligned}
A &= -\Psi, \\
\eta &= -2\Phi, \\
\mathcal{Z} &= -\frac{3}{k}\left(\Phi' + \Psi\mathcal{H}\right), \\
\sigma &= 0.
\end{aligned}
\tag{2.64}
$$

We do not present the full perturbed field equations in the synchronous and Newtonian gauges because they are not used in our modified `CAMB` code. However, note that `CAMB` works in the cold-dark-matter frame where $A = 0$, which is equivalent to the synchronous gauge written in a slightly different formalism.

2.3 Understanding the Galileon parameter space: free parameters and stability conditions

Before proceeding to showing the results, it is useful to analyse the equations of the model to determine which of the new parameters are actually extra parameters and which are derived ones. In this section, we also present two different approaches to obtain the background evolution. The first one involves integrating numerically the equations of the model, whereas the second approach makes use of analytical formulae that characterizes the so-called *tracker solution*. We comment also on the conditions for the avoidance of ghost and Laplace instabilities in the scalar sector of the model.

A main goal of this section is to present a concise description of some key aspects of the equations of the model, for ease of later reference. For this reason, in this section we take $c_G = 0$, as we do in all the other chapters. The inclusion of c_G in the considerations of this section is nevertheless straightforward.

2.3.1   Scaling degeneracy

By looking at Eqs. (2.40 - 2.44), we note that they are invariant under the following transformations:

$$
\begin{aligned}
c_2 &\longrightarrow c_2' = c_2/B^2, \\
c_3 &\longrightarrow c_3' = c_3/B^3, \\
c_4 &\longrightarrow c_4' = c_4/B^4, \\
c_5 &\longrightarrow c_5' = c_5/B^5, \\
\varphi &\longrightarrow \varphi' = \varphi B,
\end{aligned}
\tag{2.65}
$$

in which B is an arbitrary constant and the transformation of φ holds for both the background and perturbation parts. The reason for this scaling lies in the fact that each of the Galileon Lagrangians $\mathcal{L}_i$ yields terms which all have the same power in the Galileon field φ (for the counting of the power, the time and spatial derivatives of φ are treated equally as φ).

From a practical point of view, the scaling of the Galileon field φ is realized by rescaling its time derivative at the initial redshift, z_i, when the calculation starts, $\dot{\varphi}_i = \dot{\varphi}(z = z_i)$ [2]. As a result, according to Eqs. (2.65), the impact of smaller values of $\dot{\varphi}_i$ can always be compensated by larger values of the c_n parameters and vice versa. This makes the c_n parameters unbounded, thus preventing proper constraints on the parameter space. A possible way to break the scaling degeneracy is to use one of the Galileon parameters as a reference to write down invariant quantities under the scaling. For instance, taking c_3 as the reference parameter, then the invariant quantities are

$$
\left\{ \frac{c_2}{c_3^{2/3}}, \frac{c_4}{c_3^{4/3}}, \frac{c_5}{c_3^{5/3}}, c_3^{1/3}\dot{\varphi}_i \right\}.
\tag{2.66}
$$

---

[2]In principle, to achieve the exact scaling at the linear perturbation level, one has to resize the Galileon field perturbation $\delta\varphi_i$ and its time derivative $\dot{\delta\varphi}_i$ as well. However, our choices of initial conditions are $\delta\varphi_i = \dot{\delta\varphi}_i = 0$, which means that the resizing does not need to be done explicitly. We have checked that our results are insensitive to sufficiently small changes around these initial values for all length scales (or k-modes) that are of interest to us. Here, 'sufficiently small' means small enough to be still in the regime of linear perturbation theory. Typically, such a condition is quoted as $\delta\varphi_i \ll \bar{\varphi}_i$. However, the background value of the field is irrelevant in the covariant Galileon model since the background equations only involve $\dot{\bar{\varphi}}$ and $\ddot{\bar{\varphi}}$ and not $\bar{\varphi}$. As an alternative, we adopt $\delta\varphi_i \ll \dot{\bar{\varphi}}_i/H_i$ as a criterion for the validity of the linear perturbation analysis. This restricts $\delta\varphi_i$ and $\dot{\delta\varphi}_i$ to be so small that it makes no practical difference if they are set to be exactly zero.

The above equations make it explicit that the need to break the scaling degeneracy reduces the dimensionality of the parameter space of the model by one. Another approach could be to fix the value of c_2, so as to normalize the canonical kinetic term of the theory.

2.3.2 Tracker solution

The background energy and pressure densities of the Galileon field that enter Eqs. (2.31) and (2.32) are given by taking the zeroth-order part (non-hatted terms) of Eqs. (2.40) and (2.41), respectively, as

$$\bar{\rho}_\varphi = c_2 \left[\frac{1}{2} \dot{\varphi}^2 \right] + \frac{c_3}{M^3} \left[2\dot{\varphi}^3 \theta \right] + \frac{c_4}{M^6} \left[\frac{5}{2} \dot{\varphi}^4 \theta^2 \right] + \frac{c_5}{M^9} \left[\frac{7}{9} \dot{\varphi}^5 \theta^3 \right], \tag{2.67}$$

$$\bar{p}_\varphi = c_2 \left[\frac{1}{2} \dot{\varphi}^2 \right] - \frac{c_3}{M^3} \left[2\ddot{\varphi}\dot{\varphi}^2 \right] + \frac{c_4}{M^6} \left[-4\ddot{\varphi}\dot{\varphi}^3\theta - \dot{\varphi}^4\dot{\theta} - \frac{1}{2}\dot{\varphi}^4\theta^2 \right]$$
$$+ \frac{c_5}{M^9} \left[-\frac{5}{3}\ddot{\varphi}\dot{\varphi}^4\theta^2 - \frac{2}{3}\dot{\varphi}^5\dot{\theta}\theta - \frac{2}{9}\dot{\varphi}^5\theta^3 \right]. \tag{2.68}$$

Similarly, the background part of the equation of motion of the Galileon field is given by

$$0 = c_2 \left[\ddot{\varphi} + \dot{\varphi}\theta \right] + \frac{c_3}{M^3} \left[4\ddot{\varphi}\dot{\varphi}\theta + 2\dot{\varphi}^2\theta^2 + 2\dot{\varphi}^2\dot{\theta} \right] + \frac{c_4}{M^6} \left[6\ddot{\varphi}\dot{\varphi}^2\theta^2 + 4\dot{\varphi}^3\dot{\theta}\theta + 2\dot{\varphi}^3\theta^3 \right]$$
$$+ \frac{c_5}{M^9} \left[\frac{5}{9}\dot{\varphi}^4\theta^4 + \frac{20}{9}\ddot{\varphi}\dot{\varphi}^3\theta^3 + \frac{5}{3}\dot{\varphi}^4\dot{\theta}\theta^2 \right]. \tag{2.69}$$

The above equation and Eq. (2.31) or (2.32) can be solved numerically from some initial redshift, z_i, until the present day, $z = 0$. Reference [168] did this and showed that different initial conditions of the background Galileon field derivative, $\dot{\varphi}_i$, give rise to different time evolution that eventually merge into a common trajectory called the *tracker solution*. The advantage of assuming that the Galileon model follows the tracker at all times is twofold. First, it allows one to derive analytical formulae for the background evolution (just like, e.g., ΛCDM models), which greatly simplifies and speeds up the numerical calculations; second, it also allows us to reduce the number of free parameters by one, which is helpful when exploring the high-dimensional parameter space of the model. Next, we show these two advantages explicitly.

The tracker evolution is characterized by [168]

$$H\dot{\varphi} = \text{constant} \equiv \xi H_0^2, \tag{2.70}$$

where ξ is a dimensionless constant. Multiplying Eq. (2.31) by H^2, eliminating $\dot{\varphi}$ with

Eq. (2.70) and dividing the resulting equation by H_0^4, one obtains

$$
\begin{aligned}
E^4 &= \left(\Omega_{r0} a^{-4} + \Omega_{m0} a^{-3} + \Omega_{\nu 0} \frac{\bar{\rho}_\nu(a)}{\bar{\rho}_{\nu 0}} \right) E^2 \\
&+ \frac{1}{6} c_2 \xi^2 + 2 c_3 \xi^3 + \frac{15}{2} c_4 \xi^4 + 7 c_5 \xi^5,
\end{aligned}
\tag{2.71}
$$

in which $E \equiv H/H_0$, $\Omega_{i0} = \bar{\rho}_{i0}/\rho_{c0}$, where $\rho_{c0} = 3H_0^2/\kappa$ is the critical energy density today. The subscript r refers to radiation, m to baryonic and cold dark matter and ν refers to neutrinos (the function $\bar{\rho}_\nu(a)$ describes the time evolution of the neutrino density, which depends on neutrino mass). At the present day, Eq. (2.71) gives

$$
\Omega_{\varphi 0} \equiv 1 - \Omega_{r0} - \Omega_{m0} - \Omega_{\nu 0} = \frac{1}{6} c_2 \xi^2 + 2 c_3 \xi^3 + \frac{15}{2} c_4 \xi^4 + 7 c_5 \xi^5,
\tag{2.72}
$$

where we have assumed spatial flatness (as everywhere in this thesis). This equation can be regarded as a constraint equation for one of the Galileon parameters, i.e., one of the parameters can be fixed by the condition that the Universe is spatially flat. The assumption that the field follows the tracker allows us to fix one more Galileon parameter. This second constraint equation can be obtained by plugging Eq. (2.70) into Eq. (2.69), which yields

$$
c_2 \xi^2 + 6 c_3 \xi^3 + 18 c_4 \xi^4 + 15 c_5 \xi^5 = 0.
\tag{2.73}
$$

Equation (2.71) is a second-order algebraic equation for $E(a)$, whose solution reads

$$
\begin{aligned}
E(a)^2 = \frac{1}{2} &\left[\left(\Omega_{r0} a^{-4} + \Omega_{m0} a^{-3} + \Omega_{\nu 0} \frac{\bar{\rho}_\nu(a)}{\bar{\rho}_{\nu 0}} \right) \right. \\
&\left. + \sqrt{ \left(\Omega_{r0} a^{-4} + \Omega_{m0} a^{-3} + \Omega_{\nu 0} \frac{\bar{\rho}_\nu(a)}{\bar{\rho}_{\nu 0}} \right)^2 + 4 \Omega_{\varphi 0} } \right].
\end{aligned}
\tag{2.74}
$$

Finally, using Eq. (2.70) we have

$$
\dot{\varphi} = \xi H_0 / E(a).
\tag{2.75}
$$

These last two equations completely specify the tracker background evolution in the Galileon model. Note that in our treatment of the tracker solution, one essentially replaces $\dot{\varphi}_i$ by ξ in our notation, as can be checked by evaluating Eq. (2.75) at z_i. We stress, however, that one must first check whether the tracker solution is favoured by the observational data before comfortably using it in studies of the Galileon model. This check shall be done explicitly in the next chapter.

In summary, by assuming the (i) tracker solution and that (ii) the Universe is spatially flat, together with the (iii) need to break the scaling degeneracy, one is able to reduce the dimensionality of the parameter space of the Galileon model by three.

2.3.3 Stability conditions

In the next chapter, we present observational constraints on the Galileon model. However, the parameter space can be constrained *a priori* by the requirement to avoid the appearance of theoretical instabilities. The Galileon Lagrangian, being a subset of the more general Horndeski Lagrangian, is automatically protected against the propagation of Ostrogradsky ghosts as the equations are retained up to second order [140]. However, other sorts of theoretical pathologies may still arise.

In all our discussions about the Galileon model, we consider the conditions for each point in parameter space not to develop ghost degrees of freedom or Laplace instabilities in the scalar sector of the linear perturbations. We do not present a detailed derivation of these stability conditions, but refer the reader to Refs. [159, 169, 170] where these have been derived and discussed. The analytical method to derive these conditions is different in between Refs. [169, 170] and Ref. [159]. However, we have checked that the two formulae consistenly identify which regions of the parameter space are unstable (the reader can sneak a peak at Fig. 3.12). The no-ghost and no-Laplace stability conditions, despite applying to the scalar perturbations, depend only on background quantities. Hence, in our calculations, we first solve the background evolution to test whether or not a given set of parameters is stable. The calculation of the evolution of the perturbations is only performed if the point is theoretically viable. We only test the theoretical stability of any given point in the past, since there is no evidence that the instabilities cannot develop in the unprobed future.

One could also consider other theoretical conditions such as those which ensure that the Galileon field perturbation does not propagate superluminally (i.e. $c_s^2 > 1$). However, such cases do not necessarily imply the existence of pathologies such as the violation of causality (see e.g. [171]) and therefore we do not employ them. We also do not rule out *a priori* cases where $\bar{\rho}_\varphi < 0$ at some point in time, but instead let the data decide their viability.

2.4   Results

In this section we present and discuss our results. These were obtained with a suitably modified version of the `CAMB` code [172] to follow Galileon gravity models.

Table 2.1: The model parameters for the Galileon models studied in this chapter. The c_2 parameter is tuned to yield the required amount of dark energy today and its exact value depends on the choice of the initial Galileon energy density $\rho_{\varphi,i}$.

Models	c_3	c_4	c_5	c_G
Galileon 1	12.8	-1.7	1.0	0
Galileon 2	6.239	-2.159	1.0	0
Galileon 3	5.73	-1.2	1.0	0
Galileon 4	5.73	-1.2	1.0	-0.4
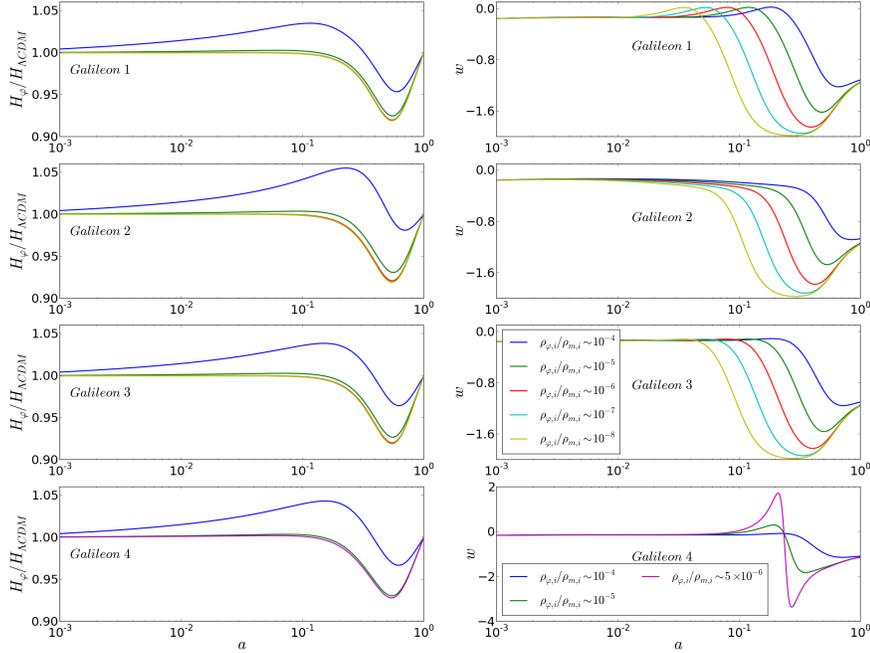
Figure 2.1: Evolution of the ratio of the Hubble expansion rates of the Galileon and ΛCDM models, $H/H_{\Lambda\text{CDM}}$ ($H = \theta/3$), and of the Galileon field equation of state parameter w. The evolutions are shown for the four models of Table 2.1 for different initial conditions, as labelled.

2.4.1 Background

In the remainder of this chapter, we compute the evolution of the cosmological background numerically (without enforcing the tracker solution) using the Friedmann equa-

Table 2.2: The values of the parameter c_2 and of the age of the Universe for all the initial conditions used in this chapter. The age for ΛCDM is 13.738 Gyr.

$\rho_{\varphi,i}/\rho_{m,i}$	c_2	Age (Gyr)
	Galileon 1	
10^{-4}	-27.00	13.978
10^{-5}	-27.49	14.317
10^{-6}	-27.56	14.366
10^{-7}	-27.58	14.374
10^{-8}	-27.59	14.375
	Galileon 2	
10^{-4}	-12.600	13.614
10^{-5}	-12.846	14.256
5×10^{-6}	-12.857	14.286
10^{-6}	-12.885	14.357
10^{-7}	-12.891	14.372
10^{-8}	-12.892	14.375
	Galileon 3	
10^{-4}	-14.760	13.854
10^{-5}	-15.122	14.296
10^{-6}	-15.179	14.363
10^{-7}	-15.188	14.373
10^{-8}	-15.189	14.375
	Galileon 4	
10^{-4}	-14.186	13.833
10^{-5}	-14.519	14.285
5×10^{-6}	-14.539	14.312

tion, Eq. (2.32), and the background Galileon equation of motion, Eq. (2.69)[3]. The value of the Galileon background energy density $\bar{\rho}_{\varphi,i}$ at the starting redshift, which we take to be $z_i = 10^6$, is determined through Eq. (2.67) by the initial values of the field time derivative $\dot{\varphi}_i$ and the expansion rate θ_i. The latter is given by the fixed matter and radiation components via Eq. (2.31) (the Galileon background energy density is negligible at early times). We specify θ_i using $\Omega_{m0} = 0.265$ and $\Omega_{r0} \approx 8 \times 10^{-5}$ for the present day values of the fractional energy density of matter and radiation, respectively [173, 174]. Since we are assuming a spatially flat Universe we need the evolution of the Galileon field to be such that $\Omega_{\varphi0} \approx 1 - \Omega_{m0} \approx 0.735$. In the previous section, we have seen that on the tracker, the flatness condition results in the constraint of Eq. (2.72). When solving the equations numerically, the strategy is to 'tune' the value of one of the Galileon parameters by a trial and error approach. In this chapter, we choose to tune c_2. As a consistency test, we have checked that Eqs. (2.31, 2.33) are satisfied by the numerical solution we obtain from `CAMB`. Moreover, we have also checked that the background expansion history from `CAMB` agrees very well with those in the literature [159, 168, 175, 176, 177, 178] and from an independent code written in `Python` by us.

We focus on four different sets of Galileon parameters which we list in Table 2.1. In [159] (to which we refer the reader for further details on the background evolution of these models) it was shown that these choices of parameters are free of ghost and Laplace instabilities (of the scalar fluctuations) for initial conditions with $\rho_{\varphi,i}/\rho_{m,i} \sim 10^{-5}$. Here we shall use this and other choices of initial conditions which have not shown any theoretical instabilities of the scalar perturbations throughout the entire expansion history. In Table 2.2 we list all these initial conditions with the derived values of the c_2 parameter and age of the Universe. In this chapter, it is not our goal to place formal constraints on the parameter space of the model and therefore we shall not be worried about the scaling degeneracy of Eqs. (2.65).

Figure 2.1 shows the time evolution of the ratio of the Hubble expansion rates, $H = \theta/3$, of the Galileon and ΛCDM models and of the Galileon field equation-of-state parameter, $w = \bar{p}_\varphi/\bar{\rho}_\varphi$. Figure 2.1 shows that, depending on the initial condition, the expansion rate

---

[3]Recall that if $c_G \neq 0$, then the equations presented in the last section should be augmented with the c_G contribution. This can be done straightforwardly by reading the background part of the c_G terms from the relevant equations.

can be faster or slower than in ΛCDM for different times during the evolution. Another noteworthy aspect of the background evolution is the possibility of having phantom dynamics, $w < -1$ [147, 148, 179]. The initial values of $\rho_{\varphi,i}$ can have a great impact on the evolution of w: the lower $\rho_{\varphi,i}$ the more negative the values of w tend to be at late times. The reason is that lower values of ρ_φ in the past force the energy density of the Galileon field to grow more drastically ($w < -1$) closer to today, in order to become the dominant component to accelerate the expansion [159, 168, 180] (see [177, 178] for expansion history observational constraints). However, for $\rho_{\varphi,i} \lesssim 10^{-5}$, the strong dependence of w on the initial conditions does not propagate into the expansion rate which is only sensitive to changes in w for times sufficiently close to today when dark energy is non-negligible. Moreover, the solutions for $\bar\rho_{\varphi,i} \lesssim 10^{-5}$ tend to have nearly the same late time evolution of w_φ. This illustrates the different initial condition being attracted to the tracker evolution. In particular, the smaller $\bar\rho_{\varphi,i}$ (smaller $\dot\varphi_i$), the earlier the solutions reach the tracker [168].

2.4.2 Linear perturbation results

We now look at the physical predictions of the full linear perturbation equations derived in the previous sections. We always use the best fit parameters from the WMAP 7-year data results [173]: $\Omega_{m0} = 0.265$, $n_s = 0.963$, $H_0 = 100h$ km/s/Mpc ($h = 0.71$), $\Omega_k = 0$, where n_s and Ω_k are the spectral index and the fractional energy density associated with the spatial curvature. Neutrinos are treated as massless in this chapter. These values are obtained for a ΛCDM model and there is no reason to believe they should be the same in a Galileon cosmology. However, in our analysis here, we prefer to focus only on the differences to ΛCDM driven by the Galileon field *per se*, and not by different cosmological parameters. The determination of the best-fitting cosmological parameters from the CMB obtained assuming Galileon cosmologies is the subject of Chapter 3. The amplitude of the primordial curvature perturbations is $A_s = 2.43 \times 10^{-9}$ at a pivot scale $k_0 = 0.002\mathrm{Mpc}^{-1}$.

As a consistency test of the results that follow, we checked that the perturbed quantities we obtain from CAMB satisfy the k-space conservation equations, Eqs. (2.57, 2.58).

CMB

In Figure 2.2, we plot the CMB power spectrum for the Galileon 3 model and ΛCDM together with the WMAP 7-year [181] (squares) and ACT [182] (circles) data. Figure 2.3 is
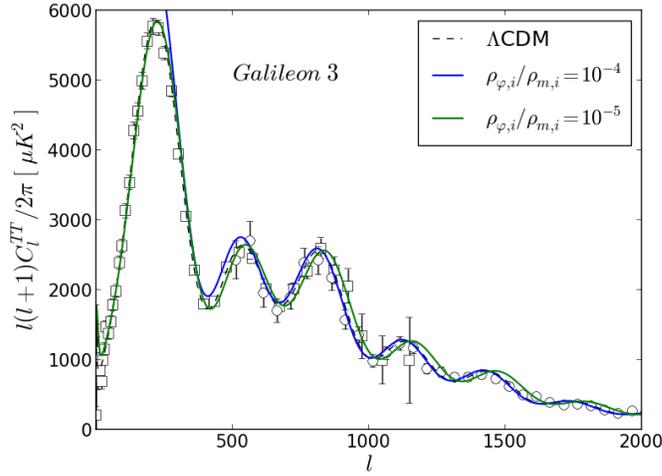
Figure 2.2: CMB temperature power spectra for the Galileon 3 model with two different initial conditions and for ΛCDM (dashed black), together with the WMAP 7-year (squares) [181] and ACT (circles) [182] data.
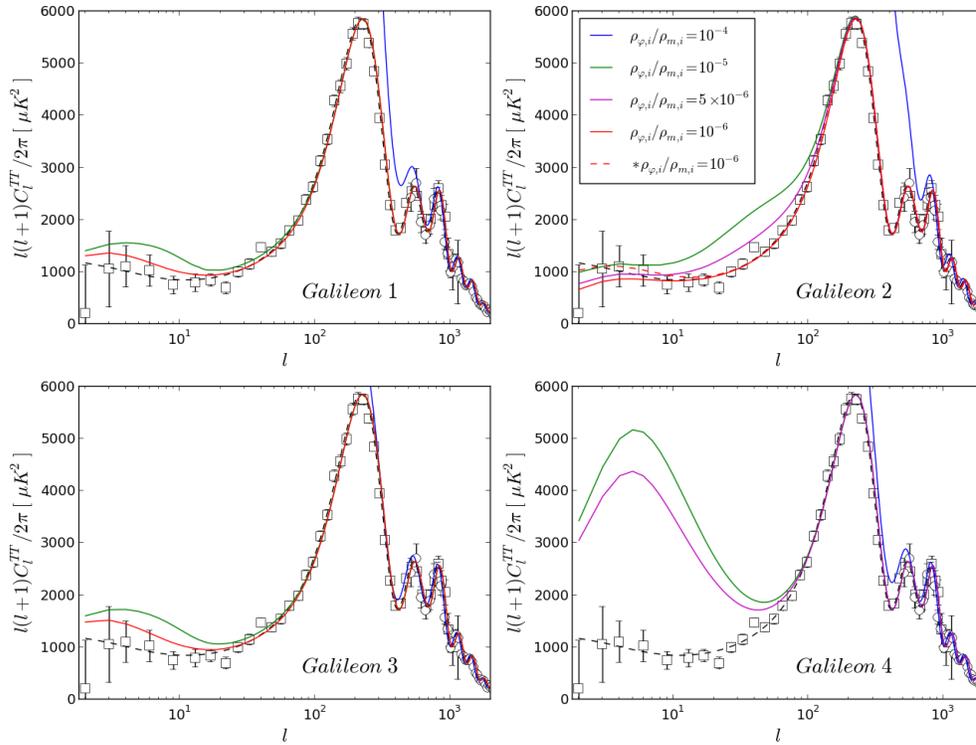
Figure 2.3: CMB power spectra for the four Galileon models for different initial conditions and ΛCDM, together with the WMAP 7-year data (squares) [181] and ACT (circles) [182] data.
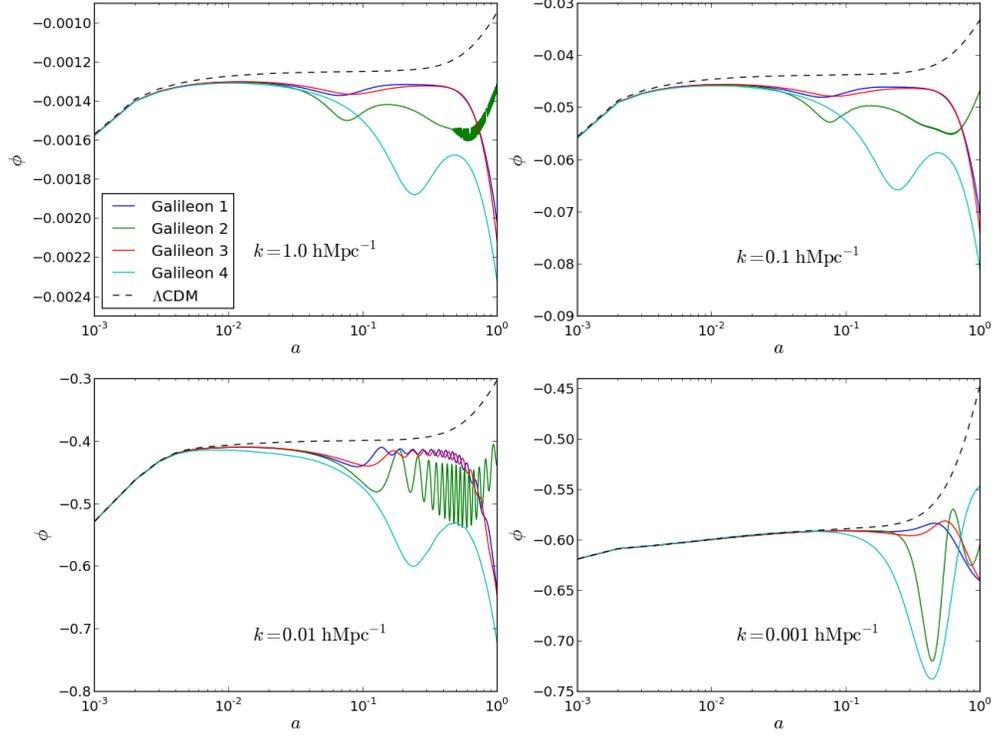
Figure 2.4: Time evolution of the Weyl (lensing) gravitational potential ϕ for the four Galileon models and ΛCDM (dashed) for $k = \{1.0, \ 0.1, \ 0.01 \text{ and } 0.001\} \ h\text{Mpc}^{-1}$. All the models have the initial condition $\rho_{\varphi,i}/\rho_{m,i} = 10^{-5}$.

the same as Figure 2.2 but for the four models of Table 2.1 with a log-scaled x-axis which highlights the low-l region. The effect of the Galileon field in the CMB power spectrum is mainly two-fold.

Firstly, the modifications of the expansion rate can shift the positions of the CMB acoustic peaks. The value of the initial condition has an impact on the background expansion rate and hence on the distance to the surface of last scattering, which translates into different positions for the peaks. For sufficiently small values of $\rho_{\varphi,i}/\rho_{m,i} \lesssim 10^{-5}$ (not plotted in Figure 2.2 since they are indistinguishable from the $\rho_{\varphi,i}/\rho_{m,i} = 10^{-5}$ case) the Galileon 3 curves have essentially the same peaks positions since the expansion rate becomes insensitive to $\rho_{\varphi,i}/\rho_{m,i}$ (cf. Figure 2.1). The same applies for the Galileon 1, Galileon 2 and Galileon 4 models.

Secondly, the late time evolution of the gravitational potential can be also different from ΛCDM, resulting in a modified signal of the ISW effect on the largest angular scales (low l

in Figure 2.3). For instance, the choice $\rho_{\varphi,i}/\rho_{m,i} = 10^{-4}$ is completely ruled out for all the models shown, since the spectrum at low l is larger than the observational data by several orders of magnitude. In this case, the ISW effect is so pronounced that it dominates over the first acoustic peak and can also have an impact on the second and third ones.

Lowering the initial amount of dark energy helps to reconcile the models with the data. However, for Galileon 4 there is still too much power on large scales. Note that this model differs from Galileon 3 by having a non-vanishing value of c_G and it is impossible to keep lowering the initial Galileon density ($\rho_{\varphi,i}/\rho_{m,i} \sim 5 \times 10^{-6}$) as Laplace instabilities start to appear. This hints that the strength of the derivative coupling c_G can have a crucial impact on the predictions. For all the other models (Galileon 1 to Galileon 3), for sufficiently small values of $\rho_{\varphi,i}/\rho_{m,i}$, the dependence on the initial conditions becomes less pronounced and the fit to the CMB improves. There are still differences from the best fit ΛCDM model and from the data at low l, but since the errorbars are also larger due to cosmic variance, Galileon 1 to Galileon 3 models may still be compatible with the observations.

It is interesting to note that the CMB power spectrum for the Galileon 1 and Galileon 3 models can be quite similar although their c_3 and c_4 parameters are different. This shows that there are, to some extent, degeneracies in the Galileon model parameter space. On the other hand, changing only one of the Galileon parameters can also change considerably the CMB predictions. For instance, in the top-right panel we plot the CMB power spectrum of a model sharing all the parameters of Galileon 2 in Table 2.1 except that $c_4 = -1.659$, for $\rho_{\varphi,i}/\rho_{m,i} = 10^{-6}$ (dashed red). Note that c_2 also differs because it is tuned to yield the required amount of dark energy today, giving $c_2 = -14.968$. We see that by changing only c_4 the predicted CMB spectrum gets closer to the data for the lowest values of l. It is also interesting to note that all the models have the value of c_5 fixed and we expect a richer phenomenology if we allow this parameter to vary as well.

To further understand the CMB predictions of the Galileon model at low l, we plot in Figure 2.4 the time evolution of the Weyl potential, ϕ, which is the relevant quantity for the ISW effect. We show the evolution for different values of k for the initial condition $\rho_{\varphi,i}/\rho_{m,i} = 10^{-5}$. The variety of evolutions can be very rich within the parameter space of the Galileon model and depends on the scale under consideration. The evolution of ϕ agrees, to some extent, with the ΛCDM model during the radiation dominated era. However, in the matter era, while ϕ is constant in the ΛCDM model, that is not the case for

Galileon gravity and the gravitational potential does evolve with time. In particular, we note a very pronounced variation with time of ϕ for Galileon 4 during the matter era and today which explains why there is so much power at low l in this model (c.f. Figure 2.3). Moreover, for the models shown, the gravitational potential suffers an overall deepening with time [159, 180, 183, 184], in clear contrast with the ΛCDM model where the gravitational potential gets shallower with the onset of the accelerated expansion. We shall analyse this feature with more detail in Sec. 3.3.2, but we anticipate here that the late-time deepening of the lensing potential has a very strong potential to rule out the entire Galileon model!

Weak lensing power spectrum

The weak lensing signal of the CMB anisotropies is determined by the projected lensing potential ψ, which is an effective potential obtained by integrating the Weyl potential, ϕ, from today to the time of last scattering [185] (see also [186] for a concise description and application to modified gravity theories).

The angular power spectrum of ψ is plotted in Figure 2.5 for the four Galileon models and we see that it can be noticeably larger than the ΛCDM result on all scales, which follows from the larger values (in magnitude) of ϕ in these models (cf. Figure 2.4). The Galileon 4 model is the one where the gravitational potential deepens the most with time and it is therefore the model with the most lensing power. The initial conditions also have an impact on the result, especially for $\rho_{\varphi,i}/\rho_{m,i} \gtrsim 10^{-6}$. For instance, for the case $\rho_{\varphi,i}/\rho_{m,i} = 10^{-4}$ (which is not plotted) the power is higher by several orders of magnitude for all the models.

This is an important result and it shows that weak lensing measurements have the capability to place strong constraints on the Galileon gravity model. In particular, the Galileon 1 to Galileon 3 models, which have CMB temperature power spectrum predictions similar to that of ΛCDM for $\rho_{\varphi,i}/\rho_{m,i} = 10^{-6}$ (red line), nevertheless have very distinctive predictions for the power spectrum of the lensing potential. In Chapter 3, measurements of $C_l^{\psi\psi}$ shall be used to constrain the model.

Matter power spectrum

Figure 2.6 shows the linear matter power spectrum predicted in the different models. We have chosen to plot the power spectra at redshift $\bar{z}_{LRG} = 0.31$, which is the median redshift
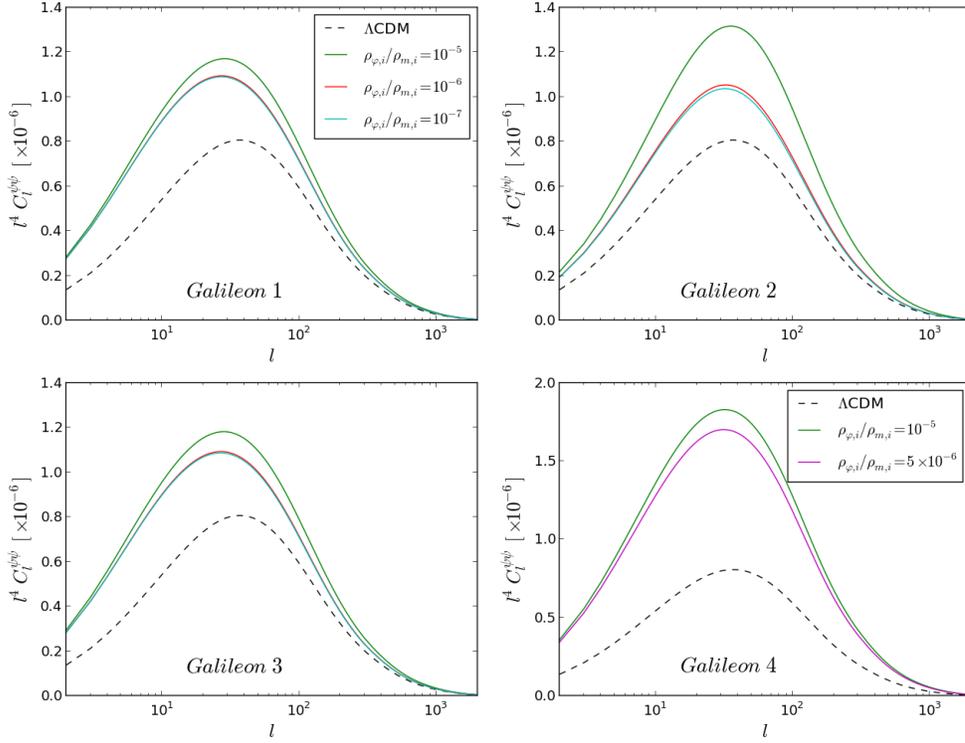
Figure 2.5: Angular power spectrum of the weak lensing potential ψ for the four Galileon models with different initial conditions and ΛCDM (dashed).

of luminous red galaxies (LRGs) in DR7 from the Sloan Digital Sky Survey (SDDS) [189]. A recent estimate of the power spectrum of LRGs is shown by the points with errorbars reproduced in each panel [187]. By plotting the matter power spectrum at the same redshift as the measurement, there is no need to make any adjustment for the growth factor to compare theory to observation. However, since we are plotting the prediction of linear perturbation theory in real space, there are three effects which could be responsible for any discrepancies between the theoretical spectra and the measurement: 1) Galaxy bias. This is generally modelled as a constant shift in the amplitude of the power spectrum on large scales, though simulations show that the bias is scale dependent, particularly for highly clustered objects [190]. 2) Redshift-space distortions. Using peculiar velocities to infer the radial distance to a galaxy introduces a systematic shift in the clustering amplitude. Again, this can be scale dependent [191]. 3) Non-linear effects. This includes the familiar mode coupling between fluctuations on different scales, but also, in the case of the Galileon models, possible screening effects which could introduce scale dependent departures from
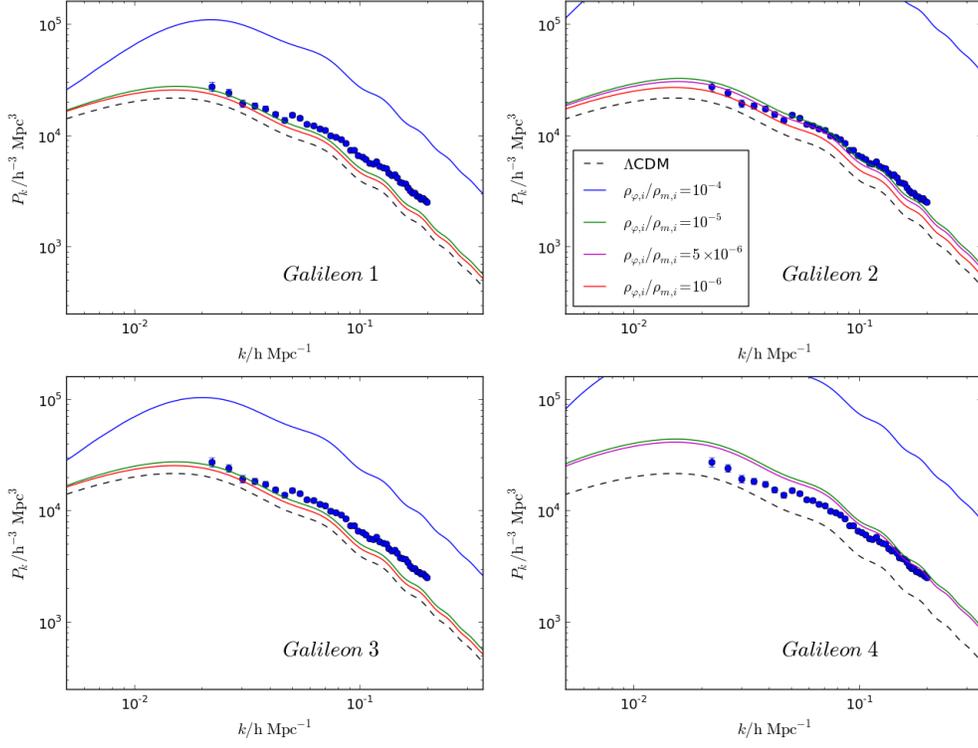
Figure 2.6: Matter power spectrum at redshift $\bar{z}_{LRG} = 0.31$ for the four Galileon models with different initial conditions and ΛCDM (dashed), together with the SDSS-DR7 LRG host halo power spectrum [187]. The measurements are scaled by a factor of 1.85^{-2} [188] and $\bar{z}_{LRG}$ is the mean redshift of the LRG sample.

the linear perturbation theory predictions. It is important to note also that the amplitude of the actual LRG power spectrum shown in Fig. 2.6 is scaled down by a factor of 1.85^{-2}, as explained in the Erratum [188].

A robust comparison between theory and observations should take all three complications above into account. This shall be done in Chapter 5 using Halo Occupation Distribution (HOD) methods applied on the results from N-body simulations. For now, we simply note that the difference to ΛCDM depends sensitively on the value of $\rho_{\varphi,i}/\rho_{m,i}$. For instance, the initial condition $\rho_{\varphi,i}/\rho_{m,i} = 10^{-4}$ has a substantial excess of power relative to ΛCDM, which suggests it may be hard to reconcile these models with the data. Lowering $\rho_{\varphi,i}/\rho_{m,i}$ brings the Galileon models into closer agreement with ΛCDM and the results become less sensitive to the initial conditions (lower initial conditions have nearly the same prediction as $\rho_{\varphi,i}/\rho_{m,i} = 10^{-6}$). However, all the models still produce an excess of power
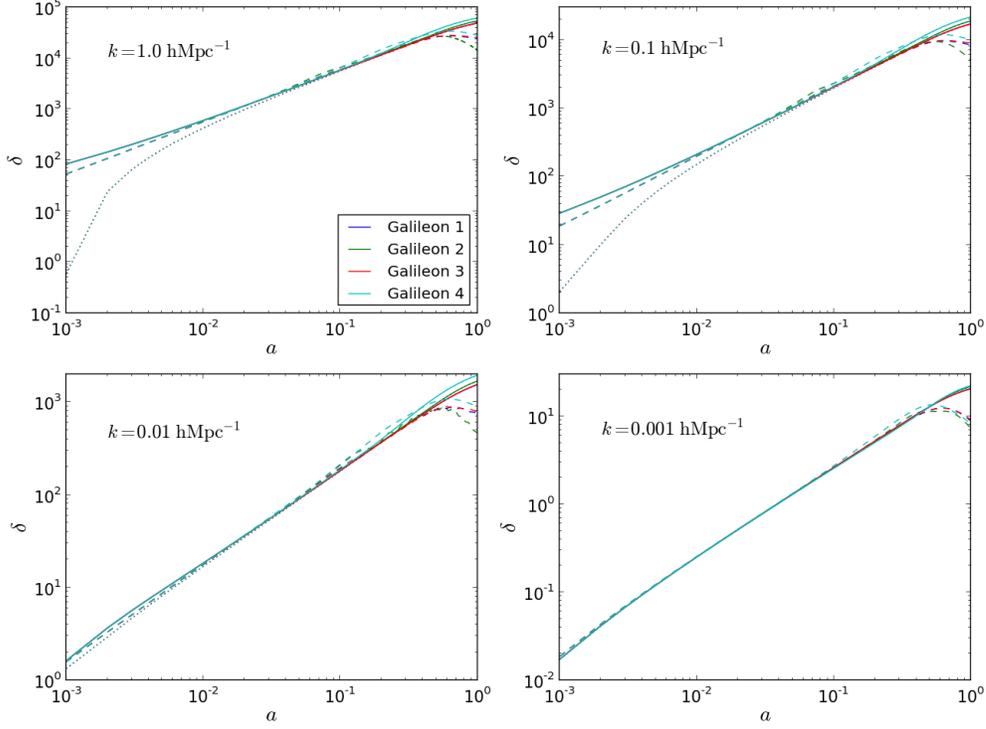
Figure 2.7: Time evolution of the linear density contrast of dark matter (DM, solid lines), $\delta_{\rm DM} = \rho_{DM}/\bar{\rho}_{DM} - 1$, baryonic matter (B, dotted lines), $\delta_{\rm B} = \rho_B/\bar{\rho}_B - 1$, and Galileon field (dashed lines), $\delta_\varphi = \rho_\varphi/\bar{\rho}_\varphi - 1$, for the four Galileon models for $k = \{1.0,\ 0.1,\ 0.01 \text{ and } 0.001\}\ {\rm hMpc}^{-1}$. All the models have initial condition $\rho_{\varphi,i}/\rho_{m,i} = 10^{-5}$.

when compared to ΛCDM indicating that the formation of linear structure is enhanced by the modifications of gravity in the Galileon model, a conclusion in agreement with previous linear perturbation studies in the literature [159, 180, 183, 192]. The Galileon 4 model is the one where the effects are the most pronounced. This indicates, once again, that the c_G parameter can have a critical impact on the results.

Clustering of the Galileon field

We now turn the attention to the time evolution of the linear density contrast of the Galileon field $\delta_\varphi = \rho_\varphi/\bar{\rho}_\varphi - 1$. This is plotted in Figure 2.7 for the initial condition $\rho_{\varphi,i}/\rho_{m,i} = 10^{-5}$. We see that the Galileon density contrast (dashed lines) can be large, being comparable with the dark matter (solid lines) and baryonic matter (dotted lines) density contrasts throughout most of the evolution. This happens for all the scales considered including small scales
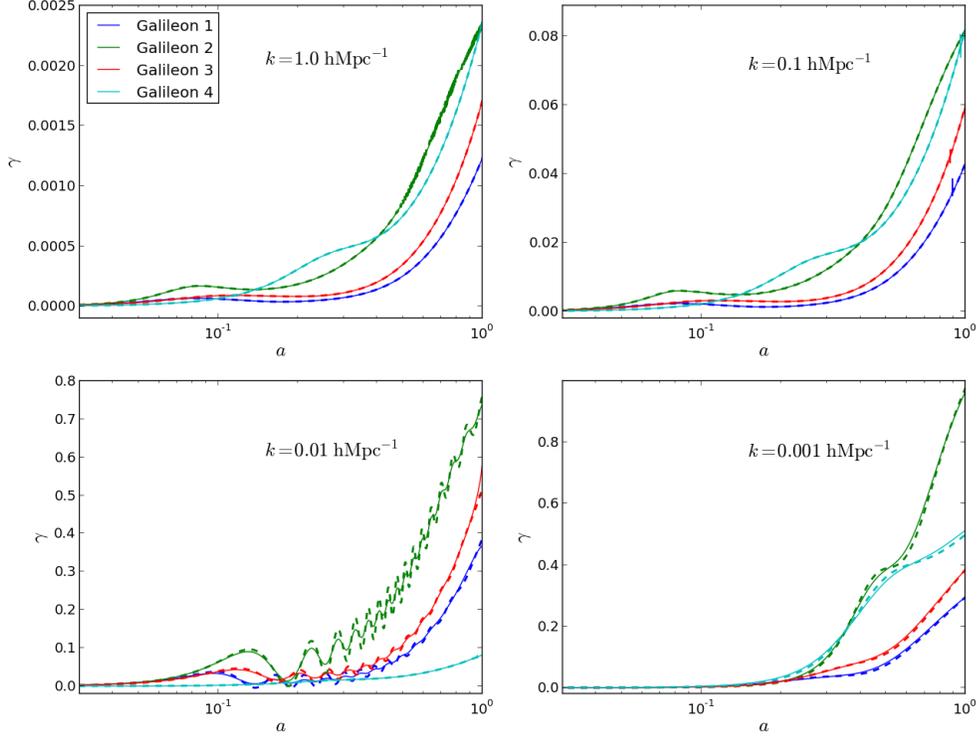
Figure 2.8: Time evolution of the k-space Galileon field perturbation γ (dashed) along with the corresponding quasi-static limit (solid), for the four Galileon models for $k = \{1.0,\ 0.1,\ 0.01\ \text{and}\ 0.001\}\ \text{hMpc}^{-1}$. All the models have initial condition $\rho_{\varphi,i}/\rho_{m,i} = 10^{-5}$.

such as $k = 1.0\ \text{hMpc}^{-1}$.

This strong clustering of the Galileon field has a large impact on the evolution of the Weyl gravitational potential ϕ which directly determines many observables such as the ISW effect (c.f. Figure 2.3), weak lensing (c.f. Figure 2.5) and clustering of matter (c.f. Figure 2.6).

Quasi-static limit approximation

In Figure 2.8 we plot the time evolution of the k-space Galileon perturbation, γ (dashed), along with the corresponding solution obtained in the quasi-static limit (solid). The quasi-static limit is the limit in which the spatial derivatives of the field are dominant over the time derivative ones. Practically, this means neglecting all terms in the field equations that are suppressed by $\mathcal{H}^2/k^2$ or φ'/k^2.

As for the evolution of the density contrast δ_{φ} and the Weyl potential ϕ, here there is also a strong scale dependence. Moreover, we see that even for near-horizon scales such as

$k = 0.001 \text{ hMpc}^{-1}$ the quasi-static limit can be a good (though not perfect) approximation to the full solution. In particular, in the Galileon 2 curves with $k = 0.01 \text{ hMpc}^{-1}$, one can see that the quasi-static approximation agrees quite well with the full solution despite the oscillations in the latter. The quasi-static limit appears therefore to be valid for many cases in the Galileon model, especially when one is interested in subhorizon scales.

2.5 Summary

In this chapter, we took the first step towards constraining Galileon gravity with linear perturbation theory by studying its cosmological preditions for a fixed number of parameter set values. For this, we derived the full CGI perturbation equations, which were then solved using a modified version of the `CAMB` code. We validated our `CAMB` code by performing several successful consistency tests.

The main results in this chapter can be summarized as follows:

- The expansion rate in Galileon cosmologies can depend sensitively on the initial value of the Galileon field energy density, especially if the latter is not small, e.g., if $\rho_{\varphi,i}/\rho_{m,i} \gtrsim 10^{-5}$ ($z_i = 10^6$). Throughout the evolution (cf. Fig. 2.1), the expansion rate can be faster or slower than in ΛCDM and the Galileon equation-of-state parameter is phantom-like ($w < -1$) at late times.

- The modified background expansion leads to a visible shift in the positions of the acoustic peaks of the CMB temperature power spectrum. The strongest effect of the Galileon field on the CMB temperature power spectrum, however, appears to be on the largest angular scales (low values of l, cf. Fig. 2.3), where the full power receives a significant contribution from the integrated Sachs-Wolfe effect. This is due to the late-time evolution of the gravitational potential ϕ, which in Galileon models tends to become deeper at late times (more negative), and does so rather rapidly, compared to ΛCDM (cf. Fig. 2.4).

- The evolution of the gravitational potential influences a number of cosmological observables, both directly and indirectly. In addition to the ISW effect, it also has a strong impact on the growth of matter density perturbations (cf. Fig.2.6) and gravitational lensing. In particular, we have shown that the Galileon model can predict considerably more power than ΛCDM for the weak lensing power spectrum (cf. Fig. 2.5), even if the predictions

of the two models for the CMB power spectrum more or less agree. In Chapter 3, we shall use the weak lensing power spectrum data from the Planck mission to constrain the Galileon model.

- We have seen that the Galileon field can cluster substantially (cf. Fig. 2.7) and that the quasi-static approximation for the evolution of the Galileon field perturbation serves as a good approximation on subhorizon scales (cf. Fig. 2.8).

- At first sight, the physics of the Galileon field appears to be described by the nine extra parameters: $\left\{ c_1, c_2, c_3, c_4, c_5, \bar{\varphi}_i, \dot{\bar{\varphi}}_i, \delta\varphi_i, \dot{\delta\varphi}_i \right\}$. However, $\bar{\varphi}_i$, is an irrelevant parameter since it never enter the equations of the model. Furthermore, the initial values of the field perturbation and its time derivative can be fixed to zero $\delta\varphi_i = \dot{\delta\varphi}_i = 0$, with no impact on the results. In this chapter (and in fact in all this thesis) we always consider $c_1 = 0$, as this is a potential term and we are interested only in cases where the acceleration is driven by kinetic terms. By assuming that (i) the background is spatially flat and (ii) that the field evolves according to the tracker solution, then two of the Galileon parameters are given in terms of the others (cf. Sec. 2.3). Finally, the need to break the scaling degeneracy of the model, allows one to fix one more parameter (cf. Sec. 2.3). If all these considerations are applied, then the Galileon model that we shall study in the remainder of this thesis contains only two extra parameters, relative to ΛCDM.

In conclusion, we have shown that the detailed study of the full perturbation equations unveils a rich phenomenology in Galileon gravity models. The results presented in this chapter also show that the model predictions depend sensitively on the exact parameter combinations. The indications are that strong constraints can be placed on the parameter space of the model, which is precisely what we shall determine in the next chapter.

Chapter 3

The observational status of Galileon gravity after Planck

To fully assess the observational viability of any cosmological model we must allow all of its parameters to vary within the observational constraints. This helps to understand any hidden degeneracies between the parameters that are hard to identify if one studies only a handful of parameter value combinations.

This chapter builds upon the methodology described in Chapter 2. We use the modified version of the `CAMB` code developed there to perform a Monte Carlto Markov Chain (MCMC) exploration of the full cosmological parameter space, and not only its Galilean subspace. We place observational constraints using the CMB temperature and CMB lensing potential data from the Planck satellite [193, 194], together with BAO data at lower redshift. Here, we shall pay special attention to the role played by the summed mass of the three active neutrinos, Σm_ν, in the constraints of the Galileon model.

We start this chapter by describing our methodology. Some of it is different from the one used to obtain the results in the last chapter, namely in what concerns the treatment of the background evolution. For clarity, we shall therefore be careful at justifying the steps we follow to constrain the Galileon model.

3.1 Methodology

3.1.1 MCMC chains setup

We use the publicly available `CosmoMC` code [195] to carry out the formal exploration of the full Galileon cosmological parameter space. We select the Metropolis-Hastings algorithm (see [195] for a concise description) as the MCMC method to draw the samples from

the posterior probability distribution, which is determined by the observational data. The code is compatible with our modified version of `CAMB` that we presented in Chapter 2. Our results were obtained by running eight chains in parallel with the stoping convergence criterion $R - 1 < 0.02$, where R is the Gelman and Rubin statistic given by $R =$"variance of chains means"/"mean of chains variances" [196]. The estimation of the likelihood from the samples was performed using the routines in the `Getdist` software supplied in the `CosmoMC` package. We do not consider the first half of the chains in the likelihood evaluation to eliminate points sampled during the 'burn-in' period of the chains.

When the MCMC algorithm tries a new point in parameter space, our code first solves the background evolution, testing whether or not it satisfies all the stability criteria (cf. Sec. 2.3.3). The calculation of the evolution of the perturbations and the subsequent likelihood evaluation is only performed if the point is theoretically viable. Without this initial check, these points would still be rejected as the instabilities drastically affect the evolution of the gravitational potential, and hence, lead to very poor fits to the CMB data. However, this step helps to speed up the overall performance of the code, and also avoids the numerical difficulties associated with the instabilities. We want to stress that these theoretical constraints are a convenient way to select only those points which give viable perturbation evolution, and once these constraints are satisfied so that a trial parameter point is not rejected straightaway, they play no further role in the calculation of likelihoods. Although we are mostly interested in scalar perturbations, we note that in principle one could impose similar conditions for the avoidance of ghost and Laplace instabilities of the tensor perturbations [169, 197] (see Sec. 3.5 below).

3.1.2 Background evolution: justifying the use of the tracker solution

In this chapter, we use the analytical formulae associated with the tracker solution of the background evolution of the Galileon model (cf. Sec. 2.3). However, one must first check if the tracker evolution is compatible with the observational data. Otherwise, by assuming the tracker we could be restricting ourselves to a corner of the parameter space of the model that could not provide a good fit. Next, we illustrate for an explicit case that the background evolution must follow the tracker solution since sufficiently early times, if the model is to fit the CMB data. In Ref. [2] (on which some of the results of this chapter are based), the same conclusion is reached when all of the parameters are allowed to vary.
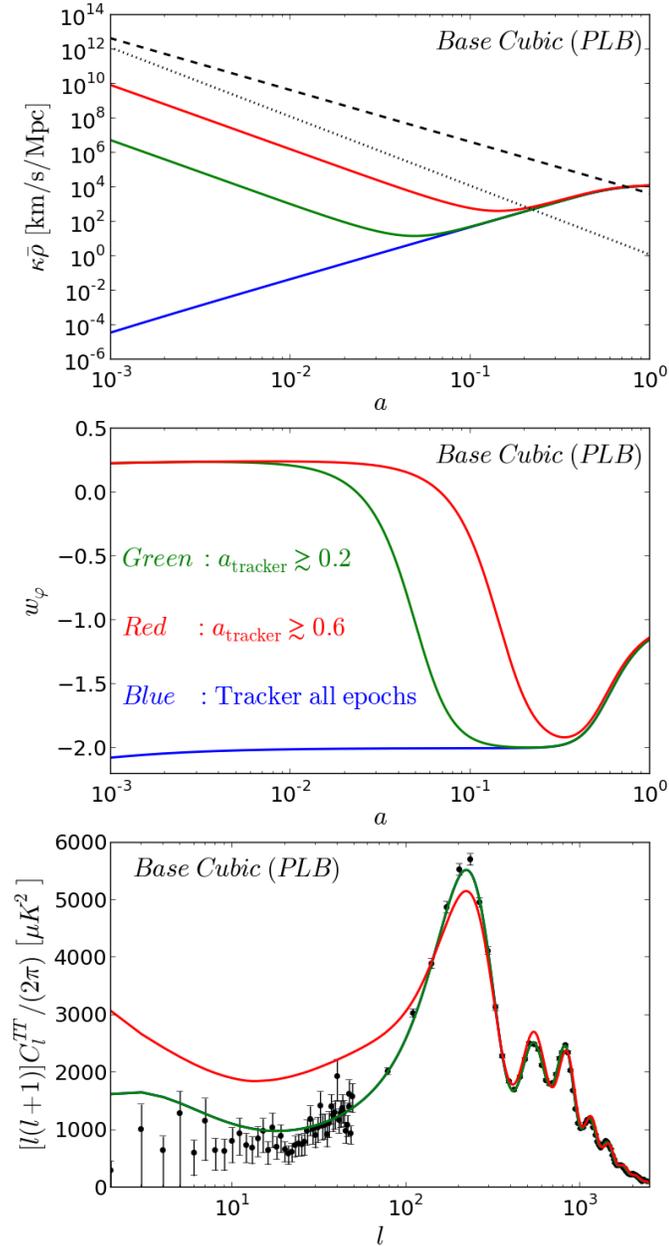
Figure 3.1: From top to bottom, the first two panels show the time evolution of the background energy density and of the Galileon field equation-of-state parameter w_φ for the base Cubic (PLB) model. The time evolution is shown for three cases that differ in the time when the background evolution follows the tracker solution: all epochs (blue), $a \gtrsim 0.2$ (green) and $a \gtrsim 0.6$ (red). The bottom panels shows the corresponding CMB power spectrum (here, the blue and green curves are overlapping). In the top panel, the dashed and dotted curves correspond, respectively, to the energy density of matter (baryons and CDM for this model) and radiation (photons and massless neutrinos for this model).

Figure 3.1 shows the time evolution of the Galileon field background energy density $\bar{\rho}_\varphi$ (upper) and equation-of-state parameter w_φ (middle), for the one of the best-fitting models that we shall find below [1], for three different epochs where the background evolution follows the tracker solution: all cosmic epochs (blue), $a \gtrsim 0.2$ (green) and $a \gtrsim 0.6$ (red). The lower panel shows the respective CMB temperature angular power spectrum. One notes that, indeed, models with different time evolution at early times eventually start following the tracker solution (as we have "hinted" already in Fig. 2.1). The latter is characterized by a phantom evolution $w_\varphi < -1$, i.e., the dark energy density grows with the expansion of the Universe. Also, the tracker is reached sooner if the Galileon density is smaller at earlier times. When solving the background equations numerically, the initial conditions are set up by different values of $\bar{\varphi}_i$ at some initial time. The figure shows that, if the background evolution is not on the tracker sufficiently before the start of the dark energy era ($a \sim 0.5$), then this leads to a poor fit to the CMB temperature data. This was a result that we could have already anticipated from Fig. 2.3, which shows for the four models studied there that if $\bar{\varphi}_i$ (or, equivalently $\bar{\rho}_{\varphi,i}$) is too large, then the fit to the CMB data is noticeaby bad. Also, the physical predictions do not depend on the time the tracker is reached, provided it does so at $a \lesssim 0.5$. This suggests that if we assume the tracker at all epochs we are not at risk of missing any best-fitting regions of the parameter space of the model.

3.1.3   Parameter space

In our constraint analysis, we shall devide the Galilean subspace into three distinct sectors. We dub Cubic and Quartic Galileon the models made up by $\{\mathcal{L}_2, \mathcal{L}_3\}$ (i.e. $c_4 = c_5 = 0$) and $\{\mathcal{L}_2, \mathcal{L}_3, \mathcal{L}_4\}$ (i.e. $c_5 = 0$), respectively. We shall use the name Quintic Galileon when referring to the most general model, i.e., $\{\mathcal{L}_2, \mathcal{L}_3, \mathcal{L}_4, \mathcal{L}_5\}$, which was the case considered in the last chapter (recall that we always assume $c_1 = 0$ and in this chapter we do not consider the $\mathcal{L}_G$ term).

In addition to the Galileon model parameters (cf. Sec. 2.3)

$$\{c_2, c_3, c_4, c_5, \xi\}, \tag{3.1}$$

---

[1]This model is the best-fitting base Cubic Galilon model to the *PLB* dataset, but what is important in the discussion here is the impact of the initial conditions, regardless of which exact model parameters we consider.

we also constrain the cosmological parameters

$$\left\{ \Omega_{b0}h^2, \Omega_{c0}h^2, \theta_{\mathrm{MC}}, \tau, n_s, A_s, \Sigma m_\nu \right\}, \tag{3.2}$$

which are, respectively, the physical energy density of baryons, the physical energy density of cold dark matter, a `CosmoMC` parameter related to the angular acoustic scale of the CMB, the optical depth to reionization, the scalar spectral index of the primordial power spectrum, the amplitude of the primordial power spectrum at a pivot scale $k = 0.05 \ \mathrm{Mpc}^{-1}$ and the summed mass of the three active neutrino species. Recall that, as we discussed in Sec. 2.3, two of the five parameters in Eq. (3.1) can be given in terms of the others using Eqs. (2.72) and (2.73).

Below, we shall see that one of the main results of this chapter is associated with the important role that the parameter Σm_ν has on the goodness of fit of Galileon models. The current cosmology-independent bounds on neutrino masses imply $0.06 \ \mathrm{eV} < \Sigma m_\nu < 6.6 \ \mathrm{eV}$ (cf. Sec. 1.1). This range of values allows neutrinos to affect substantially a number of different cosmological observables. As a result, it seems reasonable to require that consistent cosmological constraints treat Σm_ν as a free parameter. This is of particular interest in modified gravity models, where some degeneracies may arise [198, 199, 200]. To this end, we shall consider two variations of the model: one for which the number of massive neutrinos $N_{\mathrm{massive}} = 0$ and $\Sigma m_\nu = 0$, and another for which $N_{\mathrm{massive}} = 3$ and Σm_ν is a free parameter. We shall refer to the first class of models as "base" Galileon models, and shall denote the second class with a prefix ν, e.g., νCubic Galileon. For comparison purposes, we also consider a $\nu\Lambda$CDM model.

The value of the Hubble expansion rate today, $H_0 = 100h \ \mathrm{km/s/Mpc}$, is a derived parameter. For a given point in parameter space, the `CosmoMC` code determines, by trial-and-error, the value of H_0 that reproduces the sampled value of θ_{MC} (called `theta` in the code). θ_{MC} is much less correlated with the other parameters than H_0, which speeds up the convergence of the chains, despite of the additional trial-and-error calculations. Parameters such as $\Omega_{\varphi 0}$ and the *rms* linear matter fluctuations at $8 \ \mathrm{Mpc}/h$, σ_8, are also derived parameters. We always fix the number of relativistic neutrinos $N_{\mathrm{eff}} = 3.046$, the baryonic mass fraction in helium $Y_{\mathrm{P}} = 0.24$ and the running of the scalar spectral index $\mathrm{d}n_s/\mathrm{dln}k = 0$. We also set to zero the amplitude of the tensor perturbations, and its tensor spectral index, as we are only interested in scalar perturbations. However, we do comment briefly on the impact of the tensor fluctuations in Sec. 3.5.
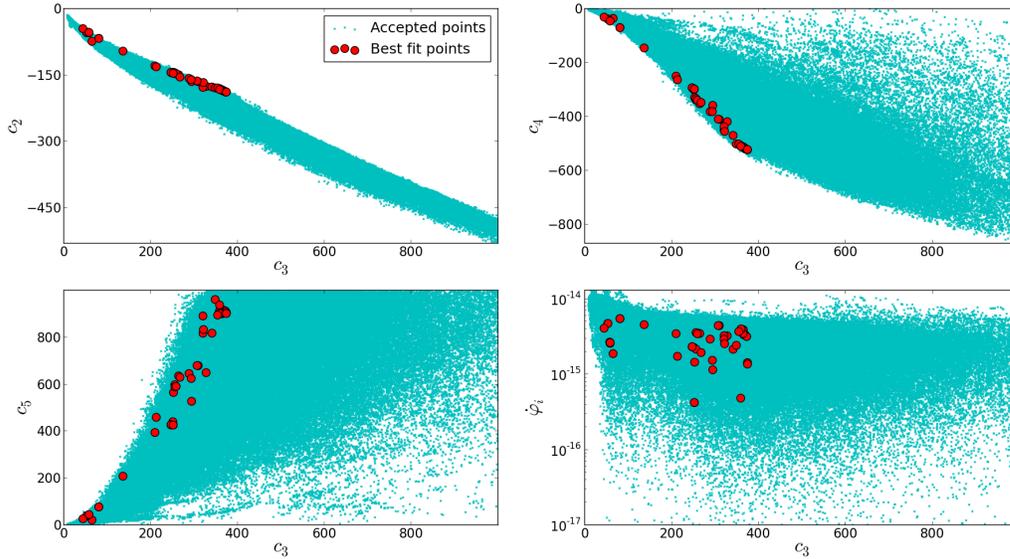
Figure 3.2: Points accepted by the Metropolis-Hastings algorithm (cyan dots), including those sampled during the burn-in period, using the CMB temperature data from the Wilkinson Microwave Anisotropy Probe (WMAP) 9-year results [201], the SNIa sample from Supernova Legacy Survey (SNLS) project [202] and BAO measurements from the 6df Galaxy Survey [203], from the Sloan Digital Sky Survey (SDSS) DR7 [204] and from the SDSS-III Baryon Oscillation Spectroscopic Survey (BOSS) [205]. In Ref. [2], this data combination is dubbed the WMAP9+SNLS+BAO dataset. The points are projected onto different planes of the Galileon subset of the parameter space. All of the Galileon parameters were allowed to vary in order to manifest the scaling degeneracy. The remaining cosmological parameters were also sampled (not shown). There are approximately 132000 points (around 22000 per chain) and the large red circles represent the fifty best-fitting points.

Scaling degeneracy of the Galileon parameters

As discussed in Sec. 2.3, one of the Galileon parameters should be fixed when running the Markov chains to overcome the scaling degeneracy of the Galileon equations. However, the scaling relation of Eqs. (2.65) does not link parameters with different signs, and as a result, one needs to be careful with the sign chosen for the fixed parameter. To determine this sign, we have run a set of chains where all of the Galileon parameters are allowed to vary. The result is shown in Fig. 3.2, where we plot all the points accepted by the MCMC algorithm (cyan dots) for four different planes of the Galileon parameter subspace for chains

constrained using the WMAP9+SNLS+BAO dataset[2] (see the figure caption). There are approximately 132000 points (22000 per chain). We highlight the points with the fifty highest likelihood values (red circles). The rest of the cosmological parameters were allowed to vary as well (not shown in this plot, see Ref. [2]). The parameters c_3, c_4 and c_5 were sampled from the interval $[-1000, 1000]$ to prevent the chains from spending too much time searching larger and larger values of the c_n. The starting point for each of the chains was set to be sufficiently close to zero so that the algorithm could quickly select the signs for the parameters which best fit the data.

As expected from the scaling relations of Eqs. (2.65), one finds a long and narrow region of degeneracy in the Galileon subset of the parameter space, along which the likelihood is kept constant. Note that although it seems that the best-fitting points are confined to $c_2 \gtrsim -200$, $c_3 \lesssim 400$ and $c_4 \gtrsim -600$, this happens only because the points have reached the prior range limit of 1000 in the c_5 direction, which therefore 'artificially' constrains the other parameters. We have checked that the degeneracy region keeps increasing on increasing the size of the prior ranges. The difference in $\chi^2 = -2\log P$ (where P is the posterior) between the best-fitting and the fiftieth best-fitting points is $\Delta\chi^2_{1th,50th} \sim -1$, but the likelihood does not change monotonically along any direction of the parameter space. The result shown in Fig. 3.2 is in partial disagreement with the conclusions drawn in [180]. In the latter, the authors found a long and narrow region of degeneracy along which the likelihood decreases for values of c_n much larger or much smaller than unity. We agree that the long region of degeneracy exists. However, the likelihood does not change appreciably towards larger values of the parameters c_n, which is what one would expect in light of the scaling relation described by Eqs. (2.65).

In Fig. 3.2 we see that the best-fitting points all lie in the region of parameter space where $c_2 < 0$, $c_3 > 0$, $c_4 < 0$, $c_5 > 0$ and $\dot{\varphi}_i > 0$, which means that when fixing one of the parameters, these sign conditions should be preserved. For completeness, we note that the result of Fig. 3.2 was obtained by solving the background equations numerically. By running a similar set of chains with the tracker solution one also encounters the long and narrow degeneracy regions, but now c_3, c_4 and c_5 can cross zero. This difference is linked to the different evolution of the background at early times when one solves for it numerically

---

[2]In this chapter, we shall present results using the more recent CMB data from the Planck satellite, but for the purpose of discussing the scaling degeneracy here we can use these WMAP9 results.

or by assuming the tracker. Although these two approaches can be equivalent in what concerns the observational data, they can be different from the point of view of the stability conditions. For instance, in Fig. 3.2, c_3, c_4 and c_5 do not cross zero because if they do, then the background evolution at early times (when it is not yet on the tracker) is such that ghost or Laplace instabilities appear. If the tracker solution is assumed at all cosmological epochs, then these points no longer develop instabilities and are therefore viable. All in all, what is important to retain here is that in both treatments of the background, c_2 never changes its sign when all of the parameters are varying. As a result, c_2 is the most reasonable choice for the fixed parameter to break the scaling degeneracy. The magnitude of c_2 is not critical, as one can always rescale the resulting constraints to any value of c_2 (with the same sign) by using Eqs. (2.65). For simplicity, we fix $c_2 = -1$. This way, the $\mathcal{L}_2$ term in Eq. (2.1) becomes the standard scalar kinetic term, but with the opposite sign.

3.1.4   Datasets

In our constraints, we consider three data combinations. The first dataset comprises the Planck data for the CMB temperature anisotropy angular power spectrum [193, 194]. These include its low-l and high-l temperature components, as well as the cross-correlation of the temperature map with the WMAP9 polarization data [201]. For this piece of the likelihood, we also vary the nuisance parameters that are used to model foregrounds, and instrumental and beam uncertainties. We denote this dataset by P.

We call our second dataset PL, which adds to P the data for the power spectrum of the lensing potential (reconstructed from the CMB), also given by the Planck satellite [206]. On smaller angular scales, the CMB lensing power spectrum can be affected by nonlinearities. However, given the current level of precision of the data, such nonlinear corrections can be ignored and one can assume that linear perturbation theory holds.

The final dataset, denoted by PLB, also includes the BAO measurements obtained from the 6df [203], SDDS DR7 [207], BOSS DR9 [208] and WiggleZ [209] galaxy redshift surveys.

Why we do not use growth rate and clustering data

Several studies have shown that the modifications to gravity in the Galileon model can significantly enhance the growth of linear matter fluctuations on sub-horizon scales [1, 159, 180, 183, 192, 197] (recall also Fig. 2.6). However, the regime of validity of linear theory

in Galileon gravity is still uncertain, since we do not have yet determined the impact of the Vainshtein screening mechanism, which is a purely nonlinear effect and is therefore absent in linear theory studies. For example, numerical simulations have shown that in other modified gravity models such as the $f(R)$ and dilaton [76, 77, 99], linear perturbation theory can fail even on scales as large as $k \sim 0.01 \ h\mathrm{Mpc}^{-1}$ because of the chameleon screening [99, 115, 210].

Our modifications to the `CAMB` code allow us to obtain the Galileon predictions for the linear matter power spectrum and growth rate and we could use them to place further constraints on the model. However, given the above reasoning, we remain cautious about using clustering data for now. We argue that a better understanding of the true impact of the Vainshtein screening is needed before attempting a more rigorous confrontation of the predicted clustering power and growth rate with the observational data. This shall be done in subsequent chapters after we study nonlinear structure formation processes.

3.2 Overview of previous observational constraints

In this section, we summarize the constraints on the Galileon model of Eq. (2.1) that were obtained in previous work. Our goal is simply to provide a general overview of the current status of Galileon constraints and not to present a thorough review. For further details, we refer the interested reader to the cited literature and references therein.

The first observational constraints on the Galileon model were derived in Ref. [177], by using only data sensitive to the background dynamics. The authors allow for non-flat spatial geometries of the Universe and find, in particular, that although the tracker solution can provide a good fit to the individual datasets (which include data from SNIa, BAO and CMB distance priors), there is some tension when one combines these observational probes.

References [180, 192] attempted to use measurements of the growth rate of structure to constrain the Galileon model. These two papers concluded that the model has difficulties in fitting the background and the growth rate data simultaneously. However, Ref. [197] performed a more detailed analysis and found that the tension is actually much less significant. The authors of Ref. [197] pointed out that Ref. [180] did not take into account the scaling degeneracy of the Galileon parameters; furthermore Ref. [192] used data that

is not corrected for the Alcock-Paczynski effect [211], having assumed also that the shape of the linear matter power spectrum of Galileon models is the same as in ΛCDM, which is not guaranteed [1, 2]. Moreover, as acknowledged in Ref. [197], the constraints obtained by confronting linear theory predictions with growth data assume the validity of linear theory on the scales used to measure the growth rate. For example, the growth rate measurements of the WiggleZ Dark Energy Survey [212] are obtained by estimating redshift space distortions in the galaxy power spectrum measured down to scales of $k \sim 0.3h\mathrm{Mpc}^{-1}$. On these scales, however, the impact of nonlinear effects, galaxy bias, and of the Vainshtein mechanism can be significant.

The first observational constraints using the full shape of the CMB temperature anisotropy power spectrum were presented by us in Ref. [2] (on which part of this chapter is based). We found that the amplitude of the low-l region of the CMB power spectrum, which is mostly determined by the Integrated Sachs-Wolfe (ISW) effect, plays a decisive role in constraining the parameter space of the Galileon model. The use of the full shape of the CMB temperature data results in much tighter constraints than those obtained by using only the information encoded in the CMB distance priors [213]. Reference [2] finds that the best-fitting Galileon models to the WMAP9 data [201] have a lower ISW power relative to ΛCDM, which results in a better fit. However, some observational tensions become apparent when background data from SNIa and BAO is added to the analysis. The results that follow recover some of those first encountered by Ref. [2], but with some aspects discussed with more detail. In the constraints of Ref. [2], the impact of massive neutrinos was also not considered, but shall be in this chapter.

3.3 Results: Cubic Galileon

The Cubic Galileon sector is defined by $c_4 = c_5 = 0$, which leaves c_3 and ξ in Eq. (3.1) as potential free parameters (recall $c_2 = -1$ to break the scaling degeneracy). However, one can use Eqs. (2.72) and (2.73) to fix two more Galileon parameters. For the case of the Cubic model we then get

$$c_3 = 1/\left(6\sqrt{6\Omega_{\varphi 0}}\right) \; ; \quad \xi = \sqrt{6\Omega_{\varphi 0}}. \tag{3.3}$$
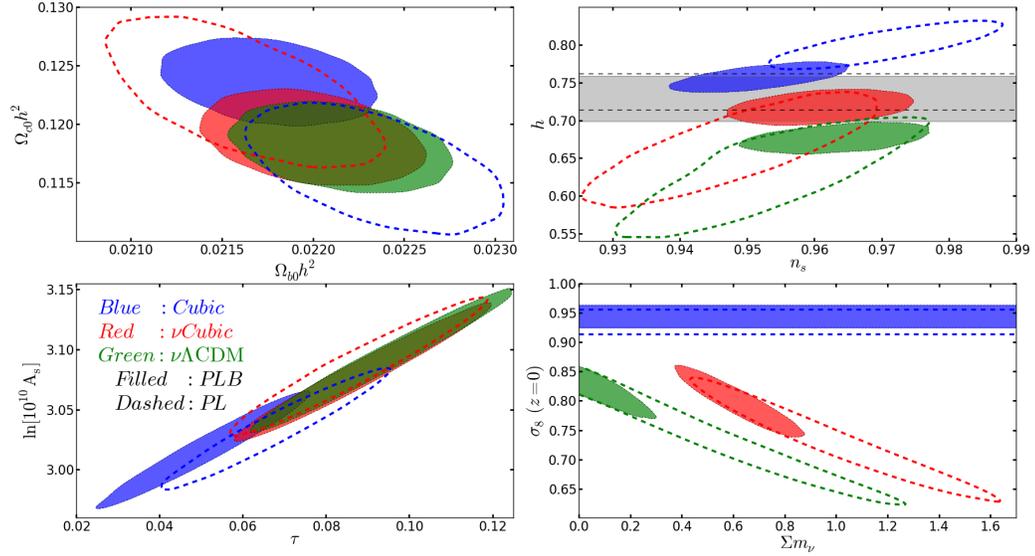
Figure 3.3: Marginalized two-dimensional 95% confidence level contours obtained using the *PL* (open dashed) and *PLB* (filled) datasets for the base Cubic Galileon (blue), νCubic Galileon (red) and $\nu\Lambda$CDM (green) models. In the top right panel, the horizontal bands indicate the 68% confidence limits of the direct measurements of h presented in Ref. [214] (open dashed) and Ref. [215] (grey filled). In the lower right panel, the horizontal dashed bands indicate the 95% confidence interval on σ_8 for the base Galileon model, for which $\Sigma m_\nu = 0$.

In this way, the only free parameters in the Cubic Galileon model are those in Eq. (3.2), just like in ΛCDM. This contrasts with popular modified gravity theories (with $f(R)$ gravity [52, 198, 199, 200] being perhaps the leading example), for which there are, in general, extra functions and parameters to tune, compared to ΛCDM.

3.3.1   Cosmological constraints

Figure 3.3 shows two-dimensional 95% confidence level marginalized contours obtained with the *PL* (dashed) and *PLB* (filled) datasets for the base Cubic (blue), νCubic (red) and $\nu\Lambda$CDM (green) models. Table 3.1 shows the best-fitting parameters and corresponding values of $\chi^2 = -2\ln\mathcal{L}$, and Table 3.2 summarizes the one-dimensional marginalized likelihood ($\mathcal{L}$) statistics.

Figure 3.4 shows $H(a)$, the CMB temperature and lensing power spectrum, the linear matter power spectrum and time evolution of the linear growth rate, $f = \mathrm{d}\ln D/\mathrm{d}\ln a$, ex-

pressed as $f\sigma_8$, for the best-fitting models. In the top right and middle left panels, the data points show the power spectrum measured by the Planck satellite[194, 206]. In the middle right panel, the data points show the SDSS-DR7 Luminous Red Galaxy host halo power spectrum from Ref. [187], but scaled down by a constant factor to match approximately the amplitude of the best-fitting νCubic (*PLB*) model. In the lower panels, the data points show the measurements extracted by using the data from the 2dF [216] (square), 6dF [217] (triangle), SDSS DR7 (LRG) [218] (circle), BOSS [204] (dot) and WiggleZ [219] (side triangles) galaxy surveys.

Observational tensions in the base Cubic model

The χ^2 values in the base Cubic model are significantly larger than those in the νCubic and $\nu\Lambda$CDM models, which indicates the markedly poorer fits of the base Cubic model. Moreover, the quality of the fit becomes worse as one combines the different datasets. In particular, when constrained with the *PLB* dataset, the base Cubic model fails to provide a reasonable fit to any of the likelihood components: $\chi^2_{Lensing} \sim 22$, for 8 degrees of freedom (dof); $\chi^2_{BAO} \sim 8$, for 6 dof [3]. This poorer fit to the data by the base Cubic model is primarily driven by the difficulty of the model in fitting, simultaneously, the BAO and the CMB peak positions.

The angular acoustic scale of the CMB fluctuations, θ^*, is essentially what determines the CMB peak positions. It is given by $\theta^* = r_s^*/d_A^*$, where

$$r_s^* = \int_{z_*}^{\infty} \frac{c_s}{H(z)} \mathrm{d}z, \tag{3.4}$$

$$d_A^* = \int_0^{z_*} \frac{1}{H(z)} \mathrm{d}z, \tag{3.5}$$

are, respectively, the sound horizon and the comoving angular diameter distance to the redshift of recombination z^*; $c_s = 1/\sqrt{3\left(1 + 3\bar{\rho}_b/(4\bar{\rho}_\gamma)\right)}$ and $\bar{\rho}_b$ and $\bar{\rho}_\gamma$ are the background energy densities of baryons (b) and photons (γ). The constraints on θ^* tend to be fairly model independent, since they depend mostly on the peak positions, rather than the amplitude of the power spectrum (cf. Tables 3.1 and 3.2). From Eq. (2.74), one can show that, at early times, $H(a)$ evolves in the same way in the Galileon and ΛCDM models. Hence, for fixed cosmological parameters, r_s^* is also the same in these two models. However, at

---

[3]In Ref. [3], without including the WiggleZ measurements in the BAO data, it was found that $\chi^2_{BAO} \sim 8$, for 3 dof.

late times, $H(a)$ is smaller in the Galileon models compared to ΛCDM. This can be seen, again, by inspecting Eq. (2.74) or by noting the late-time "dips" in $H/H_{\nu\Lambda\text{CDM}} - 1$ in the top left panel of Fig. 3.4 (although in this plot the cosmological parameters differ from model to model). The point here is that the smaller late-time expansion rate increases d_A^*, which in turn decreases θ^*. In order to fit the CMB peak positions, the "intrinsically" smaller expansion rate at late times is compensated for by larger values of the expansion rate today, h, in such a way as to preserve the values of d_A^*, and hence θ^*. The preference of the CMB data for high values of h in the base Cubic model is illustrated in top right panel of Fig. 3.3. The lensing data lowers the matter density slightly to reduce the amplitude of the lensing power spectrum (the $C_l^{\phi\phi}$ for the base Cubic (P) model is not shown in Fig. 3.4, but is similar to that of the base Cubic (PLB) model). This increases both r_s^* and d_A^*, but affects the latter more. As a result, and by the above reasoning, the addition of the CMB lensing to the CMB temperature data helps to push h to even higher values (cf. Table 3.1).

The inclusion of the BAO data counteracts the preference of the CMB data for higher values of h. The significance of this tension is illustrated by the offset between the contours obtained with the *PL* and *PLB* datasets for the base Cubic model. The addition of the BAO data also pushes the total matter density to higher values, which has an impact on the amplitude of both the CMB temperature and lensing spectra. This triggers a number of slight shifts in the remaining cosmological parameters in order to optimize the fit. Nevertheless, this optimization is not perfect, and the base Cubic model ultimately fails to fit the combined data well. In addition to the poor BAO fit, the base Cubic model predicts a high amplitude for C_l^{TT} at low-l (top right panel of Fig. 3.4), caused by a rapid late-time deepening of the lensing potential (cf. top panels of Fig. 3.5). The amplitude of the lensing power spectrum, $C_l^{\phi\phi}$, is also visibly larger than the data (middle left panel of Fig. 3.4).
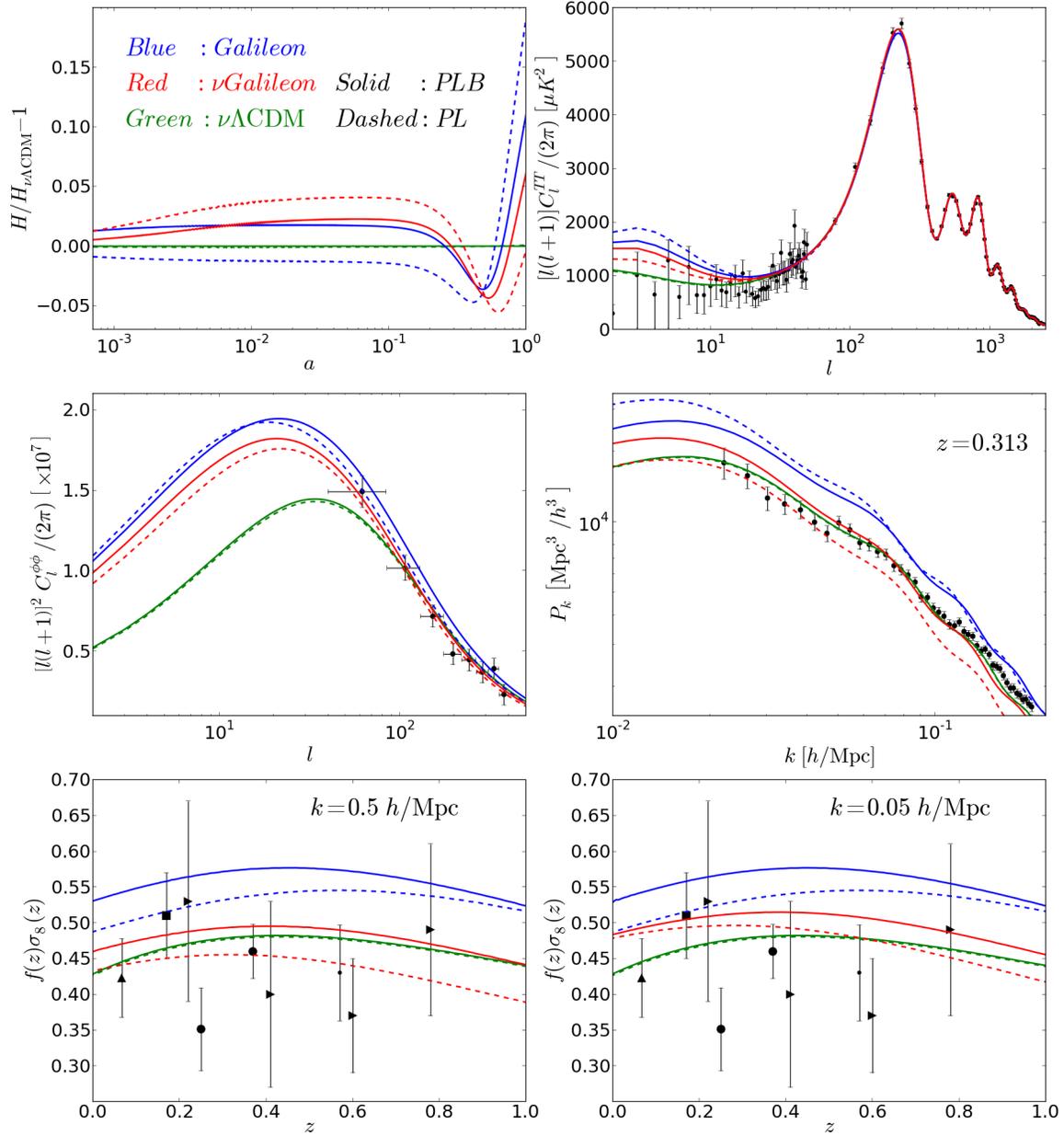
Figure 3.4: Time evolution of the Hubble expansion rate (top left), CMB temperature power spectrum (top right), CMB lensing potential power spectrum (middle left), linear matter power spectrum (middle right) and time evolution of $f\sigma_8$ for $k = 0.5h/\mathrm{Mpc}$ (bottom left) and $k = 0.005h/\mathrm{Mpc}$ (bottom right) for the best-fitting base Cubic (blue), $\nu\mathrm{Cubic}$ (red) and $\nu\Lambda\mathrm{CDM}$ (green) models obtained using the *PL* (dashed) and *PLB* (solid) datasets. In the top left panel, the $\nu\Lambda\mathrm{CDM}$ model used in the denominator is the corresponding best-fitting model to the *PLB* dataset.
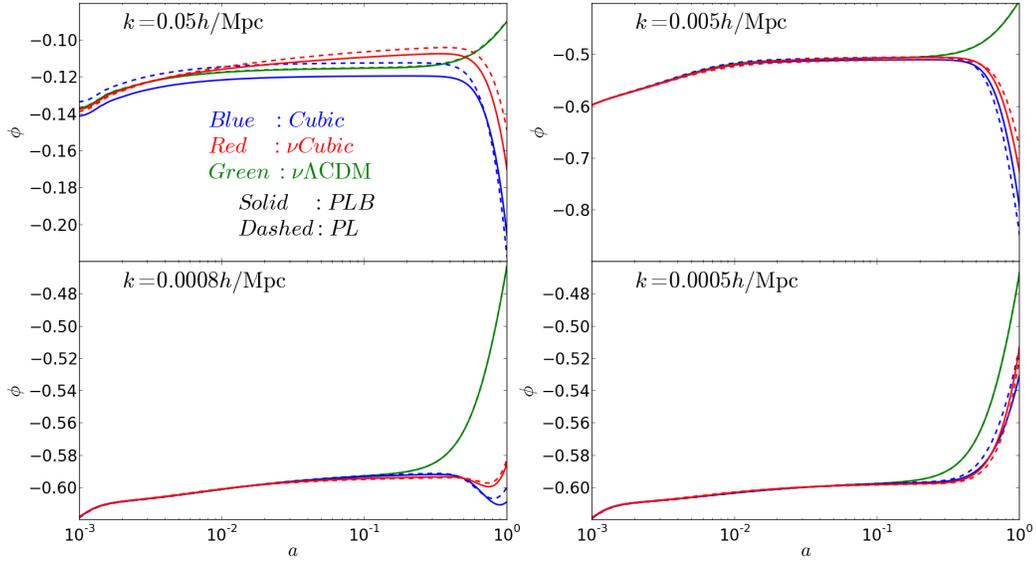
Figure 3.5: Time evolution of the lensing potential, ϕ, for the best-fitting base Cubic (blue), νCubic (red) and $\nu\Lambda$CDM (green) for the *PL* (dashed) and *PLB* (solid) datasets for $k = 0.05h/\mathrm{Mpc}$, $k = 0.005h/\mathrm{Mpc}$, $k = 0.0008h/\mathrm{Mpc}$ and $k = 0.0005h/\mathrm{Mpc}$, as labelled in each panel.
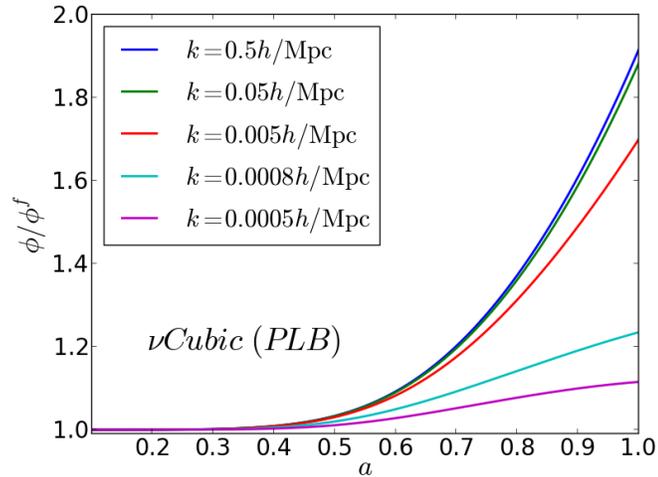
Figure 3.6: Time evolution of the ratio of the total lensing potential, ϕ, and the lensing potential caused by the matter fluid only, ϕ^f, for the νCubic (*PLB*) model and for a range of k scales, as labelled. This quantity gives a measure of fifth force induced by the Galileon field.

Table 3.1: The best-fitting parameters of the Cubic Galileon model. The upper part of the table shows the best-fitting $\chi^2 = -2\ln\mathcal{L}$ values of the components of the P, PL and PLB datasets. The goodness of fit of the Galileon models can be inferred by comparing the respective χ^2 values with those for $\nu\Lambda$CDM, which has been shown to be a good fit to these data in [194]. The lower part of the table shows the corresponding best-fitting model parameters. Recall that for the Cubic sector of Galileon gravity $c_4 = c_5 = 0$, c_3 and ξ are given by Eqs. (3.3) and $c_2 = -1$ to break the scaling degeneracy.

Parameter/Dataset		Base Cubic	νCubic	$\nu\Lambda$CDM
$(\chi_P^2; --; --)$		$(9829.8; --; --)$	$(9811.5; --; --)$	$(9805.5; --; --)$
$(\chi_P^2; \chi_L^2; --)$		$(9834.6; 8.0; --)$	$(9811.6; 4.4; --)$	$(9805.3; 8.8; --)$
$(\chi_P^2; \chi_L^2; \chi_B^2)$		$(9836.7; 19.5; 8.4)$	$(9814.0; 5.1; 2.4)$	$(9805.7; 8.7; 1.4)$
$100\Omega_{b0}h^2$:	(P, PL, PLB)	$(2.216; 2.257; 2.173)$	$(2.166; 2.176; 2.202)$	$(2.217; 2.208; 2.213)$
$\Omega_{c0}h^2$:	(P, PL, PLB)	$(0.121; 0.115; 0.124)$	$(0.123; 0.122; 0.120)$	$(0.120; 0.118; 0.119)$
$10^4\theta_{\mathrm{MC}}$:	(P, PL, PLB)	$(104.12; 104.18; 104.05)$	$(104.03; 104.06; 104.11)$	$(104.15; 104.12; 104.10)$
τ:	(P, PL, PLB)	$(0.070; 0.072; 0.052)$	$(0.099; 0.084; 0.088)$	$(0.092; 0.086; 0.088)$
n_s:	(P, PL, PLB)	$(0.963; 0.980; 0.955)$	$(0.949; 0.953; 0.958)$	$(0.960; 0.964; 0.961)$
$\ln(10^{10}A_s)$:	(P, PL, PLB)	$(3.054; 3.040; 3.021)$	$(3.111; 3.081; 3.084)$	$(3.096; 3.079; 3.081)$
Σm_ν [eV]:	(P, PL, PLB)	$(0\text{ fixed}; 0\text{ fixed}; 0\text{ fixed})$	$(1.043; 0.875; 0.538)$	$(0.061; 0.043; 0.033)$
h:	(P, PL, PLB)	$(0.774; 0.810; 0.755)$	$(0.656; 0.677; 0.722)$	$(0.674; 0.680; 0.679)$
$\sigma_8(z=0)$:	(P, PL, PLB)	$(0.959; 0.935; 0.949)$	$(0.729; 0.749; 0.822)$	$(0.835; 0.827; 0.829)$

Table 3.2: Marginalized one-dimensional constraints of the Cubic Galileon model. The table shows the 1σ limits on the cosmological parameters obtained for the *PL* and *PLB* datasets. Recall that for the Cubic sector of Galileon gravity $c_4 = c_5 = 0$, c_3 and ξ are given by Eqs. (3.3) and $c_2 = -1$ to break the scaling degeneracy.

Parameter/Dataset		Base Cubic	νCubic	$\nu\Lambda$CDM
$100\Omega_{b0}h^2$:	(*PL*, *PLB*)	$(2.233 \pm 0.028 \,; 2.175 \pm 0.024)$	$(2.161 \pm 0.030 \,; 2.198 \pm 0.024)$	$(2.182 \pm 0.035 \,; 2.215 \pm 0.025)$
$\Omega_{c0}h^2$:	(*PL*, *PLB*)	$(0.116 \pm 0.002 \,; 0.124 \pm 0.002)$	$(0.123 \pm 0.003 \,; 0.119 \pm 0.002)$	$(0.121 \pm 0.003 \,; 0.118 \pm 0.002)$
$10^4\theta_{\mathrm{MC}}$:	(*PL*, *PLB*)	$(104.17 \pm 0.061 \,; 104.05 \pm 0.055)$	$(104.04 \pm 0.066 \,; 104.10 \pm 0.056)$	$(104.08 \pm 0.073 \,; 104.14 \pm 0.057)$
τ:	(*PL*, *PLB*)	$(0.067 \pm 0.011 \,; 0.051 \pm 0.010)$	$(0.087 \pm 0.012 \,; 0.088 \pm 0.012)$	$(0.091 \pm 0.013 \,; 0.092 \pm 0.013)$
n_s:	(*PL*, *PLB*)	$(0.970 \pm 0.007 \,; 0.952 \pm 0.005)$	$(0.948 \pm 0.009 \,; 0.961 \pm 0.006)$	$(0.954 \pm 0.009 \,; 0.963 \pm 0.006)$
$\ln(10^{10}A_s)$:	(*PL*, *PLB*)	$(3.034 \pm 0.020 \,; 3.019 \pm 0.019)$	$(3.085 \pm 0.023 \,; 3.080 \pm 0.023)$	$(3.093 \pm 0.024 \,; 3.090 \pm 0.024)$
Σm_ν [eV]:	(*PL*, *PLB*)	$(0 \text{ fixed} \,; 0 \text{ fixed})$	$(0.980 \pm 0.237 \,; 0.618 \pm 0.101)$	$(< 0.551 \,; < 0.120)$
h:	(*PL*, *PLB*)	$(0.800 \pm 0.013 \,; 0.758 \pm 0.008)$	$(0.663 \pm 0.030 \,; 0.718 \pm 0.009)$	$(0.634 \pm 0.036 \,; 0.678 \pm 0.008)$
$\sigma_8(z=0)$:	(*PL*, *PLB*)	$(0.935 \pm 0.010 \,; 0.944 \pm 0.010)$	$(0.733 \pm 0.042 \,; 0.798 \pm 0.024)$	$(0.757 \pm 0.056 \,; 0.817 \pm 0.017)$

Alleviating the tensions with Σm_ν

Although at sufficiently early times massive neutrinos act as an extra source of radiation, at late times (after becoming non-relativistic), they will effectively raise the total matter density, modifying the evolution of $H(a)$ accordingly. In particular, higher values of Σm_ν increase $H(a)$ at late times, and therefore have the same impact as increasing h on the value of d_A^*. This degeneracy between Σm_ν and h eliminates the preference of the CMB data for large values of h, as shown by the νCubic contours for the *PL* dataset in Fig. 3.3. An important consequence of this is that, in the νCubic model, there is no longer a tension between the CMB and the BAO data, as illustrated by the overlap between the contours for the *PL* and *PLB* datasets and by the acceptable χ^2 values listed in Table 3.1.

The presence of the massive neutrinos causes the lensing potential to deepen less rapidly with time, which reduces the amplitude of the CMB temperature power spectrum at large angular scales. On these scales, there is still an excess of power compared to $\nu\Lambda$CDM, but the large errorbars do not allow tight constraints to be derived. The massive neutrinos also lower substantially the amount of matter clustering (lower σ_8), which results in a better fit to the CMB lensing power spectrum. Compared to the $\nu\Lambda$CDM model, the νCubic model provides a slightly better fit, as it predicts more power at $l \sim 40 - 80$ and the amplitude decreases more rapidly at higher l.

We note, for completeness, that relaxing the assumption that the universe is spatially flat may also help to alleviate the tension between the CMB and BAO peak positions. In particular, $\Omega_k < 0$ also lowers d_A^*, and as a result, may mimic to some extent the effect of $\Sigma m_\nu > 0$ on $H(a)$. The phenomenology of non-flat Galileon cosmologies is not explored in this thesis.

3.3.2 Sign of the ISW effect

The ISW effect is a secondary anisotropy on the CMB temperature maps induced by time-evolving gravitational potentials. Consider for instance a photon travelling through a supercluster whose potential is getting shallower with time. This photon will get blueshifted (increase of temperature) as it goes into the center of the potential well, but redshifted (decrease of temperature) as it comes out of it. Since the potential was deeper at the time the photon was entering it, overall the temperature of the photon will increase. This causes a

so-called "hot spot" in the CMB maps. If the potential of the supercluster is getting deeper with time, then one would end up with a "cold spot" instead.

The amplitude of the ISW effect is proportional to the time derivative of the lensing potential, $d\phi/dt$, integrated along the line of sight. In Fourier space, ϕ is given by the equation [4] (cf. Eqs. (2.47))

$$-k^3\phi = 4\pi G a^2 \left[k\left(\Pi + \chi\right) + 2aH(a)q\right], \tag{3.6}$$

where χ, q and Π are, respectively, the Fourier modes of the total density perturbation, heat flux and anisotropic stress (see Ref. [1] or Chapter 2 for more details) [5]. Figure 3.5 shows the time evolution of ϕ for the best-fitting models for four different scales $k = 0.05h/\text{Mpc}$, $k = 0.005h/\text{Mpc}$, $k = 0.0008h/\text{Mpc}$ and $k = 0.0005h/\text{Mpc}$. In the standard ΛCDM picture, ϕ grows at the transition from the radiation to the matter dominated eras, stays approximately constant during the matter era ($\Omega_m \sim 1$), and starts decaying (note the negative sign on the y-axis) at the onset of the dark energy era. The physical picture in the Cubic Galileon models is more complex. During the matter era, ϕ also remains approximately constant, although on smaller length scales $k \gtrsim 0.05h/\text{Mpc}$, the presence of the massive neutrinos can cause ϕ to decay slightly. The modifications induced by the Galileon field become apparent at later times ($a \gtrsim 0.5$) and are scale-dependent. For $k \gtrsim 0.005h/\text{Mpc}$, ϕ deepens at late times, whereas for $k \lesssim 0.0005h/\text{Mpc}$ it decays. On intermediate scales ($k \sim 0.0008h/\text{Mpc}$) the potential can remain approximately constant, even at late times, undergoing only small amplitude oscillations. To help understand the scale-dependent behaviour of ϕ in the Cubic model, we plot the time evolution of ϕ/ϕ^f for a range of scales k in Fig. 3.6. The quantity ϕ^f is given by Eq. (3.6), but considering only the contribution from the matter fluid in χ, q and Π. This isolates the impact of the Galileon field, and as such ϕ/ϕ^f provides a measure of the fifth force modifications to the lensing potential. Firstly, we note that the Galileon field contribution only becomes nonnegligible at late times, i.e., $\phi/\phi^f \approx 1$ for $a \lesssim 0.4$. At late times, on smaller length scales (larger k), the Galileon field contributes significantly to ϕ, making it deeper. On the other hand, on larger length scales (smaller k), the Galileon terms become less important, which leads to a gradual recovery

---

[4]In terms of the Ψ and Φ potentials of the linearly perturbed FRW line element in the Newtonian gauge $ds^2 = (1 + 2\Psi) dt^2 - (1 - 2\Phi) dx^i dx_i$, one has $\phi = (\Psi + \Phi)/2$.

[5]The q term is subdominant on small length scales (large k) and for matter $\Pi = 0$. In this case, one then recovers the standard Poisson equation $-k^2\phi = 4\pi G a^2 \chi$.

of the ΛCDM behaviour, i.e., ϕ decays at late times.

The physical picture depicted in Fig. 3.5 suggests that the Cubic Galileon and ΛCDM models predict opposite signs for the ISW effect on sub-horizon scales, a fact that can potentially be used to distinguish between them. The CMB temperature power spectrum is sensitive to $(\mathrm{d}\phi/\mathrm{d}t)^2$, and hence it cannot probe the sign of the ISW effect. There are however a number of different techniques that can be used to determine $\mathrm{d}\phi/\mathrm{d}t$. One of these consists of stacking CMB maps at the locations of known superclusters and supervoids. Given their size, these superstructures are not yet virialized, and hence constitute good probes of the ISW effect since their potentials are still evolving. A recent analysis of this type was performed by the Planck collaboration [220] who claimed to have found a detection of a positive ISW effect using the superstructure catalogue of Refs. [221, 222]. The significance of this detection becomes, however, substantially weaker when the catalogues of Refs. [223] and [224] are used instead. Moreover, all these signals are typically higher than the standard ΛCDM expectation [225, 226]. This fact, together with the differences between using different cluster and void catalogues, may raise concerns about the presence of unknown systematics in the analysis, such as selection effects. More recently, Refs. [227, 228] claimed the detection of a supervoid aligned with a prominent cold spot in the Planck CMB maps, as one would expect in models with positive ISW effect.

The cross-correlation of the CMB with tracers of large-scale structure (LSS) provides another way to probe the ISW effect. A positive amplitude for this cross correlation was first detected in Ref. [229], and later confirmed by Refs. [220, 230, 231], although with different significances. The cross correlation functions obtained by using different galaxy catalogues typically show positive correlation at smaller angular scales, and become consistent with zero at large angular scales (see e.g. Fig. 3 of Ref. [231]). This trend is consistent with the ΛCDM expectation (see Refs. [232, 233] for use of these data to constrain modified gravity), but Refs. [234, 235, 236, 237, 238] have raised some skepticism about the significance of these claims for a positive detection (some of this skepticism is addressed in Ref. [231]).

The potential ϕ is responsible for both the lensing of the CMB photons and the ISW effect. As a result, cross correlating CMB temperature maps with maps of the lensing potential (used to measure $C_l^{\phi\phi}$ in Fig. 3.4) can potentially be used to probe the sign and amplitude of the ISW effect. This has been made possible after the data release by the Planck collaboration [220], who found a signal that is consistent with the ΛCDM expectation that

ϕ decays at late times.

Taken at face value, the above-mentioned measurements seem to be inconsistent with the predictions of the base Cubic and νCubic Galileon models. Note that this is not a question of matching the amplitude of the signal, but instead its sign, and as a result, it may be hard to reconcile the model predictions with the claims of a positive ISW effect. Note also that although ϕ can decay in the Cubic models, this happens only on horizon-like scales, which do not affect the observational measurements. However, there is still some ongoing discussion about the understanding of the systematics in these measurements of the ISW effect. This makes us reluctant to add these data to the constraints at present. Moreover, in the case of Galileon gravity there is also the potential impact of the Vainshtein screening mechanism, which is unaccounted for in linear perturbation theory studies. For instance, on smaller scales, where the ISW detections are more significant, the screening mechanism may suppress the modifications to gravity, making the potentials decay as in ΛCDM. For the time being, we limit ourselves to noting that the positiveness of the ISW effect may turn out to be a crucial observational tension of the νCubic model. In the future, one will be able to say more about it, as more data become available and the discussion about the role of systematic effects is settled, and also when fully nonlinear predictions are used to model the signal.

3.3.3 Future constraints

We now discuss briefly the impact that additional data can have in further constraining the νCubic model.

For $l \lesssim 40$, the νCubic and ΛCDM models make quite distinct predictions for $C_l^{\phi\phi}$. As a result, future measurements of the lensing potential on these angular scales have a strong potential to discriminate between these two models, provided the errorbars are small enough [206].

The horizontal bands in the top right panel of Fig. 3.3 show the 1σ limits of the direct determinations of the Hubble constant h using Cepheid variables reported in Ref. [214] (open dashed) and Ref. [215] (grey filled). As one can see in the figure, these determinations are in tension with the CMB constraints for ΛCDM models. This fact has been the subject of discussions about the role that systematic effects can play in these direct measurements of h (see e.g. Ref. [239]). This is why we did not include them in our constraints. Here,

we simply note that νCubic models avoid the tensions apparent in ΛCDM, and therefore, adding a prior for h would favour the νCubic over ΛCDM.

Another ΛCDM tension that has become apparent after the release of the Planck data is associated with the normalization of the matter density fluctuations. In short, the values of σ_8 inferred from probes such as galaxy shear [21] and cluster number counts [240] seem to be smaller than the values preferred by the CMB constraints. Massive neutrinos have been shown to alleviate some of these problems [241, 242]. However, some residual tensions between datasets seem to remain. In the case of the νCubic model, the presence of the massive neutrinos lowers substantially the value of σ_8 w.r.t. the base model. Compared to ΛCDM, the constraints on σ_8 are rather similar, although they can extend to slightly lower values (cf. Fig. 3.3). This happens despite the enhanced gravitational strength driven by the Galileon field. It is therefore interesting to investigate whether or not the νCubic model can evade the above-mentioned ΛCDM tensions. This requires the modelling of nonlinear structure formation in the νCubic model, which is not explored in this thesis.

In the context of the νCubic model, the *PLB* dataset suggests that $\Sigma m_\nu > 0.3$ eV (at 2σ) (cf. Fig. 3.3). This contrasts with the constraints on $\nu\Lambda$CDM, for which $\Sigma m_\nu < 0.3$ eV (at 2σ). This opens an interesting window for upcoming terrestrial determinations of the absolute neutrino mass scale (see e.g. Ref. [243] for a review) to distinguish between these two models. For instance, the high energy part of the Tritium β-decay spectrum provides a robust and model-independent way to measure the mass of the electron neutrino directly. The MAINZ [23] and TROITSK [24] experiments have set $\Sigma m_\nu \lesssim 6.6$eV (at 2σ), but near-future experiments such as KATRIN [244] are expected to improve the mass sensitivity down to $\Sigma m_\nu \lesssim 0.6$eV. In the case that neutrinos are Majorana particles and provide the dominant contribution in the neutrinoless double β-decay of heavy nuclei [245], then one may achieve even higher sensitivity: in case of nondetection, these type of experiments are expected to constrain $\Sigma m_\nu \lesssim 0.3$eV. This would completely probe the quasi-degenerate neutrino hierarchy spectrum ($m_1 \sim m_2 \sim m_3 \sim m_\nu > 0.1$ eV). The forecast sensitivity of these experiments should be reached in a few years time and will say more about the viability of the $\nu\Lambda$CDM and νCubic models.

The lower panels of Fig. 3.4 show the time evolution of $f\sigma_8$ in the best-fitting models (computed using linear theory), together with the measurements from the 2dF [216] (square), 6dF [217] (triangle), SDSS DR7 (LRG) [218] (circle), BOSS [204] (dot) and WiggleZ

[219] (side triangles). In principle, these data can be used to further constrain the νCubic model. However, such a comparison between theory and observation may not be straightforward for at least three reasons. The first one is related to the validity of linear theory on the length scales probed by the surveys, on which nonlinear effects can affect the statistics of both the density and velocity fields, and hence modify significantly the linear theory expectations (see e.g. [218] for some discussion). The growth measurements are extracted from the data by analyzing the redshift space distortions induced by galaxy peculiar motions. This is usually achieved by assuming a model for how these peculiar velocities modify the true (unobserved) real space statistics. These models are typically calibrated and tested against N-body simulations, most of which are performed assuming GR (see however [115, 246, 247]). Here lies the second nontrivial aspect: to avoid obtaining results biased towards standard gravity, it seems reasonable to demand first the development of a self-consistent RSD model for modified gravity to see how it can have an impact on the extraction of the $f\sigma_8$ values from the galaxy catalogues. The third complication has to do with the scale-dependent growth introduced by the massive neutrinos, even at the linear level. In the lower panels of Fig. 3.4, one notes that the predictions of the νCubic model are, indeed, scale dependent, due to the relatively large massive neutrino fraction, compared to $\nu\Lambda$CDM. However, the measured values of $f\sigma_8$ obtained from the different surveys are derived from the clustering signal of galaxies measured over a range of different scales at once. Future constraints on the νCubic model using these data have therefore to take this scale dependence into account. We note that this third complication also applies to ΛCDM models with a large value of Σm_ν, such as those found in Refs. [241, 242]; and to $f(R)$ gravity models (see e.g. Ref [115] for a study of RSD in $f(R)$ gravity).

3.4 Results: Quartic and Quintic Galileon

The parameter space of the Quartic Galileon model is the same as the Cubic model, but with $c_4 \neq 0$. In our constraints, we use Eqs. (2.72) and (2.73) to derive c_3 and c_4 as

$$
\begin{aligned}
c_3 &= \frac{1}{2}\xi^{-1} - 2\Omega_{\varphi 0}\xi^{-3}, \\
c_4 &= -\frac{1}{9}\xi^{-2} + \frac{2}{3}\Omega_{\varphi 0}\xi^{-4},
\end{aligned}
\tag{3.7}
$$
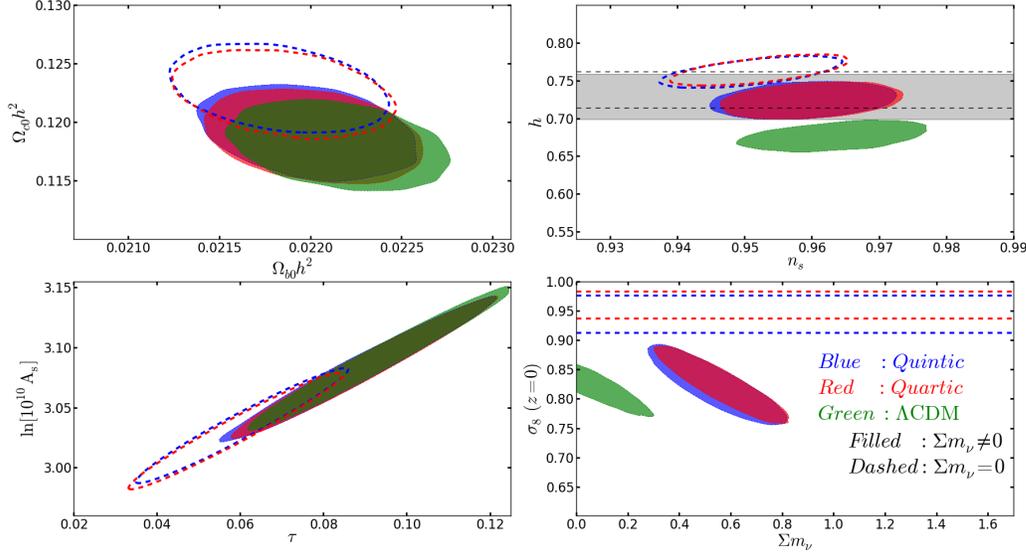
Figure 3.7: Same as Fig. 3.3 but for the base Quartic (red dashed), νQuartic (red filled), base Quintic (blue dashed) and νQuintic (blue filled) models, using the *PLB* dataset.

with ξ being the free parameter varied in the chains. In the case of the Quintic model ($c_5 \neq 0$), we vary ξ and c_3 in the chains, and derive c_4 and c_5 from

$$
\begin{aligned}
c_4 &= \frac{1}{3}\xi^{-2} - \frac{8}{9}c_3\xi^{-1} - \frac{10}{9}\Omega_{\varphi 0}\xi^{-4}, \\
c_5 &= -\frac{1}{3}\xi^{-3} + \frac{2}{3}c_3\xi^{-2} + \frac{4}{3}\Omega_{\varphi 0}\xi^{-5}.
\end{aligned}
\tag{3.8}
$$

3.4.1 Cosmological constraints

Figures 3.7, 3.8 and 3.9 show the same as Figs. 3.3, 3.4 and 3.5, respectively, but for the base Quartic (red dashed), νQuartic (red filled/solid), base Quintic (blue dashed) and νQuintic (blue filled/solid) Galileon models and using the *PLB* dataset. Table 3.3 shows the best-fitting parameter values and Table 3.4 summarizes the one-dimensional marginalized statistics.

Just as in the case of the Cubic model, the presence of massive neutrinos in the Quartic and Quintic models also alleviates substantially the observational tensions between the different datasets in *PLB* (cf. Table 3.3). The situation here is completely analogous to the case of the Cubic Galileon model discussed in the last section. Recall that the origin of these observational tensions lies in the specifics of the late-time evolution of $H(a)$, which

does not depend on the values of the c_i. Consequently, the same degeneracy between h and Σm_ν exists in the Quartic and Quintic Galileon models, which leads to good fits to the BAO, CMB temperature and CMB lensing data (cf. Fig. 3.8). It is also noteworthy that the constraints on the cosmological parameters of Eq. (3.2) are roughly the same in the Cubic, Quartic and Quintic models. Since these models differ in the Galileon subspace of parameters, this indicates that, to a reasonable extent, the constraints on the cosmological parameters do not correlate with those on the Galileon parameters.

One noticeable difference w.r.t. the Cubic Galileon case relates to the lower amplitude of the CMB temperature spectrum at low-l in both the Quartic and Quintic models. This is explained by the milder late-time evolution of ϕ, as shown in Fig. 3.9. The extra Galileon terms in the Quartic and Quintic models help to reduce the magnitudes of the fifth force, and hence ϕ is less affected by the Galileon field. This is illustrated in Fig. 3.10, which shows the same as Fig. 3.6 but for the νQuartic and νQuintic (*PLB*) models. For instance, for $a = 1$ and $k = 0.05h/\mathrm{Mpc}$, $\phi/\phi^f \sim 1.21$ in the νQuintic (*PLB*), whereas $\phi/\phi^f \sim 1.9$ in the νCubic (*PLB*). It is interesting to note the nontrivial time evolution of ϕ/ϕ^f in the νQuintic (*PLB*) model for $k = 0.0005h/\mathrm{Mpc}$, which indicates that the fifth force terms can be repulsive ($\phi/\phi^f < 1$) rather than attractive. This shows that in the more general Quintic models there is more freedom to tune the modifications to gravity, in such a way as to reduce substantially the ISW power in the low-l part of the CMB spectrum (blue lines in the top right panel of Fig. 3.8). In Sec. 3.3.2, we discussed the possible role that an observational determination of the sign of the ISW effect could play in determining the viability of the νCubic Galileon model. The physical picture depicted in Fig. 3.9 suggests that any observational tension that might fall upon the Cubic Galileon model (due to its negative ISW effect) should be less severe in the νQuartic and νQuintic models, but that it may still be hard to reconcile them with a positive ISW sign.

Table 3.3: Same as Table 3.1, but for the Quartic and Quintic models and using the *PLB* dataset. Recall that for the Quartic model constraints, $c_5 = 0$, and c_3, c_4 are derived parameters. For the Quintic model, the derived parameters are c_4 and c_5. For both models, $c_2 = -1$ to break the scaling degeneracy.

Parameter/Dataset		Base Quartic	νQuartic	Base Quintic	νQuintic
$(\chi_P^2 ; \chi_L^2 ; \chi_B^2)$		(9813.6 ; 15.6 ; 13.3)	(9805.9 ; 4.7 ; 2.2)	(9805.0 ; 20.5 ; 13.4)	(9800.4 ; 5.2 ; 2.2)
$100\Omega_{b0}h^2$:	*(PLB)*	(2.175)	(2.200)	(2.219)	(2.211)
$\Omega_{c0}h^2$:	*(PLB)*	(0.123)	(0.120)	(0.123)	(0.119)
$10^4\theta_{\mathrm{MC}}$:	*(PLB)*	(104.07)	(104.13)	(104.07)	(104.08)
τ:	*(PLB)*	(0.058)	(0.095)	(0.064)	(0.082)
n_s:	*(PLB)*	(0.951)	(0.957)	(0.950)	(0.958)
$\ln(10^{10}A_s)$:	*(PLB)*	(3.027)	(3.095)	(3.043)	(3.071)
Σm_ν [eV]:	*(PLB)*	(0 fixed)	(0.576)	(0 fixed)	(0.556)
ξ:	*(PLB)*	(2.43)	(2.29)	(4.50)	(3.89)
c_3:	*(PLB)*	(0.101)	(0.098)	(0.134)	(0.143)
c_4:	*(PLB)*	(−0.0045)	(−0.0037)	(−0.012)	(0.014)
c_5:	*(PLB)*	(0 fixed)	(0 fixed)	(0.0013)	(0.0017)
h:	*(PLB)*	(0.763)	(0.725)	(0.764)	(0.723)
$\sigma_8(z=0)$:	*(PLB)*	(0.956)	(0.816)	(0.945)	(0.814)

Table 3.4: Same as Table 3.2, but for the Quartic and Quintic models and using the *PLB* dataset. Recall that for the Quartic model constraints, $c_5 = 0$, and c_3, c_4 are derived parameters. For the Quintic model, the derived parameters are c_4 and c_5. For both models, $c_2 = -1$ to break the scaling degeneracy.

Parameter/Dataset		Base Quartic	νQuartic	Base Quintic	νQuintic
$100\Omega_{b0}h^2$:	(PLB)	(2.185 ± 0.024)	(2.201 ± 0.024)	(2.218 ± 0.024)	(2.220 ± 0.024)
$\Omega_{c0}h^2$:	(PLB)	(0.122 ± 0.002)	(0.119 ± 0.002)	(0.123 ± 0.002)	(0.119 ± 0.002)
$10^4\theta_{\mathrm{MC}}$:	(PLB)	(104.07 ± 0.057)	(104.11 ± 0.057)	(104.07 ± 0.058)	(104.10 ± 0.056)
τ:	(PLB)	(0.060 ± 0.010)	(0.088 ± 0.013)	(0.060 ± 0.010)	(0.087 ± 0.013)
n_s:	(PLB)	(0.952 ± 0.005)	(0.960 ± 0.006)	(0.951 ± 0.006)	(0.959 ± 0.006)
$\ln(10^{10}A_s)$:	(PLB)	(3.032 ± 0.019)	(3.082 ± 0.024)	(3.035 ± 0.019)	(3.081 ± 0.024)
Σm_ν [eV]:	(PLB)	(0 fixed)	(0.560 ± 0.101)	(0 fixed)	(0.540 ± 0.108)
ξ:	(PLB)	$(2.46^{+0.10}_{-0.12})$	(2.40 ± 0.13)	$(4.3^{+0.52}_{-1.58})$	$(4.23^{+0.53}_{-2.14})$
c_3:	(PLB)	$(0.101^{+0.006}_{-0.003})$	$(0.103^{+0.008}_{-0.004})$	$(0.132^{+0.019}_{-0.004})$	$(0.123^{+0.033}_{-0.006})$
c_4:	(PLB)	$(-0.0045^{+0.0005}_{-0.0010})$	$(-0.0046^{+0.0007}_{-0.0014})$	$(-0.012^{+0.002}_{-0.004})$	$(-0.010^{+0.002}_{-0.008})$
c_5:	(PLB)	(0 fixed)	(0 fixed)	$(0.0015^{+0.0009}_{-0.0005})$	$(0.0009^{+0.0017}_{-0.0005})$
h:	(PLB)	(0.764 ± 0.008)	(0.724 ± 0.010)	(0.762 ± 0.008)	(0.724 ± 0.010)
$\sigma_8(z=0)$:	(PLB)	(0.960 ± 0.012)	(0.824 ± 0.027)	(0.945 ± 0.016)	(0.823 ± 0.027)

3.4.2 Local time variation of G_{eff} in the Quartic model

As pointed out by Refs. [248, 249], the implementation of the Vainshtein screening effect in models like the Quartic and Quintic Galileons may not be enough to suppress all local modifications to gravity. Without loss of generality, the modified Poisson equation in Galileon gravity can be written as (see Chapter 4):

$$\nabla^2\Psi = \left[A(t) + B(t, \nabla^2\varphi)\right]\nabla^2\Psi^{\mathrm{GR}} + C(t, \nabla^2\varphi), \tag{3.9}$$

where ∇^2 is the three-dimensional Laplace operator, Ψ is the total modified gravitational potential and Ψ^{GR} is the GR potential that satisfies the standard Poisson equation, $\nabla^2\Psi^{\mathrm{GR}} = 4\pi G\delta\rho_m$, where $\delta\rho$ is the total matter perturbation. The shapes of the functions A, B, C depend on whether one assumes the Cubic, Quartic or Quintic models. An important aspect of the functions B and C is that they can be neglected if the spatial variations of the Galileon field are small compared to the variations in the gravitational potential, i.e., if $\nabla^2\varphi/\nabla^2\Psi^{\mathrm{GR}} \to 0$, then $B, C \to 0$.

The Vainshtein mechanism is implemented through nonlinear terms in the Galileon field equation of motion, which effectively suppress $\nabla^2\varphi$ (compared to $\nabla^2\Psi^{\mathrm{GR}}$) near overdense objects like our Sun. As a result, in the Solar System, Eq. (3.9) reduces to

$$\nabla^2\Psi = A(t)\nabla^2\Psi^{\mathrm{GR}}. \tag{3.10}$$

In the case of the Cubic Galileon model, $A(t) \equiv 1$ and one recovers exactly the standard Poisson equation in GR. However, in the Quartic and Quintic models, $A(t)$ depends on the time evolution of $\bar{\varphi}$ (which cannot be screened), and hence, residual modifications remain, even after the implementation of the Vainshtein mechanism. Figure 3.11 shows 10^4 randomly selected points from the chains used to constrain the νQuartic model with the *PLB* dataset, projected onto the $c_3 - c_4$ and $\xi - c_4$ planes. The points are coloured according to the value of G_{eff}/G (lower panel) and $\dot{G}_{\mathrm{eff}}/G$ (upper panel) today. These two quantities were evaluated by following the strategy presented in Refs. [5, 7] (which shall be explained also in Chapter 4). In short, assuming spherical symmetry, one evaluates

$$\frac{G_{\mathrm{eff}}}{G}(a, \delta) = \frac{\Psi_{,r}/r}{\Psi_{,r}^{\mathrm{GR}}/r}, \tag{3.11}$$

where $_{,r}$ denotes a partial derivative w.r.t. the radial coordinate r and $\delta = \delta\rho_m/\bar{\rho}_m$ is the density contrast of the (top-hat) matter fluctuation. In Fig. 3.11, we have assumed that in
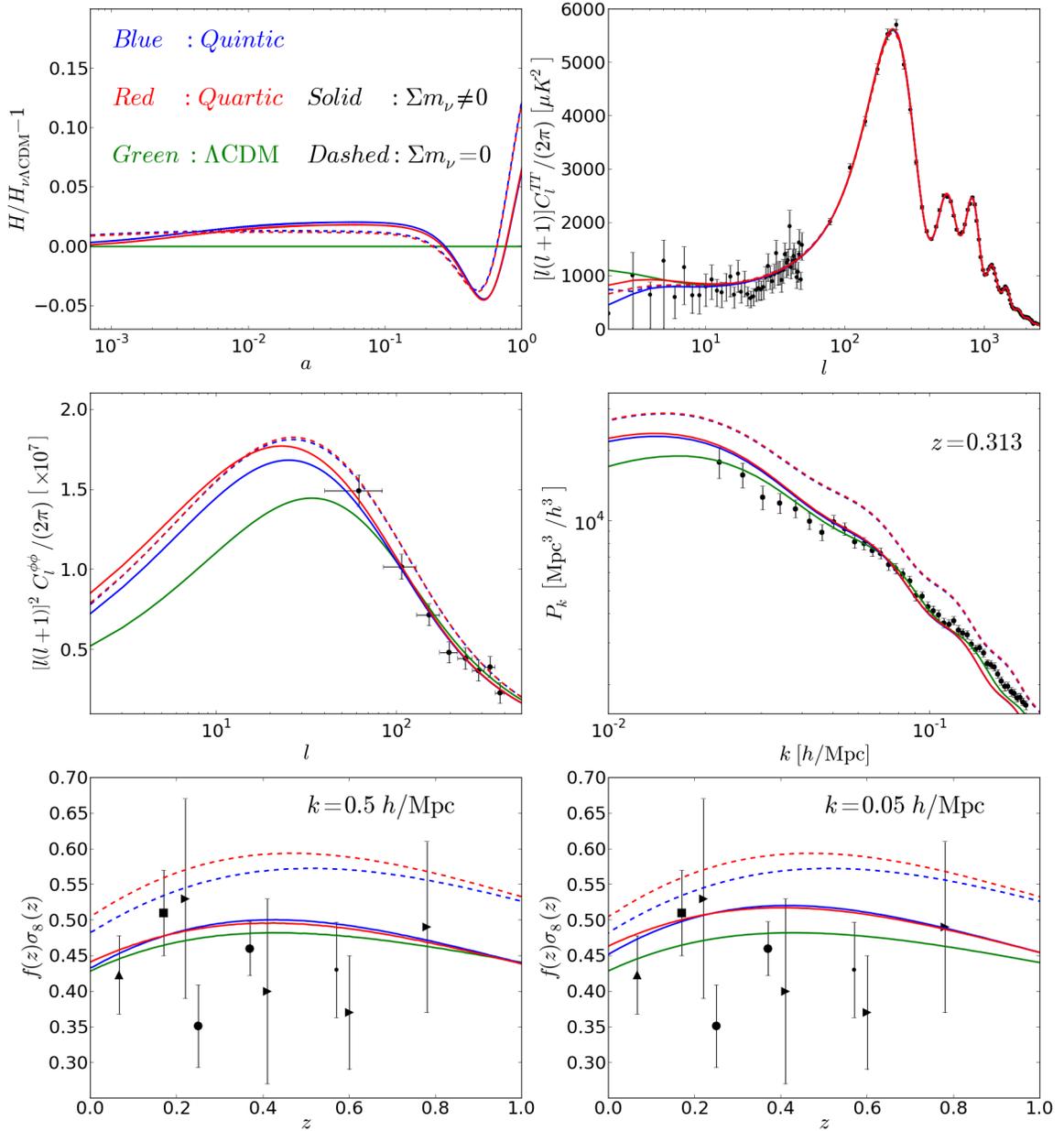
Figure 3.8: Same as Fig. 3.4 but for the base Quartic (red dashed), νQuartic (red solid), base Quintic (blue dashed) and νQuintic (blue solid) models that best fit the *PLB* dataset.
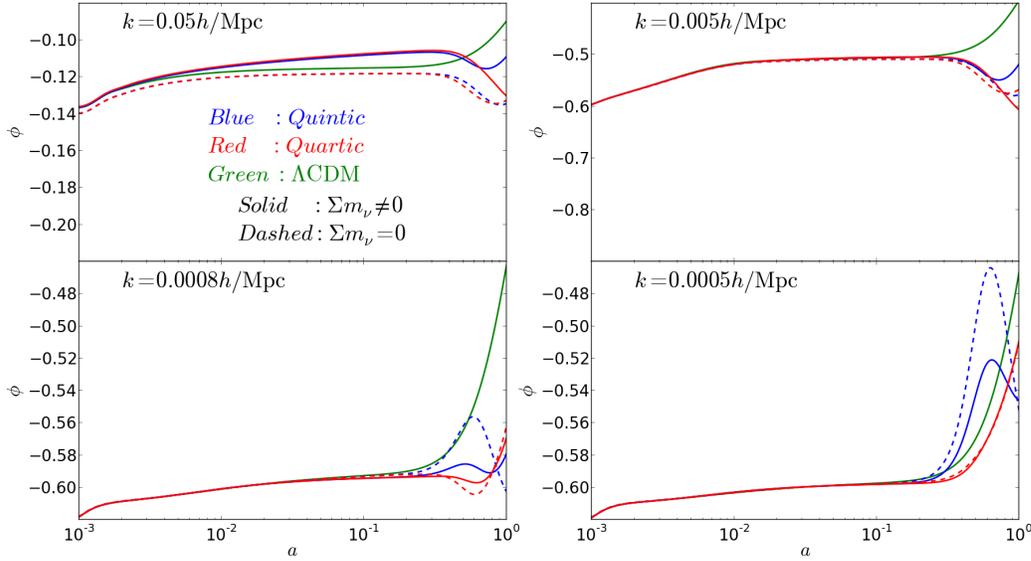
Figure 3.9: Same as Fig. 3.5 but for the base Quartic (red dashed), νQuartic (red solid), base Quintic (blue dashed) and νQuintic (blue solid) models that best fit the *PLB* dataset.
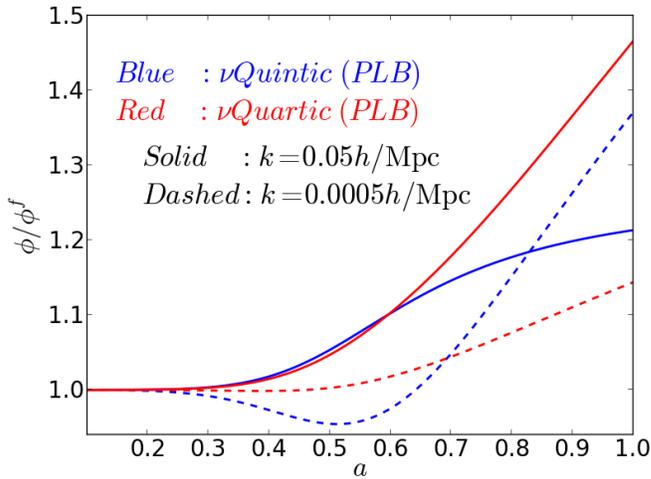
Figure 3.10: Same as Fig. 3.6 but for the νQuartic (red) and νQuintic (blue) Galileon models that best-fit the *PLB* dataset. The solid and dashed lines correspond to $k = 0.05h/\mathrm{Mpc}$ and $k = 0.0005h/\mathrm{Mpc}$, respectively.

our Solar System $\delta = 10^7$, although this is not critical for our mostly qualitative discussion[6]. The value of $\dot{G}_{\mathrm{eff}}/G$ was evaluated by taking finite differences at two consecutive times close to the present day (we have ensured that the time step used is small enough to be accurate). The figure shows that if c_4 is not sufficiently close to zero, then $G_{\mathrm{eff}}/G \neq 1$ and $\dot{G}_{\mathrm{eff}}/G \neq 0$, contrary to what one would expect in standard gravity. These modifications are caused by the function $A(t)$, whose origin can be traced back to the explicit coupling to the Ricci scalar $\mathcal{R}$ in $\mathcal{L}_4$ (cf. Eq. (2.2)). For the reasons listed in Ref. [5] (which shall be explained also in Chapter 4), the same calculations for the Quintic model are much more challenging to perform due to the extra level of nonlinearity in the equations. However, the direct coupling to $G_{\mu\nu}$ in $\mathcal{L}_5$ could presumably give rise to the same qualitative behavior.

The phenomenology of the Quartic and Quintic models near massive bodies like our Sun can be used to further constrain their parameter space. The best-fitting νQuartic (*PLB*) model predicts that the effective local gravitational strength is varying at a rate $\dot{G}_{\mathrm{eff}}/G \sim -150 \times 10^{-13}\mathrm{yr}^{-1}$. However, Lunar Laser Ranging experiments constrain $\dot{G}_{\mathrm{eff}}/G = (4 \pm 9) \times 10^{-13}\mathrm{yr}^{-1}$ [250]. From the figure we see that this is only allowed provided c_4 is very close to zero, in which case one recovers the Cubic Galileon studied in the last section

3.4.3 The Galileon subspace of parameters in the Quintic model

Figure 3.12 shows the points accepted in the chains (after the burn-in period) used to constrain the νQuintic model with the *PLB* dataset, projected onto the $c_3 - \xi$ and $c_4 - c_5$ planes. The black dots indicate the points that were tried during the sampling, but which failed to meet the conditions of no ghost and Laplace instabilities of the scalar fluctuations. It is noteworthy that these stability conditions can, on their own, rule out a significant portion of the parameter space.

In the $\xi - c_3$ plane, one can identify two branches that develop along stable but increasingly narrow regions of the parameter space, and that intersect at the location of the best-fitting regions. The narrowness of these branches may raise concerns about the fairness of the Monte Carlo sampling. Consider, for instance, a chain that is currently in the upper branch (which goes through $\xi \sim 10$ to guide the eye). Since there are only two possible directions that do not lead to instabilities, the majority of the MCMC trials will

---

[6]To first approximation, we assume also that all of the matter components (baryons, CDM and massive neutrinos) contribute equally to δ.
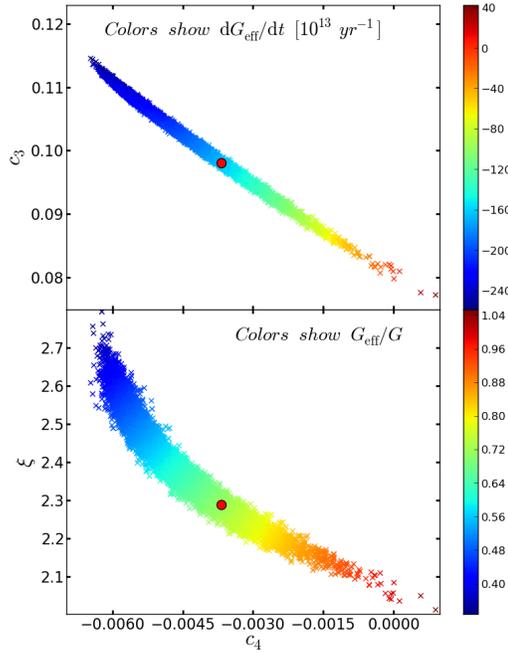
Figure 3.11: Sample of 10^4 randomly selected points from the chains used to constrain the νQuartic model with the *PLB* dataset, projected onto the Galileon subspace of parameters. The points are coloured according to their respective values of $G_{\mathrm{eff}}/G(a,\delta)$ (lower panel) and $\dot{G}_{\mathrm{eff}}/G(a,\delta)$ (upper panel), at $a=1$ and for top-hat profiles with $\delta=10^7$ (see text). The big red dot indicates the position of the best-fitting point of (cf. Table 3.3).

be rejected and the chain will remain at the same point for a large number of steps. The narrowness of the gap between the unstable points therefore makes it harder for the chains to explore the regions that lie along the direction of the gap. Consequently, the "end point" of the branches may be determined not only by its poorer fit to the data, but also by these limitations of the numerical sampling.

To address the above concerns, as a test, we have run chains with priors on ξ to force the chains to sample only the lower ($\xi \lesssim 3$) and the upper branches ($\xi \gtrsim 3$). These runs have shown that the length of the branches may extend just slightly (compared to Fig. 3.12). This is expected since the chains spend more time in each branch, and hence, have a better chance of probing the limits of the branches. To learn more about the likelihood surface along the direction of the branches, we have further forced the chains to sample only the branch regions that are sufficiently far away from the intersection (to explore the far end of the lower branch we have imposed $\xi \lesssim 3$ and $c_3 \lesssim 0.0$; and for the upper branch

we have imposed $\xi \gtrsim 12$). Also, in this second test, we have fixed all of the remaining cosmological parameters to their best-fitting values from Table 3.3. Again, as expected, these chains extended a bit more compared to Fig. 3.12. In all these tests, however, the value of χ^2 increases along these branches, indicating that the far end of the branches are indeed worse fits to the data. We have also looked at the CMB power spectrum for points located deep in the branches to confirm that the CMB spectra becomes visibly worse, compared to the best-fitting point. We therefore conclude that, despite some sampling difficulties that may arise due to the narrow stable regions, the "end points" of the branches are mostly determined by their poorer fit to the data. We stress that these complications in sampling the branches of the top panel of Fig. 3.12 are only important in determining the exact limit of confidence contours. For the purpose of identifying the best-fitting parameters, and subsequent analysis of their cosmology, these issues are not important as the best-fitting regions lie sufficiently far away from the end of the branches.

The lower panel of Fig. 3.12 zooms into the best-fitting regions of the $c_5 - c_4$ plane. The points are color coded according to their values of ξ, which helps to identify the branches in the top panel. The projection along the ξ direction gives rise to overlap of the points for which $\xi \gtrsim 3$ and for which $\xi \lesssim 3$. We also note that the high-ξ points lie on a much narrower region of the $c_5 - c_4$ plane, compared to those with lower ξ. This can be understood by recalling that c_4 and c_5 are derived parameters that depend on c_3, ξ and $\Omega_{\varphi 0}$ (cf. Eqs.(3.8)). When ξ is sufficiently large, the terms $\propto \Omega_{\varphi 0}$ in Eqs. (3.8) can be neglected. This way, the narrow constraints imposed by the stability conditions on the c_3 and ξ parameters (upper panel of Fig. 3.12) lead directly to narrow constraints on c_4 and c_5, as well. On the other hand, when ξ is smaller, the terms $\propto \Omega_{\varphi 0}$ are no longer negligible. Consequently, the different sampled values of $\Omega_{\varphi 0}$ (which are not as tightly constrained as c_3 and ξ by the stability conditions) introduce extra scatter, which broadens the shape of the region of accepted points. A closer inspection shows also that an empty (unsampled) region forms at $(c_4, c_5) \sim (-0.012, 0.0013)$ (barely visible at the resolution of the figure). This serves to show the rather nontrivial shape of the parameter space in Quintic Galileon model. For instance, the `CosmoMC` routines that evaluate the confidence contours from chain samples cannot resolve all these details clearly.
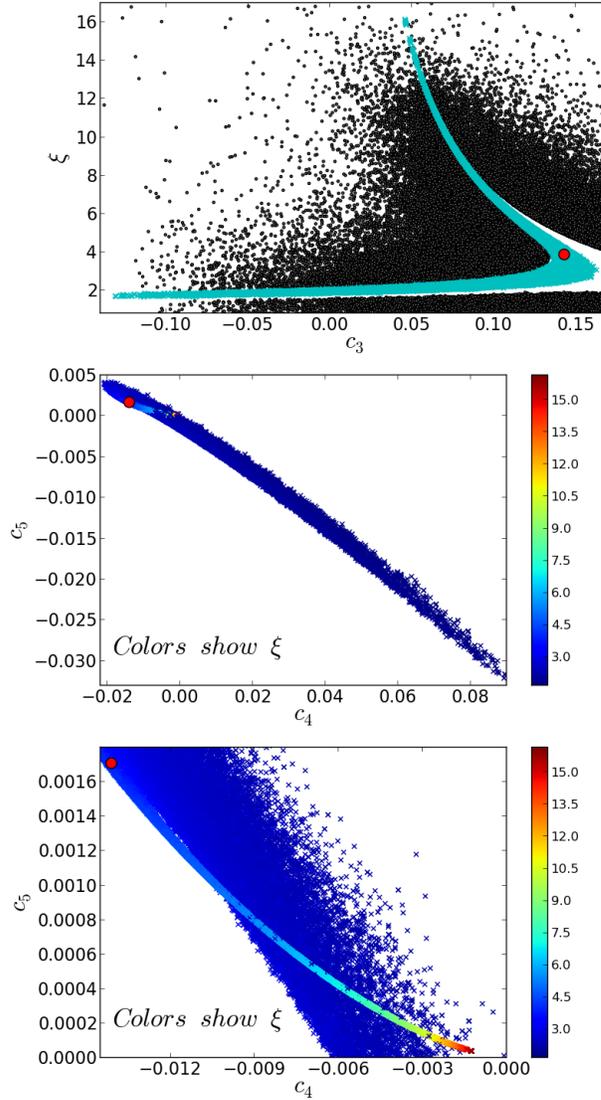
Figure 3.12: Accepted MCMC points (after the burn-in period) obtained in the constraints of the νQuintic model using the *PLB* dataset, projected onto the $\xi - c_3$ (top panels) and $c_5 - c_4$ (middle and lower panels) planes. In the middle and lower panels, the points are color coded according to their value of ξ. The lower panel zooms into a region of the middle panel. The big red dot indicates the best-fitting point. In the top panel, the black dots indicate those points that were tried during the sampling but failed to meet the conditions for the absence of ghost and Laplace instabilities of the scalar fluctuations. We checked that the boundaries of these unstable regions are consistent in between using the derivation of the stability conditions presented in Refs. [169, 170] and Ref. [159].

3.5   Tensor perturbations

In our constraints, we are mainly interested in the role played by scalar fluctuations, and as a result, we have set the amplitude of tensor fluctuations to zero (vector perturbations play a negligible role as they decay very quickly after their generation). However, before summarizing the results of this chapter, we briefly investigate the impact that the evolution of tensor fluctuations can have in Galileon gravity models.

The relevant equations for the evolution of the tensor modes can be written as [166, 251, 252]:

$$0 = \dot{\sigma}_{\mu\nu} + \frac{2}{3}\theta\sigma_{\mu\nu} + \mathcal{E}_{\mu\nu} + \frac{\kappa}{2}\pi_{\mu\nu}, \tag{3.12}$$

$$\begin{aligned}
0 = {}& \frac{\kappa}{2}\left[\dot{\pi}_{\mu\nu} + \frac{1}{3}\theta\pi_{\mu\nu}\right] - \frac{\kappa}{2}(\rho + p)\sigma_{\mu\nu} \\
& - \left[\dot{\mathcal{E}}_{\mu\nu} + \theta\mathcal{E}_{\mu\nu} - \hat{\nabla}^{\alpha}\mathcal{B}_{\beta(\mu}\epsilon_{\nu)\gamma\alpha}{}^{\beta}u^{\gamma}\right],
\end{aligned} \tag{3.13}$$

where (as in Chapter 2), $\mathcal{E}_{\mu\nu}$ and $\mathcal{B}_{\mu\nu}$ are, respectively, the electric and magnetic parts of the Weyl tensor, $\mathcal{W}_{\mu\nu\alpha\beta}$, defined by $\mathcal{E}_{\mu\nu} = u^{\alpha}u^{\beta}\mathcal{W}_{\mu\alpha\nu\beta}$ and $\mathcal{B}_{\mu\nu} = -\frac{1}{2}u^{\alpha}u^{\beta}\epsilon_{\mu\alpha}{}^{\gamma\delta}\mathcal{W}_{\gamma\delta\nu\beta}$. $\epsilon_{\mu\nu\alpha\beta}$ is the covariant permutation tensor. The Galileon field contributes to the tensor modes evolution via its modifications to the background dynamics, but also via its anisotropic stress (Eq. (2.43)), both of which are only important at late times. Explicitly, the relevant terms from Eq. (2.43) that enter Eqs. (3.12) and (3.13) are

$$\begin{aligned}
\pi_{\mu\nu}^{\varphi,\,\text{tensor}} \doteq {}& \frac{c_4}{M^6}\left[-\dot{\varphi}^4\left(\dot{\sigma}_{\mu\nu} - \mathcal{E}_{\mu\nu}\right) - \left(6\ddot{\varphi}\dot{\varphi}^3 + \frac{4}{3}\dot{\varphi}^4\theta\right)\sigma_{\mu\nu}\right] \\
& + \frac{c_5}{M^9}\left[-\left(\dot{\varphi}^5\dot{\theta} + \dot{\varphi}^5\theta^2 + 6\ddot{\varphi}\dot{\varphi}^4\theta\right)\sigma_{\mu\nu} - \left(\dot{\varphi}^5\theta + 3\ddot{\varphi}\dot{\varphi}^4\right)\dot{\sigma}_{\mu\nu} - 6\ddot{\varphi}\dot{\varphi}^4\mathcal{E}_{\mu\nu}\right],
\end{aligned} \tag{3.14}$$

where the superscript $^{\text{tensor}}$ indicates we are only considering the terms that contribute to the tensor fluctuations. Recall that for the Cubic Galileon model, $c_4 = c_5 = 0$, and as a result, there is no explicit contribution from the Galileon field to the tensor perturbations.

As in the case of scalar fluctuations, when studying the evolution of the tensor perturbations of the Galileon field, one must also ensure that they do not develop ghost nor Laplace instabilities. The conditions for the avoidance of these pathologies were derived in Ref. [169]. With our notation, the no-ghost condition is given by

$$Q_T/M_{\text{Pl}}^2 = \frac{1}{2} - \frac{3}{4}\frac{c_4}{M^6}\dot{\varphi}^4 - \frac{3}{2}\frac{c_5}{M^9}\dot{\varphi}^5 H > 0, \tag{3.15}$$

whereas the no-Laplace instability condition is given by

$$c_T^2 = \frac{1}{Q_T} \left[\frac{M_{\text{Pl}}^2}{2} + \frac{1}{4} \frac{c_4}{M^6} \dot{\varphi}^4 - \frac{3}{2} \frac{c_5}{M^9} \dot{\varphi}^4 \ddot{\varphi} \right] > 0. \tag{3.16}$$

During the sampling of the parameter space, we have only checked for the stability of the scalar fluctuations. Consequently, it is possible that some of the accepted points are associated with tensor instabilities. For the case of the Quartic model, we have checked that all of the accepted points in the chains are tensor-stable. The same however is not true for the Quintic model. This is illustrated in Fig. 3.13, which shows the points accepted in the chains used to constrain the base Quintic model with the *PLB* dataset. The red crosses, which contain the best-fitting point of Table 3.3 (black circle), indicate the regions of the parameter space which develop Laplace instabilities of the tensor perturbations. It is remarkable that taking the tensor stability conditions into account rules out more than half of the parameter space space allowed by the *PLB* dataset and scalar stability conditions. The red circle indicates the best-fitting point that is tensor-stable, for which $\Delta \chi^2 = 1.7$ compared to the best-fitting point of Table 3.3. Hence, although the stability conditions rule out a significant portion of the parameter space, they still leave behind regions which can provide a similar fit to the data, compared to the case where only scalar stability conditions are considered.

Figure 3.14 shows the CMB temperature power spectrum, the cross-correlation of the temperature and E-mode polarization of the CMB and the B-mode polarization power spectrum for the tensor-stable $\nu\Lambda$CDM (green), base Quartic (red) and base Quintic (blue) models that best-fit the *PLB* dataset. The dashed curves show the spectra obtained by setting $r_{0.05} = 0.2$, where $r_{0.05}$ is the tensor-to-scalar ratio of primordial power (at a pivot scale $k = 0.05\text{Mpc}^{-1}$). Our choice of $r_{0.05}$ is merely illustrative. The solid curves show the spectra for $r_{0.05} = 0$. We also assume a zero tensor spectral index with no running. One notes that the modifications driven by setting $r_{0.05} = 0.2$ are roughly of the same size for the three models. This shows that the tensor perturbations from the Galileon field are not affecting the overall spectra in a nontrivial and sizeable way. This justifies the approach in our model constraints, where we have neglected the role of the tensor modes. The differences between the Quartic, Quintic and $\nu\Lambda$CDM models are only visible at low-l. In the particular case of the B-mode power spectrum, it is interesting to note that for $l \gtrsim 10$, the Galileon models predict essentially the same amplitude as standard ΛCDM. As a result,
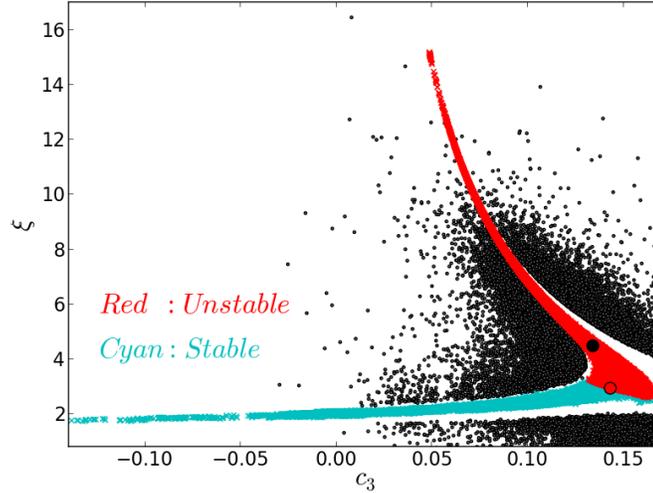
Figure 3.13: Same as the upper panel of Fig. 3.12, but for the base Quintic model and with the accepted points colored according to their stability of the tensor perturbations. The red crosses indicate points which are associated with tensor Laplace instabilities, as labelled. The big black dot indicates the best-fitting point found in the chains. The big red dot indicates the best-fitting point considering only tensor-stable points (the fact that this point looks like it lies in the tensor-unstable region is purely due to the resolution of the figure).

any detections of the B-mode signal at $l \sim 80$ such as those reported by BICEP-2 [253] are unlikely to be directly related to the Galileon field *per se*.

3.6 Summary

In this chapter, we have studied and constrained the parameter space of the covariant Galileon gravity model using the recent observational CMB (temperature and lensing) data from the Planck satellite and BAO measurements from the 2dF, 6dF, SDSS-DR7, BOSS and WiggleZ galaxy redshift surveys. The exploration of the parameter space was performed using MCMC methods with the aid of suitably modified versions of the publicly available `CAMB` and `CosmoMC` codes. The analysis of this chapter constitutes the first observational constraint study on the parameter space of the Galileon model using the full information encoded in the CMB temperature and CMB lensing potential angular power spectra. To the date of submission of this thesis, the conclusions on the observational status of the Galileon model studied here remain the most up-to-date in the literature.
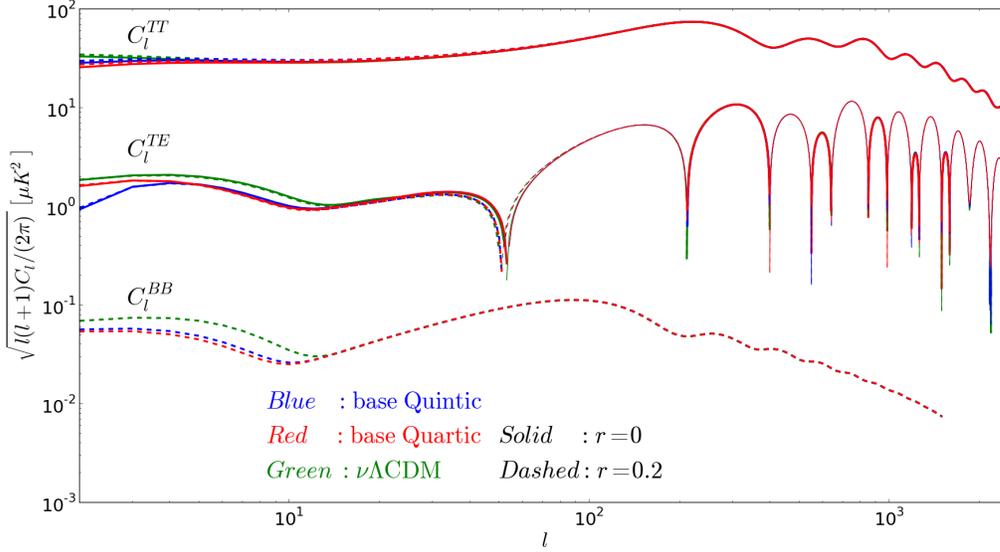
Figure 3.14: From top to bottom, the lines show, respectively, the CMB temperature power spectrum, the cross-correlation of the CMB temperature with the E-mode polarization and the B-mode polarization power spectrum for the $\nu\Lambda$CDM (green), base Quartic (red) and base Quintic (blue) models, for $r_{0.05} = 0$ (solid) and $r_{0.05} = 0.2$ (dashed). For the C_l^{TE} curves, the lines are thiner at the values of l for which the cross-correlation becomes negative. The curves for the Quintic model correspond to the best-fitting model that is tensor-stable (c.f. Fig. 3.13).

We have analysed separately three main branches of the Galileon model. These are the so-called Cubic, $\{\mathcal{L}_2, \mathcal{L}_3\}$; Quartic $\{\mathcal{L}_2, \mathcal{L}_3, \mathcal{L}_4\}$ and Quintic $\{\mathcal{L}_2, \mathcal{L}_3, \mathcal{L}_4, \mathcal{L}_5\}$ Galileon models. A major goal of the analysis here was to investigate the impact that massive neutrinos have on the observational viability of Galileon gravity. We have therefore constrained "base Galileon models", for which $\Sigma m_\nu = 0$; and νGalileon models, for which Σm_ν is a free parameter to be constrained by the data. For all models, we have assumed that the background evolution of the Galileon field follows, at all epochs, the tracker solution described in Sec. 2.3. This is justified by the fact that if the tracker is not reached before the epoch when the accelerated expansion begins ($a \sim 0.5$), then the Galileon model cannot fit the low-l part of the CMB temperature power spectrum (cf. Fig. 3.1 or Ref. [2]). The main results of this chapter can be summarized as follows:

- When $\Sigma m_\nu = 0$, all sectors of Galileon gravity have difficulties in fitting the BAO and

the CMB peak positions simultaneously. This tension is related to the specific late-time evolution of $H(a)$ (cf. Eq. (2.74)), which leads to different constraints on the value of h by the CMB (which prefers higher h) and BAO (which favours lower h) data (cf. Fig. 3.3 and 3.7). This tension applies to all sectors of the Galileon model, since $H(a)$ does not depend on the values of the c_i parameters. In addition to this observational tension, these best-fitting models also predict too much power for the CMB lensing potential spectrum (Figs. 3.4 and 3.8). In the case of the Cubic Galileon model, there is also an excess of ISW power in the low-l region of the CMB temperature power spectrum (top right panel of Fig. 3.4).

- If neutrinos are sufficiently massive, then they modify the late-time expansion history in such a way that the CMB data no longer prefers high values for h. This completely eliminates the tension with the BAO data if $\Sigma m_\nu \gtrsim 0.4$ eV (2σ) in the case of the Cubic Galileon (cf. Fig. 3.3), and $\Sigma m_\nu \gtrsim 0.3$ eV (2σ) in the cases of the Quartic and Quintic models (cf. Fig. 3.7). These best-fitting νGalileon models also reproduce much better the CMB lensing power spectrum. This fit can be even slightly better than in ΛCDM models, mainly due to a better fit to the data at $l \sim 60$ (Figs. 3.4 and 3.8). For the Cubic Galileon model, massive neutrinos also help to lower the excess of ISW power in the CMB. The neutrino mass constraints in the νGalileon models leave room for upcoming terrestrial neutrino experiments to help distinguish between these models and ΛCDM.

- In Galileon gravity, the time evolution of the lensing potential ϕ differs from the ΛCDM result at late times, and its qualitative behaviour is also scale dependent (cf. Figs. 3.5 and 3.9). In the case of the Cubic models, ϕ deepens considerably at late times on scales $k \gtrsim 0.005h/\mathrm{Mpc}$, but decays (as in ΛCDM) on scales $k \lesssim 0.0005h/\mathrm{Mpc}$. This behaviour follows from the scale dependence of the magnitude of the modifications to gravity induced by the Galileon field, which becomes weaker on horizon-like scales (cf. Fig. 3.6). The extra Galileon terms in the Quartic and Quintic sectors of the model allow for milder and smoother time evolution of ϕ for $k \gtrsim 0.005h/\mathrm{Mpc}$, but the potential can still decay for $k \lesssim 0.0005h/\mathrm{Mpc}$.

- The fact that ϕ deepens at late times for $k \gtrsim 0.005h/\mathrm{Mpc}$ in the Cubic model implies a negative ISW sign. This is opposite to what has been found recently by a number of observational studies that claimed the detection of a positive sign for the ISW effect (cf.

Sec. 3.3.2). There is still ongoing discussion about the impact that systematics (such as selection effects) might play in the significance of these observations. We have also raised the possibility that the nonlinear effects of the screening could have an impact on the ISW signal. We anticipate here that in the subsequent chapters, we will see that the effects of the screening are only very important on scales $k \gtrsim 1h/\mathrm{Mpc}$. Hence, and although we did not perform a detailed comparison with these observations, *we conclude that the ISW effect probably rules out the Cubic Galileon model. The same applies for the Quartic and Quintic sectors, even though the tension is not as strong.*

- The explicit couplings between the Galileon field derivatives and curvature tensors in the $\mathcal{L}_4$ and $\mathcal{L}_5$ Lagrangian densities (cf. Eq. (2.2)) give rise to modifications to gravity that cannot be totally suppressed by the Vainshtein mechanism (the reasons for this will become clear in the next chapter). We have shown how, by imposing a prior for the time variation of G_{eff} obtained from Lunar laser experiments, one can essentially constrain the Quartic model to look almost like the Cubic model (cf. Fig. 3.11) [7].

- Although the main focus here was on the effects of scalar perturbations, we have also looked at the impact of the tensor perturbations in the Quartic and Quintic models (the Cubic Galileon does not contribute directly to the tensor perturbations). We have seen that modifications driven by the Galileon field do not change drastically the shape and amplitude of the C_l^{TE} and C_l^{BB} spectra (cf. Fig. 3.14).

In the following chapters, we shall go beyond linear theory in our discussions about the Galileon model and focus more on the nonlinear aspects of large scale structure formation.

---

[7]We note that this observational tension arises when one considers the background evolution of the Galileon field when making a prediction for the Solar System. If $\dot{\bar{\varphi}} = 0$, then the tension goes away. In Chapter 6, we shall discuss this more indepth when we encounter a similar tension for Nonlocal gravity.

Chapter 4

Spherical collapse in Galileon gravity

As we have mentioned in the previous chapters, the inclusion of data related to the growth of structure on scales $\lesssim 10\mathrm{Mpc}/h$ in tests of Galileon gravity requires modelling of some physics which can only be tackled by going beyond linear theory. These include not only standard effects such as galaxy and halo bias, redshift space distortions and mode coupling, but also those associated with the Vainshtein screening mechanism. The latter can have a particularly strong impact on $\approx 1\mathrm{Mpc}$ scales, and thus affect the way dark matter haloes form and evolve. To model all these effects and extend the range of observational tests one typically needs to use N-body simulations, which are more computationally expensive than the linear theory calculations done using CAMB. It is therefore impractical to include results from N-body simulations in MCMC constraints. The analysis of Chapters 2 and 3, however, narrowed down significantly the regions of the parameter space of the Galileon model that are good fits to some of the most robust datasets. N-body simulations should therefore be focused on these parameter values.

Before moving on to analysing the results from N-body simulations in Chapter 5, in this chapter we study first nonlinear structure formation in Galileon models within the framework of the Excursion Set Theory (EST) formalism [254]. This formalism is not expected to achieve the same level of accuracy as N-body simulations. However, since it is analytical, it provides a neat and easy way to capture the main qualitative physical features of the models. A main goal of this chapter is to build the intuition about the phenomenology of Galileon models on small scales that will help in the interpretation of the N-body results later on.

4.1   Spherically symmetric nonlinear equations

We work with the perturbed FRW metric in the Newtonian gauge, Eq. (1.1), and assume that the fields, φ, Ψ and Φ are spherically symmetric, under which case the nonlinear field equations simplify considerably. In the equations below $\varphi = \bar{\varphi}(t) + \delta\varphi(t, \vec{x})$, where $\delta\varphi$ is the field perturbation and an overbar indicates background averaged quantities. We will always use φ to denote the scalar field, and the context should determine whether we refer to $\bar{\varphi}$ or $\delta\varphi$. To make the problem tractable we shall also employ two other simplifying assumptions. The first one is the so-called quasi-static approximation which corresponds to the limit where the time derivatives of the perturbed quantities are negligible compared to their spatial derivatives. For instance, $\partial_t\partial_t\Phi \ll \partial_r\partial_r\Phi$ or $\partial_t\partial_r\varphi \ll \partial_r\partial_r\varphi$ [1]. In [1, 183] (and in Chapter 2), it was shown that such an approximation typically works well in the Galileon model on length scales smaller than $k \sim 0.01h/\text{Mpc}$. The second simplifying assumption amounts to neglecting the terms that are suppressed by the scalar potentials, Φ and Ψ, and their first spatial derivatives, $\partial_i\Phi$ and $\partial_i\Psi$. This is known as the weak-field approximation where, for instance, $(1 - 2\Phi)\,\partial^i\partial_i\varphi \sim \partial^i\partial_i\varphi$ or $\partial_i\Phi\partial^i\Phi \ll \partial_i\partial^i\Phi$. This is plausible since these fields are typically very small ($\lesssim 10^{-4}$) on nonlinear scales.

Under the above approximations, the perturbed Poisson ($\delta G^0_0 = \kappa\delta T^0_0$), slip ($\delta G^r_r = \kappa\delta T^r_r$) and Galileon field equations of motion follow, respectively,

$$
2\frac{1}{r^2}\left(r^2\Phi_{,r}\right)_{,r} = -2\frac{c_3}{H_0^2}\dot{\varphi}^2\frac{1}{r^2}\left(r^2\varphi_{,r}\right)_{,r}
$$

$$
+\frac{c_4}{H_0^4}\left[6\frac{\dot{\varphi}^2}{a^2}\frac{1}{r^2}\left(r(\varphi_{,r})^2\right)_{,r} -12H\dot{\varphi}^3\frac{1}{r^2}\left(r^2\varphi_{,r}\right)_{,r} +3\dot{\varphi}^4\frac{1}{r^2}\left(r^2\Phi_{,r}\right)_{,r}\right]
$$

$$
+\frac{c_5}{H_0^6}\left[-4\frac{\dot{\varphi}^2}{a^4}\frac{1}{r^2}\left((\varphi_{,r})^3\right)_{,r} +12\frac{H\dot{\varphi}^3}{a^2}\frac{1}{r^2}\left(r(\varphi_{,r})^2\right)_{,r} -15H^2\dot{\varphi}^4\frac{1}{r^2}\left(r^2\varphi_{,r}\right)_{,r}\right.
$$

$$
\left.+6H\dot{\varphi}^5\frac{1}{r^2}\left(r^2\Phi_{,r}\right)_{,r} -6\frac{\dot{\varphi}^4}{a^2}\frac{1}{r^2}\left(r\varphi_{,r}\,\Phi_{,r}\right)_{,r}\right] + 8\pi G\bar{\rho}_m\delta a^2, \tag{4.1}
$$

$$
\frac{2}{r}\left(\Phi_{,r} - \Psi_{,r}\right) = \frac{c_4}{H_0^4}\left[\left(-4H\dot{\varphi}^3 - 12\ddot{\varphi}\dot{\varphi}^2\right)\frac{\varphi_{,r}}{r} - \dot{\varphi}^4\frac{\Phi_{,r}}{r} - 3\dot{\varphi}^4\frac{\Psi_{,r}}{r} + 2\frac{\dot{\varphi}^2}{a^2}\left(\frac{\varphi_{,r}}{r}\right)^2\right]
$$

$$
+ \frac{c_5}{H_0^6}\left[12\frac{\ddot{\varphi}\dot{\varphi}^2}{a^2}\left(\frac{\varphi_{,r}}{r}\right)^2 + 6\ddot{\varphi}\dot{\varphi}^4\frac{\Phi_{,r}}{r} - 6\left(\dot{H}\dot{\varphi}^4 + H^2\dot{\varphi}^4 + 4H\ddot{\varphi}\dot{\varphi}^3\right)\frac{\varphi_{,r}}{r}\right.
$$

$$
\left.- 6H\dot{\varphi}^5\frac{\Psi_{,r}}{r} + 6\frac{\dot{\varphi}^4}{a^2}\frac{\varphi_{,r}}{r}\frac{\Psi_{,r}}{r}\right], \tag{4.2}
$$

---

[1]Note that $\partial_r\varphi = \partial_r\delta\varphi$ is a perturbed quantity.

$$
\begin{aligned}
0 =\ & -c_2 \frac{1}{r^2} \left(r^2 \varphi_{,r}\right)_{,r} + \frac{c_3}{H_0^2} \left[\frac{4}{a^2} \frac{1}{r^2} \left(r(\varphi_{,r})^2\right)_{,r} - 4(\ddot{\varphi} + 2H\dot{\varphi}) \frac{1}{r^2} \left(r^2 \varphi_{,r}\right)_{,r} - 2\dot{\varphi}^2 \frac{1}{r^2} \left(r^2 \Psi_{,r}\right)_{,r} \right] \\
& + \frac{c_4}{H_0^4} \left[-\frac{4}{a^4} \frac{1}{r^2} \left((\varphi_{,r})^3\right)_{,r} + 12 \frac{\ddot{\varphi} + H\dot{\varphi}}{a^2} \frac{1}{r^2} \left(r(\varphi_{,r})^2\right)_{,r} - \left(12\dot{H}\dot{\varphi}^2 + 24\ddot{\varphi}\dot{\varphi}H + 26H^2\dot{\varphi}^2\right) \frac{1}{r^2} \left(r^2 \varphi_{,r}\right)_{,r} \right. \\
& + (12\ddot{\varphi}\dot{\varphi}^2 + 4H\dot{\varphi}^3) \frac{1}{r^2} \left(r^2 \Phi_{,r}\right)_{,r} - 12H\dot{\varphi}^3 \frac{1}{r^2} \left(r^2 \Psi_{,r}\right)_{,r} - 4\frac{\dot{\varphi}^2}{a^2} \frac{1}{r^2} \left(r\varphi_{,r} \Phi_{,r}\right)_{,r} + 12 \frac{\dot{\varphi}^2}{a^2} \frac{1}{r^2} \left(r\varphi_{,r} \Psi_{,r}\right)_{,r} \right] \\
& + \frac{c_5}{H_0^6} \left[-8\frac{\ddot{\varphi}}{a^4} \frac{1}{r^2} \left((\varphi_{,r})^3\right)_{,r} + 12\frac{\dot{H}\dot{\varphi}^2 + H^2\dot{\varphi}^2 + 2H\ddot{\varphi}\dot{\varphi}}{a^2} \frac{1}{r^2} \left(r(\varphi_{,r})^2\right)_{,r} - 12\frac{\dot{\varphi}^2}{a^4} \frac{1}{r^2} \left(\Psi_{,r} (\varphi_{,r})^2\right)_{,r} \right. \\
& - 12 \left(3H^2\ddot{\varphi}\dot{\varphi}^2 + 2\dot{H}H\dot{\varphi}^3 + 2H^2\dot{\varphi}^3\right) \frac{1}{r^2} \left(r^2 \varphi_{,r}\right)_{,r} - 24\frac{\ddot{\varphi}\dot{\varphi}^2}{a^2} \frac{1}{r^2} \left(r\varphi_{,r} \Phi_{,r}\right)_{,r} + 24\frac{H\dot{\varphi}^3}{a^2} \frac{1}{r^2} \left(r\varphi_{,r} \Psi_{,r}\right)_{,r} \\
& \left. - 6\frac{\dot{\varphi}^4}{a^2} \frac{1}{r^2} \left(r\Psi_{,r} \Phi_{,r}\right)_{,r} + 6 \left(4H\ddot{\varphi}\dot{\varphi}^3 + \dot{H}\dot{\varphi}^4 + H^2\dot{\varphi}^4\right) \frac{1}{r^2} \left(r^2 \Phi_{,r}\right)_{,r} - 15H^2\dot{\varphi}^4 \frac{1}{r^2} \left(r^2 \Psi_{,r}\right)_{,r} \right],
\end{aligned}
\tag{4.3}
$$

where r is the comoving radial coordinate and $_{,r} \equiv \mathrm{d}/\mathrm{d}r$. We have checked that these equations (together with the remaining components of the Einstein equations, which we do not show for brevity) satisfy the independent conservation equations $\nabla_\nu \delta G^{\mu\nu} = \nabla_\nu \delta T^{\mu\nu} = 0$. In the last term in Eq. (4.1), $\delta = \rho_m / \bar{\rho}_m - 1$ is the matter density contrast of the spherical top-hat overdensity w.r.t. the cosmic mean density. In this chapter, δ characterizes the density of the spherical haloes throughout their entire evolution, and not only during the stages where it is small ($|\delta| \ll 1$).

Eqs. (4.1) and (4.3) can be simplified by integrating over $\int 4\pi r^2 dr$. Doing so, and moving to the radial coordinate $\chi \equiv aH_0 r$, we can write Eqs. (4.1), (4.2) and (4.3) as

$$
\frac{\Phi_{,\chi}}{\chi} = \frac{\Omega_{m0}\delta a^{-3} + A_1 \left(\varphi_{,\chi}/\chi\right) + A_2 \left(\varphi_\chi/\chi\right)^2 + A_3 \left(\varphi_\chi/\chi\right)^3}{A_4 + A_5 \left(\varphi_\chi/\chi\right)},
\tag{4.4}
$$

$$
\frac{\Psi_{,\chi}}{\chi} = \frac{B_0 \left(\Phi_{,\chi}/\chi\right) + B_1 \left(\varphi_{,\chi}/\chi\right) + B_2 \left(\varphi_{,\chi}/\chi\right)^2}{B_3 - B_4 \left(\varphi_{,\chi}/\chi\right)},
\tag{4.5}
$$

$$
0 = C_1 \frac{\varphi_{,\chi}}{\chi} + C_2 \left(\frac{\varphi_{,\chi}}{\chi}\right)^2 + C_3 \left(\frac{\varphi_{,\chi}}{\chi}\right)^3 + C_4 \frac{\Phi_{,\chi}}{\chi} + C_5 \frac{\Psi_{,\chi}}{\chi}
$$
$$
+ C_6 \frac{\varphi_{,\chi}}{\chi} \frac{\Phi_{,\chi}}{\chi} + C_7 \frac{\varphi_{,\chi}}{\chi} \frac{\Psi_{,\chi}}{\chi} + C_8 \left(\frac{\varphi_{,\chi}}{\chi}\right)^2 \frac{\Psi_{,\chi}}{\chi} + C_9 \frac{\Phi_{,\chi}}{\chi} \frac{\Psi_{,\chi}}{\chi}.
\tag{4.6}
$$

The quantities A_i, B_i and C_i depend only on time and are given by:

$$A_1 = -2c_3\xi\varphi' - 12c_4\xi^2\varphi' - 15c_5\xi^3\varphi' \tag{4.7}$$

$$A_2 = 6c_4\xi\varphi' + 12c_5\xi^2\varphi' \tag{4.8}$$

$$A_3 = -4c_5\xi\varphi' \tag{4.9}$$

$$A_4 = 2 - 3c_4\xi^2\varphi'^2 - 6c_5\xi^3\varphi'^2 \tag{4.10}$$

$$A_5 = 6c_5\xi^2\varphi'^2 \tag{4.11}$$

$$B_0 = -2 - c_4\xi^2\varphi'^2 + 3c_5\xi^3\varphi''\varphi' \tag{4.12}$$

$$B_1 = 4c_4\left(-\xi^2\varphi' - \frac{3}{2}\xi^2\varphi''\right)$$
$$+6c_5\left(-\frac{3}{2}\xi^3\varphi'' - \xi^3\varphi'\right) \tag{4.13}$$

$$B_2 = 2c_4\xi\varphi' + 6c_5\xi^2\varphi'' \tag{4.14}$$

$$B_3 = -2 + 3c_4\xi^2\varphi'^2 + 6c_5\xi^3\varphi'^2 \tag{4.15}$$

$$B_4 = 6c_5\xi^2\varphi'^2 \tag{4.16}$$

$$C_1 = -c_2 - 2c_3\left(4\xi + \xi\frac{\varphi''}{\varphi'}\right) - c_4\left(26\xi^2 + 6\xi^2\frac{\varphi''}{\varphi'}\right)$$
$$-6c_5\left(4\xi^3 + \xi^3\frac{\varphi''}{\varphi}\right) \tag{4.17}$$

$$C_2 = 4c_3 + 6c_4\left(2\xi + \xi\frac{\varphi''}{\varphi'}\right)$$
$$+6c_5\left(2\xi^2 + \xi^2\frac{\varphi''}{\varphi'}\right) \tag{4.18}$$

$$C_3 = -4c_4 - 4c_5\xi\frac{\varphi''}{\varphi'} \tag{4.19}$$

$$C_4 = 2c_4\left(3\xi^2\varphi'' + 2\xi^2\varphi'\right)$$
$$+3c_5\left(3\xi^3\varphi'' + 2\xi^3\varphi'\right) \tag{4.20}$$

$$C_5 = -2c_3\xi\varphi' - 12c_4\xi^2\varphi' - 15c_5\xi^3\varphi' \tag{4.21}$$

$$C_6 = -4c_4\xi\varphi' - 12c_5\xi^2\varphi'' \tag{4.22}$$

$$C_7 = 12c_4\xi\varphi' + 24c_5\xi^2\varphi' \tag{4.23}$$

$$C_8 = -12c_5\xi\varphi' \tag{4.24}$$

$$C_9 = -6c_5\xi^2\varphi'^2, \tag{4.25}$$

which we have written by assuming the tracker evolution for the background. One can use Eqs. (4.4) and (4.5) to eliminate $\Phi_{,\chi}$ and $\Psi_{,\chi}$ in Eq. (4.6). The resulting equation is a

sixth-order algebraic equation for $\varphi_{,\chi}/\chi$, which can be cast as

$$
\begin{aligned}
0 \;=\;& \eta_{02}\delta^2 + \eta_{01}\delta + (\eta_{11}\delta + \eta_{10})\left[\frac{\varphi_{,\chi}}{\chi}\right] + (\eta_{21}\delta + \eta_{20})\left[\frac{\varphi_{,\chi}}{\chi}\right]^2 + (\eta_{31}\delta + \eta_{30})\left[\frac{\varphi_{,\chi}}{\chi}\right]^3 \\
&+\; \eta_{40}\left[\frac{\varphi_{,\chi}}{\chi}\right]^4 + \eta_{50}\left[\frac{\varphi_{,\chi}}{\chi}\right]^5 + \eta_{60}\left[\frac{\varphi_{,\chi}}{\chi}\right]^6 .
\end{aligned}
\tag{4.26}
$$

The coefficients η_{ab} are given in terms of the functions A_i, B_i and C_i in Eqs. (4.4), (4.5) and (4.6). Their expression is very lengthy and for brevity we do not show them explicitly.

The strategy used to determine the total gravitational force is as follows. For every moment in time and for a given matter overdensity δ one has to solve the algebraic equation, Eq. (4.26), to determine the gradient of the Galileon field inside the overdensity. Note that in the case of a top-hat profile, this gradient will be proportional to the radial coordinate, just like in GR. Having obtained the solution for $\varphi_{,\chi}/\chi$, one can then plug it into Eqs. (4.4) and (4.5) to determine the total gravitational force (GR + fifth force), which is given by $\Psi_{,\chi}$.

In the following, it will be convenient to measure the impact of the fifth force in terms of an effective gravitational constant G_{eff}. The latter is determined by the ratio of the total force to the normal gravity contribution:

$$
\frac{G_{\mathrm{eff}}}{G}(a,\delta) = \frac{\Psi_{,\chi}/\chi}{\Psi_{,\chi}^{\mathrm{GR}}/\chi} = \frac{\Psi_{,\chi}/\chi}{\Omega_{m0}\delta a^{-3}/2}.
\tag{4.27}
$$

In the Galileon model, G_{eff} is in general time and density dependent, but it is constant within a top-hat density profile.

Model parameters

In this chapter, we focus on the Quintic and Quartic Galileon models. Throughout, whenever we refer to these models, we will be referring to the models with the parameters given in Table 4.1. These are the model parameters that best-fit the WMAP9+SNLS+BAO dataset used in Ref. [2].

The time evolution of the expansion rate, the Galileon equation of state parameter $w_\varphi = \bar{p}_\varphi/\bar{\rho}_\varphi$ and the effective cosmological equation of state

$$
w_{\mathrm{eff}} = \left(\bar{\rho}_r/3 + w_\varphi\bar{\rho}_\varphi\right)/\left(\bar{\rho}_r + \bar{\rho}_m + \bar{\rho}_\varphi\right),
\tag{4.28}
$$

are shown in Fig. 4.1 for the Quintic and Quartic Galileon models. In the top left panel, we show both the numerical solution (solid) and the analytical tracker expression (dashed) for the expansion rate (Eq. (2.74)). One can see the very good agreement between the two

Table 4.1: Parameters of the Cubic, Quartic and Quintic Galileon models obtained from the constraint analysis presented in Ref. [2] with the WMAP9+SNLS+BAO dataset used there. In the analysis that led to these parameters, c_3 was the fixed parameter to break the scaling degeneracy (cf. Sec. 2.3). The value of c_2 was fixed by trial-and-error to yield a spatially flat Universe.

Parameter	Quintic Galileon	Quartic Galileon	Cubic Galileon
χ^2	7989.97	7995.60	8006.50
$\Omega_{r0}h^2$	4.28×10^{-5}	4.28×10^{-5}	4.28×10^{-5}
$\Omega_{b0}h^2$	0.02178	0.02182	0.02196
$\Omega_{c0}h^2$	0.125	0.126	0.1274
h	0.735	0.733	0.7307
n_s	0.947	0.945	0.953
τ	0.0680	0.0791	0.0763
$\log\left[10^{10}A_s\right]$	3.127	3.152	3.154
$\log\left[\rho_{\varphi,i}/\rho_{m,i}\right]$	-6.51	-37.39	-4.22
$c_2/c_3^{2/3}$	-3.59	-4.55	-5.378
c_3	10	20	10
$c_4/c_3^{4/3}$	-0.199	-0.096	0 (fixed)
$c_5/c_3^{5/3}$	0.0501	0 (fixed)	0 (fixed)
$\dot{\varphi}_i c_3^{1/3}$	2.31×10^{-14}	1.54×10^{-20}	1.104×10^{-9}
Age (Gyr)	13.778	13.770	13.748
$\sigma_8(z=0)$	0.975	0.998	0.997
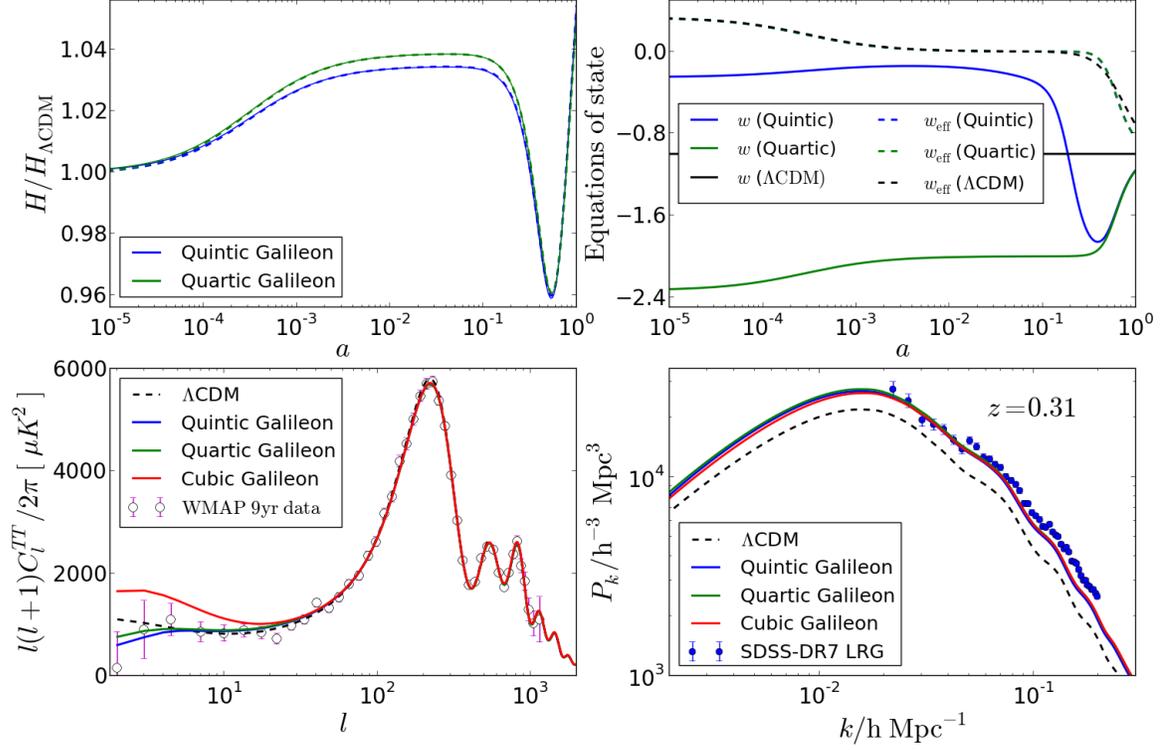
Figure 4.1: Cosmology of the best-fitting Cubic, Quartic and Quintic cosmologies that best-fit the WMAP9+SNLS+BAO dataset used in Ref. [2]. (Top left) Time evolution of the expansion histories of the Quintic (blue) and Quartic (green) Galileon models, plotted as $H/H_{\Lambda CDM}$. The solid lines represent the full numerical solution, whereas the dashed lines show the tracker solution of Eq. (2.74). (Top right) Time evolution of the Galileon field (solid) and cosmological (dashed) equations of state, w and w_{eff}, respectively, for the ΛCDM (black), Quartic (green) and Quintic (blue) Galileon models. (Bottom left) CMB temperature fluctuations angular power spectra, as function of the multipole moments, for the ΛCDM (dashed black), Cubic (solid red), Quartic (solid green) and Quintic (solid blue) Galileon models. Also shown are the data points with errorbars of the WMAP 9-yr results [201]. (Bottom right) Linear matter power spectrum, as function of scale k, for the ΛCDM (dashed black), Cubic (solid red), Quartic (solid green) and Quintic (solid blue) Galileon models. The power spectrum is shown for $z = 0.31$, which is the mean redshift of the Luminous Red Galaxies of the SDDS DR7 used to estimate the host halo spectrum shown as the data points with errorbars [187]. The amplitude of the latter is scaled by 1.85^{-2}.

at all the epochs shown. In the bottom panels of Fig. 4.1, we show the predicted power spectra for the CMB temperature fluctuations (bottom left) and for the linear clustering of matter (bottom right). We show the predictions of the Quintic and Quartic Galileon models, as well as the Cubic Galileon model[2] and the ΛCDM model with the WMAP 9-year parameters [201]. The spectra for these three models has already been discussed in Chapter 3 in light of the more recent Planck CMB results.

4.2 Fifth force solutions

In Eq. (4.27), we have parametrized the modifications to gravity (the fifth force) as a rescaling of the effective gravitational constant, which is time and density dependent. The process of determining the total force involves solving a nonlinear algebraic equation, Eq. (4.26), which in general has more than one branch of real solutions. Therefore, care must be taken in making sure that the physical branch exists and is correctly identified. We discuss these issues next.

4.2.1 Quintic Galileon

In the case of the Quintic Galileon model, Eq. (4.26) has six branches of solutions, which in general can be either complex or real. We require the physical branch to be real and to satisfy:

$$\frac{\varphi_{,\chi}}{\chi}\left(\delta \to 0\right) \to 0. \tag{4.29}$$

This is the solution that exhibits the physical behavior that there should be no fifth force if there are no density fluctuations sourcing it. This is what characterizes the linear regime as well. We must ensure that this solution exists at every moment in time, and for every value of $\delta \geq -1$.

However, as we will show next, the Quintic Galileon model equations do not satisfy this requirement. To better understand why this happens, one can differentiate Eq. (4.26)

---

[2]The Cubic Galileon model is also the best-fitting one to the WMAP9+SNLS+BAO dataset, obtained with the strategy presented in Ref. [2]. The nonlinear structure formation in this model shall be studied in Chapter 5.
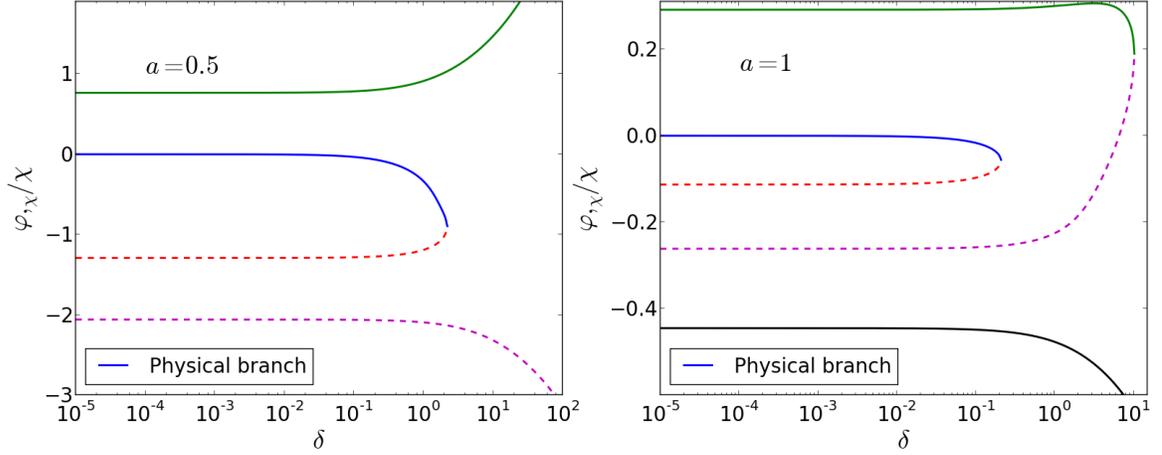
Figure 4.2: Evolution of the branches of solutions of Eq. (4.26) as function of the density constrast δ, for $a = 0.5$ (left panel) and $a = 1$ (right panel). The physical branch corresponds to the solid blue line for which $\varphi_{,\chi}/\chi\,(\delta = 0) = 0$. For visualization purposes, in the $a = 1$ panel we do not show the branch $\varphi_{,\chi}/\chi\,(\delta = 0) = -11.477$, which is far below the scale of the plot and has little importance for the discussion.

w.r.t. δ to obtain a differential equation for $\varphi_{,\chi}/\chi$:

$$\frac{\mathrm{d}}{\mathrm{d}\delta}\left[\frac{\varphi_{,\chi}}{\chi}\right] = \frac{-2\eta_{02}\delta - \eta_{01} - \eta_{11}\left[\frac{\varphi_{,\chi}}{\chi}\right] - \eta_{12}\left[\frac{\varphi_{,\chi}}{\chi}\right]^2 - \eta_{31}\left[\frac{\varphi_{,\chi}}{\chi}\right]^3}{\eta_{11}\delta + \eta_{10} + 2\left(\eta_{21}\delta + \eta_{20}\right)\left[\frac{\varphi_{,\chi}}{\chi}\right] + 3\left(\eta_{31}\delta + \eta_{30}\right)\left[\frac{\varphi_{,\chi}}{\chi}\right]^2 + 4\eta_4\left[\frac{\varphi_{,\chi}}{\chi}\right]^3 + 5\eta_5\left[\frac{\varphi_{,\chi}}{\chi}\right]^4 + 6\eta_6\left[\frac{\varphi_{,\chi}}{\chi}\right]^5}.$$

(4.30)

 Just to illustrate our point, it suffices to consider the equations at $a = 0.5$ and $a = 1$ (we have checked that our conclusion holds for other epochs too). When $\delta = 0$, Eq. (4.26) has four real roots $\{-2.059,\ -1.292,\ 0,\ 0.765\}$ at $a = 0.5$, whereas at $a = 1$ there are six real roots $\{-11.477,\ -0.445,\ -0.261,\ -0.113,\ 0,\ 0.291\}$. These can be used as the initial conditions to solve Eq. (4.30) and evolve the different branches. The result is shown in Fig. 4.2. The physical branch is the one that starts from zero at $\delta = 0$, but one sees that it cannot be evaluated beyond $\delta \approx 2$ and $\delta \approx 0.2$ at $a = 0.5$ and $a = 1$, respectively. At these values of δ, the differential equation becomes singular because the physical branch becomes complex (and therefore unphysical), together with the branch represented by the dashed red line. The same thing happens for the (unphysical) branches represented by the solid green and dashed magenta lines at $a = 1$, although at different values of δ. We have explicitly looked at Eq. (4.26) for cases near these critical values of δ to confirm that the breakdown of the differential equation is related to the absence of real roots. Moreover,

we have also checked that the problem persists for different choices of the Galileon and cosmological parameters around the regions of parameter space preferred by the CMB, SNIa and BAO data [2].

The spherical collapse in the Galileon model has been also studied in [255]. In the latter, the authors found that physical fifth force solutions exist both at low and high densities. In particular, by taking the limit $\delta \gg 1$, the authors derive the conditions for the existence of real solutions for Eq. (4.26). This assumes that the physical solution does not become complex for intermediate densities, which is what is shown not to happen in Fig. 4.2. Here, we do not attempt a thorough comparison between our results, although we point out that contrary to [255], we focus on the parameters of the model that fit the observational data.

At this point, one may wonder whether this problem can be avoided by relaxing the quasi-static and weak-field approximations used to derive Eqs. (4.1), (4.2) and (4.3). However, note that Fig. 4.2 shows that the physical solution does not even exist in high density regions, where the terms that have been neglected are expected to be small, and hence our approximations are justified (we will return to this point in the next section). Another way to try to circunvent the problem is to explore different choices of the Galileon and cosmological parameters. However, even if for a different choice of parameters one could find physical solutions for all δ, such parameters would already be ruled out by the CMB, SNIa and BAO data. For these reasons, our study of the spherical collapse in the Quintic model stops here!

4.2.2   Quartic Galileon

When $c_5 = 0$, Eq. (4.26) becomes

$$0 \;=\; \eta_{01}\delta + (\eta_{11}\delta + \eta_{10})\left[\frac{\varphi_{,\chi}}{\chi}\right] + \eta_{20}\left[\frac{\varphi_{,\chi}}{\chi}\right]^2 + \eta_{30}\left[\frac{\varphi_{,\chi}}{\chi}\right]^3 , \qquad (4.31)$$

which is third order, and therefore admits analytical solutions given by the general expression

$$\frac{\varphi_{,\chi}}{\chi} = -\frac{1}{3\eta_{30}}\left[\eta_{20} + \mu_k\Gamma + \frac{\Sigma_0}{\mu_k\Gamma}\right] , \; k \in \{1,2,3\} , \qquad (4.32)$$

where

$$\Gamma = \left[\frac{\Sigma_1 + \sqrt{\Sigma_1^2 - 4\Sigma_0^3}}{2} \right]^{1/3}, \tag{4.33}$$

$$\Sigma_0 = \eta_{20}^2 - 3\eta_{30} \left(\eta_{11}\delta + \eta_{10} \right), \tag{4.34}$$

$$\Sigma_1 = 2\eta_{20}^3 - 9\eta_{30}\eta_{20} \left(\eta_{11}\delta + \eta_{10} \right) + 27\eta_{30}\eta_{01}, \tag{4.35}$$

and the three branches of solutions (labelled by k) correspond to

$$\mu_1 = 1, \quad \mu_2 = \exp\left[-i\pi/3\right], \quad \mu_3 = \exp\left[i\pi/3\right]. \tag{4.36}$$

The physical branch, Eq. (4.29), corresponds to the $k = 3$ solution, which is a complex number. As a result, Γ must be complex as well and we can write it as

$$\Gamma = \Sigma_0^{1/2} \exp\left[i\theta/3\right], \tag{4.37}$$

with θ given by

$$\cos\theta = \frac{\Sigma_1/2}{\Sigma_0^{3/2}}, \quad \theta \in [0, \pi]. \tag{4.38}$$

Using these expressions, Eq. (4.32) can be written as

$$\frac{\varphi_{,\chi}}{\chi} = -\frac{1}{3\eta_{30}} \left[\eta_{20} + 2\sqrt{\Sigma_0} \cos\left(\frac{\theta}{3} - \frac{2\pi}{3} \right) \right], \tag{4.39}$$

which allows us to analytically determine the magnitude of the effective gravitational strength (G_{eff}) using Eq. (4.27).

The value of G_{eff} as a function of the scale factor a and density δ is shown in the colour map of Fig. 4.3, for the Quartic Galileon model. The left and right panels correspond to $\delta > 0$ and $\delta < 0$, respectively. For $\delta > 0$ we see that, contrary to the case of the Quintic Galileon model, there are physical solutions for sufficiently large values of the density contrast δ. When $a \lesssim 0.5$ one has $G_{\text{eff}}/G \approx 1$. At later times, however, G_{eff}/G progressively deviates from unity, and this happens in a density dependent way. In the linear regime ($\delta \ll 1$), G_{eff} increases with time, being roughly 40% larger than G today. However, for $\delta \gtrsim 1$, one sees that gravity becomes weaker with time ($G_{\text{eff}}/G < 1$). In particular, at the present day, the effective gravitational strength is reduced to $\sim 60\%$ of the standard gravity value.

The effects of the fifth force that modify G_{eff} in the Quartic model can be thought of as being two-fold. Firstly, one has the extra terms proportional to $\varphi_{,\chi}/\chi$, that add up to

the total gravitational strength in Eqs. (4.4) and (4.5). Secondly, there are also the time-dependent coefficients A_4, B_0 and B_3 that multiply the standard gravity terms, and that arise from the explicit couplings of the Galileon field to curvature in $\mathcal{L}_4$ (cf. Eq. (2.2)). The effect of the screening can be seen by writting Eq. (4.26) in the limit where $\delta \gg 1$,

$$0 \approx \eta_{01} + \eta_{11}\left[\frac{\varphi_{,\chi}}{\chi}\right]. \tag{4.40}$$

Here, one sees that in regions where the density is sufficiently high, the spatial gradient of the Galileon field, $\varphi_{,\chi}/\chi$, does not depend on δ. The Vainshtein mechanism in the Quartic model works because

$$\left|\frac{\varphi_{,\chi}}{\chi}\right| = \left|\frac{\eta_{01}}{\eta_{11}}\right| \ll \left|\frac{\Psi_{,\chi}}{\chi}\right| \sim \delta \quad (\delta \gg 1), \tag{4.41}$$

and increasing the density δ further does not increase the gradient of the Galileon field. However, the coefficients A_4, B_0 and B_3 depend only on the background evolution of the Galileon field, and will not be affected by the Vainshtein mechanism. This is why G_{eff}/G does not approach unity when $\delta \gg 1$ (cf. Fig. 4.3). This result has in fact been found to be generically possible in the framework of the most general second-order scalar tensor theory [248, 249], which encompasses the Quartic Galileon model studied here.

The fact that the effective gravitational strength is time-varying if the density is high is an unpleasant novelty of the model. In fact, this may imply that the Quartic Galileon model is automatically ruled out by the local gravity tests that constrain the modifications to gravity to be very small. For instance, [248, 249] have claimed that Lunar Laser Ranging experiments [250] can place very strong constraints on models like the Quartic Galileon. Indeed, in Chapter 3, we saw that the Lunar Laser Ranging bounds essentially constraint the Quartic model to look almost exactly like the Cubic model, ie., $|c_4| \ll 1$ (cf. Fig. 3.11). One may invoke the validity of the quasi-static approximation in an attempt to ease this problem. For instance, if the time derivative of the Galileon field perturbation is not completely negligible, then its contribution to the coefficients A_4, B_0 and B_3 could help soften the time variation of G_{eff}. However, we argue that this should not be the case. The successful implementation of the screening in the Quartic Galileon model means that the fluctuations of the Galileon field, $\delta\varphi$, have to be much smaller than the metric perturbation, i.e., $\delta_\varphi \ll \Psi$ (cf. Eqs. (4.40) and (4.41)). Since Ψ is typically very small for collapsed objects like cluster- and galaxy-mass haloes or the Sun ($\Psi \sim 10^{-6}$ to 10^{-4}) [3], then $\delta\varphi$ has to be even

---

[3]Near black holes, for instance, one can have larger metric perturbations $\Psi \sim 1$.
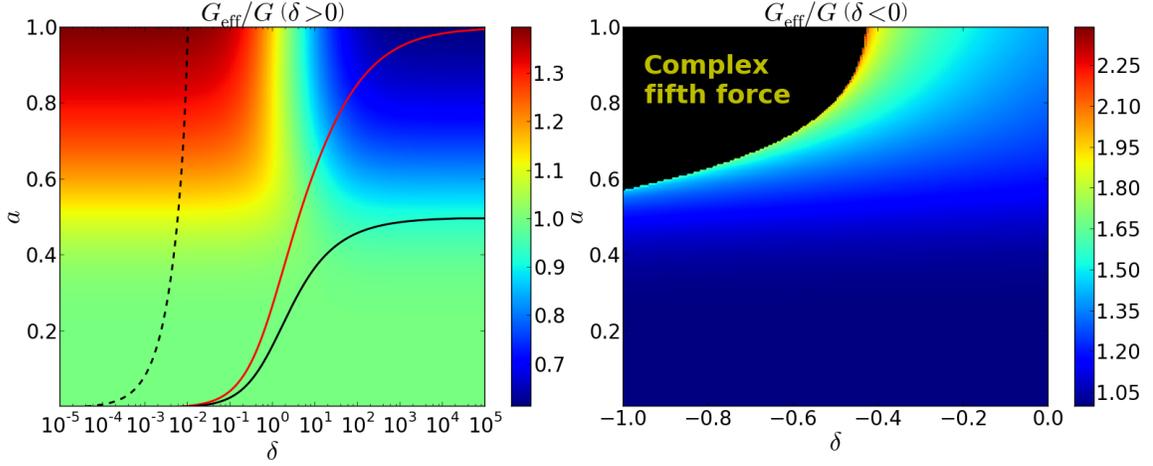
Figure 4.3: Time and density dependence of the effective gravitational strength G_{eff} of Eq. (4.27) for $\delta > 0$ (left panel) and $\delta < 0$ (right panel). The colour scale bars at the right of each panel show the value of G_{eff}/G. In the left panel the solid red and solid black lines represent the trajectory in $a - \delta$ space of a halo that collapses at $a = 1$ ($z = 0$) and $a = 0.5$ ($z = 1$) in the Quartic Galileon model, respectively. The dashed black line shows the trajectory of a large linear density region with density contrast $\delta = 0.01$ today. In the right panel, the region marked in black in the top left corner shows the values of a and δ for which the solution of the fifth force becomes a complex number. To facilitate the visualization, note that the colour scale in the two panels is not the same.

smaller. This justifies the use of the weak-field assumption for the Galileon perturbation, $\delta\varphi$. Consequently, for consistency, the time variation of $\delta\varphi$ has to be very small as well, $\dot{\delta\varphi} \ll \dot{\Psi} \ll \dot{\varphi}$. The same reasoning applies to the Quintic model studied in the last subsection. In the remaining of the chapter, we will focus on the cosmological interpretation of the results [4].

For $\delta < 0$, in Fig. 4.3, we see again that the modifications to gravity arise only for $a \gtrsim 0.5$, but here gravity can only become stronger. In addition, there are no physical solutions for the epochs and densities indicated by the black region in the top left corner of the right panel of Fig. 4.3. In particular, the fifth force becomes complex in the most empty voids ($\delta \sim -1$) for $a \gtrsim 0.6$; at $a = 1$, underdense regions where $\delta \lesssim -0.4$ also

---

[4]We note that if we solve the model equations in perturbed Minkowski space (instead of FRW), then $\dot{\varphi} = 0$ and $G_{\mathrm{eff}} \to 1$, when $\delta \gg 1$. We discuss this issue further in Chapter 6, when we encounter a similar problem in Nonlocal gravity models.

do not admit a real fifth force. As we will see in the next chapter, this is a problem that exists also in the Cubic Galileon model. One may wonder whether this absence of real physical solutions for the fifth force could be due to the fact that the quasi-static limit is not be a good approximation in low density regions. However, the recent work of Ref. [256] suggests that this is not the case. We shall return to these discussions in Chapter 7, when we study the properties of cosmic voids. For the analysis in this chapter, however, we can put these issues aside as we are interested in the formation of haloes, for which these low densities are irrelevant.

4.3 Excursion set theory in Galileon gravity

In this section, we layout the main premises of excursion set theory [254, 257] and of the dynamics of the gravitational collapse of spherical overdensities in the Galileon model (see, e.g. [258, 259, 260, 261, 262, 263, 264, 265, 266, 267] and references therein for applications of the spherical collapse model and excursion set theory to other modified gravity models).

4.3.1 Basics of excursion set theory

Unconditional probability distribution and halo mass function

The main postulate of excursion set theory is that dark matter haloes form from the gravitational collapse of regions where the linear density contrast smoothed over some comoving length scale R,

$$
\begin{aligned}
\delta_{\mathrm{lin}}\left(\mathbf{x}, R\right) &= \int W\left(|\mathbf{x} - \mathbf{y}|, R\right) \delta_{\mathrm{lin}}\left(\mathbf{y}\right) \mathrm{d}^3\mathbf{y} \\
&= 4\pi \int k^2 \tilde{W}\left(k, R\right) \delta_{\mathrm{lin},\mathrm{k}} e^{i\mathbf{k}\mathbf{x}} \mathrm{d}k,
\end{aligned}
\tag{4.42}
$$

exceeds a certain critical density threshold $\delta_{\mathrm{lin},\mathrm{crit}}$ (to be defined below). Here $W\left(|\mathbf{x} - \mathbf{y}|, R\right)$ is the real space filter (or window) function of comoving size R, and $\tilde{W}\left(k, R\right)$ and $\delta_{\mathrm{lin},\mathrm{k}}$ are the Fourier transforms of $W\left(|\mathbf{x} - \mathbf{y}|, R\right)$ and $\delta_{\mathrm{lin}}\left(\mathbf{y}\right)$, respectively. We use the subscript "$_{\mathrm{lin}}$" to remind ourselves of the situations where the density contrast should be interpreted as being small ($|\delta| \ll 1$), i.e., in the linear regime.

The mass of the halo is given by

$$
M = 4\pi \bar{\rho}_{m0} R^3 / 3.
\tag{4.43}
$$

For the same comoving radius R, the halo mass is different for models with different matter densities $\bar{\rho}_{m0}$. As the standard practice, we assume that the probability distribution of the initial (for us, initial refers to $z_i = 300$) linear density contrast $\delta_{\text{lin}}(\mathbf{x})$ is a Gaussian with zero mean

$$\text{Prob.}\,(\delta_{\text{lin}}, S)\,\mathrm{d}\delta_{\text{lin}} = \frac{1}{\sqrt{2\pi S}} \exp\left[-\frac{\delta_{\text{lin}}^2}{2S}\right]\mathrm{d}\delta_{\text{lin}}, \tag{4.44}$$

in which $S \equiv S(R)$ is the variance of the density contrast field on the scales of the size of the filter function R, and is given by

$$S(R) \equiv \sigma^2(R) = 4\pi \int k^2 P_k \tilde{W}\,(k, R)\,\mathrm{d}k, \tag{4.45}$$

where P_k is the linear matter power spectrum. Note that for a fixed model, the variables R, M and S are related to one another and will be used interchangeably throughout when referring to the scale of the haloes.

In hierarchical models of structure formation, $S(R)$ is a monotonically decreasing function of R. Consequently, the probability that the density field on a region smoothed over a very large R exceeds the critial density $\delta_{\text{lin,crit}}$ is very small, since the variance is also very small. As one smooths the density field with decreasing R, the field $\delta_{\text{lin}}\,(\mathbf{x}, R)$ undergoes a random walk with "time" variable S. In the excursion set theory language, $\delta_{\text{lin,crit}}$ defines a "barrier" that the random walks cross, and the aim is to determine the probability distribution, $f(S)\mathrm{d}S$, that the first up-crossing of the barrier occurs at $[S, S + \mathrm{d}S]$. In the particular case where the filter function is a top-hat in k-space, then the random walk of the density field will be Brownian. As we will see below, in the case of the Galileon model, the critical density for collapse does not depend on the scale S considered. This is called a "flat barrier". In this case, $f(S)$ admits a closed analytical formula given by [254]

$$f(S) = \frac{1}{\sqrt{2\pi}}\frac{\delta_c}{S^{3/2}} \exp\left[-\frac{\delta_c^2}{2S}\right], \tag{4.46}$$

where δ_c denotes the initial critical density, $\delta_{\text{lin,crit}}$, for a spherical overdensity to collapse at a given redshift, linearly extrapolated to the present day, assuming ΛCDM linear growth factor[5]. This linear extrapolation is done only for historical reasons so that the values of δ_c we present in this chapter can be more easily compared with previous work. Note also that, for consistency, one must compute the variance S in Eq. (4.45) using the initial power

---

[5]In the case of δ_c, we will avoid writting the subscript $_{\text{lin}}$ to ease the notation.

spectrum of the models, but evolved to $z = 0$ with the ΛCDM linear growth factor. We use the BBKS fitting formula [268], whose accuracy in reproducing the ΛCDM and Quartic Galileon model P_k at the initial time is more than sufficient for the purposes of the qualitative discussion we present here[6]. We will follow the standard procedure of adopting a filter function that is a top-hat in real space, whose Fourier transform is given by

$$\tilde{W}(k, R) = 3 \frac{\sin(kR) - kR\cos(kR)}{(kR)^3}. \tag{4.47}$$

Note that, strictly speaking, for this filter function the excursion set random walks are not Brownian, and as a result, there is some degree of approximation in taking Eq. (4.46). On the other hand, this choice of filter function is that which is compatible with our definition of the mass of the smoothed overdense region (Eq. (4.43)).

In this chapter, the halo mass function is the comoving differential number density of haloes of a given mass per natural logarithmic interval of mass. This quantity is obtained by associating $f(S)\mathrm{d}S$ with the fraction of the total mass that is incorporated in haloes, whose variances fall within $[S, S + \mathrm{d}S]$ (or equivalently, whose masses fall within $[M, M + \mathrm{d}M]$). The mass function observed at redshift z is then given by

$$\begin{aligned}
\frac{\mathrm{d}n(M)}{\mathrm{d}\ln M}\mathrm{d}\ln M &= \frac{\bar{\rho}_{m0}}{M} f(S)\mathrm{d}S \\
&= \frac{\bar{\rho}_{m0}}{M} \frac{\delta_c}{\sqrt{2\pi S}} \left| \frac{\mathrm{d}\ln S}{\mathrm{d}\ln M} \right| \exp\left(-\frac{\delta_c^2}{2S} \right) \mathrm{d}\ln M.
\end{aligned} \tag{4.48}$$

This is known as the Press-Schechter mass function [269]. The redshift dependence is included into δ_c (cf. Fig. 4.4). In principle, one can distinguish the formation time from the observation time of the haloes (see e.g. [270]). For simplicity, in this chapter we assume that these are the same, i.e., $z = z_{\mathrm{form}} = z_{\mathrm{obs}}$.

Conditional probability distribution and halo bias

Equations (4.46) and (4.48) assume that the starting point of the excursion set random walk is the origin of the $\delta_{\mathrm{lin}} - S$ plane. The mass function computed using Eq. (4.48) gives the abundance of haloes that have collapsed from the mean cosmological background. However, it is well known that the clustering of haloes is biased towards the underlying clustering of dark matter, i.e., the number density of haloes is different in different regions.

---

[6]Note that one can use ΛCDM to compute the matter power spectrum of the Galileon model at the initial time, but one has to use the parameters given in Table 4.1.

Within the framework of excursion set theory, this is described by the so-called halo bias parameter δ_h [271]. The latter is determined by computing the abundance of haloes that have formed from a region characterized by $S = S_0$ and $\delta_{\mathrm{lin}} = \delta_0$, and compare it with the abundance of the haloes that have formed from the mean background ($S = \delta_{\mathrm{lin}} = 0$). It can be shown that δ_h is given by [271]

$$\delta_h = (1 + \delta_{\mathrm{env}}) \frac{f(S|S_0, \delta_0)\mathrm{d}S}{f(S)\mathrm{d}S} - 1, \tag{4.49}$$

where δ_{env} is the density contrast of the underlying dark matter region or environment where the haloes are forming. $f(S|S_0, \delta_0)$ is the probability distribution that a random walk that starts (or passes through) (δ_0, S_0) crosses the critical barrier δ_c at $[S, S + \mathrm{d}S]$, and is given by

$$f(S|S_0, \delta_0) = \frac{1}{\sqrt{2\pi}} \frac{\delta_c - \delta_0}{(S - S_0)^{3/2}} \exp\left[-\frac{(\delta_c - \delta_0)^2}{2(S - S_0)}\right], \tag{4.50}$$

for a flat barrier. Here, δ_0 is the linearly extrapolated (with the ΛCDM linear growth factor to today) initial density of the underlying dark matter region, so that its density is δ_{env}, at a given redshift[7]. From Eqs. (4.50) and (4.49) one sees that dense regions can boost the clustering of haloes, since the effective height of the barrier becomes lower ($\delta_c - \delta_0 < \delta_c$). On the other hand, the clustering can also be suppressed if the mass of the haloes is comparable to the mass available in the region specified by S_0. For example, haloes with variance $S < S_0$ will not form because the random walks cannot cross the barrier before their starting point (this effect is known as halo exclusion).

One is often interested in the limit of very large regions with small density contrast ($S_0 \ll 1$, $0 < \delta_0 \ll 1$), where the treatment simplifies considerably. In this case, we can Taylor expand δ_h as [272]:

$$\delta_h = \sum_{k=0}^{\infty} \frac{b_k}{k!} \delta^k \approx b_0 + b_1 \delta_{\mathrm{env}} + \mathcal{O}\left(\delta_{\mathrm{lin,env}}^2\right), \tag{4.51}$$

where we have truncated the series at the linear term, as we are assuming low density regions (from here on δ_{env} should be interpreted as a small linear overdensity). Since we are taking the limit where the dark matter regions look like the mean background, $S_0, \delta_0 \to 0$,

---

[7]Just like for δ_c, we will avoid writting the subscript $_{\mathrm{lin}}$ in δ_0 to ease the notation.

then $b_0 = 0$. The linear term b_1 is then the leading one, and is given by

$$
\begin{aligned}
b_1 &= \frac{\mathrm{d}}{\mathrm{d}\delta_{\mathrm{env}}}\delta_h|_{\delta_{\mathrm{env}}=0} \\
&= \frac{1}{f(S)}\left[f(S) + \left(\frac{\mathrm{d}\delta_0}{\mathrm{d}\delta_{\mathrm{env}}}\right)\frac{\mathrm{d}}{\mathrm{d}\delta_0}f(S|0,\delta_0)|_{\delta_0=0}\right] \\
&= 1 + \left(\frac{\mathrm{d}\delta_0}{\mathrm{d}\delta_{\mathrm{env}}}\right)\frac{\delta_c^2/S - 1}{\delta_c} \\
&= 1 + g(z)\frac{\delta_c^2/S - 1}{\delta_c}.
\end{aligned}
\tag{4.52}
$$

To find the expression of $g(z)$, one notes that

$$
\begin{aligned}
\delta_{\mathrm{env}} &= \frac{D^{\mathrm{model}}(z)}{D^{\mathrm{model}}(z_i)}\delta_{\mathrm{env,i}} = \frac{D^{\mathrm{model}}(z)}{D^{\mathrm{model}}(z_i)}\frac{D^{\Lambda\mathrm{CDM}}(z_i)}{D^{\Lambda\mathrm{CDM}}(0)}\delta_0 \\
&= \frac{D^{\mathrm{model}}(z)}{D^{\Lambda\mathrm{CDM}}(0)}\delta_0,
\end{aligned}
\tag{4.53}
$$

where $\delta_{\mathrm{env,i}}$ is the initial density of the regions whose density today in a given model is δ_{env}. In Eq. (4.53), $D^{\mathrm{model}}(z)$ is the linear growth factor of a given model and we have assumed that $D^{\mathrm{model}}(z_i) = D^{\Lambda\mathrm{CDM}}(z_i)$ (see next subsection). Thus, $g(z)$ is simply given by

$$
g(z) \equiv \frac{\mathrm{d}\delta_0}{\mathrm{d}\delta_{\mathrm{env}}} = \frac{D^{\Lambda\mathrm{CDM}}(0)}{D^{\mathrm{model}}(z)}.
\tag{4.54}
$$

In Eq.(4.52), the model dependence is included in $g(z)$ and δ_c. In particular, $g(z)$ accounts for the fact that different models have different values of δ_0 to yield the same δ_{env} at redshift z.

4.3.2 Linear growth factor and spherical collapse dynamics

The final ingredient to derive the mass function and the linear halo bias is to determine the threshold barrier δ_c, and to specify the equation that governs the evolution of the linear overdensities (which determines $g(z)$, Eq. (4.54)). For scales inside the horizon, the latter can be written as

$$
\ddot{\delta}_{\mathrm{lin}} + 2H\dot{\delta}_{\mathrm{lin}} - 4\pi G\bar{\rho}_m\delta_{\mathrm{lin}} = 0,
\tag{4.55}
$$

or equivalently, by changing the time varible to $N = \ln a$, as

$$
D'' + \left(\frac{E'}{E} + 2\right)D' - \frac{3}{2}\frac{G_{\mathrm{eff}}(a)}{G}\frac{\Omega_{m0}e^{-3N}}{E^2} = 0,
\tag{4.56}
$$

where the linear growth factor $D(a)$ is defined as $\delta_{\mathrm{lin}}(a) = D(a)\delta_{\mathrm{lin}}(a_i)/D(a_i)$. The initial conditions are set up at $z_i = 300$ using the known matter dominated solution $D(a_i) =$

$D'(a_i) = a_i$ [8]. These initial conditions are the same for all the models we will study (cf. Eq. (4.53)). The linear growth factor obtained by solving Eq. (4.56) enters the calculation of the linear halo bias through $g(z)$.

Recall we have defined δ_c as the linearly extrapolated value (using the ΛCDM linear growth factor) of the initial density of the spherical overdensity for it to collapse at a given redshift. To determine this value, we consider the evolution equation of the physical radius ζ of the spherical halo at time t, which satisfies the Euler equation

$$\frac{\ddot{\zeta}}{\zeta} - \left(\dot{H} + H^2\right) = -\frac{\Psi_{,\zeta}}{\zeta} = -H_0^2 \frac{\Psi_{,\chi}}{\chi}$$
$$= -\frac{G_{\text{eff}}(a, \delta)}{G} \frac{H_0^2 \Omega_{m0} \delta a^{-3}}{2}, \tag{4.57}$$

where we have used Eq. (4.27) in the last equality. Note that $\zeta = ar = \chi/H_0^2$, where r is the comoving radial coordinate. Changing the time variable to N and defining $y(t) = \zeta(t)/(aR)$, Eq. (4.57) becomes

$$y'' + \left(\frac{E'}{E} + 2\right) y' + \frac{G_{\text{eff}}(a, y^{-3} - 1)}{G} \frac{\Omega_{m0} e^{-3N}}{2E^2} \left(y^{-3} - 1\right) y = 0, \tag{4.58}$$

where we have used that $\delta = y^{-3} - 1$ invoking mass conservation [9]. The initial conditions are then given by $y(a_i) = 1 - \delta_{\text{lin,i}}/3$ and $y'(a_i) = \delta_{\text{lin,i}}/3$ (here, $\delta_{\text{lin,i}}$ is the initial linear density contrast). The value of δ_c is found by a trial-and-error approach to determine the initial density $\delta_{\text{lin,i}}$ that leads to collapse ($y = 0$, $\delta \to \infty$) at redshift z, evolving this afterwards until the present day using the ΛCDM linear growth factor.

It is important to note that, despite the presence of the Vainshtein screening, the modifications to gravity incorporated into G_{eff} do not introduce any scale dependence in the dynamics of the collapse of the spherical overdensities. The reason for this is that the implementation of the Vainshtein mechanism does not depend on the size of the halo R, but only on its density. Consequently, the critical barrier δ_c is "flat", i.e., it is only time-dependent and not S-dependent. In fact, in the previous subsection we have already anticipated this result, which is the one for which Eqs. (4.46), (4.48) and (4.50) are valid. The situation is different, for instance, in models that employ the chameleon screening mechanism. In these cases, the fifth force is sensitive to the size of the halo, and the barrier can have a nontrivial shape [261].

---

[8]Not to be confused with the initial times of Table 4.1.

[9]Explicitly: $\bar{\rho}_m a^3 R^3 = (1 + \delta) \bar{\rho}_m r^3 \Rightarrow \delta = (aR/r)^3 - 1 = y^{-3} - 1$.

Limitations of the spherical top-hat profile description

It is well known that the Sheth-Tormen mass function [273, 274, 275] fits ΛCDM N-body simulation results better than Eq. (4.48). The reason is because the Sheth-Tormen mass function is derived by assuming the ellipsoidal collapse of the overdensities, which is a more realistic description of the intrinsically triaxial proccesses of gravitational instability. In the excursion set picture, the ellipsoidal collapse translates into a mass dependent (i.e. 'non-flat') critical barrier. In this chapter, we are only interested in a qualitative analysis and, therefore, the spherical collapse model is sufficient. However, even if one models the Galileon mass function with the standard Sheth-Tormen formulae (as we shall do in Chapter 5), some complications may still arise. We comment on two such complications.

Firstly, the Sheth-Tormen mass function contains two free parameters (a and p in Eq. (10) of [273]), which were originally fitted against N-body simulations of ΛCDM models. The ellipsoidal collapse captures a number of departures from the spherical collapse, but the magnitude of such departures can be different for different models. As a result, one expects these two parameters to be different in Galileon gravity. Secondly, in the paradigm of hierarchichal structure formation, larger objects form by the merging or accretion of smaller objects. As a result, the assumption that the overdense regions remain a top-hat throughout all stages of the collapse may not be a good approximation, specially when it comes to capture the effects of the screening mechanism. For example, consider the formation of a very massive halo; then, in the case of the spherical top-hat collapse, the effects of the screening mechanism only become important in the late stages of the collapse, when the density of the region is sufficiently high. In reality, however, the screening mechanism should start to have an impact on the formation of this very massive halo much earlier, because the halo forms via the continuous merging/accretion of higher-density objects that has been affected by the screening since earlier times.

The investigation of the performance of the excursion set theory formalism in reproducing the simulation results of Galileon gravity models [6, 276] is the subject of Chapter 5.

4.4   Results

In this section we present our results for the halo mass function and halo bias. These will be shown for the WMAP9 best-fitting ΛCDM model [201] (dashed black) and three

Table 4.2: Summary of the models for which we study the mass function and halo bias. We also show the collapse threshold δ_c at redshift zero for each of these models.

Model	$\Omega_{m0}h^2$	$H(a)$	G_{eff}/G	$\delta_c\,(z=0)$
ΛCDM	0.137	ΛCDM	1	1.677
QCDM	0.148	Eq. (2.74)	1	1.565
Linear force Quartic Galileon	0.148	Eq. (2.74)	Eq. (4.27) ($\delta \ll 1$)	1.497
Full Quartic Galileon	0.148	Eq. (2.74)	Eq. (4.27)	1.594

variants of the Quartic Galileon model. The first one is the "full" Quartic Galileon (solid blue) model characterized by Eqs. (2.74) and (4.27). The second model is a linear force Quartic Galileon model (solid green), in which G_{eff}/G is obtained by taking the limit where $|\delta| \ll 1$ (cf. Fig.4.3). Comparing these two models allows one to measure the effects of the δ-dependence of G_{eff}. The last variant is a model we call QCDM (solid red), in which the modifications to gravity are absent $G_{\text{eff}}/G = 1$, but the expansion history and matter density are the same as in the other two variants. This model is useful to isolate the changes introduced by the modified gravitational strength, excluding those that arise through the different matter density and modified expansion rate. These models are summarized in Table 4.2.

4.4.1 Evolution of the critical density δ_c

Before presenting the predictions for the halo mass function and bias, it is instructive to look at the time dependence of δ_c. This is shown in the top panel of Fig. 4.4, and the bottom panel shows the difference with respect to the ΛCDM model. Comparing the ΛCDM and QCDM models, the differences are driven by the different matter densities and by the different expansion rates. The physical matter density, $\Omega_{m0}h^2$, is smaller in the ΛCDM than in the QCDM model (cf. Table 4.2), so that structure formation is enhanced in the latter. On the other hand, the expansion rate acts as a friction term that slows down structure formation. In Fig. 4.1, we saw that $H^{\Lambda\text{CDM}} > H^{\text{QCDM}}$ for $0.3 \lesssim a \lesssim 0.8$. During these times, the friction will be higher in ΛCDM, but lower for all other times. The net effect
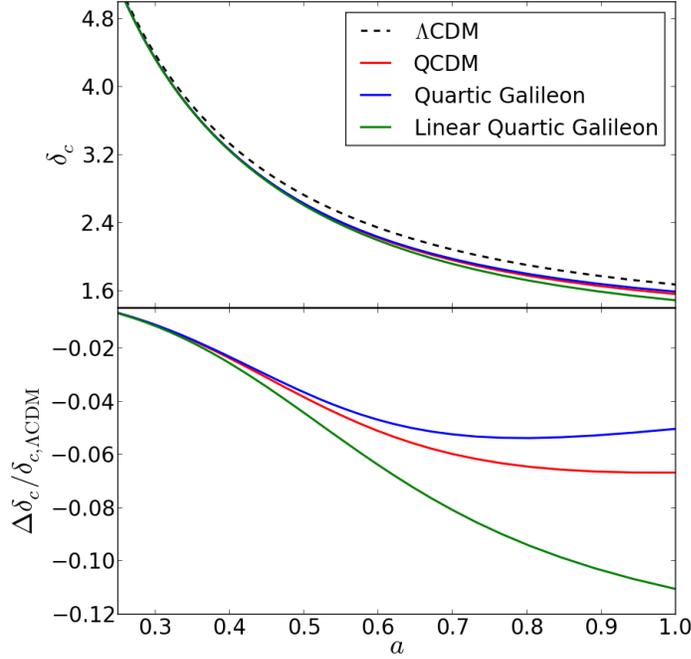
Figure 4.4: The top panel shows the time evolution of the linearly extrapolated value (assuming ΛCDM linear growth factor) of the initial critical density for the halo collapse to occur at scale factor a for the ΛCDM (dashed black), QCDM (solid red), linear force Quartic model (solid green) and full Quartic Galileon model (solid blue). The bottom panel shows the difference relative to ΛCDM.

is that structure formation is suppressed overall in the ΛCDM model, which is why δ_c is larger: the initial critical densities have to be larger to account for the slower collapse. One also notes that the relative difference between these two models starts to flatten for $a \gtrsim 0.5$. This is due to the fact that, after this time, H^{QCDM} starts to grow relative to $H^{\Lambda\mathrm{CDM}}$, which effectively brings the rate of the growth of structure closer together in the two models.

The differences between the three variants of the Quartic Galileon model are driven only by the differences in G_{eff}. In particular, in the linear force model, δ_c is smaller than in QCDM because gravity is stronger at late times ($a \gtrsim 0.5$) and the initial densities have to be smaller for the collapse to occur at the same epoch. On the other hand, δ_c is larger in the full Quartic Galileon model compared to QCDM, which means that the collapsing halo feels an overall weaker gravity. This is illustrated by the solid red in the left panel of Fig. 4.3, which represents the trajectory in $a - \delta$ space of a halo that collapses at the present day. Here, one sees that by the time the fifth force deviates from unity ($a \gtrsim 0.5$), the density
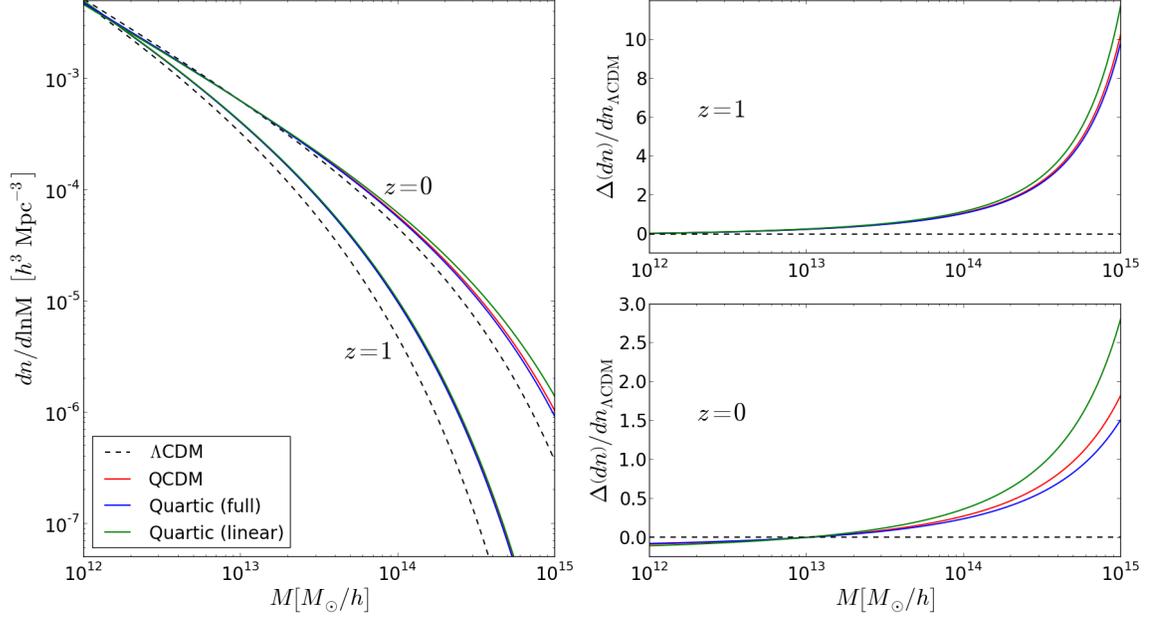
Figure 4.5: The left panel shows the halo mass function of Eq. (4.48) for the ΛCDM (dashed black), QCDM (solid red), linear force Quartic model (solid green) and full Quartic Galileon model (solid blue), for two different redshifts $z = 1$ and $z = 0$. The two panels on the right show the difference relative to ΛCDM for the two redshifts.

of the halo is already sufficiently large for it to feel the negative fifth force ($G_{\rm eff}/G < 1$). It is interesting to note that this brings the full model predictions closer to ΛCDM because the resulting weaker gravity in the Quartic Galileon model compensates the faster growth driven by the higher matter density.

As we look back in time, the curves of the three Quartic model variants get closer to one another. This is expected because $G_{\rm eff}/G \approx 1$ in the three models for $a \lesssim 0.5$, and therefore there is nothing driving any differences. The solid black line in the left panel of Fig. 4.3 shows the trajectory in $a - \delta$ space of a halo that collapses at $a = 0.5$ ($z = 1$), where one sees that it never crosses any region where $G_{\rm eff}/G$ significantly deviates from unity.

4.4.2 Halo mass function

The left panel of Fig. 4.5 shows the mass function of Eq. (4.48) predicted for the models of Table 4.2 at redshifts $z = 1$ and $z = 0$. All the models show the standard result that the number density of haloes decreases with halo mass. Moreover, the number of the most massive haloes progressively increases with time, while the number of lowest mass

haloes decreases (the latter effect is not seen due to the range of abundances plotted). This is a result of hierarchical structure formation: with time, low-mass haloes merge to form higher mass objects. The two panels on the right show the difference with respect to the ΛCDM model at each redshift.

At $z = 0$, all the variants of the Quartic Galileon model predict more massive haloes, but fewer low-mass haloes compared to ΛCDM. This is expected because δ_c is smaller in all the Quartic variants (structure formation is enhanced), which favours the merging of smaller haloes into bigger ones. The linear force model has the lowest value of δ_c, and therefore is the model in which these differences to ΛCDM are more pronounced. In the excursion set language, the explanation is that lower values of δ_c shift the peak of the first-crossing distribution $f(S)$, Eq. (4.46), towards lower S, or equivalently, towads higher M^{10}. This enhances the abundance of high-mass haloes, but suppresses at the same time the number of low-mass haloes. The opposite happens in the case of the full Quartic Galileon model. In this case, the δ-dependence of G_{eff} results in an overall weaker gravity for haloes that form at $z > 1$, which increases δ_c. As a result, one finds that there are fewer high-mass haloes compared to QCDM; the overall weaker gravitational strength felt by the collapsing haloes in the Quartic Galileon model compensates slightly the effects of the higher matter density.

The differences between the results for the three variants of the Quartic Galileon model become less pronounced as one looks back in time. This follows from the fact that $G_{\mathrm{eff}}/G \sim 1$ at sufficiently early times $a \lesssim 0.5$, and so the models become essentially undistinguishable.

4.4.3   Halo bias

Figure 4.6 shows the linear halo bias of Eq. (4.52) for the models listed in Table 4.2. The left panel shows the standard qualitative behaviour that high-mass haloes cluster more ($b_1 > 1$, biased haloes) and low-mass haloes cluster less ($b_1 < 1$, anti-biased haloes), with respect to the underlying linear dark matter distribution. The mass M^* that separates these two regimes is determined by $S(M^*) = \delta_c^2$. This is a result of hierarchical structure formation which predicts that, in higher-density regions, low-mass haloes are more likely

---

[10]In other words, if δ_c is lower then the random walks first up-cross the barrier sooner (low S), rather than later (high S).

to merge to form higher-mass haloes. This results in an overabundance of the latter, and in a suppresion of the former. In this chapter, we are more interested in the differences between models in this qualitative picture, which are determined by two factors. The first one is the different dynamics of the collapse, and is encapsulated in the different values of δ_c. In particular, larger values of δ_c lead to higher bias at all mass scales (cf. Eq. (4.52)). The second factor is the different dynamics of the linear evolution of the regions where the haloes are forming, and is described by the term $g(z)$ in Eq. (4.52). Larger values of $g(z)$ increase the bias for $M > M^*$ ($\delta_c^2/S > 1$), but decrease it for $M < M^*$ ($\delta_c^2/S < 1$).

Following these considerations, the bias is generally smaller in the three variants of the Quartic Galileon model because of the lower value of δ_c compared to ΛCDM (cf. Fig. 4.4). Moreover, $g(z)$ is also smaller in the Quartic model variants than in ΛCDM, which is why the differences become more pronounced (more negative in the right panels of Fig. 4.6) with increasing mass. Note that, at the low-mass end of the panels, the changes in δ_c and $g(z)$ in the Quartic Galileon model variants with respect to ΛCDM shift the bias in opposite directions. However, the bias is still smaller in any of the Quartic model variants for low-mass haloes, which shows that the changes in δ_c play the dominant role over $g(z)$ in determining the differences between these models and ΛCDM. The linear force Quartic Galileon model is that where the haloes are less biased at all mass scales because it is the model where gravity is strongest (lowest δ_c value). One also notes that the difference between the linear force model and QCDM becomes slighlty more pronounced with halo mass, since $g(z)$ is smaller in the former compared to the latter. The case of the full Galileon model is perhaps the most interesting one due to the δ-dependence in G_{eff}. The dashed black and solid red lines in Fig. 4.3, show, respectively, the trajectories in $a - \delta$ space of a linear overdensity that has $\delta = 0.01$ and of a halo that collapses today. One sees that at late times, $a \gtrsim 0.5$, the spherical halo feels an overall weaker gravity compared to QCDM (larger δ_c), but that the larger region, where the density is small, feels an overall stronger gravity (smaller $g(z)$) compared to QCDM. As a result, in light of the changes driven by δ_c and $g(z)$, one has that at the high-mass end, these effects shift the linear bias in opposite directions, and the net result is an approximate cancellation, w.r.t. QCDM. On the other hand, at lower mass scales, the changes in δ_c and $g(z)$ both shift the bias upwards, which therefore becomes larger in the full Quartic model compared to QCDM.

Similarly to what we have seen in the previous subsections, the bias of haloes that form
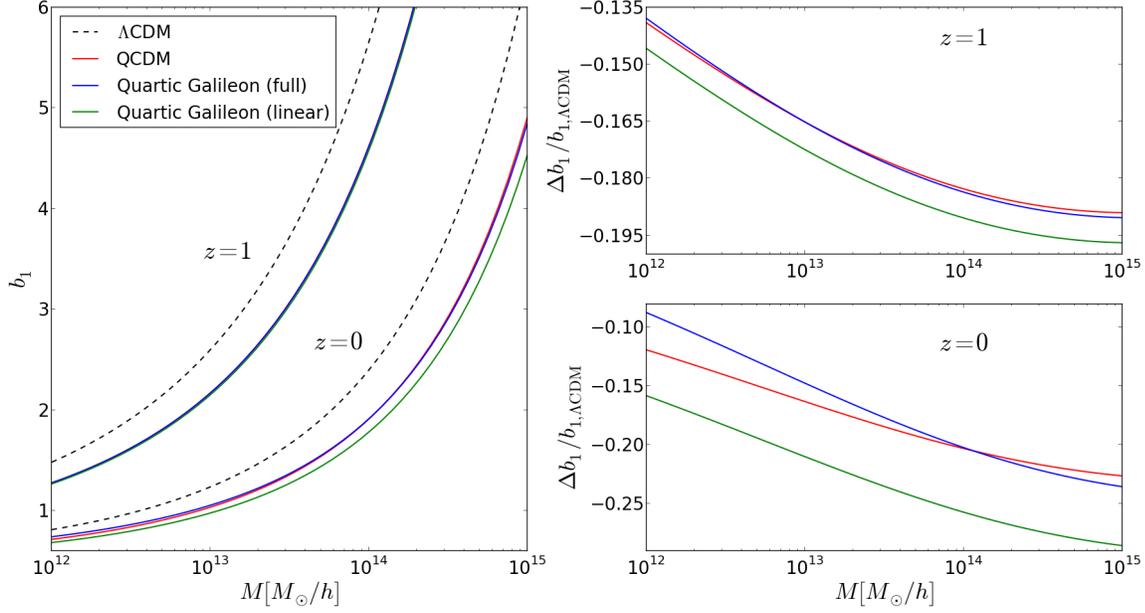
Figure 4.6: The left panel shows the linear halo bias parameter of Eq. (4.52) for the ΛCDM (dashed black), QCDM (solid red), linear force Quartic model (solid green) and full Quartic Galileon model (solid blue), for two different redshifts $z = 1$ and $z = 0$. The two panels on the right show the difference relative to ΛCDM for the two redshifts.

at $z \gtrsim 1$ ($a \lesssim 0.5$) tend to become the same in the three variants of the Quartic Galileon model, because at these early times the three models are undistinguishable.

4.5 Summary

In this chapter, we studied the nonlinear growth of large scale structure in the Quartic and Quintic Galileon gravity models in the context of excursion set theory. For this, we have derived the nonlinear Einstein and Galileon field equations assuming spherical symmetry, the quasi-static approximation and the weak field approximation. In these models, the spatial gradient, $\varphi_{,\chi}/\chi$, of the Galileon field contributes to the fifth force and its value is obtained by solving a nonlinear algebraic equation, Eq. (4.26). Using these equations, we studied the spherical collapse of matter overdensities and analysed the preditions for the halo mass function and halo bias. Our main findings can be summarized as follows:

- In the case of the Quintic Galileon model, if δ is above order unity, then the field equations do not admit physical solutions. This is because the branch of solutions for $\varphi_{,\chi}/\chi$ that

vanishes when $\delta = 0$ (which characterizes the physical behaviour) becomes a complex root of Eq. (4.26) (cf. Fig. 4.2). Evidently, the impossibility of evaluating the fifth force at these densities prevents the study of the spherical collapse in the Quintic model. In the case of the Quartic model, we showed that the physical solutions exist in sufficiently high density regions, but do not exist at late times if the density is sufficiently low (cf. Fig. 4.3). For the halo spherical collapse study we presented, such low densities are not important and the problem is irrelevant.

- At early times ($z \gtrsim 1$, or $a \lesssim 0.5$) in the Quartic model, the effective gravitational strength is $G_{\rm eff}/G \approx 1$ (cf. Fig. 4.3). With time, $G_{\rm eff}/G$ increases if the overdensity is small ($\delta \ll 1$), and at the present day one has $G_{\rm eff}/G \approx 1.4$. On the other hand, if the overdensity is of order unity or above, the value of $G_{\rm eff}/G$ decreases with time, and at the present day it is $G_{\rm eff}/G \approx 0.6$ for $\delta \gg 1$. Thus, the modifications to gravity are not completely screened at high densities. The reason for this is that the Galileon field contributes to $G_{\rm eff}/G$ not only through its spatial gradients, but also through the background time evolution that multiplies the standard gravity terms (cf. Eqs. (4.4), (4.5) and (4.6)). The latter will still be present, even at high densities where the Vainshtein screening successfully suppresses the spatial gradients.

- The dynamics of the spherical collapse of (top-hat) overdensities is sensitive to the density of the halo, but not to its size or mass. In other words, the critical density for collapse, δ_c, which determines the height of the barrier in the excursion sets, is "flat". Our results show that δ_c becomes smaller when one changes from the ΛCDM to the QCDM model. This is mostly because of the higher matter density in the latter, which makes the haloes collapse faster. In the linear force Quartic model, the fifth force is non-negligible and positive for $a \gtrsim 0.5$, which further decreases the critical density δ_c because it further boosts the collapse of the haloes. In the case of the full Quartic model, the spherical haloes feel a negative fifth force in the collapsing stages for $a \gtrsim 0.5$ (cf. Fig 4.3), which makes δ_c larger than in QCDM.

- The excursion set theory results show that, at $z = 0$, all the variants of the Quartic Galileon model predict more high-mass haloes than ΛCDM, but fewer low-mass haloes (c. f. Fig. 4.5). This is mainly due to the higher matter density in the Galileon models, which enhances structure formation, and thus makes it easier for smaller haloes to merge

into more massive ones. In the case of the linear force model, the enhanced gravitational strength leads to more haloes at the high-mass end. On the other hand, in the full Quartic Galileon model, the haloes that collapse at $z = 0$ feel overall a weaker gravity, and therefore, the model predicts fewer high-mass haloes compared to QCDM.

- The excursion set theory linear bias parameter in the variants of the Quartic Galileon model is generally smaller than in ΛCDM, with the differences becoming more pronounced with increasing halo mass. In the Galileon model, the bias of dark matter haloes is determined by the interplay of the different values of δ_c and $g(z)$ (cf. Eq. (4.52)). While larger values of δ_c can only lead to higher bias, larger values of $g(z)$, (which corresponds to slower growth rate of the underlying dark matter field), make high-mass haloes more biased, but low-mass haloes less biased.

In summary, the simplified study of nonlinear structure formation in this chapter provides us with some first insights into the N-body simulation results that will follow in subsequent chapters. In particular, in Chapter 5, we shall use some of the excursion set methodology presented here to develop a halo model [277] for Galileon gravity, and see how it compares with the results from the simulations. In principle, the analysis of this chapter can also be used to compute halo mergers trees with less work than by using N-body simulations, which could be used to study galaxy formation in the Galileon model.

Chapter 5

N-body simulations and halo modelling in Galileon gravity cosmologies

In this chapter, our goal is to bring the excursion set theory predictions of the previous chapter on to a more quantitative level, by comparing and calibrating them with the results from N-body simulations. In particular, we calibrate the free parameters of the Sheth-Tormen formulae for the halo mass function and linear halo bias [273, 274, 275] to the N-body simulations of the Cubic and Quartic Galileon models. We also fit the halo concentration-mass relation in the simulations, which we use, together with the Sheth-Tormen formulae, to build a halo model for the nonlinear matter power spectrum.

The first part of this chapter is dedicated to presenting the strategy used to simulate Cubic Galileon cosmologies, which is based on the algorithm of Ref. [124]. We shall also use simulation results of the Quartic Galileon model, which requires a more involved algorithm. This is due to the higher degree of nonlinearity of the equations, but also due to the existence of anisotropic stress in the Quartic model. The details about Quartic Galileon model simulations shall not be presented in this thesis, but the interested reader can find them in Ref. [276]. Recall that in the last chapter, by studying the behavior of the fifth force in the Quintic model assuming spherical symmetry in the quasi-static limit, we have seen that the model fails to admit physical solutions where the density perturbations become of order unity. The study of nonlinear structure formation in the Quintic model therefore requires a more careful assessment of this problem, which is beyond the scope of this thesis.

In Chapters 2 and 3 we have seen that the Galileon models (without massive neutrinos) that fit the CMB data tend to predict rather high amplitudes for the clustering of matter

on large scales, compared to ΛCDM (cf. lower right panel of Fig. 4.1). This is illustrated by the larger values of σ_8 in these models in Table 4.1. Although we know from Chapter 3 that the presence of massive neutrinos helps to lower this amplitude, it is interesting to ask the question of whether or not the high values of σ_8 constitute an observational tension. In these previous chapters, we argued that a decisive statement could only be made after more careful modelling of galaxy/halo bias, redshift space distortions and nonlinearities of the screening mechanism. In this chapter, armed with the results from N-body simulation and the calibrated analytical formulae we shall finally answer the above question by conducting a Halo Occupation Distribution (HOD) analysis.

5.1   N-body simulations of Cubic Galileon cosmologies

In this section, we describe the strategy to solve the equations of the Cubic Galileon model using the modified gravity N-body code ECOSMOG [124, 278]. As we shall see below, the Cubic Galileon model is, in many aspects, similar to the Dvali-Gabadadze-Porrati (DGP) model [64, 138, 139, 279], of which a number of N-body studies have already been performed [124, 280, 281, 282, 283, 284].

5.1.1   Force equations in the quasi-static and weak-field limits

The N-body code solves the equations written in the quasi-static and weak-field limits (cf. Sec. 4.1). The validity of these assumptions can always be assessed by checking if the simulation results reproduce the full linear theory predictions on the scales where linear theory should hold. In our notation, ∂_i denotes a partial derivative w.r.t. the i-th spatial coordinate ($i = x, y, z$), and the indices are lowered and raised using the spatial metric γ_{ij} and its inverse γ^{ij}, respectively (cf. Eq. 1.1).

Under the above approximations, the Poisson equation and the Galileon field equation of motion are given, respectively, by

$$\partial^2 \Phi = 4\pi G a^2 \delta \rho_m - \frac{\kappa c_3}{\mathcal{M}^3} \dot{\varphi}^2 \partial^2 \varphi, \tag{5.1}$$

$$\frac{2c_3}{\mathcal{M}^3} \dot{\varphi}^2 \partial^2 \Psi = \left[-c_2 - \frac{4c_3}{\mathcal{M}^3} \left(\ddot{\varphi} + 2H\dot{\varphi} \right) \right] \partial^2 \varphi + \frac{2c_3}{a^2 \mathcal{M}^3} \left[(\partial^2 \varphi)^2 - (\partial_i \partial_j \varphi)^2 \right], \tag{5.2}$$

These two equations can be combined in an equation that involves solely the Galileon field

and the matter density perturbation:

$$\partial^2 \varphi + \frac{1}{3\beta_1 a^2 \mathcal{M}^3} \left[(\partial^2 \varphi)^2 - (\partial_i \partial_j \varphi)^2 \right] = \frac{M_{\text{Pl}}}{3\beta_2} 8\pi G a^2 \delta\rho_m, \tag{5.3}$$

where we have used the relation $\Phi = \Psi$ in the Cubic Galileon model, as a consequence of the vanishing anisotropic stress (cf. Chapter 2). Here, $\partial^2 = \partial_i \partial^i$ is the spatial Laplacian differential operator and $(\partial_i \partial_j \varphi)^2 = (\partial_i \partial_j \varphi)(\partial^i \partial^j \varphi)$. $\delta\rho_m$ is the matter density perturbation, $\rho_m = \bar{\rho}_m(t) + \delta\rho_m(t, \vec{x})$. The dimensionless functions β_1 and β_2 are defined as

$$\beta_1 = \frac{1}{6c_3} \left[-c_2 - \frac{4c_3}{\mathcal{M}^3} (\ddot{\varphi} + 2H\dot{\varphi}) + 2 \frac{\kappa c_3^2}{\mathcal{M}^6} \dot{\varphi}^4 \right], \tag{5.4}$$

$$\beta_2 = 2 \frac{\mathcal{M}^3 M_{\text{Pl}}}{\dot{\varphi}^2} \beta_1. \tag{5.5}$$

Equation (5.3) has the same structural form (in terms of the spatial derivatives of the scalar field) as the equation of motion of the DGP brane-bending mode [285]. The differences lie only in the distinct time evolution of the functions β_1 and β_2. In particular, in the DGP model $\beta_1 = \beta_2$. To facilitate the comparison between the different models with equations of the same form as Eqs. (5.1) and (5.3), we can redefine the field perturbation as

$$\delta\varphi \to \frac{\beta}{\beta_2} \delta\varphi, \tag{5.6}$$

where β is a free function. With this redefinition, Eqs. (5.1) and (5.3) become

$$\partial^2 \Phi = 4\pi G a^2 \delta\rho_m - \frac{\kappa c_3}{\mathcal{M}^3} \frac{\beta}{\beta_2} \dot{\varphi}^2 \partial^2 \varphi, \tag{5.7}$$

$$\partial^2 \varphi + \frac{1}{3 (\beta_1 \beta_2 / \beta) a^2 \mathcal{M}^3} \left[(\partial^2 \varphi)^2 - (\partial_i \partial_j \varphi)^2 \right] = \frac{M_{\text{Pl}}}{3\beta} 8\pi G a^2 \delta\rho_m. \tag{5.8}$$

In this way, we can choose β to make the right-hand side of Eq. (5.8) look like in a given model, such as the DGP model. In this case, the differences between the two models in the scalar field equation are fully captured by the different values of $\beta_1 \beta_2 / \beta$ in the coefficient of the nonlinear derivative terms. In the top panel of Fig. 5.1, we show the time evolution of $-\beta_1 \beta_2 / \beta$ for the Cubic Galileon (solid blue) and DGP (dashed green) models taking $\beta = \beta_{DGP}$. Here, the DGP model is the self-accelerating branch that best fits the WMAP 5yr CMB data [69] and that has been simulated in [124]. Note that in the DGP model, $\beta_1 \beta_2 / \beta_{DGP} = \beta_{DGP}$. We see that for both models the value of $-\beta_1 \beta_2 / \beta_{DGP}$ decreases overall but in different ways. In particular, the value of $-\beta_1 \beta_2 / \beta_{DGP}$ in the Cubic Galileon model can be smaller or larger than in the DGP model throughout cosmic history. Since

this term multiplies the nonlinear derivative terms, its different time evolution in these two models translates into a different efficiency for the screening mechanism.

Note however, that besides the different coefficients of the nonlinear derivative terms, different models can also differ in the coefficient of $\partial^2\varphi$ in the Poisson equation Eq. (5.7). In particular, in the Cubic Galileon model, such a coefficient is time-dependent whereas in the DGP model, for instance, it is simply a constant equal to $1/2$ [124].

Equation (5.8) can be regarded as a second-order algebraic equation for $\partial^2\varphi$. To avoid numerical problems related to the choice of which branch of solutions to take, we first solve this equation analytically to obtain[1]:

$$\partial^2\varphi = \frac{-\alpha \pm \sqrt{\alpha^2 + 4\left(1 - \varepsilon\right)\Sigma}}{2\left(1 - \varepsilon\right)}, \tag{5.9}$$

in which

$$\alpha \equiv 3\left(\beta_1\beta_2/\beta\right)a^2\mathcal{M}^3, \tag{5.10}$$

$$\Sigma \equiv \left(\partial_i\partial_j\varphi\right)^2 + \alpha\frac{8\pi Ga^2 M_{\mathrm{Pl}}}{3\beta}\delta\rho_m - \varepsilon\left(\partial^2\varphi\right). \tag{5.11}$$

In our simulations, we follow the strategy of [124, 282] and set the free constant coefficient $\varepsilon = 1/3$. The reason behind $1/3$ is linked to the so-called *operator splitting trick* [276, 282] which is explained below. The choice of the solution branch is determined by the condition that the physical result that $\partial^2\varphi \to 0$, when $\rho \to 1$, should be recovered, i.e., if there are no density fluctuations then there should be no fifth force [124]. As a result, one should choose the sign of the square root in Eq. (5.9) to be the sign of α, or equivalently, the sign of $\beta_1\beta_2/\beta$. With such a choice, Eq. (5.9) can be written as

$$\partial^2\varphi = \frac{-\alpha + \mathrm{sign}(\alpha)\sqrt{\alpha^2 + 4\left(1 - \varepsilon\right)\Sigma}}{2\left(1 - \varepsilon\right)}. \tag{5.12}$$

To determine the particle trajectories, the N-body code first solves the Galileon field equation (Eq. (5.12)) to determine $\partial^2\varphi$. The solution is then plugged into the Poisson equation (Eq. (5.7)), which is solved to obtain the gradient of Φ, which gives the total force (GR + fifth force) under which the simulation particles move.

The discretization of Eqs. (5.7) and (5.12) is identical to the case of the DGP model (apart from the different coefficients, cf. Sec.5.1.1). Such equations are lengthy and were already presented in [124], to which we refer the interested reader.

---

[1]Equation (5.9) is obtained by solving the equivalent equation $\left(1 - \varepsilon\right)\left(\partial^2\varphi\right)^2 + \alpha\left(\partial^2\varphi\right) - \Sigma = 0$.

Operator splitting trick

In the expression for Σ above, one can decompose the tensor $\partial_i \partial_j \varphi$ into its trace and trace-less parts, respectively, as

$$\partial_i \partial_j \varphi = \frac{1}{3} \gamma_{ij} \partial^2 \varphi + \hat{\partial}_i \hat{\partial}_j \varphi, \tag{5.13}$$

where the operator $\hat{\partial}$ is defined by $\gamma^{ij} \hat{\partial}_i \hat{\partial}_j \varphi = 0$. Using this split, it can be shown that if $\varepsilon = 1/3$, then Σ becomes

$$\Sigma = (\hat{\partial}_i \hat{\partial}_j \varphi)^2 + \alpha \frac{8\pi G a^2 M_{\mathrm{Pl}}}{3\beta} \delta \rho_m, \tag{5.14}$$

that is, we have eliminated the dependence on $\partial^2 \varphi$. The `ECOSMOG` code solves Eq. (5.9) by iteratively relaxing a discretized version of it on a grid [278]. It is possible to show that Σ, as given by Eq. (5.14), does not depend on the value of φ_{ijk} after one writes the derivatives as finite differences (where φ_{ijk} is the value of the field at the grid cell labelled by $\{ijk\}$). This is why the choice of $\varepsilon = 1/3$ is useful, as in this way, when the code is iterating over the values of φ_{ijk}, the latter appears only linearly on the left-hand side of Eq. 5.9 (after discretizing $\partial^2 \varphi$). This is found to significantly improve the convergence rate of the code. Moreover, by removing φ_{ijk} from inside of the square-root, one is also protected against imaginary square-root problems that could arise from a bad initial choice for the value of φ_{ijk} at the start of the iteration. More details on the operator splitting trick can be found in Refs. [276, 282].

5.1.2   Vainshtein screening

Equation (5.8) tells us that different models can be compared by the different coefficients of the nonlinear derivative term responsible for the screening. It is therefore instructive to understand how such derivative couplings work to suppress the modifications of gravity. For simplicity, here we look only at the case of spherically symmetric configurations of the gravitational and scalar fields (this was already done for the case of the Quartic Galileon model in the previous chapter). Therefore, assuming that φ and Φ depend only on the radial coordinate, r, Eq. (5.8) becomes:

$$\frac{1}{r^2} \frac{d}{dr} \left[r^2 \varphi_{,r} \right] + \frac{2}{3} \frac{1}{\mathcal{M}^3 a^2 (\beta_1 \beta_2 / \beta)} \frac{1}{r^2} \frac{d}{dr} \left[r \varphi_{,r}^2 \right] = \frac{M_{\mathrm{Pl}}}{3\beta} 8\pi G a^2 \delta \rho, \tag{5.15}$$
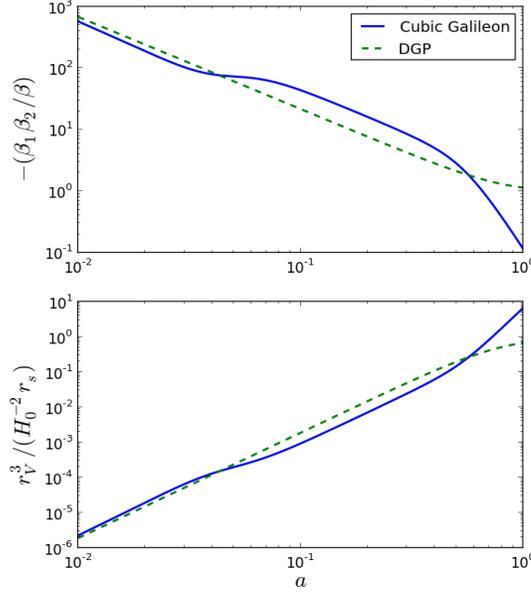
Figure 5.1: Time evolution of the quantity $-\beta_1\beta_2/\beta$, with $\beta = \beta_{DGP}$ (cf. Eqs. (5.4), (5.5) and (5.8)) (top panel), and of the Vainstein radius r_V (bottom panel) for the Cubic Galileon (solid blue) and DGP (dashed green) models. In the bottom panel, we have assumed $r_c = H_0^{-1}$ so that r_V can be plotted in the same units for both models. The Cubic Galileon model plotted is the model of Table 4.1 while the DGP model is the model simulated in [124].

which can be integrated once to yield

$$\varphi_{,r} + \frac{2}{3} \frac{1}{\mathcal{M}^3 a^2 \left(\beta_1\beta_2/\beta\right)} \frac{1}{r} \varphi_{,r}^2 = \frac{2M_{\text{Pl}}}{3\beta} \frac{GM(r)}{r^2} a^2, \tag{5.16}$$

where $M(r) = 4\pi \int_0^r \delta\rho_m(\xi)\xi^2 d\xi$ is the matter contribution to the mass enclosed within a radius r. Eq. (5.16) is a second-order algebraic equation for $\varphi_{,r}$. Taking for simplicity a top-hat density distribution of radius R, the physical solutions are given by:

$$\varphi_{,r} = \frac{4M_{\text{Pl}}a^2 r^3}{3\beta r_V^3} \left[\sqrt{\left(\frac{r_V}{r}\right)^3 + 1} - 1\right] \frac{GM(R)}{r^2}, \tag{5.17}$$

for $r \geq R$ and

$$\varphi_{,r} = \frac{4M_{\text{Pl}}a^2 R^3}{3\beta r_V^3} \left[\sqrt{\left(\frac{r_V}{R}\right)^3 + 1} - 1\right] \frac{GM(r)}{r^2}, \tag{5.18}$$

for $r < R$. In Eqs. (5.17) and (5.18) we have identified a distance scale, r_V, known as the Vainshtein radius, which is given by

$$r_V^3 = \frac{8M_{\text{Pl}}r_S}{9M^3\beta_1\beta_2}, \tag{5.19}$$

where $r_S \equiv 2GM(R)$ is the Schwarzschild radius of the top-hat source. The last term in the modified Poisson equation (Eq. (5.7)) represents the fifth force mediated by the Galileon field:

$$F_{5th} = -\frac{\kappa c_3}{\mathcal{M}^3} \frac{\beta}{\beta_2} \dot{\varphi}^2 \varphi_{,r} \,. \tag{5.20}$$

Taking the limits where $r \gg r_V$ and $r \ll r_V$ one has

$$F_{5th} = -\frac{2c_3 a^2 \dot{\varphi}^2}{3\mathcal{M}^3 M_{\text{Pl}} \beta_2} \frac{GM(R)}{r^2} \quad r \gg r_V, \tag{5.21}$$

$$F_{5th} \sim 0 \quad\quad\quad\quad\quad r \ll r_V. \tag{5.22}$$

Consequently, r_V gives a measure of the length scale below which the screening mechanism starts to operate to recover the normal general relativistic force law. If $\beta_1 \beta_2 \to \infty$ then both the coefficient of the nonlinear derivative terms in Eq. (5.8) and r_V tend to zero. In this case, the additional gravitational force is not suppressed below any distance scale. This shows how the derivative interactions of the scalar field are able to suppress the fifth force.

The lower panel of Fig. 5.1 shows the time evolution of the Vainshtein radius, r_V, for the Cubic Galileon and DGP models. In the latter we have assumed that $r_c = H_0^{-1}$, where r_c is the DGP crossover scale[2], so that r_V could be plotted for the two models with the same units of $r_S H_0^{-2}$. For both models, r_V increases with time, but it does so at different rates. In particular, at $a \approx 0.5$, the Vainshtein radius of a given matter source in the Cubic Galileon model is comparable to that in the DGP model. From $a \approx 0.5$ until the present time, the Vainshtein radius in the Cubic Galileon model is larger than in the DGP model, with the values differing by approximately one order of magnitude at $a = 1$. In practice, this means that in the Cubic Galileon model, the fifth force resulting from a given matter source at $a = 1$ is screened out to a distance which can be about ten times larger than in the DGP model.

Problems with imaginary square roots

The quadratic nature of Eq. (5.16) raises the possibility that, under some circumstances, there might not be real solutions. From Eqs. (5.17), (5.18) and (5.19) we see that the condi-

---

[2]Very briefly, the crossover scale, r_c, is a parameter of the DGP model that gives a measure of the length scale below which gravity is four-dimensional and above which it is five-dimensional [64].

tion for the existence of real solutions is given by:

$$\Delta \equiv 1 + \frac{1}{\beta_1\beta_2}\frac{64\pi GM_{\rm Pl}}{9\mathcal{M}^3 r^3}\int_0^r \delta\rho_m(\xi)\xi^2 d\xi \geq 0. \tag{5.23}$$

This equation shows that in low density regions, such as voids, where $\delta\rho_m < 0$, it is possible for Δ to be negative (note that $\beta_1\beta_2 > 0$). In fact, this is exactly what we have found in our simulations of the Cubic Galileon model: for $a \gtrsim 0.8$, there are regions in the simulation box for which there are no real solutions for the fifth force. Such a problem, nevertheless, is absent from the DGP simulations performed with the same N-body code [124]. The reason is primarily related to the different time evolution of the quantity $\beta_1\beta_2/\beta$ (or equivalently $\beta_1\beta_2$) in both models. Looking at Eq. (5.23), one sees that the smaller the value of $\beta_1\beta_2$, the easier it is for Δ to be negative in low density regions. In Fig. 5.1, we have seen that at late times, $\beta_1\beta_2$ is smaller in the Cubic Galileon model than it is in the DGP model, which is why the imaginary square root problem shows up in the former and not in the latter.

This problem can be a consequence of the quasi-static limit approximation. The terms we have neglected while deriving the quasi-static field equations may not be completely negligible in certain circumstances, such as when the matter density is very low. In particular, such terms might be the missing contribution to Eq. (5.12) that prevents the imaginary solutions [3]. In the simulations for this chapter, we work our way around this problem by simply setting $\Delta = 0$ whenever this quantity becomes negative. Such a solution, although crude and not theoretically self-consistent, should not have a measurable impact on the small scale nonlinear matter power spectrum and halo mass functions. The reason is that the clustering power on small scales is dominated by the high density regions where the problem does not appear.

We stress however that even if the fifth force would not have become imaginary, one would still have an inaccurate calculation in low densities because the quasi-static limit is not expected to be a good approximation there. For instance, this is the case of the DGP simulations that have been performed so far [124, 280, 281, 282, 283, 284]. The case of the Cubic Galileon is more severe because it forces one to fix some terms in the equations in an *ad hoc* way. It should be noted that it is not clear that our solution to the imaginary fifth force problem is making the calculation more inaccurate than in the DGP simulations. To fully

---

[3]The recent work of Ref. [256], however, suggests that even after relaxing the quasi-static approximation the problem persists.

address this question one would have to simulate the full model equations (i.e. without assuming the quasi-static limit), which is beyond the scope of the analysis here.

5.2   Halo Model of the nonlinear matter power spectrum

In this section, we describe the halo model of the nonlinear matter power spectrum, as well as the halo properties that are needed as input. In particular, we define and present the halo mass function, linear halo bias and halo density profiles.

5.2.1   Halo model

In the halo model approach, one of the main premises is that all matter in the Universe is in bound structures. Thus, the two-point correlation function of the matter density field can be decomposed into the contributions from the correlations between mass elements that belong to the same halo (the 1-halo term) and to different haloes (the 2-halo term). In terms of the matter power spectrum, this can be written as (see Ref. [277] for a comprehensive review)

$$P_k = P_k^{1h} + P_k^{2h}, \tag{5.24}$$

where

$$
\begin{aligned}
P_k^{1h} &= \int dM \frac{M}{\bar{\rho}_{m0}^2} \frac{dn(M)}{d\ln M} |u(k,M)|^2, \\
P_k^{2h} &= I(k)^2 P_{k,\text{lin}},
\end{aligned}
\tag{5.25}
$$

are, respectively, the 1-halo and 2-halo terms, with

$$I(k) = \int dM \frac{1}{\bar{\rho}_{m0}} \frac{dn(M)}{d\ln M} b_{\text{lin}}(M) |u(k,M)|. \tag{5.26}$$

In the above expressions, k is the comoving wavenumber; $\bar{\rho}_{m0}$ is the present-day background matter density; $P_{k,\text{lin}}$ is the matter power spectrum obtained using linear theory; $dn(M)/d\ln M$ denotes the comoving number density of haloes per differential logarithmic interval of mass (we shall refer to this quantity as the *mass function*); $b_{\text{lin}}(M)$ is the linear halo bias; $u(k,M)$ is the Fourier transform of the density profile of the haloes truncated at the size of the halo and normalized such that $u(k \to 0, M) \to 1$. In order to compute the matter power spectrum of Eq. (5.24), one has to model these quantities first. This is done next, where we follow the notation used in Chapter 4.

5.2.2 Halo mass function

We express the halo mass function as in the first line of Eq. (4.48), but taking the following expression for $f(S)$

$$f(S) = A\sqrt{\frac{q}{2\pi}}\frac{\delta_c}{S^{3/2}}\left[1 + \left(\frac{q\delta_c^2}{S}\right)^{-p}\right]\exp\left[-q\frac{\delta_c^2}{2S}\right],$$

(5.27)

where $\delta_c \equiv \delta_c(z)$ is the critical initial overdensity for a spherical top-hat to collapse at redshift z, extrapolated to $z = 0$ with the ΛCDM linear growth factor (as we did in Chapter 4). The choice of parameters $(q, p) = (1, 0)$ leads to the Press-Schechter mass function [269], used in the previous chapter. However, Refs. [273, 274, 275] found that the choice of parameters $(q, p) = (0.75, 0.30)$ (which is motivated by the ellipsoidal collapse of structures, and not spherical) provides a much more accurate description of the mass function measured from N-body simulations of ΛCDM models. For Galileon gravity models, it is not necessarily true that this choice of (q, p) parameters also results in a good fit to N-body results. In the next section, we recalibrate these two parameters to our simulations of the Cubic and Quartic Galileon models. The normalization constant A is fixed by requiring that $\int f(S)\mathrm{d}S = 1$. The mass function computed using Eq. (5.27) is known as the Sheth-Tormen mass function.

5.2.3 Linear halo bias

By following the same steps as in Chapter 4, one can show that the Sheth-Tormen halo bias is given by

$$b(M) = 1 + g(z)\left(\frac{q\delta_c^2/S - 1}{\delta_c} + \frac{2p/\delta_c}{1 + (q\delta_c^2/S)^p}\right).$$

(5.28)

Provided the (q, p) parameters are calibrated to fit the mass function, the linear halo bias $b(M)$ should, according to the excursion set theory logic, give automatically a reasonably good fit to the simulation results. This is one of the well-known lessons of Refs. [273, 274, 275] for the CDM family of models. The results in the next section show that this remains true for the Cubic and Quartic Galileon models.

5.2.4   Halo density profiles

We assume that the radial profile of the dark matter haloes [4] is of the NFW type [286]

$$\rho_{\mathrm{NFW}}(r) = \frac{\rho_s}{r/r_s \left[1 + r/r_s\right]^2},$$

(5.29)

where ρ_s and r_s are often called the *characteristic density* and the *scale radius* of the halo.

The mass of the NFW density profile, M_Δ, can be obtained by integrating Eq. (5.29) up to some radius R_Δ (the meaning of the subscript Δ will become clear later)

$$M_\Delta = \int_0^{R_\Delta} \mathrm{d}r 4\pi r^2 \rho_{\mathrm{NFW}}(r) = 4\pi \rho_s \frac{R_\Delta^3}{c_\Delta^3} \left[\ln\left(1 + c_\Delta\right) - \frac{c_\Delta}{1 + c_\Delta}\right],$$

(5.30)

where we have used the concentration parameter

$$c_\Delta = \frac{R_\Delta}{r_s}$$

(5.31)

(not to be confused with the c_i parameters in the action of the Galileon model).

In our simulations, the halo mass is defined as

$$M_\Delta = \frac{4\pi}{3} \Delta \bar{\rho}_{c0} R_\Delta^3,$$

(5.32)

i.e., M_Δ is the mass enclosed by the comoving radius R_Δ, within which the mean density is Δ times the critical density of the Universe today, $\bar{\rho}_{c0}$. Here, we consider $\Delta = 200$, but for now let us keep the discussion as general as possible. By combining Eqs. (5.30) and (5.32), one finds ρ_s as a function of c_Δ:

$$\rho_s = \frac{1}{3} \Delta \bar{\rho}_{c0} c_\Delta^3 \left[\ln\left(1 + c_\Delta\right) - \frac{c_\Delta}{1 + c_\Delta}\right]^{-1}.$$

(5.33)

All that is needed to fully specify the NFW profile is to determine the value of r_s, which is done by direct fitting to the halo density profiles measured from the simulations. In the literature, however, it has become more common to specify the concentration-mass relation $c_\Delta(M_\Delta)$, instead of the equivalent values of r_s. Previous studies [287, 288, 289, 290] have found that the concentration-mass relation is well described by a power law function. The parameters of the power law, however, seem to have a sizeable cosmology dependence, even for different choices of cosmological parameters in ΛCDM models (see e.g. Ref. [289]). In the next section, we will see that the $c_\Delta(M_\Delta)$ relation in Galileon models can also be

---

[4]Not to be confused with the top-hat profile assumption used in the spherical collapse to obtain the values of the critical density δ_c.

well fitted by a power law, but with fitting parameters that differ considerably from those obtained for ΛCDM. Having found the $c_\Delta(M_\Delta)$ relation from the simulations, then the NFW density profile becomes completely specified by the mass M_Δ of the halo.

Finally, because what enters Eqs. (5.25) and (5.26) is the Fourier transform of the profiles, $u(k, M)$, and not the profiles themselves, we simply mention that it is possible to show that

$$
\begin{aligned}
u_{\mathrm{NFW}}(k, M) &= \int_0^{R_\Delta} \mathrm{d}r 4\pi r^2 \frac{\sin kr}{kr} \frac{\rho_{\mathrm{NFW}}(r)}{M_\Delta} \\
&= 4\pi \rho_s r_s^3 \left\{ \frac{\sin(kr_s)}{M} \mathrm{Si}\left([1 + c_\Delta kr_s] - \mathrm{Si}(kr_s)\right) \right. \\
&\quad + \frac{\cos(kr_s)}{M} \mathrm{Ci}\left([1 + c_\Delta kr_s] - \mathrm{Ci}(kr_s)\right) \\
&\quad \left. - \frac{\sin(c_\Delta kr_s)}{M(1 + c_\Delta) kr_s} \right\},
\end{aligned}
\tag{5.34}
$$

where $\mathrm{Si}(x) = \int_0^x \mathrm{d}t \sin(t)/t$ and $\mathrm{Ci}(x) = -\int_x^\infty \mathrm{d}t \cos(t)/t$. Note that, indeed, $u(k \to 0, M) \to 1$, as required.

5.3 Results

In this section, we test the predictions of the halo model formulae presented in the last section with the results from N-body simulations of the Cubic [6] and Quartic [276] Galileon models.

5.3.1 Summary of the simulations

The simulations we use in this chapter were performed with the ECOSMOG code [278], which is a modified version of the RAMSES code [291] that includes extra solvers for the scalar degrees of freedom that appear in modified gravity theories. The code solves the equation of motion of the scalar field by performing Gauss-Seidel iterative relaxations on an adaptively refined grid. The grid is refined whenever the number of particles within a grid cell exceeds some user-specified threshold, N_{th}. This ensures that high-density regions are sufficiently well resolved, while saving computational resources in regions where the density is lower. The strategy to simulate the equations of the Cubic Galileon was presented in Sec. 5.1 and the strategy to simulate the equations of the Quartic Galileon model
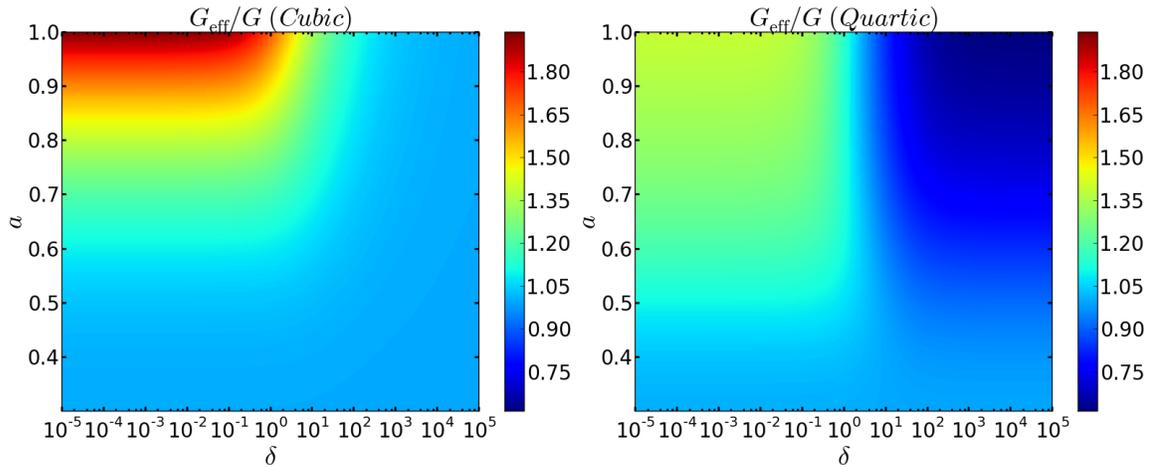
Figure 5.2: Time and density dependence of the effective gravitational strength G_{eff} of Eq. (4.27) for the Cubic (left panel) and Quartic (right panel) Galileon models. The colour scale bars at the right of each panel show the value of G_{eff}/G. The color scale is the same for both panels.

follows that described in Ref. [276]. For more details about the code implementation, in particular in Galileon cosmologies, we refer the reader to Refs. [6, 124, 276, 278].

The results that follow correspond to the *full*, *linear* and *QCDM* variants that we have introduced already in Chapter 4 (c.f. Table 4.2).

The simulations were performed in a box of size $L = 200\text{Mpc}/h$, with $N_p = 512^3$ dark matter particles and grid refinement criteria $N_{\text{th}} = 8$. For each of the model variants, we have simulated five different realizations of the initial density field, by choosing different random seeds. This allows for statistical averaging, which we use to construct errorbars for the simulation results by measuring the variance within the different realizations. Although in this chapter we show results only for one box size, we note that in Refs. [6, 276] the same models were simulated using different box sizes and particle numbers, and gave converged results.

Model parameters

The results of the Cubic and Quartic Galileon models that follow correspond to the model parameters shown in Table 4.1. Figure 5.2 shows the effective gravitational strength for the Cubic and Quartic Galileon models, $G_{\text{eff}}(a, \delta)$ (cf. Eq. (4.27)). The right panel of Fig. 5.2 is the same as the left panel of Fig. 4.3, but we show it again to facilitate the comparison

Table 5.1: Best-fitting Sheth-Tormen (q, p) parameters to the simulation results for the variants of the Cubic and Quartic Galileon models at $a = 0.60$, $a = 0.80$ and $a = 1.00$. The uncertainty in the values of q and p is $\Delta_q = 3.5 \times 10^{-3}$ and $\Delta_p = 1.5 \times 10^{-3}$, respectively. These parameters were determined by minimizing the quantity $\sum_i |n^{\mathrm{sims}}(> M_i)/n^{\mathrm{ST}}(> M_i, q, p) - 1|$, where n^{sims} is the cumulative mass function measured in the simulations, n^{ST} is the analytical result given by the Sheth-Tormen mass function and the index $'i'$ runs over the number of bins in the cumulative mass function.

Model	$a = 0.60$	$a = 0.80$	$a = 1.00$
	(q, p)	(q, p)	(q, p)
QCDM$_{\mathrm{Cubic}}$	$(0.699, 0.336)$	$(0.727, 0.349)$	$(0.791, 0.354)$
Cubic Galileon	$(0.699, 0.334)$	$(0.720, 0.346)$	$(0.770, 0.349)$
Linearized Cubic Galileon	$(0.685, 0.326)$	$(0.692, 0.308)$	$(0.734, 0.301)$
QCDM$_{\mathrm{Quartic}}$	$(0.671, 0.339)$	$(0.692, 0.349)$	$(0.713, 0.354)$
Quartic Galileon	$(0.713, 0.359)$	$(0.840, 0.389)$	$(1.024, 0.407)$
Linearized Quartic Galileon	$(0.649, 0.316)$	$(0.671, 0.316)$	$(0.692, 0.321)$

with the corresponding result for the Cubic Galileon model (left panel of Fig. 5.2). The physical picture depicted in Fig. 5.2 indicates that the modelling of halo properties can be very different in these two models, in particular because of the different behavior in high-density regions. The values of δ_c and $g(z)$ that enter the calculation of the mass function and halo bias in the Cubic and Quartic Galileon models were computed by following the strategy layed out in Chapter 4 (we do not display the values for brevity, but the interested reader can find them in Table II of Ref. [7]).

5.3.2 Mass function

In Figs. 5.3 and 5.4, we show our results for the cumulative mass function of the Cubic and Quartic Galileon models, respectively. These were obtained with the phase-space friends-of-friends halo finder code `Rockstar` [292]. Throughout, we use M and M_{200} interchangeably to denote halo mass. The symbols with errorbars indicate the simulation
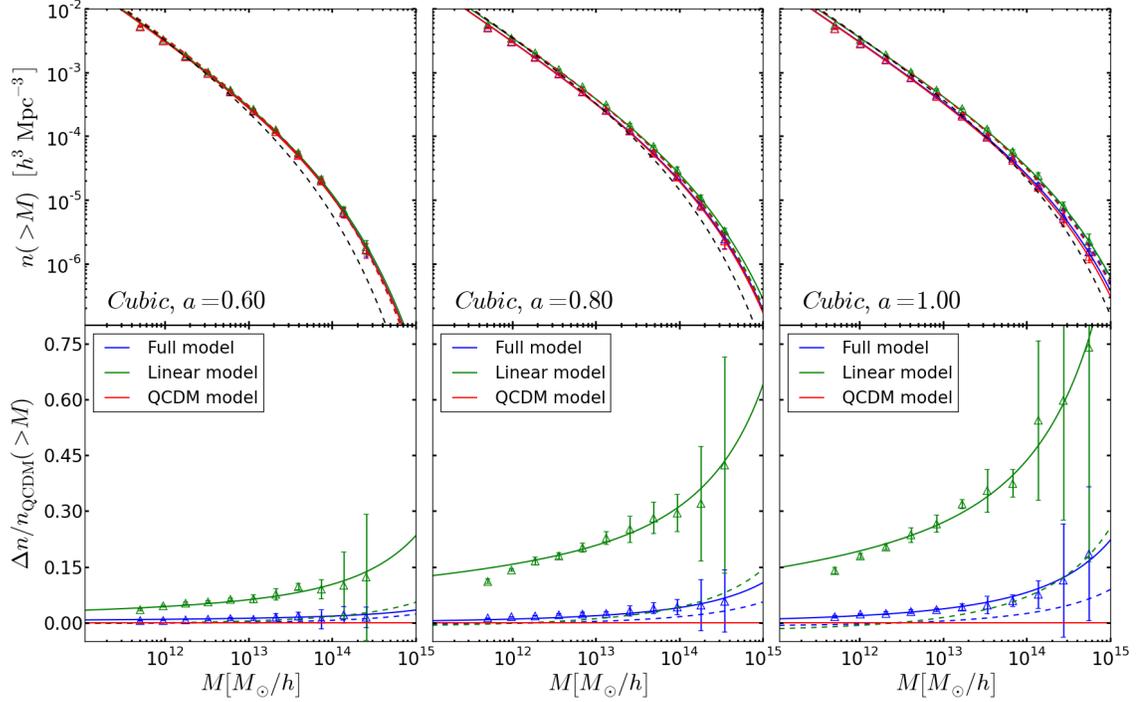
Figure 5.3: The upper panels show the cumulative mass function of the three variants of the Cubic model at $a = 0.60$, $a = 0.80$ and $a = 1.00$. The triangles with errorbars show the simulation results considering only haloes (and not subhaloes) with mass $M_{200} > 100 M_p$, where $M_p = \Omega_{m0} \bar{\rho}_{c0} L^3 / N_p$ is the particle mass. The solid lines correspond to the cumulative Sheth-Tormen mass function using the best-fitting (q, p) parameters to the simulation results given in Table 5.1. The dashed lines are computed in the same way as the solid lines, but with the standard Sheth-Tormen parameter values $(q, p) = (0.75, 0.30)$. For reference, the Sheth-Tormen cumulative mass function for a ΛCDM model with WMAP9 parameters [201] is shown by the black dashed curve in the upper panels. The color scheme indicated in the figure applies to the lines and symbols. In the lower panels, the relative difference of the simulation results w.r.t. the QCDM simulation results is shown, and the relative difference of the analytical predictions is plotted w.r.t. the analytical predictions of the QCDM model. Also in the lower panels, the solid red and dashed red lines are both zero, by definition.
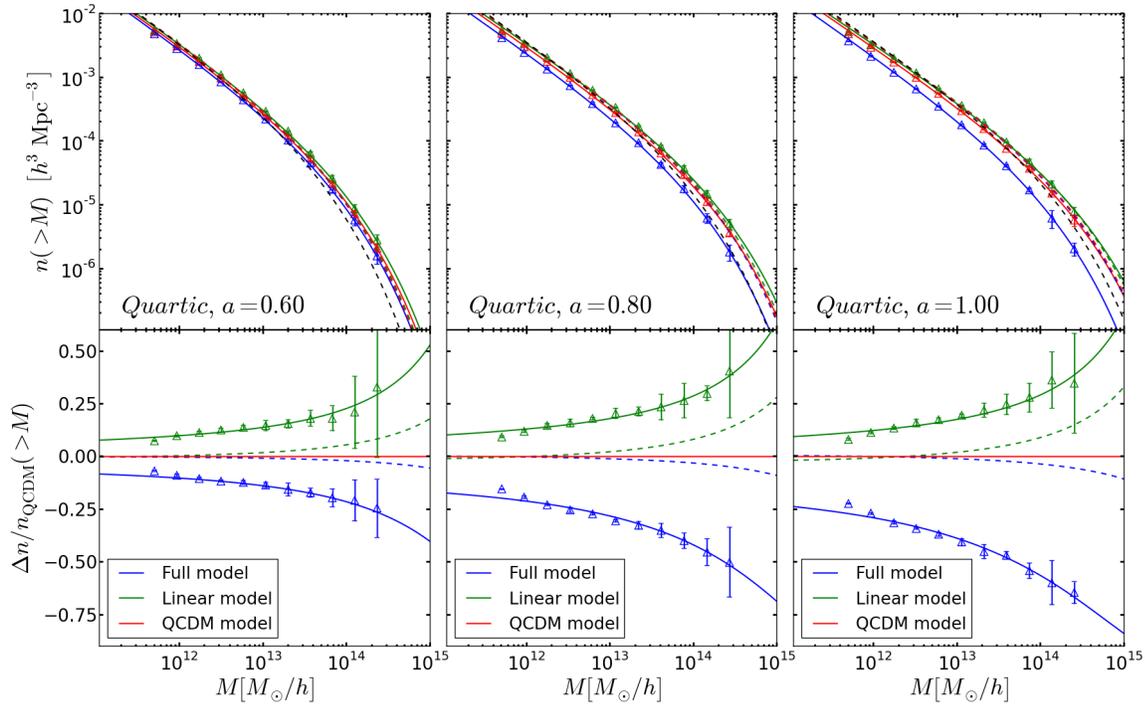
Figure 5.4: Same as Fig. 5.3, but for the Quartic Galileon model.

results and the dashed lines show the Sheth-Tormen mass function with the standard parameters $(q, p) = (0.75, 0.30)$. One can see that the mass function computed in this way fails to provide a reasonable description of the simulation results, as it significantly underestimates the effects of the modifications to gravity seen in the simulations.

It is not completely surprising that the use of the standard Sheth-Tormen parameters $(q, p) = (0.75, 0.30)$ fails in the Galileon model, since these were chosen to fit ΛCDM simulations [273, 274, 275]. The ellipsoidal collapse motivates a departure from $(q, p) = (1, 0)$ (which corresponds to the spherical collapse case), but the magnitude of this departure is determined by fitting to numerical results. Very crudely, one can say that the fitted (q, p) parameters absorb some of the uncertain details of the nonlinear structure formation, which cannot be accurately described by the ellipsoidal collapse. In models that differ significantly from ΛCDM, like the Cubic or Quartic Galileon models, it is to be expected that the specifics of the ellipsoidal collapse should also be different. In practice, this translates into different values for the (q, p) parameters. The solid lines in Figs. 5.3 and 5.4 show the Sheth-Tormen mass function predicted using the best-fitting (q, p) parameters to the simulation results. The latter were determined for each variant of the Cubic and Quartic

Galileon models at $a = 0.6$, $a = 0.8$ and $a = 1$. Their values are shown in Table 5.1. By allowing (q, p) to differ from the standard values, one sees that the analytical predictions can actually provide an extremely good fit to the simulation results in the entire mass range probed.

In the case of the Cubic model, one sees that the screening mechanism works well at suppressing the enhancement in the number density of haloes. For instance, the linear variant predicts an enhancement in the number density of haloes with $M \sim 10^{14} M_\odot/h$ at $a = 1$ of about 45%, whereas in the case of the full model, in which the screening is at play, the enhancement is smaller than 10%. On the other hand, in the case of the Quartic model, the overall weakening of gravity in the full variant (cf. Fig. (5.2)) leads to a significant suppresion in the number density of collapsed objects. In particular, haloes with $M \sim 10^{14} M_\odot/h$ are $\sim 50\%$ less abundant compared to QCDM. In the case of the linearized variant, the same massive haloes are $\sim 30\%$ more abundant w.r.t. QCDM.

Before proceeding, a comment should be made about the definition of halo mass in the simulations and in the analytical formulae. Assuming mass conservation, Eq. (4.43) can be associated with the virial mass of the halo, whose definition differs in different models. Here, we are comparing the mass M of Eq. (4.43) with the values of M_{200} measured from the simulations. One does not expect these two mass definitions to be exactly the same, but nor would one expect them to differ significantly. These ambiguities in the mass definition can, anyway, be absorbed in the fitted values of the Sheth-Tormen (q, p) parameters. We expect these fitting parameters to slightly change with different mass definitions. However, note that this is also the case for the ΛCDM model, and is not peculiar to Galileon gravity.

5.3.3   Linear halo bias

In our simulations, we measure the halo bias by evaluating the ratio

$$b(k, M) = \frac{P_{\rm hm}(k, M)}{P(k)}, \tag{5.35}$$

where $P(k)$ is the total matter power spectrum and $P_{\rm hm}(k, M)$ is the halo-matter cross spectrum for haloes of mass M. We used a *Delaunay Tessellation* field estimator code [293, 294] to obtain the halo and matter density fields from which we computed these power spectra. In the numerator of Eq. (5.35), we consider the cross power spectrum, rather than the halo-halo counts power spectrum, to reduce the impact of shot noise on our measurements. Our

estimate for the linear halo bias is given by the asymptotic value of $b(k, M)$ on large scales (small k). The result is shown in Fig. 5.5 for the Cubic (upper panels) and Quartic (lower panels) Galileon models. In Fig. 5.5, one sees that Eq. (5.28) provides a good description of the linear halo bias seen in the simulations if one uses the (q, p) parameters that best-fit the mass function of the simulations (solid lines). This shows that the excursion set theory approach and the steps involved in the derivation of Eq. (5.28) are still valid in the Cubic and Quartic Galileon models. However, the use of the best-fitting (q, p) parameters does not lead to a significant improvement over the use of the standard Sheth-Tormen values, $(q, p) = (0.75, 0.30)$ in matching the simulation results. The linear halo bias seems to be less sensitive than the halo mass function to the exact choice of (q, p). This can be understood as the linear halo bias is computed as the ratio of two mass functions (cf. Sec. 4.3.1), and consequently, some of the dependence on the values of (q, p) cancels to some extent. Note that despite the weaker sensitivity to the exact choice of the Sheth-Tormen parameters, these must still differ from the Press-Schechter limit $(q, p) = (1, 0)$, which is known to fail to reproduce the results from N-body simulations [273, 274, 275].

5.3.4 Halo occupation distribution analysis

As indicated by the values of $\sigma_8 \sim 1$ in Table 4.1, the amplitude of the linear matter power spectrum in the Cubic and Quartic Galileon models is higher than in standard ΛCDM models, for which $\sigma_8 \sim 0.82$ [201]. Consequently, it is interesting to investigate if the enhanced clustering power in the Galileon models is still consistent with the observed large scale clustering of the host haloes of Luminous Red Galaxies (LRGs) of the SDSS DR7 [187]. The screening mechanism could potentially suppress part of the enhancement. However, we will see in Sec. 5.3.6 that for scales $k \lesssim 0.1h/\mathrm{Mpc}$, the effects of the Vainshtein mechanism on the power spectrum are small in the Cubic and Quartic Galileon models (see Figs. 5.8 and 5.9 below). On the other hand, the result of Fig. 5.5 shows that massive haloes in Galileon cosmologies can be less biased than in ΛCDM, which effectively suppresses the halo power spectrum. As a result, a robust comparisson between theory and observations requires an exploration of this degeneracy between the enhanced linear growth of structure and the lower halo bias parameter. We carry on such an exploration by performing a halo occupation distribution (HOD) analysis of LRG clustering.

In the HOD formalism, one asks what is the probability distribution $P(N, M)$ that a
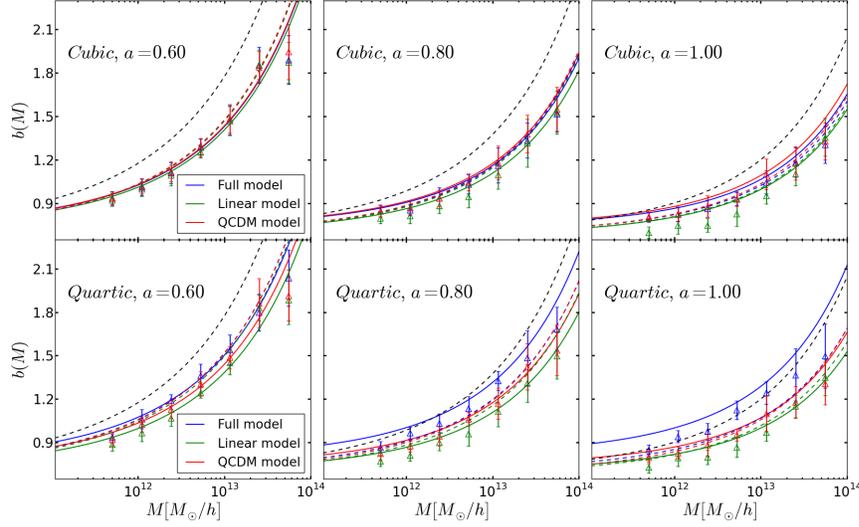
Figure 5.5: Linear halo bias of the three variants of the Cubic (upper panels) and Quartic Galileon (lower panels) models at $a = 0.60$, $a = 0.80$ and $a = 1.00$. The triangles with errorbars show the simulation results considering only haloes (and not subhaloes) with mass $M_{200} > 100 M_p$, where $M_p = \Omega_{m0} \bar{\rho}_{c0} L^3 / N_p$ is the particle mass. The solid and dashed lines correspond to the linear halo bias parameter of Eq. (5.28) computed with the (q, p) parameters from Table 5.1 and $(q, p) = (0.75, 0.30)$, respectively. The linear halo bias for a ΛCDM model with WMAP9 parameters [201] is shown by the black dashed lines. The color scheme indicated in the figure applies to the lines and symbols.

dark matter halo of mass M contains N galaxies. The HOD models are typically parametrized by the mean of their distribution, $\langle N|M \rangle$, which can be separated into the mean number of *central* and *satellite* galaxies that reside in haloes of mass M [295]. For simplicity, and since independent HOD studies have suggested that the satellite fraction is small for LRGs [296, 297, 298], we neglect the contribution from satellite galaxies and assume that the haloes can either host one LRG (the central) or none at all. Our aim is to determine if it is possible, in the Cubic and Quartic Galileon cosmologies, to realistically populate the dark matter haloes with LRGs in order to reproduce the observed clustering amplitude and galaxy number density. We parametrize the HOD as

$$\langle N|M \rangle = \frac{1}{2} \left[1 + \mathrm{erf} \left(\frac{\log_{10} (M/M_{\min})}{\sigma_{\log_{10} M}} \right) \right], \tag{5.36}$$

where $M_{\min}$ and $\sigma_{\log_{10} M}$ are the HOD parameters. These can be constrained by construct-

ing the following χ^2 quantity

$$\chi^2 = \chi^2_{b_g} + \chi^2_{n_g} = \frac{\left(b_g - \bar{b}_g\right)^2}{\Delta b_g} + \frac{\left(n_g - \bar{n}_g\right)^2}{\Delta n_g}, \tag{5.37}$$

where

$$n_g = \int \mathrm{d}M \frac{\mathrm{dn}}{\mathrm{dM}} \langle N|M\rangle, \tag{5.38}$$

$$b_g = \int \mathrm{d}M \frac{\mathrm{dn}}{\mathrm{dM}} \langle N|M\rangle\, b(M), \tag{5.39}$$

are the number density and effective linear bias parameter of the galaxies, respectively. The likelihood of M_{min} and $\sigma_{\log_{10}M}$ is then $\mathcal{P} \propto \exp\left[-\chi^2/2\right]$.

In Eq. (5.37), $\bar{n}_g$ and $\bar{b}_g$ are, respectively, the number density and galaxy bias of the LRG sample presented in Ref. [187], which the HOD model should reproduce. We take $\bar{n}_g = 4 \times 10^{-5} h^3/\mathrm{Mpc}^3$, which corresponds roughly to $\int n(z)\mathrm{d}z$, where $n(z)$ is the redshift dependence of the observed galaxy number density (see Fig. 1 of Ref. [187]). The value of $\bar{b}_g$ can be inferred from the ratio R of the amplitudes of the observed LRG host halo power spectrum (in redshift space) and the theoretical linear prediction for each model (in real space). To first approximation we can write:

$$R \equiv \frac{P^s_{k,\mathrm{LRG}}(z_{\mathrm{eff}})}{P^r_{k,\mathrm{lin}}(z_{\mathrm{eff}})} = \left(\frac{\bar{b}_g}{1.85}\right)^2 \left[1 + \frac{2f}{3\bar{b}_g} + \frac{f^2}{5\bar{b}_g^2}\right], \tag{5.40}$$

where $f = \mathrm{dln}D/\mathrm{dln}a$ is the logarithmic derivative of the linear growth factor at $z_{\mathrm{eff}} = 0.313$, which is the effective redshift of the LRG sample. On the RHS of Eq. (5.40), the term within squared brackets approximately describes the boost in the real space power spectrum caused by the peculiar velocities of galaxies on large scales. The $\bar{b}_g^2$ factor accounts for the shift in the power due to the galaxy bias. Although $\bar{b}_g$ is the bias of the LRGs, the method used in Ref. [187] effectively leads to a normalization of the LRG host halo power spectrum with a factor $(1.85)^{-2}$ (see their Erratum [188]). For the Cubic and Quartic Galileon models, we have that $f_{\mathrm{Cubic}} \approx f_{\mathrm{Quartic}} \approx 0.75$ and $R_{\mathrm{Cubic}} \approx R_{\mathrm{Quartic}} \approx 1.10$ (see Fig. 4.1). Solving Eq. (5.40) yields $\bar{b}_g \approx 1.68$. For reference, in a ΛCDM model with WMAP9 parameters [201], one has $f \approx 0.66$ and $R \approx 1.40$ which leads to $\bar{b}_g \approx 1.96$. In Eqs. (5.38) and (5.39), we use the calibrated Sheth-Tormen formulae for the mass function and linear halo bias at $a = 0.80$, which is sufficiently close to $a_{\mathrm{eff}} = 1/(1 + z_{\mathrm{eff}}) \approx 0.76$. We assume fractional errors of 10% and 5% on the number density and galaxy bias, respectively, i.e.,
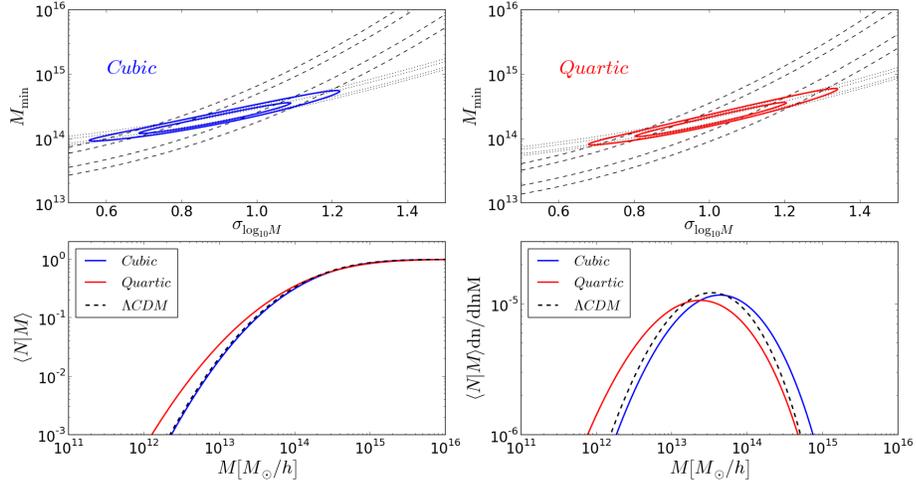
Figure 5.6: The upper panels show the 68% and 95% confidence contours on the M_{min} and $\sigma_{\log_{10}M}$ parameters of Eq. (5.36) obtained using Eq. (5.37) for the full variants of the Cubic (left) and Quartic (right) Galileon models. The black dashed and dotted contours indicate the constraints derived by using only $\chi^2_{b_g}$ and only $\chi^2_{n_g}$ in Eq. (5.37), respectively. The solid contours show the combined constraints. The lower left and lower right panels show, respectively, the best-fitting $\langle N|M \rangle$ and $\langle N|M \rangle \, \mathrm{d}n/\mathrm{d}\ln M$ for the full Cubic (blue) and Quartic (red) Galileon models, and ΛCDM with WMAP9 parameters [201] (black dashed). The quantity plotted in the lower right panel shows the contribution from haloes of different mass to the galaxy number density.

$\Delta n_g = 0.1\bar{n}_g$ and $\Delta b_g = 0.05\bar{b}_g$. We have checked that our results do not depend on these assumptions for the size of the errors.

The constraints on the parameters M_{min} and $\sigma_{\log_{10}M}$ for the full Cubic and Quartic variants are shown in the upper panels of Fig. 5.6. The dashed and dotted contours show the confidence regions obtained by considering only $\chi^2_{b_g}$ or $\chi^2_{n_g}$ in Eq. (5.37), respectively. The fact that the two contours overlap means that there are some LRG HODs that can match both the observed large scale clustering amplitude and number density. The best-fitting HOD models are shown in the lower left panel of Fig. 5.6. We also show the best-fitting HOD for ΛCDM. It is remarkable that the Cubic and ΛCDM models predict almost the same HOD. This shows that the boost in the linear matter power spectrum can be compensated by the modifications to the halo abundance and linear bias in the Cubic model to preserve the way the LRGs populate the dark matter haloes. In the case of the Quartic

Table 5.2: Best-fitting (α, β) parameters in the parametrization $\log_{10}(c_{200}) = \alpha + \beta \log_{10}\left(M_{200}/\left[10^{12} M_\odot/h\right]\right)$ to the simulation results for the variants of the Cubic and Quartic Galileon models at $a = 0.60$, $a = 0.80$ and $a = 1.00$. The uncertainty in the values of α and β is $\Delta_\alpha = \Delta_\beta = 0.001$. These parameters were determined by minimizing the quantity $\sum_i |c_{200}^{\text{sims}}(M_i)/c_{200}^{\text{param}}(M_i, \alpha, \beta) - 1|$, where $c_{200}^{\text{sims}}(M_i)$ is the concentration measured in the simulations, $c_{200}^{\text{param}}(M_i, \alpha, \beta)$ is the concentration given by the parametrization and the index $'i'$ runs over the number of mass bins.

Model	$a = 0.60$	$a = 0.80$	$a = 1.00$
	(α, β)	(α, β)	(α, β)
$\text{QCDM}_{\text{Cubic}}$	$(0.670, -0.024)$	$(0.801, -0.078)$	$(0.825, -0.068)$
Cubic Galileon	$(0.674, -0.025)$	$(0.797, -0.076)$	$(0.818, -0.067)$
Linearized Cubic Galileon	$(0.740, -0.030)$	$(1.001, -0.080)$	$(1.129, -0.076)$
$\text{QCDM}_{\text{Quartic}}$	$(0.667, -0.026)$	$(0.794, -0.079)$	$(0.833, -0.079)$
Quartic Galileon	$(0.569, -0.029)$	$(0.562, -0.033)$	$(0.542, -0.017)$
Linearized Quartic Galileon	$(0.781, -0.028)$	$(0.956, -0.084)$	$(1.011, -0.078)$

model, the lower amplitude of the halo mass function (c.f. Fig. 5.4) and the higher linear halo bias (c.f. Fig.5.5) make the HOD extend towards slightly lower halo masses. The lower right panel of Fig. 5.6 shows the halo mass function weighted by the best-fitting HOD model, $\langle N|M\rangle \, dn/d\ln M$. The latter peaks at $M \sim [2 - 4] \times 10^{13} M_\odot/h$ and predicts a negligible fraction of LRGs residing in haloes with mass $< 10^{12} M_\odot/h$, for all the models. Note that otherwise this would represent an observational tension since LRGs have stellar masses that are typically $> 10^{11} M_\odot/h$ [299, 300, 301], and are not expected to reside in dark matter haloes whose mass is comparable to theirs.

From the above analysis, we therefore conclude that it is unlikely that the Cubic and Quartic Galileon models are in tension with the large-scale galaxy distribution, despite both having values of $\sigma_8 \approx 1$.
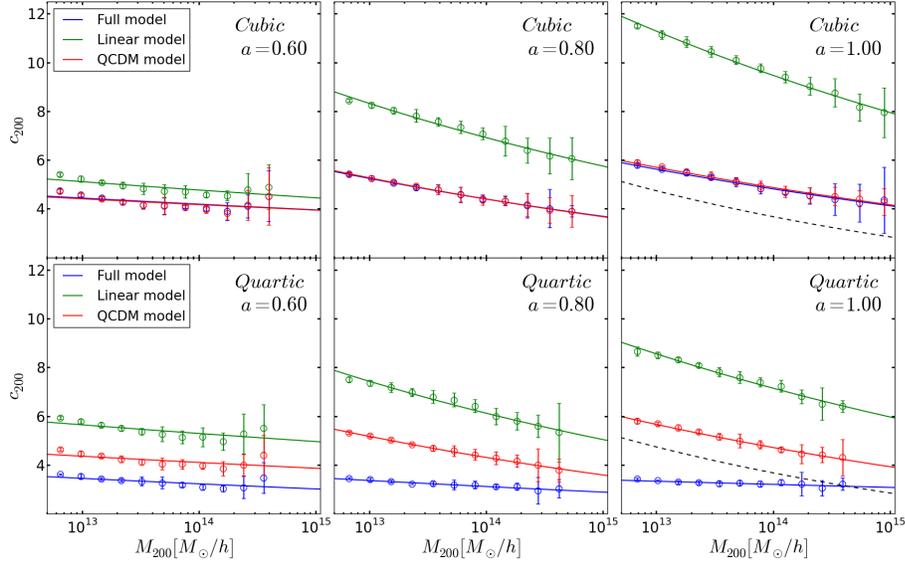
Figure 5.7: Halo concentration-mass relation, $c_{200}(M_{200})$, of the three variants of the Cubic (upper panels) and Quartic (lower panels) Galileon models, for $a = 0.60$, $a = 0.80$ and $a = 1.00$. The circles with errorbars show the simulation results considering haloes (and not subhaloes) with $M_{200} > 1000M_p$, where $M_p = \Omega_{m0}\bar{\rho}_{c0}L^3/N_p$ is the particle mass. The solid lines show the best-fitting power laws from Table 5.2. For comparison, in the $a = 1.00$ panels, we also show the fit found in Ref. [302] for a ΛCDM model with the WMAP5 parameters [303]. The color scheme indicated in the figure applies to the lines and symbols.

5.3.5   Concentration-mass relation

In Fig. 5.7, we show the concentration-mass relation, $c_{200}(M_{200})$, measured in the simulations of the Cubic (upper panels) and Quartic Galileon models (lower panels). We have checked that the haloes in the simulations are well described by the NFW profile, Eq. (5.29), for all model variants and epochs. The values of c_{200} were obtained via Eq. (5.31), by using the values of R_{200} and r_s determined by the `Rockstar` code [292]. The simulation results are well fitted by a power law $\log_{10}(c_{200}) = \alpha + \beta\log_{10}\left(M_{200}/\left[10^{12}M_\odot/h\right]\right)$, with the best-fitting parameters shown in Table 5.2. In the Galileon models, one encounters the standard picture that halo concentrations tend to increase with time for fixed mass, and tend to decrease with halo mass at a given epoch [304, 305]. The exact mass and time dependence, however, differs within the variants of the Cubic and Quartic Galileon models. In the $a = 1.00$ panels, we also show a similar power law fitted by Ref. [302] to simulation

results of ΛCDM models with WMAP5 parameters [303].

In the case of the Cubic Galileon model, one sees that the Vainshtein mechanism is extremely efficient in restraining the modifications to gravity from having an impact on the concentrations of the haloes. The values of c_{200} in the full and in the QCDM variants of the Cubic model are essentially indistinguishable over the mass range probed by the simulations. This is because by the time the modifications to gravity occur, $a \gtrsim 0.6$ (cf. Fig. 5.2), the Vainshtein radius of the haloes, which is a growing function of time (cf. Fig. 5.1), is larger than the haloes themselves. At $a = 1$, the haloes of all the variants of the Cubic model are more concentrated than in standard ΛCDM. The reason for this can be traced back to the fact that the haloes in the Cubic models form earlier than in ΛCDM (cf. Fig. 5.3). This makes them to be more concentrated since they formed at an epoch when the background matter density was higher. The same reasoning can also be used to explain why the halo concentrations are higher in the linear variant w.r.t. the QCDM variant. In this case, however, the deepening of the gravitational potential at late times (cf. Fig. 5.2) in the linear variant is also expected to play a significant role (see also Refs. [306, 307]).

The picture in the full Quartic model differs significantly because of the overall weakening of gravity in regions of high density. Following the above reasoning, haloes of a given mass form later in the full Quartic model, which leads to a lower concentration compared to any other variant of the model. The values of c_{200} also barely evolve with time in the full Quartic Galileon model. This can be due to the fact that the gravitational potential inside haloes in the full Quartic model becomes shallower at late times (cf. Fig. 5.2). Additionally, the mass dependence of the concentration is much shallower than in any other variant, including those of the Cubic Galileon model. Comparing with ΛCDM at $a = 1$, the full Quartic Galileon model predicts lower halo concentrations, although the difference becomes smaller with increasing halo mass.

Before proceeding, note that since the effects of the fifth force are not felt inside the haloes in the full Cubic Galileon, then our current knowledge about the baryonic processes that are relevant for galaxy formation should prevail [5]. As a result, it should be more or less straightforward to implement semi-analytical models of galaxy formation in Cubic Galileon cosmologies. The same, however, does not apply to the Quartic Galileon model.

---

[5]See, for instance, Ref. [308] for a study of stellar oscillations in models of modified gravity that employ the chameleon screening mechanism [70, 309].

5.3.6   Halo model matter power spectrum

Our results for the nonlinear matter power spectrum of the Cubic and Quartic Galileon models are shown in Figs. 5.8 and 5.9. These simulation power spectra were measured using the POWMES code [310]. We discuss now the performance of the halo model in describing the simulation results, by separating the discussion into large, intermediate and small scales.

Large scales. On scales $k \lesssim 0.2h/\mathrm{Mpc}$, the halo model prediction matches the simulation results. On these scales, the halo model is dominated by the 2-halo term in Eq. (5.24), which reduces simply to the linear matter power spectrum $P_{k,\mathrm{lin}}$. More precisely, in the limit in which $k \ll 1h/\mathrm{Mpc}$, Eq. (5.26) becomes

$$I(k) \approx \int \mathrm{d}M \frac{1}{\bar{\rho}_{m0}} \frac{\mathrm{d}n(M)}{\mathrm{d}\ln M} b_{\mathrm{lin}}(M) = 1, \tag{5.41}$$

where we have used the fact that $u(k \to 0, M) \to 1$ and the last equality is ensured by the definition of the Sheth-Tormen mass function and linear halo bias (see e.g. Refs. [277, 311, 312]). We note that the integral of Eq. (5.41) is hard to evaluate numerically because, at low M, neither the mass function nor the halo bias approach zero. Here, we make use of the fact that the last equality of Eq. (5.41) holds by construction. Effectively, we choose a sufficiently small lower limit ($M \sim 10^6 M_\odot/h$), and then simply add the missing contribution to the integral, such that it adds up to unity. We have computed the integrals using both Python and Mathematica routines, which gave the same results [6]. Note also that $P_k^{2\mathrm{h}}$ differs only from $P_{k,\mathrm{lin}}$ for $k \gtrsim 1h/\mathrm{Mpc}$, where $P_k^{1\mathrm{h}}$ already provides the dominant contribution to the total power. This is a general result that is not restricted to the Galileon models studied here [277]; in practice, this means that in the halo model approach, it makes almost no difference to use the 2-halo term or the linear matter power spectrum.

Intermediate scales. On scales $0.2h/\mathrm{Mpc} \lesssim k \lesssim 2h/\mathrm{Mpc}$, the halo model predictions in all the variants of the Cubic and Quartic Galileon models tend to underpredict the clustering power measured in the simulations. In particular, the mismatch ranges between $\sim 50\%$ and $\sim 20\%$ across all the variants and epochs. These differences are not entirely unexpected and their explanation can be related to some of the approximations associated with the halo

---

[6]The same Mathematica routines were used to obtain the results of Ref. [112].
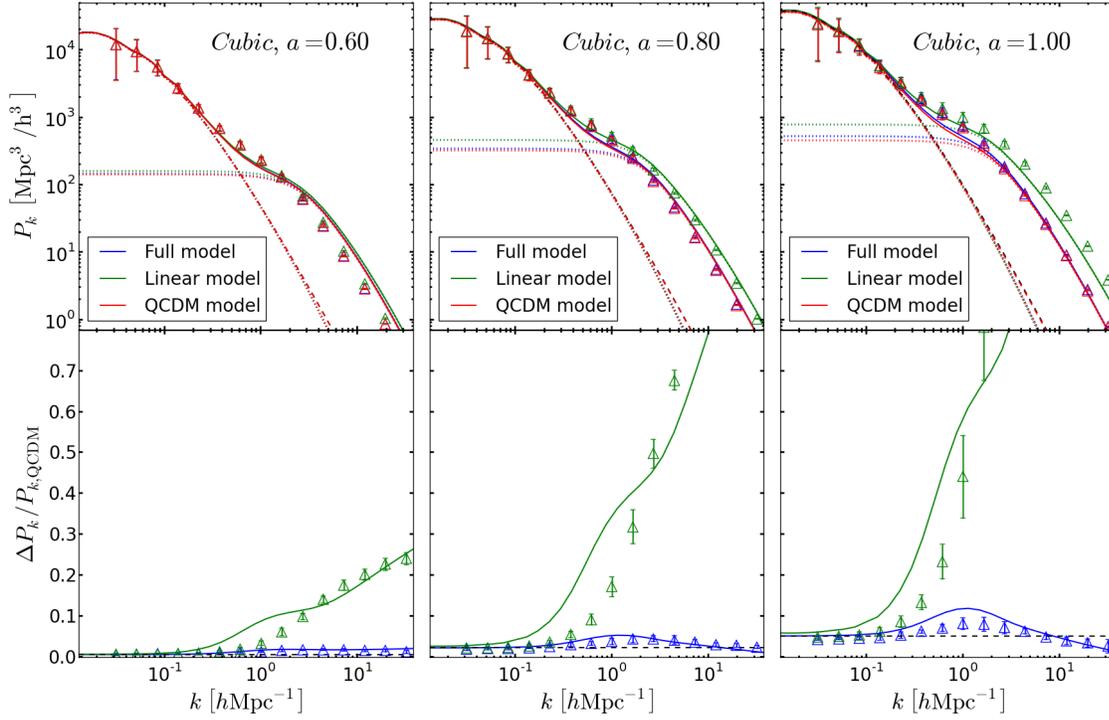
Figure 5.8: The upper panels show the nonlinear matter power spectrum of the three variants of the Cubic Galileon model, at $a = 0.60$, $a = 0.80$ and $a = 1.00$. The lower panels show the relative difference w.r.t. QCDM. The triangles with errorbars show the simulation results. The dashed black and dashed red lines show the linear theory prediction for the Cubic Galileon model and its QCDM variant, respectively (these two curves are practically indistinguishable in the upper panels). The solid lines show the nonlinear matter power spectrum in the halo model obtained using Eqs. (5.24), (5.25) and (5.26). The two sets of dotted lines show the contributions from the 1-halo and 2-halo terms. The former is shown by the lines that approach a constant value at small k; the latter is shown by the lines that coincide with the linear theory lines at small k. The color scheme indicated in the figure applies to the lines and symbols. In the lower panels, the relative difference of the simulation results w.r.t. the QCDM simulation results is shown, and the relative difference of the analytical predictions is plotted w.r.t. the QCDM analytical predictions.
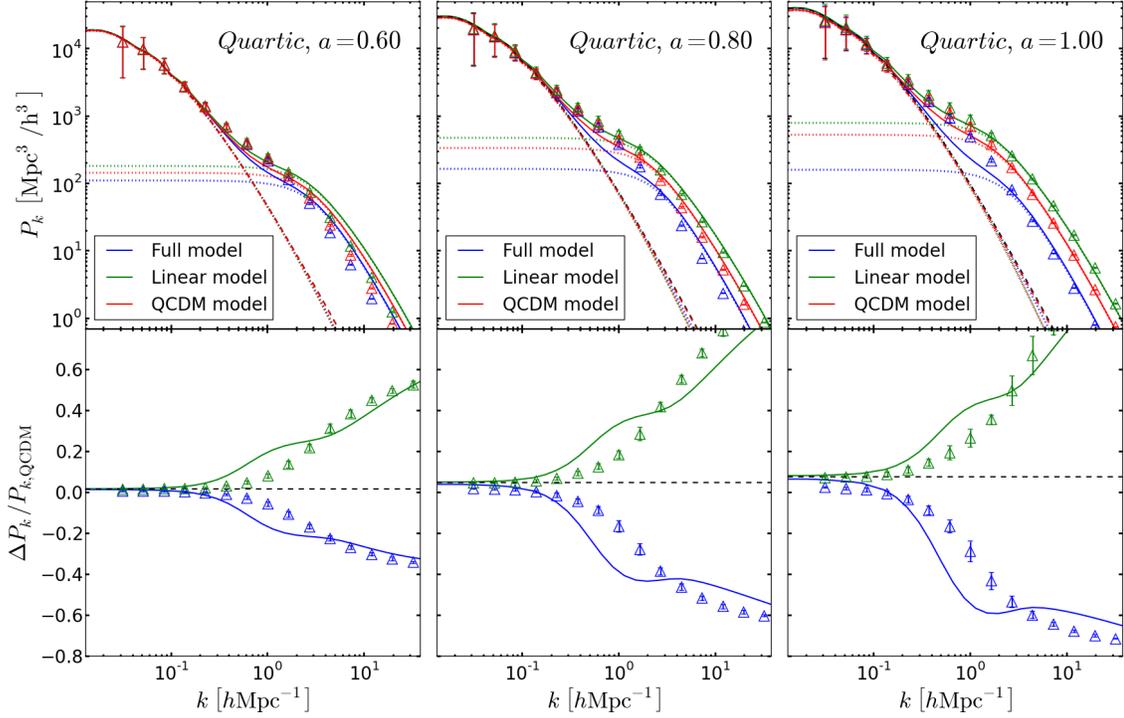
Figure 5.9: Same as Fig. 5.8, but for the Quartic Galileon model.

model. In particular, the 2-halo term can be written more accurately as

$$
\begin{aligned}
P_k^{2\mathrm{h}} = & \int \mathrm{d}M_1 \frac{1}{\bar{\rho}_{m0}} \frac{\mathrm{d}n(M_1)}{\mathrm{d}\ln M_1} |u(k, M_1)| \\
& \int \mathrm{d}M_2 \frac{1}{\bar{\rho}_{m0}} \frac{\mathrm{d}n(M_2)}{\mathrm{d}\ln M_2} |u(k, M_2)| P_k^{\mathrm{hh}}(M_1, M_2),
\end{aligned}
$$

(5.42)

where $P_k^{\mathrm{hh}}(M_1, M_2)$ is the halo-halo power spectrum of haloes with mass M_1 and M_2. In the standard halo model approach, one approximates $P_k^{\mathrm{hh}}(M_1, M_2) = b(M_1)b(M_2)P_{k,\mathrm{lin}}$, which is done purely for convenience. This way, the two integrals in Eq. (5.42) can be separated and one recovers Eqs. (5.25) and (5.26). This approximation is expected to be valid on large scales. However, on intermediate and small scales, neither the bias parameter nor the matter power spectrum are well approximated by linear theory. Indeed, using the linear halo bias on these scales leads to an overestimation of the power, and using the linear power spectrum leads to an underestimation. As a result, the net effect of these approximations can, in principle, cancel to some extent. Nevertheless, it seems reasonable to expect that this cancellation may not be perfect. Note that this applies not only to the Galileon models studied here, but also to the standard ΛCDM model. In fact, the *halofit*

approach is partly motivated as an alternative to the halo model that is more accurate on intermediate scales [313, 314]. Recently, Ref. [315] extended the *halofit* approach to describe the nonlinear power spectrum in $f(R)$ gravity models. In the lower panels of Figs. 5.8 and 5.9, the halo model prediction overestimates the effects of the modifications to gravity, compared to the simulation results. This overestimation is similar to that found in Ref. [284] for Dvali-Gabadadze-Porrati (DGP) models and Refs. [112, 316] for $f(R)$ models of gravity. However, Ref. [112] has also shown how a simple modification of the 2-halo term can make the analytical predictions much more accurate.

Small scales. On scales $k \gtrsim 2h/\mathrm{Mpc}$, the agreement between the halo model and simulation results becomes generally better than on intermediate scales, especially at $a = 1$. On these scales, the 1-halo term dominates the total power spectrum, and the good performance of the halo model in matching the power spectrum of the simulations is related to the fact that we have used the fitted mass function and the fitted $c_{200}(M_{200})$ relation. For instance, in the case of the full variant of the Quartic model at $a = 1$, the use of the standard Sheth-Tormen mass function would significantly overpredict the simulation results (cf. Fig. 5.4). This would in turn lead to a significant overprediction of the clustering power on small scales as well (not shown to make the plot clearer). Nevertheless, this variant, together with the linear variant of the Cubic model, still shows a visible discrepancy between the halo model and simulation results on these small scales at $a = 1$. In particular, at $k \sim 1h/\mathrm{Mpc}$, the halo model of the linear Cubic variant predicts $\sim 30\%$ less power than the simulations; whereas in the case of the full Quartic variant, the halo model overpredicts the power in the simulations by $\sim 40\%$. Moreover, the performance of the halo model on small scales becomes worse at earlier times. A possible reason for this mismatch can be related to the relaxation state of the haloes. If the haloes are not relaxed, then this can bias the estimation of the concentration, which could explain the differences. To investigate this, we have measured the impact of artifically enhancing and suppressing the amplitude of the concentration-mass relation by 25% on all mass scales. This test has shown that even a drastic modification of 25% in the halo concentration parameter does not fully reconcile the halo model with the simulation results. Hence, the discrepancies on small scales are likely to be associated with the approximations of the halo model itself. For instance, recall that the halo model assumes that all the matter in the Universe lies within gravitationally bound structures, which is not the case in N-body simulations. The *halofit* approach is also

known to be more accurate than the halo model on small scales [313, 314]. A more detailed study of the validity of the assumptions of the halo model is beyond the scope of the analysis of this chapter. In terms of the relative difference, however, these discrepancies cancel to some extent, and the agreement between the halo model and the simulations becomes much better. This is particularly noticeable in the case of the Cubic Galileon model.

Physically, just as we saw in the previous sections, in Fig. 5.8, we reencounter the extreme effectiveness of the screening mechanism in the Cubic model in suppressing any modifications to gravity on small scales. For instance, at $k \sim 1h/\mathrm{Mpc}$ and $a = 1$, the increase in power relative to QCDM is of order 10%, which is considerably smaller than the $\sim 50\%$ boost seen with the linear variant. The suppression effects of the screening mechanism become even more apparent for $k \gtrsim 1h/\mathrm{Mpc}$. The physical picture is much different in Fig. 5.9 because of the weaker gravity in the Quartic model, which follows from the implementation of the Vainshtein mechanism. In this case, the simulations of the full Quartic model show $\sim 30\%$ less clustering power than QCDM at $k \sim 1h/\mathrm{Mpc}$ and $a = 1$; while the simulations of the linear model show an enhancement of about 25%.

For more details about the results for the power spectrum in the Cubic and Quartic Galileon models we refer the reader to Refs. [6] and [276], respectively.

5.4   Summary

In this chapter, we studied the properties of dark matter haloes in the Cubic and Quartic Galileon gravity cosmologies. We have made use of N-body simulation results, as well as semi-analytical predictions to investigate the halo mass function, the linear halo bias parameter, the halo concentration-mass relation and the nonlinear matter power spectrum. We have also assessed the performance of standard semi-analytical formulae in describing the results from the N-body simulations. The strategy to solve the equations of the Cubic Galileon model in a N-body code was presented in Sec. 5.1. Our simulations of the Quartic model were based on the code of Ref. [276].

Our main results can be summarized as follows:

- If one uses the standard Sheth-Tormen fitting parameters $(q, p) = (0.75, 0.30)$, then the formulae for the halo mass function fail to provide a reasonable match to the results of the N-body simulations (see Figs. 5.3 and 5.4).

- By fitting the (q, p) parameters to match the halo mass function measured from the simulations (cf. Table 5.1), then indeed, the Sheth-Tormen formula provides a very good description of the halo abundances over the entire mass range probed by our simulations. Moreover, the Sheth-Tormen linear halo bias formula computed with the best-fitting (q, p) also provides a good description of the results of the simulations. This implies that the principles of the excursion set theory still hold in Galileon gravity models.

- In previous chapters we have mentioned the possibility that the enhanced clustering amplitude of the linear matter power spectrum in the Cubic and Quartic Galileon models ($\sigma_8 \sim 1$, for $\Sigma m_\nu = 0$) could potentially lead to some tension with the observed clustering amplitude of LRGs. However, the effect of a boosted linear power spectrum is degenerate with a lower linear halo bias parameter (c.f. Fig. 5.5), which can help to ease an eventual tension. In this chapter, armed with accurate analytical formulae, we have addressed this issue by performing a halo occupation distribution analysis of LRGs. Our analysis showed that the interplay between the modifications to the large scale clustering power, halo abundance and halo bias in the Cubic and Quartic Galileon models can be explored to yield realistic LRG halo distributions that match both the observed clustering amplitude and galaxy number density. We conclude that the Cubic and Quartic models are not in tension with the LRG clustering data.

- The halo concentration-mass relation, $c_{200}(M_{200})$, in the Cubic and Quartic Galileon models is well fitted by a power law (cf. Fig. 5.7 and Table 5.2). The standard picture that the concentration increases with time for fixed mass, and decreases with mass at a given epoch prevails in all but one of the models we studied. The exception is the full variant of the Quartic model, in which the weaker gravity leads to halo concentrations with a very weak mass and time dependence.

- On linear scales ($k \lesssim 0.2h/\mathrm{Mpc}$), the halo model prediction agrees very well with the matter power spectrum measured from the simulations because both reduce to the linear theory result. On intermediate scales ($0.2h/\mathrm{Mpc} \lesssim k \lesssim 2h/\mathrm{Mpc}$), the halo model typically underpredicts the power spectrum of the simulations by 20% to 50% across all

the model variants at all the epochs shown (cf. Fig. 5.8 and Fig. 5.9). This is a consequence of approximations that are made in the derivation of the halo model equations, which sacrifice accuracy in the mildy-nonlinear regime in favour of analytical convenience. The agreement between the halo model and simulations becomes better on small scales ($k \gtrsim 2h/\mathrm{Mpc}$) at $a = 1$. We believe this is closely related to the fact that we have used analytical formulae that match the mass function and concentration parameter from the simulations. There are still visible differences between the formulae and the simulation results on smaller scales for the linear variant of the Cubic and full variant of the Quartic model. Morevoer, these differences also exist for all variants at earlier times. We have checked that any discrepancies on small scales are likely to be due to the approximations made in the halo model, and not to an incorrect modelling of the halo properties that enter the calculation of the 1-halo term.

- In all of our results, we have found that the screening mechanism works very effectively in the Cubic Galileon model, especially on small scales. This is particularly noticeable in our results for the halo concentration-mass relation and the nonlinear matter power spectrum on small scales, for which the full and QCDM variants of the Cubic model give essentially the same predictions. In the case of the Quartic model, the screening mechanism cannot suppress all of the modifications to gravity, which becomes weaker in high density regions. This leads to clear differences in our results for the full and QCDM variants of the model.

With its two free parameters recalibrated, the Sheth-Tormen mass function and its application in the halo model approach, has proven sufficient to give a reasonable match to the results of the Cubic and Quartic Galileon simulations. Although in this analysis we focused only on two particular models, we believe that the strategy presented here of directly fitting the halo properties to simulations can also be applied to other modified gravity theories [258, 259, 260, 261, 262, 266, 267, 317]. For some models, we believe this can improve the performance of the semi-analytical formulae. These are a much faster alternative to N-body simulations, and can be used to generate quick estimates for the large-scale structure in modified gravity. The development of these semi-analytical models, in addition to enabling a clearer way of pinpointing the physical effects (which are often hidden in the brute-force calculations of a N-body simulation), can also be important for current and up-

coming large-scale structure surveys, which will require vast regions of parameter spaces to be spanned in a timely manner.

Finally, we stress that although both the Cubic and Quartic Galileon models are in tension with the observational data (recall the ISW discussion in Chapter 3), it is still valuable to investigate the impact that models like these can have on nonlinear structure formation. This allows for a better understanding of the ways to distinguish between different modified gravity theories and also for a more robust interpretation of the data from current and future large scale structure surveys. Indeed, in Chapter 7, we shall use the Cubic Galileon model as a working case to investigate ways to test gravity on large scales using lensing.

Chapter 6

Nonlinear structure formation in Nonlocal Gravity

We now turn our attention to large scale structure formation in *nonlocal gravity* models. In these models, the modifications to gravity arise via the addition of nonlocal terms (i.e. which depend on more than one point in spacetime) to the Einstein field equations. These terms typically involve the inverse of the d'Alembertian operator, $\Box^{-1}$, acting on curvature tensors. To ensure causality, such terms must be defined with the aid of retarded Green functions (or propagators). However, such retarded operators cannot be derived from standard action variational principles (see e.g. Sec. 2 of Ref. [63] for a discussion). One way around this is to specify the model in terms of its equations of motion and not in terms of its action. One may still consider a nonlocal action to derive a set of causal equations of motion, so long as in the end one replaces, by hand, all of the resulting operators by their retarded versions. Both of these approaches, however, imply that nonlocal models of gravity must be taken as purely phenomenological and should not be interpreted as fundamental theories. In general, one assumes that there is an unknown fundamental (local) quantum theory of gravity, and the nonlocal model represents only an effective way of capturing the physics of that theory in some appropriate limit.

It was in the above spirit that Ref. [61] proposed a popular nonlocal model of gravity capable of explaining cosmic acceleration. In this model, which has been extensively studied (see e.g. Refs. [62, 63, 318, 319, 320, 321, 322, 323, 324, 325, 326] and references therein), one adds the term $\mathcal{R}f\left(\Box^{-1}\mathcal{R}\right)$ to the Einstein-Hilbert action, where $\mathcal{R}$ is the Ricci scalar and f is a free function. As described in Ref. [63], the function f can be constructed in such a way that it takes on different values on the cosmological background and inside gravitationally bound systems. In particular, at the background level, f can be tuned to reproduce ΛCDM-like expansion histories, but inside regions like the Solar System, one can assume

that f vanishes, thus recovering GR completely. This model, however, seems to run into tension with data sensitive to the growth rate of structure on large scales [325, 326].

More recently, nonlocal terms have also been used to construct theories of massive gravity. An example of this is obtained by adding directly to the Einstein field equations a term like $m^2 \left(g_{\mu\nu}\square^{-1}\mathcal{R}\right)^T$ [327, 328, 329, 330], where m is a mass scale and ^{T} means the extraction of the transverse part (see also Refs. [331, 332, 333, 334] for models in which $\square^{-1}$ acts on the Einstein and Ricci tensors). This model has no ΛCDM limit for the background evolution, but it can still match the current background expansion and growth rate of structure data with a similar goodness-of-fit [330]. Furthermore, Ref. [329] has investigated spherically symmetric static solutions in this model, concluding that it does not suffer from instabilities that usually plague theories of massive gravity. A similar model was proposed by Ref. [136], which is characterized by a term $\propto m^2\mathcal{R}\square^{-2}\mathcal{R}$ in the action (see Eq. (6.1)). Reference [335] showed that this model can reproduce current type Ia Supernovae (SNIa) data, although it also has no ΛCDM limit for the background expansion. The time evolution of linear matter density fluctuations in this model also differs from that in ΛCDM, but the work of Ref. [335] suggests that the differences between these two models are small enough to be only potentially distinguishable by future observational missions.

In this chapter, we extend the previous work done for the model of Refs. [136, 335] by examining its predictions in the nonlinear regime of structure formation. We do this by running a set of N-body simulations, which we use to analyse the model predictions for the nonlinear matter and velocity divergence power spectra, and also halo properties such as their abundance, bias and concentration. By following the steps presented in the last chapter for the Galileon models, we shall also assess the performance of the Sheth-Tormen and halo model formulae in describing the simulations of Nonlocal gravity. The halo modelling notation in this chapter follows closely that used in the last chapter. To the best of our knowledge, the analysis presented here constitutes the first study of the nonlinear regime of structure formation in nonlocal gravity cosmologies using N-body simulations.

6.1 The $\mathcal{R}\square^{-2}\mathcal{R}$ nonlocal gravity model

6.1.1 Action and field equations

We consider the nonlocal gravity model of Refs. [136, 335], whose action is given by

$$A = \frac{1}{2\kappa} \int \mathrm{d}x^4 \sqrt{-g} \left[\mathcal{R} - \frac{m^2}{6} \mathcal{R}\Box^{-2}\mathcal{R} - \mathcal{L}_m \right],$$

(6.1)

where g is the determinant of the metric $g_{\mu\nu}$, $\mathcal{L}_m$ is the Lagrangian density of the matter fluid, $\mathcal{R}$ is the Ricci scalar and $\Box = \nabla^\mu \nabla_\mu$ is the d'Alembertian operator. To facilitate the derivation of the field equations, and to solve them afterwards, it is convenient to introduce two auxiliary scalar fields defined as

$$U = -\Box^{-1}\mathcal{R},$$

(6.2)

$$S = -\Box^{-1}U = \Box^{-2}\mathcal{R}.$$

(6.3)

The solutions to Eqs. (6.2) and (6.3) can be obtained by evaluating the integrals

$$U \equiv -\Box^{-1}\mathcal{R} = U_{\mathrm{hom}}(x) - \int \mathrm{d}^4 y \sqrt{-g(y)} G(x,y) \mathcal{R}(y),$$

(6.4)

$$S \equiv -\Box^{-1}U = S_{\mathrm{hom}}(x) - \int \mathrm{d}^4 y \sqrt{-g(y)} G(x,y) U(y),$$

(6.5)

where U_{hom} and S_{hom} are any solutions of the homogeneous equations $\Box U = 0$ and $\Box S = 0$, respectively, and $G(x,y)$ is any Green function of $\Box$. The choice of the homogeneous solutions and of the Green function specify the meaning of the operator $\Box^{-1}$. To ensure causality, one should use the retarded version of the Green function, i.e., the solutions of U (or S) should only be affected by the values of R (or U) that lie in its past light-cone. The homogeneous solutions can be set to any value, which is typically zero, without any loss of generality. In principle, the model predictions can be obtained by solving Eqs. (6.4) and (6.5). However, it is convenient to use the fields U and S to cast the nonlocal action of Eq. (6.1) in the form of a local scalar-tensor theory [319, 336, 337] as

$$A = \frac{1}{2\kappa} \int \mathrm{d}x^4 \sqrt{-g} \left[\mathcal{R} - \frac{m^2}{6} \mathcal{R}S - \xi_1 \left(\Box U + \mathcal{R} \right) - \xi_2 \left(\Box S + U \right) - \mathcal{L}_m \right],$$

(6.6)

where ξ_1 and ξ_2 are Lagrange multipliers. The field equations can then be written as

$$G_{\mu\nu} - \frac{m^2}{6} K_{\mu\nu} = \kappa T_{\mu\nu},$$

(6.7)

$$\Box U = -\mathcal{R},$$

(6.8)

$$\Box S = -U,$$

(6.9)

with

$$K_{\mu\nu} \equiv 2SG_{\mu\nu} - 2\nabla_\mu \nabla_\nu S - 2\nabla_{(\mu} S \nabla_{\nu)} U + \left(2\Box S + \nabla_\alpha S \nabla^\alpha U - \frac{U^2}{2} \right) g_{\mu\nu},$$

(6.10)

and where $T^{\mu\nu} = (2/\sqrt{-g})\,\delta\left(\mathcal{L}_m\sqrt{-g}\right)/\delta g_{\mu\nu}$ is the energy-momentum tensor of the matter fluid. The use of the scalar fields U and S therefore allows one to obtain the solutions by solving a set of coupled differential equations, instead of the more intricate integral equations associated with the inversion of a differential operator. These two formulations are, however, not equivalent as explained with detail in many recent papers (see e.g. Refs.[62, 327, 328, 332, 337, 338, 339]): Eqs. (6.7), (6.8) and (6.9) admit solutions that are not solutions of the original nonlocal problem. For instance, if U^* is a solution of Eq. (6.8), then $U^* + U_{\text{hom}}$ is also a solution for any U_{hom}, since $\Box U_{\text{hom}} = 0$ (the same applies for the field S and Eq. (6.9)). If one wishes the differential equations (6.7), (6.8) and (6.9) to describe the nonlocal model, then one must solve them with the one and only choice of initial conditions that is compatible with the choice of homogeneous solutions in Eqs. (6.4) and (6.5). All other initial conditions lead to spurious solutions and should not be considered.

In the remainder of this chapter, we shall not worry too much about the theoretical aspects of the model, and prefer to focus more on its phenomenology and impact on observations (as is the overall philosophy of this thesis).

6.1.2 Background equations

At the level of the cosmological background ($\Phi = \Psi = 0$), the two Friedmann equations can be written as

$$3H^2 = \kappa\bar{\rho}_m + \kappa\bar{\rho}_{de}, \tag{6.11}$$

$$-2\dot{H} - 3H^2 = \kappa\bar{p}_m + \kappa\bar{p}_{de}, \tag{6.12}$$

where we have encapsulated the effects of the nonlocal term into an effective background "dark energy" density, $\bar{\rho}_{de}$, and pressure $\bar{p}_{de}$, which are given, respectively, by

$$\kappa\bar{\rho}_{de} = \frac{m^2}{6}\left[6\bar{S}H^2 + 6H\dot{\bar{S}} - \bar{U}\dot{\bar{S}} - \frac{\bar{U}^2}{2}\right], \tag{6.13}$$

$$\kappa\bar{p}_{de} = -\frac{m^2}{6}\left[2\bar{S}\left(2\dot{H} + 3H^2\right) + \ddot{\bar{S}} + 4H\dot{\bar{S}} + \bar{U}\dot{\bar{S}} - \frac{\bar{U}^2}{2}\right]. \tag{6.14}$$

Additionally, Eqs. (6.8) and (6.9) yield

$$\ddot{\bar{U}} + 3H\dot{\bar{U}} = 6\left(\dot{H} + 2H^2\right), \tag{6.15}$$

$$\ddot{\bar{S}} + 3H\dot{\bar{S}} = -\bar{U}. \tag{6.16}$$

In the above equations, a dot denotes a partial derivative w.r.t. physical time, t, an overbar indicates that we are considering only the background average and $H = \dot{a}/a$ is the Hubble expansion rate.

The background evolution in the $\mathcal{R}\square^{-2}\mathcal{R}$ model has to be obtained numerically. The differential equations are evolved starting from deep into the radiation dominated era ($z = 10^6$) with initial conditions for the auxiliary fields $\bar{U} = \dot{\bar{U}} = \bar{S} = \dot{\bar{S}} = 0$. Note that, in the radiation era, the Ricci scalar vanishes ($\bar{\mathcal{R}} = 6\dot{H} + 12H^2 = 0$). Hence, from Eqs. (6.4) and (6.5) one sees that these initial conditions are indeed compatible with the choice $U_{\text{hom}} = S_{\text{hom}} = 0$. The value of the parameter m is determined by a trial-and-error scheme to yield the value of $\bar{\rho}_{de0}$ that makes the Universe spatially flat, i.e., $\bar{\rho}_{r0} + \bar{\rho}_{m0} + \bar{\rho}_{de0} = \bar{\rho}_{c0} \equiv 3H_0^2/\kappa$, where the subscripts $_r$, $_m$ refer to radiation and matter, respectively, the subscript $_0$ denotes present-day values, and $H_0 = 100h\,\text{km/s/Mpc}$ is the present-day Hubble rate.

6.1.3 Spherically symmetric nonlinear equations

By assuming that the potentials Φ and Ψ are spherically symmetric, one can write the $(0,0)$ and (r,r) components of Eq. (6.7), and Eqs. (6.8) and (6.9), respectively, as

$$
\frac{2}{r^2}\left(r^2\Phi_{,r}\right)_{,r} - \frac{m^2}{6}\left[6SH^2 + \frac{4S}{r^2}\left(r^2\Phi_{,r}\right)_{,r} - \frac{2}{r^2}\left(r^2 S_{,r}\right)_{,r}\right.
$$
$$
\left. + 2S_{,r}\,\Phi_{,r} - S_{,r}\,U_{,r} - \frac{U^2}{2}\right] = \kappa\bar{\rho}_m\delta a^2, \tag{6.17}
$$

$$
\frac{2}{r}\left(\Phi_{,r} - \Psi_{,r}\right) - \frac{m^2}{6}\left[4S\dot{H}a^2 + 6SH^2a^2 + \frac{4S}{r}\left(\Phi_{,r} - \Psi_{,r}\right)\right.
$$
$$
\left. + 4S_{,r}\,\Phi_{,r} - 2S_{,r}\,\Psi_{,r} - 4\frac{S_{,r}}{r} + 2S_{,r}\,U_{,r} - \frac{U^2}{2}\right] = 0, \tag{6.18}
$$

$$
\frac{1}{r^2}\left(r^2 U_{,r}\right)_{,r} + U_{,r}\left(\Psi_{,r} - \Phi_{,r}\right) = 2\frac{1}{r^2}\left(r^2\Psi_{,r}\right)_{,r} - 4\frac{1}{r^2}\left(r^2\Phi_{,r}\right)_{,r}\,, \tag{6.19}
$$

$$
\frac{1}{r^2}\left(r^2 S_{,r}\right)_{,r} + S_{,r}\left(\Psi_{,r} - \Phi_{,r}\right) = U, \tag{6.20}
$$

where $_{,r}$ denotes a partial derivative w.r.t. the comoving radial coordinate r. When writing Eqs. (6.17)-(6.20), we have already employed the quasi-static and weak-field approximations (cf. Sec. 4.1). The above equations still contain terms with $\Psi_{,r}$ and $\Phi_{,r}$, because these terms contain the fields U and S, and up to now, we have not discussed the validity of applying these approximations to the auxiliary fields. However:

1. Equation (6.19) tells us that the U field is of the same order as the scalar potentials, $U \sim \Phi, \Psi$. Consequently, the quasi-static and weak-field limits also hold for U;

2. Equation (6.20) tells us that $S_{,rr} \sim \Phi, \Psi$, which means we can also neglect all terms containing S, $S_{,r}$ and $S_{,rr}$.

Under these considerations, the above equations simplify drastically. In particular, the only equation that remains relevant for the study of the spherical collapse of matter overdensities is Eq. (6.17), which can be written as:

$$\frac{1}{r^2} \left(r^2 \Phi_{,r} \right)_{,r} = 4\pi G_{\text{eff}} \bar{\rho}_m \delta a^2, \tag{6.21}$$

where

$$G_{\text{eff}} = G \left[1 - \frac{m^2 \bar{S}}{3} \right]^{-1} . \tag{6.22}$$

Equation (6.21) is the same as in standard gravity, but with Newton's constant replaced by the time-dependent gravitational strength, G_{eff}. This time dependence follows directly from the term $2SG_{\mu\nu}$ in the field equations, Eq. (6.7), which in turn follows from the variation of the term $\propto SR$ in the action Eq. (6.6). The fact that G_{eff} depends only on time tells us that gravity is modified with equal strength everywhere, regardless of whether or not one is close to massive bodies or in high-density regions. This may bring into question the ability of this model to pass the stringent Solar System tests of gravity [40, 248, 340]. We come back to this discussion in Sec. 6.2.3. We note also that from Eq. (6.18), it follows that $\Phi = \Psi$ in the quasi-static and weak-field limits.

6.1.4 Model parameters

The results presented in this chapter are for the cosmological parameter values listed in Table 6.1. These parameters were found by following the steps outlined in Chapter 3 for ΛCDM, although in the latter, neutrino masses are also varied in the constraints (cf. Table 3.1). In this chapter, however, we treat neutrinos as massless for simplicity.

The CMB temperature power spectra of the ΛCDM and $\mathcal{R}\square^{-2}\mathcal{R}$ models for the parameters listed in Table 6.1 are shown in Fig. 6.1. The $\mathcal{R}\square^{-2}\mathcal{R}$ model predictions were obtained with a suitably modified version of the CAMB code [172]. The derivation of the perturbed equations that enter the calculations in CAMB follows the strategy shown in Chapter 2 for the Galileon model, and for brevity we do not repeat it here. The result in Fig. 6.1 shows that the $\mathcal{R}\square^{-2}\mathcal{R}$ model is able to fit the CMB data with a goodness-of-fit that is similar to that of ΛCDM. In Sec. 6.2, we shall compare the results of the $\mathcal{R}\square^{-2}\mathcal{R}$ model with those of
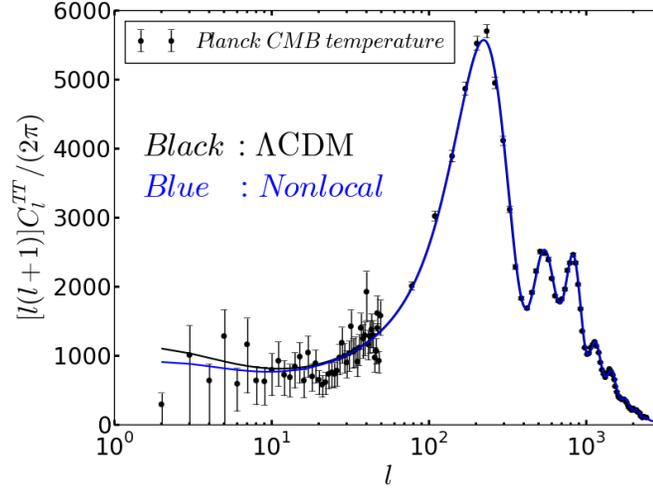
Figure 6.1: CMB temperature power spectrum of the ΛCDM (black) and $\mathcal{R}\square^{-2}\mathcal{R}$ (blue) models for the cosmological parameters of Table 6.1. The data points with errorbars show the power spectrum measured by the Planck satellite [193, 194].

Table 6.1: Cosmological parameters adopted in this chapter. The scalar amplitude at recombination A_s refers to a pivot scale $k = 0.05\mathrm{Mpc}^{-1}$. These values were determined by following the strategy outlined in Chapter 3 for ΛCDM, but assuming that neutrinos are massless. The $\mathcal{R}\square^{-2}\mathcal{R}$ model parameter m is derived by the condition to make the Universe spatially flat, i.e. , $1 = \Omega_{r0} + \Omega_{b0} + \Omega_{c0} + \Omega_{de0}(m)$.

Parameter	Planck (temperature+lensing) + BAO
$\Omega_{r0}h^2$	4.28×10^{-5}
$\Omega_{b0}h^2$	0.02219
$\Omega_{c0}h^2$	0.1177
h	0.6875
n_s	0.968
τ	0.0965
$\log_{10}\left[10^{10}A_s\right]$	3.097
Ω_{de0}	0.704
m	0.288

Table 6.2: Summary of the three models we simulate in this chapter. All models share the cosmological parameters of Table 6.1. The QCDM model has the same expansion history as the $\mathcal{R}\square^{-2}\mathcal{R}$ model, but with GR as the theory of gravity (cf. Sec. 6.2.1).

Model	$H(a)$	G_{eff}/G
"Full" $\mathcal{R}\square^{-2}\mathcal{R}$	$H(a)_{\mathcal{R}\square^{-2}\mathcal{R}}$	Eq. (6.22)
QCDM	$H(a)_{\mathcal{R}\square^{-2}\mathcal{R}}$	1
ΛCDM	$H(a)_{\Lambda\mathrm{CDM}}$	1

standard ΛCDM. In this chapter, we are mostly interested in the phenomenology driven by the modifications to gravity in the $\mathcal{R}\square^{-2}\mathcal{R}$ model. This is why we shall use the same cosmological parameters for both models. We refer the reader to Ref. [341] for an exploration of the parameter space in the $\mathcal{R}\square^{-2}\mathcal{R}$ model with CMB data.

6.2 Results

6.2.1 N-body simulations summary

Our simulations of the Nonlocal gravity model were performed with a modified version of the publicly available RAMSES N-body code [291]. Our modifications to the code consist of (i) changing the routines that compute the background expansion rate to interpolate the $\mathcal{R}\square^{-2}\mathcal{R}$ model expansion rate from a pre-computed table generated elsewhere; (ii) rescaling the total force felt by the particles in the simulation by $G_{\mathrm{eff}}(a)/G$, whose values are also interpolated from a table generated beforehand.

In the following sections we show the N-body simulation results obtained for three models. We simulate the "full" $\mathcal{R}\square^{-2}\mathcal{R}$ model of action Eq. (6.1), whose expansion history and G_{eff}/G are given by Eqs. (6.11) and (6.22), respectively. We also simulate a standard ΛCDM model and a model with the same expansion history as the $\mathcal{R}\square^{-2}\mathcal{R}$ model, but with $G_{\mathrm{eff}}/G = 1$. We call the latter model QCDM, and comparing its results to ΛCDM allows us to pinpoint the impact of the modified $H(a)$ alone on the growth of structure. The specific impact of the modified G_{eff} can then be measured by comparing the results from the "full" $\mathcal{R}\square^{-2}\mathcal{R}$ model simulations with those from QCDM. Table 6.2 summarizes the models we

consider in this chapter (these model variants are analogous to those of Table 4.2 for the Galileon model).

We simulate all models on a cubic box of size $L = 200$ Mpc$/h$ with $N_p = 512^3$ dark matter particles. We take $N_{\text{th}} = 8$ as the grid refinement criterion in RAMSES. The initial conditions are set up at $z = 49$, using the ΛCDM linear matter power spectrum with the parameters of Table 6.1. For each model, we simulate five realizations of the initial conditions (generated using different random seeds), which we use to construct errorbars for the simulation results by determining the variance across the realizations.

6.2.2 Linear growth and δ_c curves

Before discussing the results from the simulations, it is instructive to look at the model predictions for the linear growth rate of structure and for the time dependence of the critical density $\delta_c(z)$.

From top to bottom, Fig. 6.2 shows the time evolution of the fractional difference of the expansion rate relative to ΛCDM, $H/H_{\Lambda\text{CDM}} - 1$, the effective gravitational strength G_{eff}/G and the fractional difference of the squared linear density contrast relative to ΛCDM, $(\delta/\delta_{\Lambda\text{CDM}})^2 - 1$. The expansion rate in the $\mathcal{R}\square^{-2}\mathcal{R}$ model is lower than in ΛCDM for $a \gtrsim 0.1$. This reduces the amount of Hubble friction and therefore boosts the linear growth rate. The gravitational strength in the $\mathcal{R}\square^{-2}\mathcal{R}$ model starts growing after $a \gtrsim 0.2$, being approximately 6% larger than in GR at the present day. This also boosts the linear growth of structure, but has a smaller impact compared to the effect of the lower expansion rate. This is seen by noting that the differences between QCDM and ΛCDM in the bottom panel are larger than the differences between QCDM and the $\mathcal{R}\square^{-2}\mathcal{R}$ model.

Figure 6.3 shows the time dependence of δ_c. In the top panel, all models exhibit the standard result that δ_c decreases with time, i.e., the initial overdensity of the spherical top-hat should be smaller, if the collapse is to occur at later times. Compared to ΛCDM, at late times ($a \gtrsim 0.3$), the QCDM and $\mathcal{R}\square^{-2}\mathcal{R}$ models predict lower values for δ_c. This is as expected since structure formation is boosted at late times in these models, and as a result, this needs to be compensated by smaller values of the initial overdensities for the collapse to occur at the same epoch as in ΛCDM. Just like in the case of the linear growth rate, the differences w.r.t. the ΛCDM results are mainly affected by the lower expansion rate, and not by the larger values of G_{eff}/G. At earlier times ($a \lesssim 0.3$), all models have essentially the
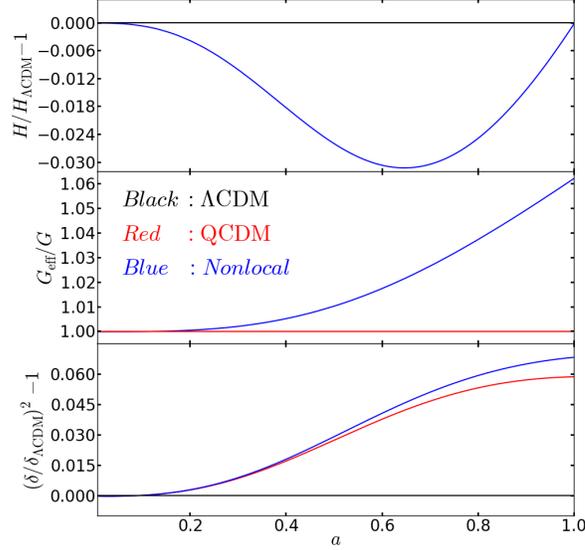
Figure 6.2: The upper panel shows the evolution of the expansion rate, plotted as the fractional difference w.r.t. the ΛCDM (black) result, $H(a)/H_{\Lambda\text{CDM}} - 1$ as a function of the expansion factor, a. $H(a)$ is the same for the $\mathcal{R}\Box^{-2}\mathcal{R}$ (blue) and QCDM (red) models. The middle panel shows the evolution of the effective gravitational strength, G_{eff}/G. This is unity in the ΛCDM and QCDM models at all times. The lower panel shows the evolution of the squared linear density contrast, δ^2, plotted as the fractional difference w.r.t. the ΛCDM prediction.

same expansion rate and gravitational strength, and as a result, the values of δ_c are roughly the same.

6.2.3 Interpretation of the constraints from Solar System tests of gravity

The absence of a screening mechanism in the $\mathcal{R}\Box^{-2}\mathcal{R}$ model may raise concerns about the ability of the model to satisfy Solar System constraints [40]. For instance, for the parameters of Table 6.1, the $\mathcal{R}\Box^{-2}\mathcal{R}$ model predicts that the rate of change of the gravitational strength today, $\dot{G}_{\text{eff}}/G$, is

$$\frac{\dot{G}_{\text{eff}}}{G} = H_0 \frac{\mathrm{d}}{\mathrm{d}N}\left(\frac{G_{\text{eff}}}{G}\right) \approx 92 \times 10^{-13} \text{ yrs}^{-1}, \tag{6.23}$$

which is at odds with the observational contraint $\dot{G}_{\text{eff}}/G = (4 \pm 9) \times 10^{-13} \text{ yr}^{-1}$, obtained from Lunar Laser Ranging experiments [250]. Hence, it seems that this type of local constraints can play a crucial role in determining the observational viability of the $\mathcal{R}\Box^{-2}\mathcal{R}$
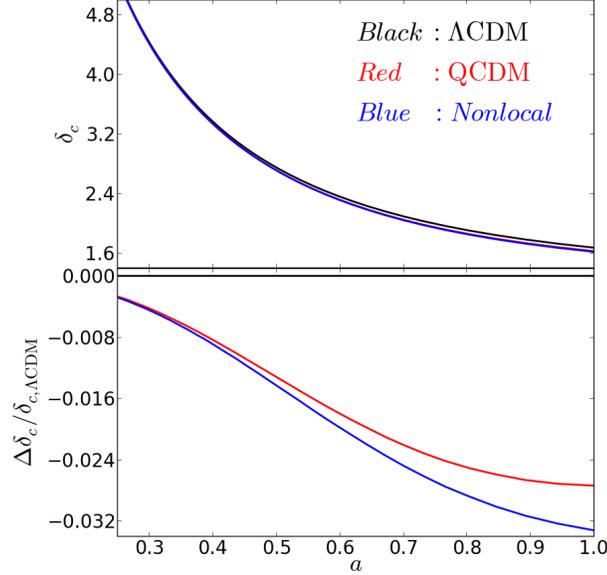
Figure 6.3: The upper panel shows the time evolution of the critical initial density for a spherical top-hat halo to collapse at scale factor a (linearly extrapolated to the present-day using the ΛCDM linear growth factor), for the ΛCDM (black), QCDM (red) and $\mathcal{R}\square^{-2}\mathcal{R}$ (blue) models. The lower panel shows the fractional difference w.r.t. ΛCDM.

model, potentially ruling it out (see e.g. Refs. [248, 340] for a similar conclusion, but in the context of other models).

It is interesting to contrast this result with that of the nonlocal model of Ref. [61], which we call here the $f(X)$ model (for brevity), where $f(X)$ is a free function that appears in the action and $X = \square^{-1}R$. The equations of motion of this model can be schematically written as

$$G_{\mu\nu}\left[1 + \chi(X)\right] + \Delta G_{\mu\nu} = T_{\mu\nu}, \tag{6.24}$$

where $\Delta G_{\mu\nu}$ encapsulates all the extra terms that are not proportional to $G_{\mu\nu}$ and the factor $\chi(X)$ is given by

$$\chi = f(X) + \square^{-1}\left[R\frac{\mathrm{d}f}{\mathrm{d}X}(X)\right]. \tag{6.25}$$

For the purpose of our discussion, it is sufficient to look only at the effect of χ in Eq. (6.24). This rescales the gravitational strength as

$$\frac{G_{\mathrm{eff}}}{G} = \{1 + \chi\}^{-1}, \tag{6.26}$$

which is similar to the effect of S in the $\mathcal{R}\Box^{-2}\mathcal{R}$ model. There is, however, one very important difference associated with the fact that in the case of the $f(X)$ model, one has the freedom to choose the functional form of the terms that rescale G_{eff}. To be explicit, we write the argument of f as

$$X = \Box^{-1}\mathcal{R} = \Box^{-1}\bar{\mathcal{R}} + \Box^{-1}\delta\mathcal{R}, \tag{6.27}$$

where $\bar{\mathcal{R}}$ and $\delta\mathcal{R}$ are, respectively, the background and spatially perturbed part of $\mathcal{R}$. As explained in Ref. [63], the relative size of $\bar{\mathcal{R}}$ and $\delta\mathcal{R}$ is different in different regimes. At the background level, $\Box^{-1}\delta\mathcal{R} = 0$ and so the operator $\Box^{-1}$ acts only on $\bar{\mathcal{R}}$. On the other hand, within gravitationally bound objects we have $\Box^{-1}\delta\mathcal{R} > \Box^{-1}\bar{\mathcal{R}}$. Now recall that the covariant $\Box$ operator acts with different signs on purely time- and space-dependent quantities [1]. As a result, the sign of X on the background differs from that within bound systems, such as galaxies or our Solar System. This can be exploited to tune the function f in such a way that it vanishes when the sign of X is that which corresponds to bound systems. In this way, $\chi = 0$ and one recovers GR completely [2]. When X takes the sign that corresponds to the background, then the function f is tuned to reproduce a desired expansion history, typically ΛCDM. In the case of the $\mathcal{R}\Box^{-2}\mathcal{R}$ model, S is fixed to be $S = \Box^{-2}\left(\bar{\mathcal{R}} + \delta\mathcal{R}\right)$ and one does not have the freedom to set it to zero inside bound objects. Consequently, the time-dependent part of S is always present in Eq. (6.22), which could potentially lead to a time-dependent gravitational strength that is at odds with the current constraints.

For completeness, one should be aware of a caveat. In the above reasoning, we have always assumed that the line element of Eq. (1.1) is a good description of the geometry of the Solar System. The question here is whether or not the factor $a(t)^2$ should be included in the spatial sector of the metric when describing the Solar System. This is crucial as the presence of $a(t)$ in Eq. (1.1) determines if S varies with time or not. If $a(t)$ is considered, then S varies with time and G_{eff} is time-varying as well. In this way, the model fails the Solar System tests. On the other hand, if one does not consider $a(t)$ in the metric, then G_{eff} is forcibly constant, and there are no apparent observational tensions. Such a static analysis was indeed performed by Refs. [136, 329], where it was shown that the model can cope well with the local constraints. Recall that these issues are similar to those we encountered in

---

[1] For instance, in flat four-dimensional Minkowski space we have $\Box = +\frac{\partial^2}{\partial t^2} - \frac{\partial^2}{\partial x^2} - \frac{\partial^2}{\partial y^2} - \frac{\partial^2}{\partial z^2}$.

[2] In Eq. (6.24), $\Delta G_{\mu\nu}$ also vanishes if $\chi = 0$.

Table 6.3: Best-fitting Sheth-Tormen (q, p) parameters to the simulation results at $a = 0.6$, $a = 0.8$ and $a = 1.0$. The uncertainty in the values of q and p is $\Delta_q = 3.5 \times 10^{-3}$ and $\Delta_p = 1.5 \times 10^{-3}$, respectively. These parameters are those that minimize the quantity $\sum_i |n^{\mathrm{sims}}(> M_i)/n^{\mathrm{ST}}(> M_i, q, p) - 1|$, in which n^{sims} is the cumulative mass function measured from the simulations and n^{ST} is the analytical result given by the Sheth-Tormen mass function. Here, the index i runs over the number of bins used in the simulation results. The standard ST values $(q, p) = (0.75, 0.3)$ are also shown as a reminder.

Model	$a = 0.6$	$a = 0.8$	$a = 1.0$
	(q, p)	(q, p)	(q, p)
Standard	$(0.750, 0.300)$	$(0.750, 0.300)$	$(0.750, 0.300)$
ΛCDM	$(0.713, 0.323)$	$(0.756, 0.326)$	$(0.756, 0.341)$
QCDM	$(0.727, 0.321)$	$(0.756, 0.331)$	$(0.763, 0.344)$
$\mathcal{R}\Box^{-2}\mathcal{R}$	$(0.720, 0.321)$	$(0.741, 0.326)$	$(0.756, 0.336)$

previous chapters for the Quartic Galileon model, in which the background evolution of the Galileon field may also drive a sizeable $\dot{G}_{\mathrm{eff}}$ locally (cf. Fig. 4.3).

The clarification of the above tension boils down to determining the impact of the global expansion of the Universe on local scales. It is not clear to us that if a field is varying on a time-evolving background, then it should not do so in a small perturbation around that background. However, we acknowledge this is an open question to address, and such study is beyond the scope of the analysis in this chapter. In what follows, we limit ourselves to assuming that Eq. (6.22) holds on all scales, but focus only on the cosmological (rather than local) interpretation of the results.

6.2.4 Halo mass function

Our results for the cumulative mass function of the ΛCDM (black), QCDM (red) and $\mathcal{R}\Box^{-2}\mathcal{R}$ (blue) models are shown in Fig. 6.4 at $a = 0.60$, $a = 0.80$ and $a = 1.00$. The symbols show the simulation results obtained with the halo catalogues we built using the `Rockstar` halo finder [292]. The results in the figure correspond to catalogues with subhaloes filtered
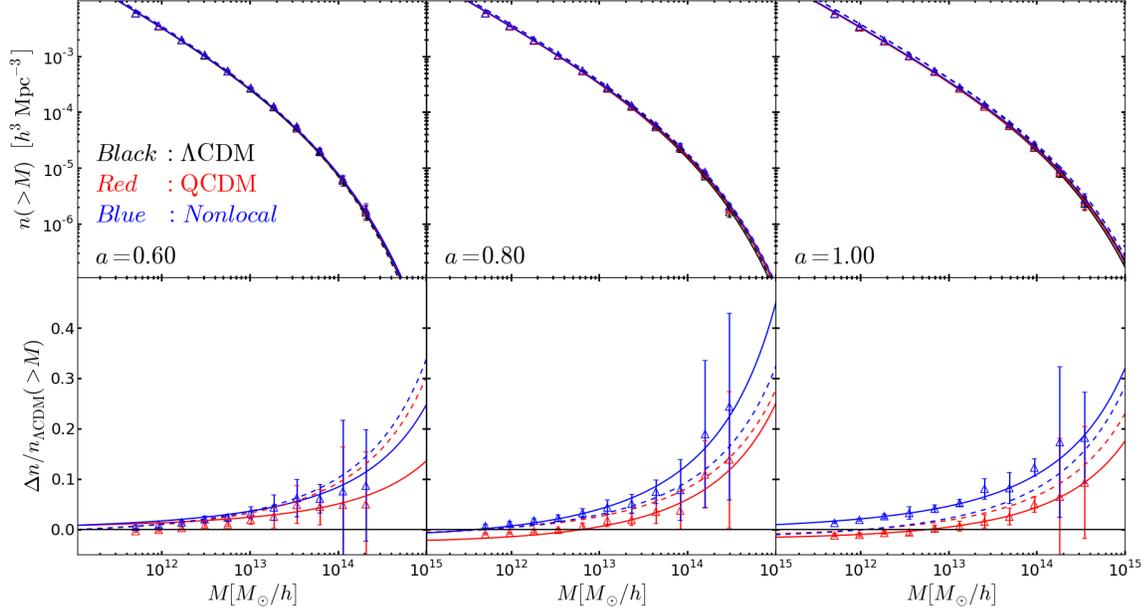
Figure 6.4: The cumulative mass function of dark matter haloes (upper panels) for the ΛCDM (black), QCDM (red) and $\mathcal{R}\Box^{-2}\mathcal{R}$ (blue) models, at three epochs $a = 0.6$, $a = 0.8$ $a = 1.0$, as labelled. The lower panels show the difference relative to ΛCDM. The symbols show the simulation results, and the errorbars indicate twice the variance across the five realizations of the initial conditions. We have used the phase-space friends-of-friends `Rockstar` code [292] to build the halo catalogues (without subhalos) used to compute the halo abundances. We only show the results for haloes with mass $M_{200} > 100 \times M_p \sim 5 \times 10^{11} M_\odot/h$, where $M_p = \rho_{m0} L^3/N_p$ is the particle mass in the simulations. The lines correspond to the ST mass function obtained using the fitted (solid lines) and the standard (dashed lines) (q, p) parameters listed in Table 6.3.

out. The lines show the ST analytical prediction computed for the fitted (solid lines) and standard (dashed lines) ST (q, p) parameters of Table 6.3. From the figure, one notes that although performing the fitting helps to improve the accuracy of the analytical formulae, overall the use of the standard values for (q, p) provides a fair estimate of the halo abundances in the $\mathcal{R}\square^{-2}\mathcal{R}$ model, and of its relative difference w.r.t. ΛCDM. This is not the case, for instance, in Galileon gravity models, for which it is necessary to recalibrate substantially the values of (q, p) if the ST mass function is to provide a reasonable estimate of the effects of the modifications to gravity (cf. Chapter 5). In the case of the $\mathcal{R}\square^{-2}\mathcal{R}$ model, the fact that the standard values of $(q, p) = (0.75, 0.30)$ work reasonably well means that the modifications in the $\mathcal{R}\square^{-2}\mathcal{R}$ model, relative to ΛCDM, are mild enough for its effects on the mass function to be well captured by the differences in $\delta_c(z)$.

At $a = 1.00$, the mass function of the QCDM model shows an enhancement at the high-mass end ($M \gtrsim 5 \times 10^{12} M_\odot/h$), and a suppression at the low-mass end ($M \lesssim 5 \times 10^{12} M_\odot/h$), relative to ΛCDM. This is what one expects in hierarchical models of structure formation if the growth rate of structure is boosted, as smaller mass objects are assembled more efficiently to form larger structures, leaving fewer of them. The effects of the enhanced $G_{\rm eff}/G$ maintain this qualitative picture, but change it quantitatively. More explicitly, the mass scale below which the mass function drops below that of ΛCDM is smaller than the mass range probed by our simulations; and the enhancement of the number density of massive haloes is more pronounced. In particular, compared to ΛCDM, haloes with masses $M \sim 10^{14} M_\odot/h$ are $\sim 5\%$ and $\sim 15\%$ more abundant in the QCDM and $\mathcal{R}\square^{-2}\mathcal{R}$ models, respectively. Figure 6.4 also shows that the relative differences w.r.t. ΛCDM do not change appreciably with time after $a \sim 0.80$. At earlier times ($a \sim 0.60$), the halo abundances in the QCDM and $\mathcal{R}\square^{-2}\mathcal{R}$ models approach one another, and their relative difference to ΛCDM decreases slightly, compared to the result at later times.

6.2.5 Halo bias

The linear halo bias predictions for the ΛCDM (black), QCDM (red) and $\mathcal{R}\square^{-2}\mathcal{R}$ (blue) models are shown in Fig. 6.5 at $a = 0.6$, $a = 0.8$ and $a = 1.0$. The symbols show the simulation results, which were obtained as in Sec. 5.3.3.

The simulation results show that, within the errorbars, the linear halo bias parameter for the three models is indistinguishable at all epochs shown. This shows that the modifi-
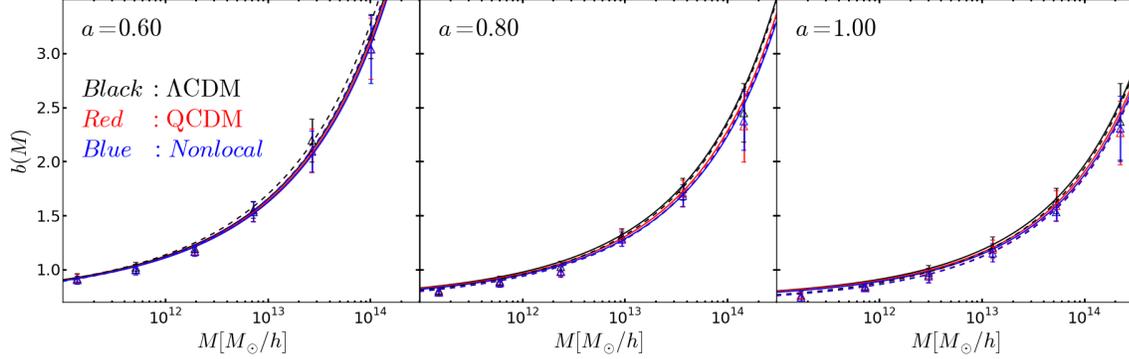
Figure 6.5: Linear halo bias in the ΛCDM (black), QCDM (red) and $\mathcal{R}\square^{-2}\mathcal{R}$ (blue) models, for three epochs $a = 0.6$, $a = 0.8$ and $a = 1.0$, as labelled. The symbols show the asymptotic value of the halo bias on large scales measured from the simulations as $b(M) = P_{\mathrm{hm}}(k \to 0, M)/P(k)$, considering only haloes (and not subhaloes) with mass $M_{200} > 100 \times M_p \sim 5 \times 10^{11} M_\odot/h$, where $M_p = \rho_{m0} L^3/N_p$ is the particle mass. Only the mass bins for which the values of $P_{\mathrm{hm}}(k, M)/P(k)$ have reached a constant value on large scales are shown. The errorbars show twice the variance across the five realizations of the initial conditions. The solid and dashed lines show the prediction from the ST formula, Eq. (5.28), computed, respectively, with the best-fitting and standard (q, p) parameters listed in Table 6.3.

cations to gravity in the $\mathcal{R}\square^{-2}\mathcal{R}$ model are not strong enough to modify substantially the way that dark matter haloes trace the underlying density field. The ST formula, Eq. (5.28), reproduces the simulation results very well. Note also that there is little difference between the curves computed using the fitted (solid lines) and the standard (dashed lines) (q, p) parameters of Table 6.3. We conclude the same as in the case of the mass function that, in the context of the $\mathcal{R}\square^{-2}\mathcal{R}$ model, there is no clear need to recalibrate the (q, p) parameters in order to reproduce the bias results from the simulations.

6.2.6 Halo concentration

Figure 6.6 shows the halo concentration-mass relation for the ΛCDM (black), QCDM (red) and $\mathcal{R}\square^{-2}\mathcal{R}$ (blue) models, at $a = 0.60$, $a = 0.80$ and $a = 1.00$. The symbols correspond to the mean values of c_{200} identified in the same halo catalogues used in Fig. 6.4. For all models, and at all epochs and mass scales shown, one sees that the halo concentrations are
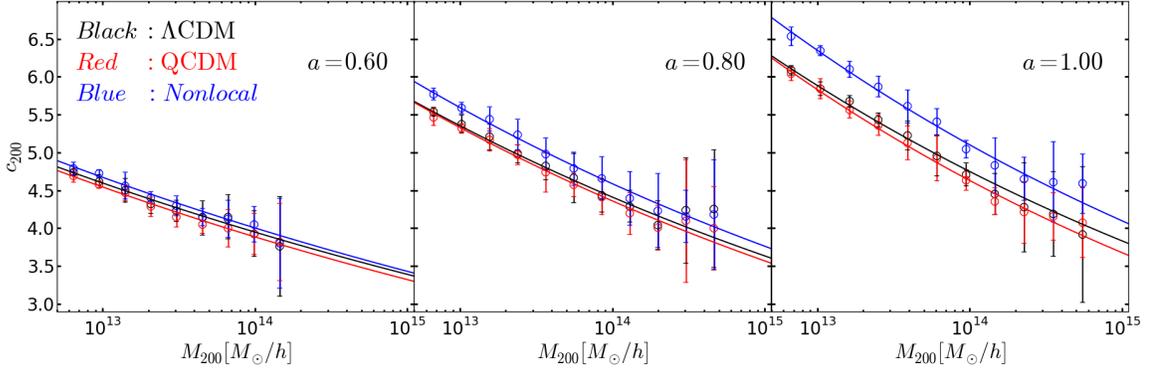
Figure 6.6: Halo concentration-mass relation in the ΛCDM (black), QCDM (red) and $\mathcal{R}\square^{-2}\mathcal{R}$ (blue) models, for three epochs $a = 0.6$, $a = 0.8$ and $a = 1.0$, as labelled. The symbols show the mean halo concentration in each mass bin, considering only haloes (and not subhaloes) with mass $M_{200} > 1000 \times M_p \sim 5 \times 10^{12} M_\odot/h$, where $M_p = \rho_{m0} L^3/N_p$ is the particle mass. In the $a = 0.6$ panel, we omit the results from the two highest mass bins due to their few number of objects. The errorbars show twice the variance of the mass-binned mean concentration across the five realizations of the initial conditions. The solid lines show the best-fitting power law relations of Table 6.4.

.

Table 6.4: Concentration-mass relation best-fitting (α, β) parameters in the parametrization $\log_{10}(c_{200}) = \alpha + \beta\log_{10}\left(M_{200}/\left[10^{12} M_\odot/h\right]\right)$ to the simulation results at $a = 0.6$, $a = 0.8$ and $a = 1.0$. The uncertainty in the values of α and β is $\Delta_\alpha = \Delta_\beta = 0.001$. These are the parameters that minimize the quantity $\sum_i(c_{200}^{\text{sims}}(M_i) - c_{200}^{\text{param}}(M_i, \alpha, \beta))^2/(2\Delta c_{200}^{\text{sims}}(M_i))^2$, where $c_{200}^{\text{sims}}(M_i)$ is the mean halo concentration measured from the simulations, $\Delta c_{200}^{\text{sims}}(M_i)$ is the variance of the mean across the five realizations and $c_{200}^{\text{param}}(M_i, \alpha, \beta)$ is the concentration given by the parametrization. Here, the index i runs over the number of mass bins.

Model	$a = 0.6$	$a = 0.8$	$a = 1.0$
	(α, β)	(α, β)	(α, β)
ΛCDM	$(0.729, -0.066)$	$(0.813, -0.084)$	$(0.863, -0.093)$
QCDM	$(0.726, -0.068)$	$(0.814, -0.087)$	$(0.866, -0.100)$
$\mathcal{R}\square^{-2}\mathcal{R}$	$(0.737, -0.067)$	$(0.834, -0.086)$	$(0.898, -0.095)$

well fitted by the power law function (solid lines),

$$\log_{10}(c_{200}) = \alpha + \beta \log_{10} \left(M_{200} / \left[10^{12} M_\odot / h \right] \right), \tag{6.28}$$

with the best-fitting (α, β) parameters given in Table 6.4. In the $\mathcal{R}\Box^{-2}\mathcal{R}$ and QCDM models, one recovers the standard ΛCDM result that halo concentration grows with time at fixed mass, and that, at a given epoch, the concentration decreases with halo mass.

At early times ($a \lesssim 0.6$), all models predict essentially the same concentration-mass relation. At later times, however, the halo concentrations in the $\mathcal{R}\Box^{-2}\mathcal{R}$ model become increasingly larger compared to ΛCDM. In particular, at $a = 1.00$, the halos are $\approx 8\%$ more concentrated in the $\mathcal{R}\Box^{-2}\mathcal{R}$ model, compared to ΛCDM, for the entire mass range probed by the simulations. This can be attributed to a combination of two effects. Firstly, the enhanced structure formation in the $\mathcal{R}\Box^{-2}\mathcal{R}$ model may cause the haloes to form at earlier times. This leads to higher concentrations since the haloes form at an epoch when the matter density in the Universe was higher. Secondly, the increasingly larger value of G_{eff} is also expected to play a role via its effect in the deepening of the gravitational potentials. In other words, even after the halo has formed, the fact that gravity keeps getting stronger with time may also help to enhance the concentration of the haloes (see also Refs. [306, 342, 343, 344]). In the case of the QCDM model, one finds that the halo concentrations are hardly distinguishable (within errorbars) from those in the ΛCDM model, at all times and for all mass scales. This suggests that the differences between the expansion history of the QCDM and ΛCDM models (cf. Fig. 6.2) are not large enough to have an impact on the formation time of the haloes. Once the haloes have formed in these two models, one can think as if the clustering inside these haloes decouples from the expansion. As a result, and since the gravitational strength is the same (cf. Table 6.2), one sees no significant differences in the concentration of the haloes from the QCDM and ΛCDM simulations.

6.2.7 Nonlinear matter power spectrum

Figure 6.7 shows our results for the nonlinear matter power spectrum. The power spectrum from the simulations was measured using the `POWMES` code [310]. The solid (dashed) lines show the halo model prediction obtained using Eq. (5.24) with the fitted (standard) (q, p) parameters of Table 6.3. The dotted lines show the predictions obtained using linear theory. Next, we organize the discussion as in Sec. 5.3.6 for the Galileon model by discussing the
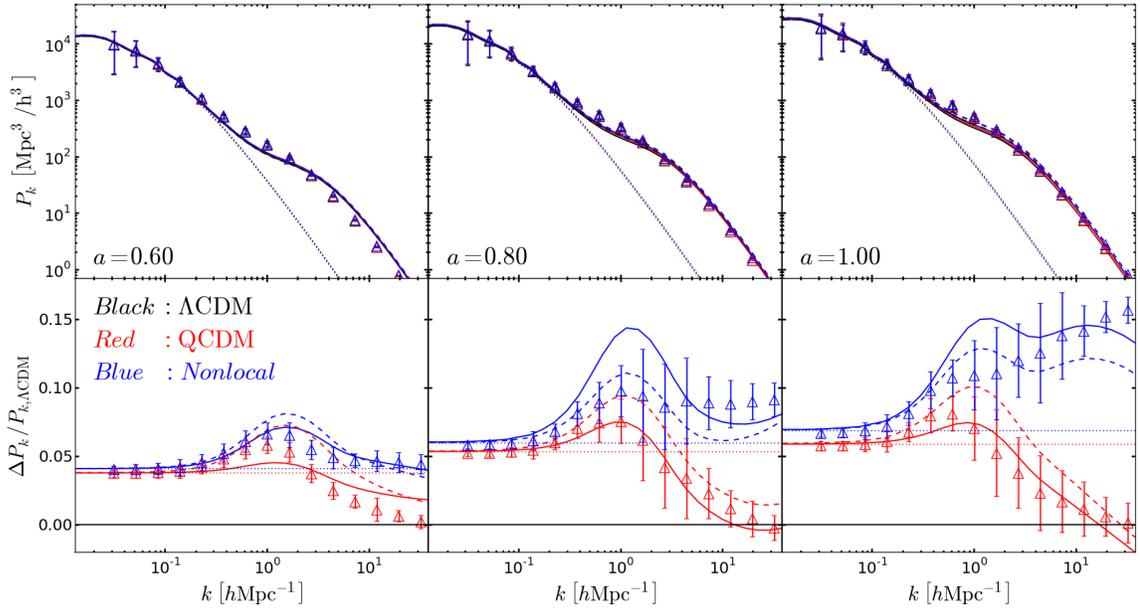
Figure 6.7: The nonlinear matter power spectrum (upper panels) in the ΛCDM (black), QCDM (red) and $\mathcal{R}\square^{-2}\mathcal{R}$ (blue) models, at three epochs $a = 0.6$, $a = 0.8$ and $a = 1.0$, as labelled. The lower panels show the different w.r.t. ΛCDM. The symbols show the simulation results, where the errorbars show twice the variance across the five realizations of the initial conditions. The solid lines show the halo model prediction obtained using Eq. (5.24), with the best-fitting (q, p) parameters listed in Table 6.3. The dashed lines show the power spectrum when using the standard ST $(q, p) = (0.75, 0.30)$ parameter values. The dotted lines show the result from linear perturbation theory. These lines are indistinguishable in the upper panels.

results separately for large, intermediate and small length scales. Some of the discussion is overlapping with that from the previous chapter, and as a result, we shall be brief here.

Large scales. On scales $k \lesssim 0.1h/\mathrm{Mpc}$, the halo model is dominated by the 2-halo term, which is practically indistinguishable from the linear matter power spectrum (cf. Sec. 5.3.6). As a result, the agreement between the halo model and the simulation results on large (linear) scales is guaranteed.

Intermediate scales. On scales $0.1h/\mathrm{Mpc} \lesssim k \lesssim 1h/\mathrm{Mpc}$, the halo model underpredicts slightly the power spectrum measured from the simulations, for all models and at all epochs shown. This is due to a fundamental limitation of the halo model on these scales, which follows from some simplifying assumptions about the modelling of halo bias on these intermediate scales (recall the simple explanation given in Sec. 5.3.6). Nevertheless, in terms of the relative difference to ΛCDM, the halo model limitations cancel to some extent, which leads to a better agreement with the simulation results. It is also worth mentioning that the performance of the halo model when ones uses the standard $(q, p) = (0.75, 0.30)$ values (dashed lines) is comparable to the case where one uses the values that best fit the mass function results (solid lines).

Small scales. On scales of $k \gtrsim 1h/\mathrm{Mpc}$, the halo model predictions are dominated by the 1-halo term, whose agreement with the simulations becomes better than on intermediate scales, especially at $a = 1.00$. There are still some visible discrepancies at $a = 0.60$, which are similar to those found in Sec. 5.3.6 for the Cubic and Quartic Galileon models. However, similarly to what happens on intermediate scales, the halo model performs much better when one looks at the relative difference w.r.t. ΛCDM. The predictions obtained by using the standard (q, p) parameter values (dashed lines), although not as accurate as the results obtained by using the fitted (q, p) values (solid lines), are still able to provide a good estimate of the effects of the modifications to gravity in the $\mathcal{R}\square^{-2}\mathcal{R}$ model on the small-scale clustering power.

In the QCDM model, the relative difference w.r.t. ΛCDM becomes smaller with increasing k. In particular, for $k \gtrsim 10h/\mathrm{Mpc}$ at $a = 1.0$, the clustering amplitude of these two models becomes practically indistinguishable. This result can be understood with the aid of the halo model expression for the 1-halo term, P_k^{1h}, (cf. Eq. (5.25)), which depends on the halo mass function and concentration-mass relation. Firstly, one notes that for smaller

length scales, the integral in P_k^{1h} becomes increasingly dominated by the lower mass end of the mass function. Consequently, the fact that the mass function of the QCDM model approaches that of ΛCDM at low masses (becoming even smaller for $M \lesssim 5 \times 10^{12} M_\odot/h$ at $a = 1.00$), helps to explain why the values of $\Delta P_k/P_{k,\Lambda\text{CDM}}$ decrease for $k \gtrsim 1h/\text{Mpc}$. Secondly, according to Fig. 6.6, the halo concentrations are practically the same in the ΛCDM and QCDM models. In other words, this means that inside small haloes (those relevant for small scales), matter is almost equally clustered in these two models, which helps to explain why $\Delta P_k/P_{k,\Lambda\text{CDM}}$ is compatible with zero for $k \gtrsim 10h/\text{Mpc}$ (Ref. [60] finds similar results for K-mouflage gravity models).

The same reasoning also holds for the $\mathcal{R}\square^{-2}\mathcal{R}$ model, which is why one can also note a peak in $\Delta P_k/P_{k,\Lambda\text{CDM}}$ at $k \sim 1h/\text{Mpc}$. However, in the case of the $\mathcal{R}\square^{-2}\mathcal{R}$ model, the mass function is larger at the low-mass end and the halo concentrations are also higher, compared to QCDM and ΛCDM. These two facts explain why $\Delta P_k/P_{k,\Lambda\text{CDM}}$ does not decrease in the $\mathcal{R}\square^{-2}\mathcal{R}$ model, being roughly constant at $a = 1.00$ for $k \gtrsim 1h/\text{Mpc}$. In particular, we have explicitly checked that if one computes the halo model predictions of the $\mathcal{R}\square^{-2}\mathcal{R}$ model, but using the concentration-mass relation of ΛCDM, then one fails to reproduce the values of $\Delta P_k/P_{k,\Lambda\text{CDM}}$ on small scales. This shows that a good performance of the halo model on small scales is subject to a proper modelling of halo concentration, which can only be accurately determined in N-body simulations.

6.2.8 Nonlinear velocity divergence power spectrum

Figure 6.8 shows the nonlinear velocity divergence power spectrum, $P_{\theta\theta}$,[3] for the three models of Table 6.2 and for $a = 0.60$, $a = 0.80$ and $a = 1.00$. The computation was done by first building a Delaunay tessellation using the particle distribution of the simulations [293, 294], and then interpolating the density and velocity information to a fixed grid to measure the power spectra. The upper panels show that on scales $k \lesssim 0.1h/\text{Mpc}$, the results from the simulations of all models approach the linear theory prediction, which is given by

$$P_{\theta\theta}^{\text{linear}} = a^2 \left(\frac{H}{H_0} \right)^2 f^2 P_k^{\text{linear}}, \tag{6.29}$$

---

[3]Here, θ is the Fourier mode of the divergence of the peculiar physical velocity field v, defined as $\theta(\vec{x}) = \nabla v(\vec{x})/H_0$.
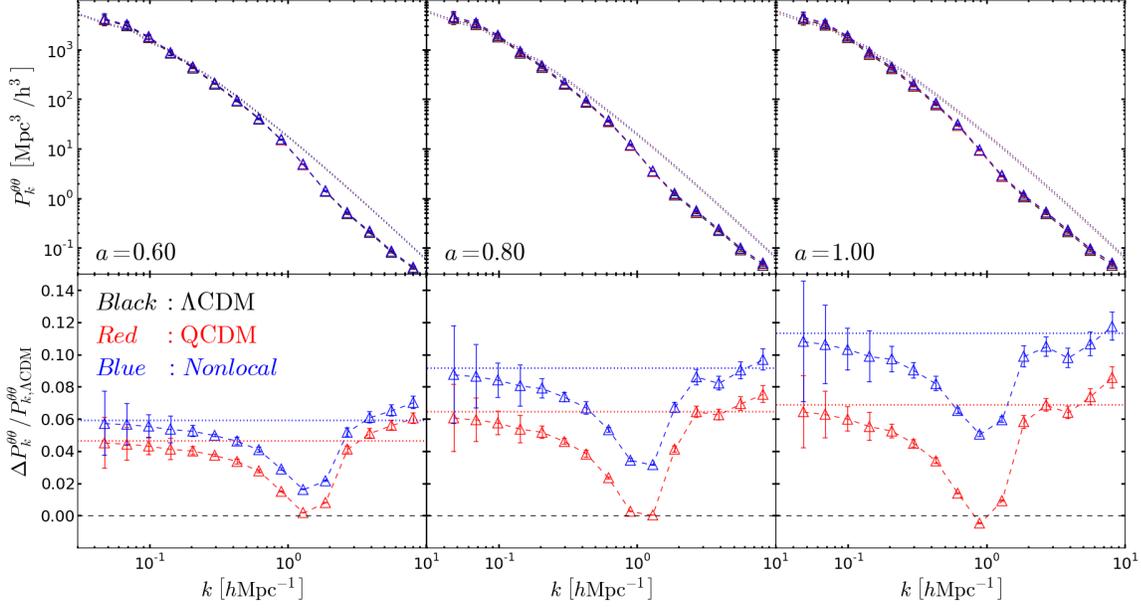
Figure 6.8: The nonlinear peculiar velocity divergence power spectrum (upper panels) in the ΛCDM (black), QCDM (red) and $\mathcal{R}\square^{-2}\mathcal{R}$ (blue) models, for three epochs $a = 0.6$, $a = 0.8$ and $a = 1.0$, as labelled. The lower panels show the difference w.r.t. ΛCDM. The symbols show the simulation results, where the errorbars show the variance across the five realizations of the initial conditions. The dashed lines only link the symbols to help the visualization. The dotted lines in the bottom panels show the prediction of linear perturbation theory.

where P_k^{linear} is the linear matter power spectrum and $f = \text{dln}\delta_{\text{lin}}/\text{dln}a$. On smaller scales, the formation of nonlinear structures tends to slow down the coherent (curl-free) bulk flows that exist on larger scales. This leads to an overall suppression of the divergence of the velocity field compared to the linear theory result for scales $k \gtrsim 0.1h/\text{Mpc}$, as shown in the upper panels.

In the lower panels, the simulation results also agree with the linear theory prediction for $k \lesssim 0.1h/\text{Mpc}$. On these scales, the time evolution of the power spectrum of all models is scale independent and the relative difference encapsulates the modifications to the time evolution of P_k^{linear}, H and f, in Eq. (6.29). On smaller scales, the values of $\Delta P_k^{\theta\theta}/P_{k,\Lambda\text{CDM}}^{\theta\theta}$ decay w.r.t. the linear theory result until approximately $k = 1h/\text{Mpc}$. This suppression follows from the fact that the formation of nonlinear structures is enhanced in the QCDM and $\mathcal{R}\square^{-2}\mathcal{R}$ models, relative to ΛCDM (cf. Figs. 6.4 and 6.7). Hence, on these scales, the sup-

pression in the velocity divergence caused by nonlinear structures is stronger in the QCDM and $\mathcal{R}\square^{-2}\mathcal{R}$ model, compared to ΛCDM. Finally, on scales $k \gtrsim 2 - 3h/\mathrm{Mpc}$, the relative difference to ΛCDM grows back to values comparable to the linear theory prediction. On these scales, one does not expect haloes to contribute considerably to $P_k^{\theta\theta}$ for two main reasons. First, as haloes virialize, the motion of its particles tends to become more random, which helps to reduce the divergence of the velocity field there. Secondly, and perhaps more importantly, $P_k^{\theta\theta}$ is computed from a volume-weighted field, and as a result, since haloes occupy only a small fraction of the total volume, they are not expected to contribute significantly to the total velocity divergence power spectrum. On the other hand, considerable contributions may arise from higher-volume regions such as voids, walls or filaments, where coherent matter flows exist. For instance, matter can flow along the direction of dark matter filaments, or inside a large wall or void that is expanding (see e.g. [36, 345, 346]). These small scale flows are larger in the QCDM and $\mathcal{R}\square^{-2}\mathcal{R}$ models at a fixed time, as shown by the growth of the values of $\Delta P_k^{\theta\theta}/P_{k,\Lambda\mathrm{CDM}}^{\theta\theta}$ on small scales.

On scales $k \gtrsim 2 - 3h/\mathrm{Mpc}$, one may find it odd that the QCDM model predicts roughly the same matter power spectrum as ΛCDM (cf. Fig. 6.7), but has a different velocity divergence power spectrum. This has to do with the weight with which different structures contribute to P_k and $P_k^{\theta\theta}$. For instance, P_k is computed from a mass-weighted density field, and hence, it is dominated by the highest density peaks, which are due to dark matter haloes. In other words, it is very insensitive to the behavior of the clustering of matter in voids, walls or filaments due to their lower density. On the contrary, $P_k^{\theta\theta}$, which is computed from a volume-weighted field, is forcibly less sensitive to dark matter haloes due to their low volume fraction. The values of $P_k^{\theta\theta}$ are then mostly determined by the velocity field inside voids, walls and filaments. These structures are typically larger than haloes and therefore they are more sensitive to the background expansion of the Universe. Consequently, they are more likely to be affected by modifications to $H(a)$, compared to haloes which detach from the overall expansion sooner. This can then explain the differences in the sizes of the modifications to P_k and $P_k^{\theta\theta}$ on small scales in the QCDM model, relative to ΛCDM. To test this we have computed $P_k^{\theta\theta}$ by artificially setting $\theta(\vec{x}) = 0$ in regions where the density contrast exceeds $\delta = 50$. This should roughly exclude the contribution from haloes to the values of $P_k^{\theta\theta}$. We have found no visible difference w.r.t. the results of Fig. 6.8, which shows that the small scale behavior of the velocity divergence is not affected

by what happens inside dark matter haloes. We have performed the same calculation, but by setting $\theta(\vec{x}) = 0$ whenever $\delta < 0$, to exclude the contribution from voids. We have found that at $a = 1$, the relative difference of QCDM to ΛCDM at $k \sim 10 h/\mathrm{Mpc}$ drops from $\sim 9\%$ (as in Fig. 6.8) to $\sim 7\%$. This seems to suggest that the dominant effect in the small scale behavior of $P_k^{\theta\theta}$ comes from walls and/or filaments. The velocity divergence in these structures is typically large (see e.g. Fig. 2 of Ref. [108]) and they also occupy a sizeable fraction of the total volume as well. A more detailed investigation of these results is, however, beyond the scope of the present analysis.

6.3 Summary

In this chapter, we studied the nonlinear regime of structure formation in nonlocal gravity cosmologies using N-body simulations, and also in the context of the semi-analytical ellipsoidal collapse and halo models.

The action or equations of motion of nonlocal gravity models are typically characterized by the inverse of the d'Alembertian operator acting on curvature tensors. Here, we focused on the model of Refs. [136, 335], in which the standard Einstein-Hilbert action contains an extra term proportional to $\mathcal{R}\square^{-2}\mathcal{R}$ (cf. Eq. (6.1)). The constant of proportionality is fixed by the dark energy density today, and hence this model contains the same number of free parameters as ΛCDM, although it has no ΛCDM limit for the background dynamics or gravitational interaction.

Our goal was not to perform a detailed exploration of the cosmological parameter space in the $\mathcal{R}\square^{-2}\mathcal{R}$ model. Instead, for the $\mathcal{R}\square^{-2}\mathcal{R}$ model we used the same cosmological parameters as for ΛCDM (cf. Table 6.1). In this way, one isolates the impact of the modifications to gravity from the impact of having different cosmological parameter values. Nevertheless, the comparison presented in Fig. 6.1 suggests that the model fits the CMB temperature data as well as ΛCDM (as confirmed by the more recent work of Ref. [341]). Our main results can be summarized as follows:

- The expansion rate in the $\mathcal{R}\square^{-2}\mathcal{R}$ model is smaller than in ΛCDM at late times, and the gravitational strength is enhanced by a time-dependent factor (cf. Fig. 6.2). Both effects help to boost the linear growth of structure (cf. Fig. 6.2) and also speed up the collapse of spherical matter overdensities (cf. Fig. 6.3). In particular, at the present day, the amplitude

of the linear matter (velocity divergence) power spectrum is enhanced by $\approx 7\%$ ($\approx 12\%$) in the $\mathcal{R}\square^{-2}\mathcal{R}$ model, compared to ΛCDM. These results are in agreement with Ref. [335]. The critical density for collapse today, $\delta_c(a = 1)$, is $\approx 3\%$ smaller in the $\mathcal{R}\square^{-2}\mathcal{R}$ model, relative to ΛCDM (cf Fig. 6.3). For these results, the modified expansion history plays the dominant role in driving the differences w.r.t. ΛCDM, compared to the effect of the enhanced $G_{\rm eff}$.

- At late times ($a > 0.6$), the number density of haloes with masses $M \gtrsim 10^{12} M_\odot/h$ is higher in the $\mathcal{R}\square^{-2}\mathcal{R}$ model, compared to ΛCDM. The difference becomes more pronounced at the high-mass end of the mass function. In particular, at $a = 1$, haloes with mass $M \sim 10^{14} M_\odot/h$ are $\approx 15\%$ more abundant in the $\mathcal{R}\square^{-2}\mathcal{R}$ model than in ΛCDM. At $M = 10^{12} M_\odot/h$ this difference is only $\approx 2\%$. The effects of the modified $H(a)$ and $G_{\rm eff}$ on the enhancement of the high-mass end of the mass function are comparable.

- The ST mass function describes well the halo number densities as well as the relative differences w.r.t. ΛCDM, for all of the epochs studied (cf. Fig. 6.4). We find that the use of the standard $(q, p) = (0.75, 0.30)$ ST parameter values provides a fair estimate of the modifications to the mass function in the $\mathcal{R}\square^{-2}\mathcal{R}$ model. However, recalibrating these parameters to the simulation results helps to improve the accuracy of the fit (cf. Table 6.3).

- The linear halo bias parameter in the $\mathcal{R}\square^{-2}\mathcal{R}$ model is barely distinguishable from that in ΛCDM for all masses and epochs studied (cf. Fig. 6.5). In other words, the modifications to gravity in the $\mathcal{R}\square^{-2}\mathcal{R}$ model play a negligible role in the way dark matter haloes trace the underlying density field. The ST halo bias formula therefore provides a good description of the simulation results. There is also almost no difference between the semi-analytical predictions for the bias computed using the best-fitting and standard values for the (q, p) ST parameters.

- The halo concentration-mass relation is well-fitted by a power law function (cf. Fig. 6.6), but with fitting parameters that differ from those of ΛCDM (see Table 6.4). For $a \lesssim 0.6$, the concentration of the haloes in the $\mathcal{R}\square^{-2}\mathcal{R}$ model is roughly the same as in ΛCDM, but it increases with time. In particular, at $a = 1.0$ ($a = 0.8$) and for all masses, haloes are $\approx 8\%$ ($\approx 4\%$) more concentrated in the $\mathcal{R}\square^{-2}\mathcal{R}$ model, compared to ΛCDM.

- The modifications to gravity in the $\mathcal{R}\square^{-2}\mathcal{R}$ model lead only to a modest enhancement of the clustering power. For instance, at $a = 1.0$ ($a = 0.8$) the amplitude of the nonlinear

matter power spectrum is never larger than $\approx 15\%$ ($\approx 10\%$) on all scales (cf. Fig. 6.7). These differences might be hard to disentangle using data from galaxy clustering given the known uncertainties in modelling galaxy bias. On small scales, $k \gtrsim 1h/\mathrm{Mpc}$, the differences w.r.t. ΛCDM are completely determined by the enhanced G_{eff}, and not by the modifications to $H(a)$.

• Similarly to the case of the matter power spectrum, the modifications in the $\mathcal{R}\square^{-2}\mathcal{R}$ model lead only to modest changes in the amplitude of the nonlinear velocity divergence power spectrum. In particular, at $a = 1.0$ ($a = 0.8$) the enhancement relative to ΛCDM is kept below $\approx 12\%$ ($\approx 10\%$) on all scales.

• The $\mathcal{R}\square^{-2}\mathcal{R}$ model possesses no screening mechanism to suppress the modifications to gravity on small scales. As a result, Solar System tests of gravity can be used to constrain the model. For example, the $\mathcal{R}\square^{-2}\mathcal{R}$ model predicts that $\dot{G}_{\mathrm{eff}}/G \approx 92 \times 10^{-13}\ \mathrm{yrs}^{-1}$, which is incompatible with the current bound from Lunar Laser Ranging experiments, $\dot{G}_{\mathrm{eff}}/G = (4 \pm 9) \times 10^{-13}\ \mathrm{yr}^{-1}$ [250]. The local time variation of G_{eff} follows from the background evolution of the auxiliary scalar field S, and it seems nontrivial to devise a mechanism that can suppress it around massive objects or in high-density regions [248, 340]. In this chapter, we focused only on a particular choice of cosmological parameters. As a result, it might be possible that certain parameter combinations can be made compatible with Solar System tests, whilst still being able to yield viable cosmological solutions. Nevertheless, it seems clear that these tests should be taken into account in future constraint studies, as they might have the potential to rule out these models observationally.

In conclusion, the $\mathcal{R}\square^{-2}\mathcal{R}$ model, despite having no ΛCDM limit for the dynamics of the background and gravitational interaction, exhibits changes of only a few percent in observables sensitive to the nonlinear growth of structure. Some of these effects are degenerate with baryonic mechanisms such as AGN feedback or galaxy bias, or even with massive neutrinos [3, 4, 200, 347]. This makes it challenging to distinguish this model from ΛCDM, but the precision of upcoming observational missions such as Euclid [348, 349], DESI [350] or LSST [351] should make this possible.

Chapter 7

Lensing by clusters and voids in modified lensing potentials

In this chapter, we focus on the lensing signal associated with galaxy clusters and cosmic voids in modified gravity theories that modify directly the lensing potential. This is a topic that has not been extensively investigated in the literature. The reason for this, we believe, is historical as many of the first modified gravity models to be compared to observations were models like $f(R)$ [52] or Dvali-Gabadadze-Porrati (DGP) [352] gravity, which do not modify the lensing potential directly through a modified Poisson equation. This is because, in these models, the amplitude of the fifth force vanishes for relativistic particles like photons, which means that any modifications to lensing arise through changes in the mass distribution, and not due to changes to the photon geodesic equation. Consequently, one expects that lensing observations can serve as stronger probes of modified gravity models that also modify directly the lensing potential. The Cubic Galileon and Nonlocal gravity models that we studied previously in this thesis are two such examples of models that modify lensing directly, and we take them as our working test cases in this chapter. Other models that also modify lensing directly include massive gravity [353, 354, 355, 356, 357, 358, 359], K-mouflage gravity [12, 58, 59, 60], and several other special cases of Horndeski's general model [144].

In a first part of this chapter, we focus on one possible consequence of modifications to the lensing potential, which is that they may introduce model-dependent systematics in the estimation of cluster masses from lensing. To investigate this, we model galaxy clusters as NFW haloes [286], and fit the predicted lensing convergence signal to the data obtained from weak and strong lensing observations for 19 X-ray selected clusters from the Cluster Lensing and Supernova Survey with the *Hubble Space Telescope* (CLASH) [137, 360, 361]. Our goal is to compare the resulting mass estimates to the values obtained assuming

ΛCDM. In most of the current data analysis, one often makes model-dependent assumptions which may lead to results that are biased towards the assumed models. For example, the analysis of Ref. [137] assumes a fiducial ΛCDM background to compute angular diameter distances. Assumptions like these must be identified and carefully assessed before using the observations to test alternative models. Given the subtle nature of some steps involved in the analysis of lensing data we shall pay special attention to them and explain how they can be taken into account.

In a second part of this chapter, we focus on lensing by cosmic voids, which (contrary to clusters) are the regions of the Universe where the density is the lowest, and hence, where one expects fifth force effects to be maximal (due to the weaker screening efficiency). We find voids in the simulations using a *watershed* based algorithm [362] and investigate the effects of the fifth force on the number of voids and on their density and force profiles. We also put forward a simple fitting formula that matches very well the void profiles found in the simulations for different variants of the modified gravity models, for different density tracer types (dark matter and haloes) and for a wide range of void sizes. The formula admits a closed expression (in terms of hypergeometric functions) for the mass within a given radius, which makes it convenient to use in force profile calculations and lensing studies. Our goal is to provide intuition about the potential of lensing by voids to test gravity outside the solar system. We do not attempt to make any observationally conclusive statement, but we do comment on a number of extra steps that need to be taken to compare our results with observations.

7.1   Lensing equations

In this section, we specify our notation and briefly describe the calculation of the relevant lensing quantities (see e.g. Refs. [363, 364, 365] for comprehensive reviews).

7.1.1   Cluster lensing basics

In our setup, we consider a set of source galaxies at redshift z_s, whose light gets deflected by a lens at z_d. We use D_d, D_s and D_{ds} to denote, respectively, the angular diameter distances between the observer and the lens, the observer and the sources, and the lens and the sources. In our calculations, we always assume that the lenses are spherically symmetric

and use the thin-lens approximation in which one neglects the size of the lens compared to the much larger values of D_d, D_s and D_{ds}. We also neglect the lensing distortions induced by foreground and background structures, compared to the lensing signal of the lens. In our notation, $r = \sqrt{x^2 + y^2}$ is a two-dimensional radial coordinate defined on the lens plane and with origin at the lens center (x and y are cartesian coordinates); l denotes the optical axis (line-of-sight) direction, perpendicular to the lens plane, and with origin also at the lens center; and $R = \sqrt{r^2 + l^2}$, is a three-dimensional radial coordinate with origin at the lens center.

Light rays coming from the sources are deflected at the lens position by an angle $\vec{\alpha}$, which is related to the true (unobserved) angular position, $\vec{\beta}$, and the observed one, $\vec{\theta}$, by

$$\vec{\beta} = \vec{\theta} - \vec{\alpha}(\vec{\theta}). \tag{7.1}$$

The local properties of the lensing signal are fully determined by spatial second derivatives of the scaled projected lensing potential of the lens, ψ, which is given by

$$\psi(\theta = r/D_d) = \frac{D_{ds}}{D_d D_s} \frac{2}{c^2} \int_{-D_d}^{D_{ds}} \Phi_{\text{len}}(r, l) \mathrm{d}l, \tag{7.2}$$

where c is the speed of light and $\Phi_{\text{len}} \equiv (\Phi + \Psi)/2$ is the total three-dimensional lensing potential. The Jacobian matrix of the lensing mapping of Eq. (7.1) is given by

$$\frac{\partial \vec{\beta}}{\partial \vec{\theta}}(\vec{\theta}) = \begin{bmatrix} 1 - \kappa - \gamma_1 & -\gamma_2 \\ -\gamma_2 & 1 - \kappa + \gamma_1 \end{bmatrix}, \tag{7.3}$$

where

$$\begin{aligned} \kappa(\theta) &= \frac{1}{2} \bar{\nabla}_\theta^2 \psi = \frac{1}{2} \left(\partial_{\theta_x}^2 + \partial_{\theta_y}^2 \right) \psi, \\ &= \frac{D_d^2}{2} \bar{\nabla}_r^2 \psi = \frac{D_d^2}{2} \left(\partial_x^2 + \partial_y^2 \right) \psi \end{aligned} \tag{7.4}$$

is the *lensing convergence*[1], and

$$\begin{aligned} \gamma_1 &= \frac{1}{2} \left(\partial_{\theta_x}^2 - \partial_{\theta_y}^2 \right) \psi, \\ \gamma_2 &= \partial_{\theta_x} \partial_{\theta_y} \psi, \end{aligned} \tag{7.5}$$

are the two components of the *complex lensing shear*, $|\gamma| = \sqrt{\gamma_1^2 + \gamma_2^2}$. The convergence is responsible for an isotropic focusing (or defocusing) of the light rays, whereas the shear field

---

[1] The overbar on the ∇ operator indicates that it is the two-dimensional Laplacian. Also, note that $r = D_d \theta$.

causes distortions in the shapes of the observed source galaxies. For spherically symmetric cases, the *tangential lensing shear* γ_t is given in terms of the convergence κ as [366]

$$\gamma_t = \overline{\kappa} - \kappa, \qquad \text{where} \qquad \overline{\kappa} = \frac{2}{r^2} \int_0^r y\kappa(y)\mathrm{d}y. \tag{7.6}$$

In lensing studies, one can split the analysis into the weak and strong lensing regimes. In the weak lensing regime, the directly observable quantity is the locally averaged complex ellipticity field in the lens plane, $\langle \epsilon \rangle$, which can be constructed from measurements of background galaxy shapes. At each point of the lens field, an average is taken over a number of nearby sources to smooth out the intrinsic ellipticity of the galaxies from that caused by the lens (see e.g. [364, 367, 368]). Observationally, the field $\langle \epsilon \rangle$ is directly related to the *reduced shear*, g, as $\langle \epsilon \rangle \longleftrightarrow g \equiv \gamma/(1 - \kappa)$. The strong lensing regime takes place in regions of high mass concentration (e.g. in the inner regions of galaxy clusters). There, the lensing quantities κ and γ become large and the equations become nonlinear. As a consequence, highly distorted images like giant arcs or arclets and multiple images of the same background source can form. This happens close to the location of the critical curves of the lens, which are defined as the set of points on the lens plane where the lensing matrix, Eq. (7.3), becomes singular, i.e.,

$$\det\left(\partial\vec{\beta}/\partial\vec{\theta}\right) = (1 - \kappa)^2 - \gamma^2 = 0. \tag{7.7}$$

Observationally, one identifies multiple images and giant-arcs to infer the position and shape of the critical lines. Then, given a theoretical prediction for κ and γ, one can check if $\det\left(\partial\vec{\beta}/\partial\vec{\theta}\right)$ vanishes at the location of the critical lines.

7.1.2 Convergence in ΛCDM

In ΛCDM, in the absence of anisotropic stress, $\Phi = \Psi$, and as a result, the lensing potential is equal to the dynamical potential, $\Phi_{\mathrm{len}} = (\Phi + \Psi)/2 = \Phi = \Psi$. Both satisfy the Poisson equation, $\nabla^2_{(r,l)}\Phi(r, l) = 4\pi G\rho(r, l)$, where $\rho(r, l)$ is the three-dimensional density distribution. The lensing convergence is obtained by integrating the Poisson equation along the line of sight, l. After some straightforward algebra, and by making use of the thin-lens approximation and Eqs. (7.2) and (7.4), it is possible to show that [363, 364, 365]

$$\kappa(\theta = r/D_d) = \frac{4\pi G}{c^2}\frac{D_{ds}D_d}{D_s}\Sigma(\theta = r/D_d) \equiv \frac{\Sigma(\theta = r/D_d)}{\Sigma_c}, \tag{7.8}$$

where $\Sigma(r) = \int \rho(r,l)\mathrm{d}l$ is the surface mass density of the lens and $\Sigma_c = c^2 D_s / (4\pi G D_{ds} D_d)$ is called the critical surface mass density for lensing. Once κ is determined, then the lensing shear can be obtained from it by making use of Eq. (7.6).

7.1.3 Convergence in Nonlocal and Cubic Galileon Gravity

As in ΛCDM, in the Nonlocal and Cubic Galileon models one also has that $\Phi = \Psi$ (in the absence of anisotropic stress). Hence, the calculation of the lensing quantities in these two models remains as in ΛCDM, apart from (i) the modified background expansion history, which enters in the calculation of the angular diameter distances; and (ii) the modified lensing potential, which enters in the calculation of the lensing convergence.

In the case of the Nonlocal model, the modified lensing convergence is obtained by replacing G in Eq. (7.8) by the effective gravitational strength G_{eff} of Eq. (6.22). In the case of the Cubic Galileon model, one makes use of the spherically symmetric formulae presented in Sec. 5.1.2 to compute $\nabla^2 \Phi_{\mathrm{len}} \to \Phi_{\mathrm{len},RR} + 2\frac{\Phi_{\mathrm{len},R}}{R}$ (which can be done analytically), which is then numerically integrated along the line-of-sight to determine κ. As in ΛCDM, γ_t can be determined from κ via Eq. (7.6), for both these models.

The background quantities of the Cubic Galileon model are computed using the tracker solution presented in Sec. 2.3. For the Nonlocal model, the background quantities have to be solved numerically as in Chapter 6.

7.2 Galaxy cluster lensing masses

In this section, we describe our methodology to estimate the lensing masses of the 19 CLASH survey galaxy clusters [137]. We shall pay particular attention to a number of subtleties that need to be accounted for to self-consistently compare the data with the predictions from the alternative models studied here.

7.2.1 Cluster density profiles

In order to compute the lensing convergence we need to specify the density profile of the galaxy clusters, which we model as dark matter haloes with NFW density profiles. The relevant NFW formulae have already been shown in Sec. 5.2.4. Here, we simply note that the surface mass density of a NFW halo admits an analytical solution given by [363, 366,

369]

$$\Sigma_{\rm NFW}(r = D_d\theta) = \int \rho_{\rm NFW}(r,l){\rm d}l =$$ (7.9)

$$= \begin{cases} \frac{2r_s\rho_s}{x^2-1}\left(1 - \frac{2}{\sqrt{1-x^2}}{\rm arctanh}\left[\sqrt{\frac{1-x}{1+x}}\right]\right) & x < 1 \\ \frac{2r_s\rho_s}{3} & x = 1 \\ \frac{2r_s\rho_s}{x^2-1}\left(1 - \frac{2}{\sqrt{x^2-1}}{\rm arctan}\left[\sqrt{\frac{x-1}{1+x}}\right]\right) & x > 1 \end{cases}$$

where $x = r/r_s$.

7.2.2 Fitting methodology

We use the radially-binned lensing convergence profiles obtained for 19 X-ray selected galaxy clusters from CLASH in Ref. [137]. There, the analysis was performed with a numerical algorithm called `SaWLens` [370], which iteratively reconstructs the lensing potential for each cluster on a two-dimensional grid that covers the cluster field. The analysis is purely non-parametric, i.e., it makes no assumptions about the mass distribution of the cluster. We refer the reader to Refs. [137, 370, 371] for the details about how `SaWLens` operates. For the discussion here, what is important to note is that what `SawLens` actually reconstructs is the lensing potential scaled to a source redshift of infinity, $\psi_\infty = \psi(z_s = \infty)$, by assuming a fiducial cosmological model. We use κ_∞ to denote the lensing convergence associated with ψ_∞, which is related to the convergence at the true source redshift, z_s, via

$$\kappa_{z_s} = Z^{\rm fid}(z_d, z_s)\kappa_\infty,$$ (7.10)

where we use the subscript z_s to emphasize that κ_{z_s} corresponds to the convergence associated with z_s. The function $Z \equiv Z(z_d, z_s)$ *transports* the convergence from a source redshift of infinity to the source redshift that corresponds to the galaxies on each `SaWLens` grid cell/pixel (we use the words cell and pixel interchangeably). It is given by

$$Z^{\rm fid}(z_d, z_s) = \frac{D_{s,\infty}^{\rm fid} D_{ds}^{\rm fid}}{D_{ds,\infty}^{\rm fid} D_s^{\rm fid}},$$ (7.11)

where the superscript $^{\rm fid}$ indicates angular diameter distances that are calculated assuming the fiducial background cosmology and the subscript $_\infty$ means that the calculation assumes that $z_s = \infty$. In the reconstruction process of Ref. [137], the fiducial cosmology is a ΛCDM model with $\Omega_{m0} = 0.27$. From hereon, we use $\kappa_\infty^{\rm fid}$ to denote the convergence profiles

obtained in this way, where the superscript $^{\text{fid}}$ makes it explicit that the data is linked to the fiducial model. It is therefore important to investigate the extent to which the $\kappa_\infty^{\text{fid}}$ profiles can be used in studies of alternative cosmologies.

Consider the case that we wish to estimate the lensing masses of the CLASH clusters in a model with a cosmological background that is different from the fiducial model originally used to analyse the observations in Ref. [137]. In principle, we could suitably modify the `SaWLens` algorithm to reconstruct the convergence maps in the alternative model, $\kappa_\infty^{\text{alt}}$, instead of $\kappa_\infty^{\text{fid}}$. However, this would not be practical as it would imply rerunning the entire analysis pipeline for different background cosmologies. A more economical strategy is to note that the two convergence maps, $\kappa_\infty^{\text{fid}}$ and $\kappa_\infty^{\text{alt}}$, can be related by

$$Z^{\text{fid}}(z_d, z_s)\kappa_\infty^{\text{fid}} = Z^{\text{alt}}(z_d, z_s)\kappa_\infty^{\text{alt}}, \tag{7.12}$$

where Z^{alt} is defined as in Eq. (7.11) but with the distances calculated in any alternative, and not the fiducial, cosmology. The above equation holds (up to a correction that we discuss in the next subsection) since both $Z^{\text{fid}}\kappa_\infty^{\text{fid}}$ and $Z^{\text{alt}}\kappa_\infty^{\text{alt}}$ correspond to κ_{z_s}, i.e., the convergence at the true source redshift [2]. Using the above equation, the radially binned convergence profiles obtained using the fiducial cosmology in Ref. [137], $\kappa_\infty^{\text{fid}}(\theta)$, can be directly compared to the prediction of the alternative model $\kappa_\infty^{\text{alt}}$, provided the latter is multiplied by the factor $Z^{\text{alt}}(z_d, z_s)/Z^{\text{fid}}(z_d, z_s)$. This is the approach that we adopt here. Specifically, we aim to obtain constraints on M_{200} and c_{200} in non-fiducial backgrounds by minimizing the χ^2 quantity

$$\chi^2 = \vec{V}\mathcal{C}_\kappa^{-1}\vec{V}, \tag{7.13}$$

where

$$\vec{V_i} = \kappa_{\infty,i}^{\text{fid}} - \Upsilon\kappa_\infty^{\text{alt}}(M_{200}, c_{200}, \theta_i), \tag{7.14}$$

is the i-th entry of the vector $\vec{V}$; $\kappa_{\infty,i}^{\text{fid}}$ is the reconstructed lensing convergence in the i-th radial bin, θ_i; $\mathcal{C}_\kappa$ is the covariance matrix of the radially binned data [3]; and for brevity of

---

[2]For example, for ΛCDM with an alternative background and for fixed surface mass density, for simplicity, Eq. (7.12) becomes $\Sigma(\theta)/\Sigma_c^{\text{alt}} = \Sigma(\theta)/\Sigma_c^{\text{fid}} \longrightarrow \Sigma_c^{\text{alt}} = \Sigma_c^{\text{fid}}$.

[3]The bootstrap realizations used to derive the covariance matrices in Ref. [137] also make use of the fiducial cosmological background. Here, we use the errors as obtained for the fiducial cosmology and do not attempt to estimate the dependence of the covariance matrix on the assumed cosmology. This does not alter our conclusions as this choice only affects the precise size of the confidence intervals, without introducing any important systematics.
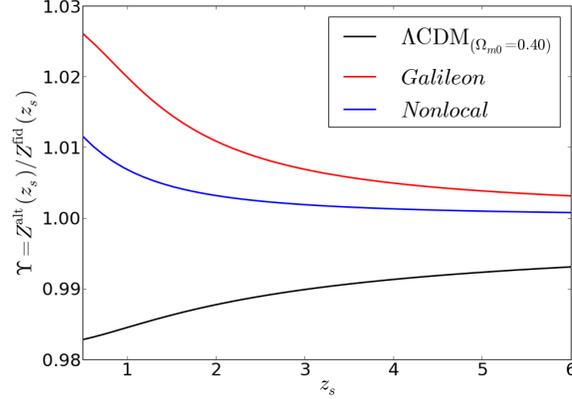
Figure 7.1: Dependence of the factor $\Upsilon = Z^{\mathrm{alt}}(z_d, z_s)/Z^{\mathrm{fid}}(z_d, z_s)$, Eq. (7.15), on the source redshift z_s for a ΛCDM model with $\Omega_{m0} = 0.4$ (black), Galileon gravity (red) and Nonlocal gravity (blue). The cosmological background of these models is different from the fiducial ΛCDM model with $\Omega_{m0} = 0.27$ used by Ref. [137]. In this figure, $z_d = 0.35$, which is typical for the CLASH clusters.

notation, we introduce the *scaling factor*

$$\Upsilon(z_d, z_s) = \frac{Z^{\mathrm{alt}}(z_d, z_s)}{Z^{\mathrm{fid}}(z_d, z_s)}. \tag{7.15}$$

Although Ω_{m0} is a parameter that enters the calculation of the lensing convergence, we have checked that its impact is very small compared to the size of the effects of M_{200} and c_{200}. In other words, assuming a particular value for Ω_{m0} does not introduce any significant biases in the cluster mass and concentration estimates (see Ref. [9] for more details). In our cluster results below, we fix the cosmological matter density to be $\Omega_{m0} = 0.27$, for all our models. In this way, the ΛCDM model becomes the fiducial one used in Ref. [137].

The validity of Eq. (7.12) and the choice of source redshifts

As discussed above, $\kappa_\infty^{\mathrm{fid}}$ is reconstructed by applying the transformation of Eq. (7.10) in each cell of the SaWLens grid that covers the cluster field. In this process, the value of z_s is determined by the redshift of the galaxies used to measure the ellipticity field at that pixel, or by the redshift of the galaxies associated with a given multiple image system. On the other hand, our methodology is based on Eq. (7.12), in which one scales the lensing quantities from $z_s = \infty$ to a source redshift z_s, but neglects the redshift distribution of the background lensed galaxies. The validity of Eq. (7.12) then becomes linked to the impact

of the spread of the redshift distribution of the source galaxies across each cluster field. For the CLASH clusters analysed in Ref. [137], the redshift distribution of the background galaxies is manifest in four main aspects:

(i) in the weak lensing regime, different ellipticity pixels are associated with different source redshifts since the shapes are measured using different galaxies across the cluster field;

(ii) related to the above, the ellipticity of each pixel results from a local average of neighbouring galaxy shapes, which can have different redshifts;

(iii) the ellipticity field used by `SaWLens` is a combined catalog of measurements from space- and ground-based telescopes, which probe different galaxy redshift ranges. The measurements of these two catalogs (see Ref. [137]) are corrected for this, but assuming the fiducial cosmology;

(iv) in the strong lensing regime, each pixel is associated with the redshift of the multiple images contained within it, which can be different in different multiple image systems for the same cluster and also different from the galaxy populations used in the weak lensing measurements.

To get a feeling for the size of our approximation, we show in Fig. 7.1 the z_s dependence of the factor Υ (Eq. (7.15)) for the Galileon (red) and Nonlocal (blue) models, and a ΛCDM model with $\Omega_{m0} = 0.4$ (black). The quantity Υ encapsulates all of the dependence on z_s in the χ^2 minimization used to estimate the cluster parameters. For illustrative purposes, we choose $z_d = 0.35$. This corresponds roughly to the mean redshift of the CLASH clusters, although the exact value is not important for the discussion here. We note that what is relevant is the slope of the curves and not their absolute value. Consider for the sake of argument an extreme case where the source galaxies are distributed between $z_s = [1, 3]$, but that we choose to use $z_s = 2$ in Eq. (7.15). Focusing on the case of the Galileon model, we have that $\Upsilon(z_s = 1) \approx 1.019$, $\Upsilon(z_s = 2) \approx 1.011$ and $\Upsilon(z_s = 3) \approx 1.007$. These values differ by no more than $\approx 1\%$, and hence our choice of z_s should not lead to serious biases in the results. The error would be even smaller in the Nonlocal model or ΛCDM with $\Omega_{m0} = 0.40$, since in these cases the $\Upsilon(z_s)$ curves are shallower than in the Galileon case. The error of neglecting the redshift distribution becomes smaller for higher values of z_s, for which the curves in Fig. 7.1 become visibly flatter. This is relevant for strongly lensed systems, which tend to be associated with galaxies at higher redshifts.

In cluster weak lensing studies, it is common to determine an effective source galaxy redshift, $z_{s,\text{eff}}$, defined as

$$\frac{D_{ds}}{D_s}(z_{s,\text{eff}}) = \left\langle \frac{D_{ds}}{D_s} \right\rangle, \tag{7.16}$$

where $\langle D_{ds}/D_s \rangle$ is an average over all source galaxies. Reference [137] quotes $z_{s,\text{eff}}$ values for the CLASH clusters (see also Ref. [361]). For example, Abell 209 ($z_d = 0.206$) has $\langle D_{ds}/D_s \rangle = 0.75 \pm 0.04$ (1σ), which corresponds to $z_{s,\text{eff}} = 1.03^{+0.25}_{-0.15}$ (this estimate comes from Table 3 of Ref. [361]). This uncertainty on $z_{s,\text{eff}}$ is much smaller than our rather extreme example above ($z_s = 2 \pm 1$), which further convinces us that the approximation of Eq. (7.12) is a good one. For completeness, we note that the determination of these values of $z_{s,\text{eff}}$ involves knowledge of the background cosmology, and hence they are also model dependent. However, again taking Abell 209 as an example, in the Galileon model one has $D_{ds}/D_s(z_{s,\text{eff}} = 1.03) = 0.76$, which is well within the uncertainty (± 0.04) quoted above for this cluster. We can therefore neglect this model dependency and use the values of $z_{s,\text{eff}}$ listed in Ref. [137]. In particular, in our χ^2 minimization, we shall use the effective source redshift values found for the background sources of the ground-based ellipticity measurements [137].

To summarize this discussion, although Eq. (7.12) is only approximate, the results shown in Fig. 7.1 suggest that our results are insensitive to the exact choice of z_s.

7.2.3   Other subtleties in using cluster lensing data to test gravity

Before proceeding further into estimating the CLASH cluster masses in modified gravity models, we discuss some other subtle issues that may arise when combining current lensing modelling techniques with modified gravity. Although it turns out these other issues do not play a direct role in our main results, we believe such a discussion is instructive and leads to a clearer and broader understanding of the results of this and other work in the literature.

Parametric vs. nonparametric analysis

The non-parametric reconstruction of the lensing potential used in this chapter builds solely upon the observed lensing constraints, without making any assumptions about the

mass distribution of the cluster. Such a model-independent [4] method is particularly well suited to modified gravity studies. Consider the alternative scenario of a parametric approach. In this case one starts by making an *Ansatz* about the mass distribution in the cluster. Typically, this can involve describing the main dark matter distribution using a single (or more in the case of mergers) NFW profile. Then, one could also model substructure by identifying the position of the most massive cluster galaxies and assigning them a given density profile. (see e.g. Refs. [372, 373, 374, 375, 376, 377, 378, 379, 380, 381, 382, 383, 384, 385, 386, 387]). The free parameters of such a mass model are then iterated over until the lensing constraints are satisfied. In the context of modified gravity there are at least two subtle issues associated with such a parametric lensing analysis. First, in order to compute the lensing effects due to the postulated mass distribution one must assume a theory of gravity: for the same mass distribution, different models of gravity could induce different lensing effects. Parametric methods are therefore biased towards the assumed theory of gravity. Second, the lensing properties of a given point in the cluster field are determined by the sum of the lensing signal predicted by each element of the mass model (main halo plus the substructures). This superposition is valid in GR (which is linear in the Newtonian limit), but not necessarily in alternative (typically nonlinear) models of gravity. These issues can be circumvented if one reconstructs directly the lensing potential and its derivatives but not the mass distribution. It is for this reason that we choose to use the `SaWLens` results of Ref. [137] in our analysis.

Interpretation of stacked cluster lensing profiles

To overcome systematic effects due to intervening structure, cluster substructure and cluster asphericity, it has become common to build average (stacked) lensing profiles by using cluster lensing data from independent lines of sight [383, 384, 388]. The averaged profiles are then fitted again to infer an average mass and concentration that characterizes the stack. From a conceptual point of view, the same procedure can be applied assuming modified gravity models. Here, we comment that the interpretation of the stacked data may be somewhat more complex due to the effects of modified gravity. Consider for simplicity the stacking of the convergence radial profiles of N clusters at redshifts $z_{1..N}$ with mass and concentration values $M_{1..N}$ and $c_{1..N}$, respectively. The background galaxies can be as-

---

[4]Apart from the issue of the fiducial cosmological background model discussed above.
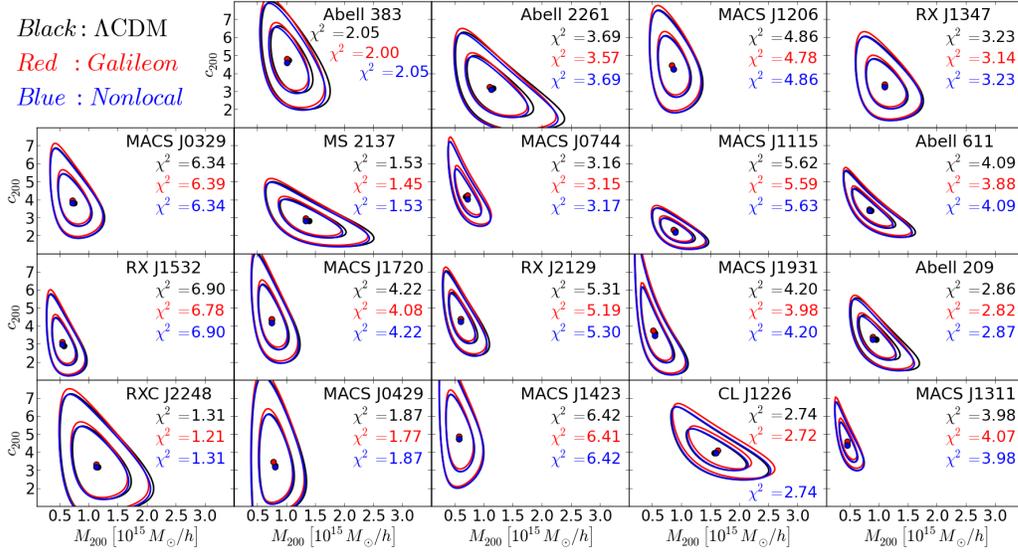
Figure 7.2: Two-dimensional 68% and 95% confidence limits on the $c_{200} - M_{200}$ plane for all of the CLASH clusters assuming ΛCDM (black), Galileon gravity (red) and Nonlocal gravity (blue). The position of the best-fitting points is marked by the dots, and their respective χ^2 values are shown in each panel.

sumed to lie at the same source redshift. For instance, Ref. [383] stacks four massive clusters by co-adding (with some weighting) their profiles. The resulting mean profile is then re-fitted to determine a mean mass and concentration of the stack. Now consider fitting such a stack to two gravity models which display different time evolution for an unscreened gravitational strength. For these two models, clusters located at different redshifts would contribute differently to the mean mass/concentration estimate since their lensing signal is amplified differently. For such a scenario, an interesting analysis would be to split the stack into smaller ones binned by cluster redshift and check for differences in the resulting mean mass/concentration of the smaller stacks. The situation becomes even more complex (but interesting) in models with screening, due to its scale-dependence, whose efficiency is in general redshift dependent as well.

We stress that the above issues do not pose a serious problem to using stacked data to test modified gravity, but simply that the extra physics can enrich the interpretation of the results. In this chapter, however, we shall not be concerned with these issues since we fit each of the CLASH clusters individually.
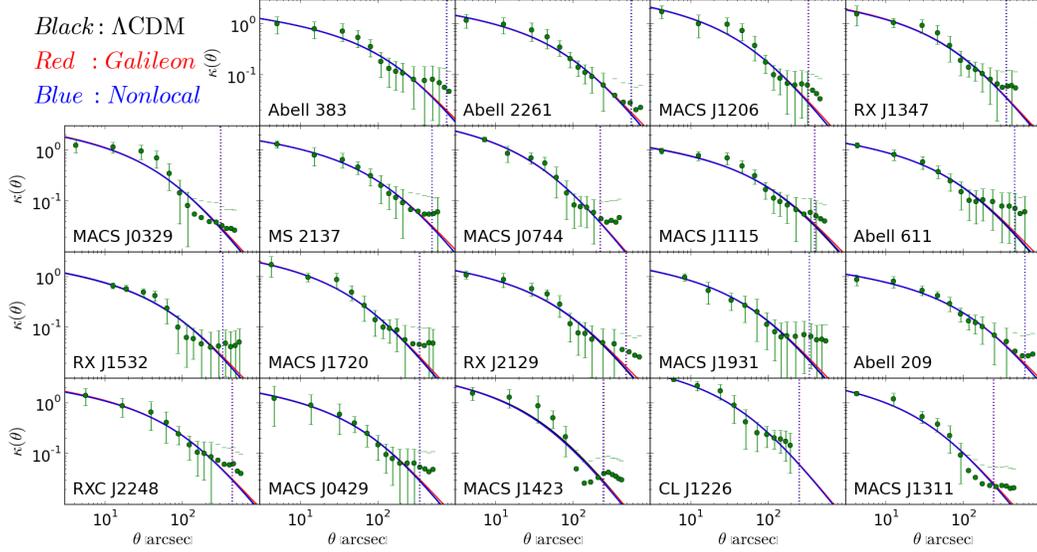
Figure 7.3: Best-fitting lensing convergence profiles, $\kappa(\theta) = \Upsilon \kappa_\infty$, obtained for all of the CLASH clusters assuming ΛCDM (black), Galileon gravity (red) and Nonlocal gravity (blue) . The green dots are the radially binned data as described in Ref. [137] and the errorbars are the square root of the diagonal entries of the covariance matrix of the data. To guide the eye, the dotted vertical lines indicate the inferred values of R_{200}, which are barely distinguishable for the three models.

7.2.4 Lensing mass estimates in the modified gravity models

Figure 7.2 shows the constraints on the c_{200}-M_{200} plane obtained for each of the CLASH clusters in ΛCDM (black), Galileon (red) and Nonlocal gravity (blue) cosmologies. The dots indicate the position of the best-fitting values. The best-fitting lensing convergence profiles are shown in Fig. 7.3 (what is shown is $\Upsilon \kappa_\infty(\theta)$). The concentration-mass relation of the CLASH clusters for the three models is shown in Fig. 7.4, together with results from N-body simulations [7, 8, 389]. First, we note that our cluster mass and concentration estimates for ΛCDM are in agreement with those obtained in Ref. [137]. Second, these three figures all show that the constraints on the cluster parameters are, within errorbars, the same in the three cosmological models. Although there are tiny differences in the resulting best-fitting values of M_{200} and c_{200} for the three models ($\lesssim 5\%$), they all lie well within the 1σ limits (whose precision varies within $\sim 50\% - 80\%$). The shapes of the contours are also remarkably similar and the goodness-of-fit is essentially the same in all models, as can

be seen by comparing the respective χ^2 values in Fig. 7.2. In Fig. 7.3, one notes that for almost all of the clusters, the best-fitting convergence profiles underpredict the data points at large angular scales (although well within the errorbars). However, close to the edge of the clusters, the contribution from the surrounding large scale structure may have a non-negligible impact. This can partly explain why the data points tend to go up at large scales, as investigated, for instance, in Ref. [390].

The shaded bands in Fig. 7.4 show the best-fitting mean concentration-mass relations found in N-body simulations for the ΛCDM (gray) model in Ref. [389] [5], the Cubic Galileon model (red) in Chapter 5 and the Nonlocal model (blue) in Chapter 6. In these bands, the lower and upper bounds correspond, respectively, to the relations at $z = 0.666$ ($a = 0.60$) and $z = 0$ ($a = 1$) (this redshift range is approximately that of the CLASH clusters). Figure 7.4 shows that there is good agreement between the simulation results and the concentration/mass estimates of the CLASH clusters in the three models of gravity. However, there are a number of issues that prevent a direct comparison between the simulation results and the estimated concentration and mass values. First, the shaded bands of the Galileon and Nonlocal models in Fig. 7.4 have been extrapolated to masses larger than the mass range used to find the best-fitting concentration mass relations from the simulations. Second, the concentration mass relation was fitted using all haloes, without applying any selection criteria to consider only relaxed ones [288]. This may be particularly relevant for the CLASH clusters, which are characterized by regular X-ray surface brightness morphologies [360], and are therefore expected to be relaxed and close to virial equilibrium (see also Refs. [391, 392] for a recent discussion on the impact of baryonic processes in the density profiles of clusters). Third, the concentration-mass relation in the simulations was obtained by fitting NFW profiles to the three-dimensional spherically averaged mass distribution of the haloes, whereas the symbols in Fig. 7.4 are the values obtained by also assuming spherical symmetry, but fitting to two-dimensional (projected) lensing convergence profiles (see e.g. Sec.6.2 of Ref. [137] for an analysis of the impact of this *projection bias* in the CLASH sample). Finally, the upper and lower bounds of the bands correspond to the mean relation found in the simulations, but the intrinsic scatter around the mean concentration-mass relation should also be taken into account. Nevertheless, to guide the eye, we opted to keep

---

[5]See Fig. 9 of Ref. [137] for the comparison of the CLASH c_{200}-M_{200} relation in ΛCDM with other relations in the literature.
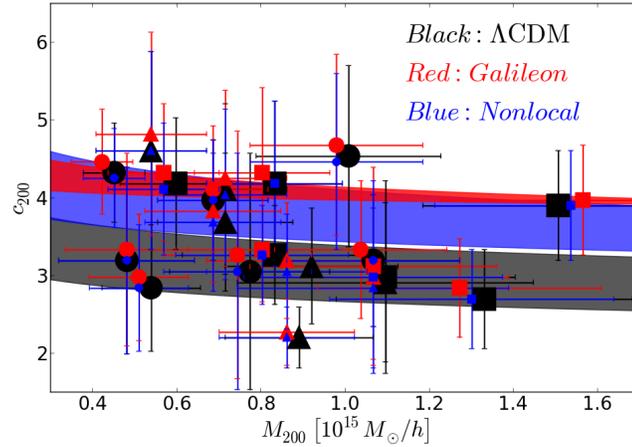
Figure 7.4: Concentration-mass relation of the CLASH clusters assuming ΛCDM (black), Galileon gravity (red) and Nonlocal gravity (blue). The errorbars indicate the marginalized 68% confidence limits. We use different symbols for different clusters to facilitate the identification of which cluster is which across the three models. The shaded bands indicate the mean concentration-mass relations from N-body simulations between $z = 0.66$ (lower bound) and $z = 0$ (upper bound) found for ΛCDM (gray) in Ref. [389], Cubic Galileon model (red) in Chapter 5 and Nonlocal model (blue) in Chapter 6.

the simulation results in Fig. 7.4, but advise that further work is needed before performing a more thorough comparison (see the analysis of Ref. [393] in ΛCDM models for an illustration of the steps to follow).

The left panel of Fig. 7.5 shows the best-fitting lensing convergence for all of the CLASH clusters in the Galileon (red) and Nonlocal (blue) cosmologies, plotted as the respective difference to the best-fitting profiles in ΛCDM. As expected from the above results, on the scales that are probed by the CLASH data, $\theta \lesssim 500 - 700$ arcsec, the three models are in very good agreement. In the case of the Galileon model, this is because the screening is very effective on these scales inside R_{200} (Ref. [128] finds a similar screening efficiency inside R_{200} for DGP gravity, which employs also the Vainshtein mechanism). This can be noted by comparing the enhancement in the amplitude of κ on larger scales, where the screening becomes less efficient. In the case of the Nonlocal model, although the modifications to the gravitational strength are not screened, they are not strong enough to have a significant impact on the lensing convergence profiles. *We therefore conclude that, for the case of the CLASH clusters analysed here, the impact of modifying the lensing gravitational potential*

according to Cubic Galileon or Nonlocal gravity is completely negligible in the estimation of their lensing masses.

7.2.5   The connection with tests of gravity

Before proceeding to the analysis of the lensing signal by cosmic voids, we briefly discuss the link between our cluster lensing results for the Galileon and Nonlocal models with observational tests originally designed for other models.

Dynamical masses from the phase-space density around massive clusters

Recently, the authors of Refs. [125, 126, 394, 395] have proposed methods to test the law of gravity on Mpc scales by using information from the galaxy velocity field in the infall regions around massive clusters (see also Ref. [11]). These techniques were designed with models of gravity that modify the dynamical potential (i.e. that felt by nonrelativistic objects like galaxies), but do not modify the lensing potential (i.e. that felt by relativistic particles like photons). Popular models such as $f(R)$ and DGP gravity fall in the above category, and as such, the lensing mass estimates, M_{len}, for these models would automatically be the same as in GR. On the other hand, the velocity dispersion of surrounding galaxies as they fall towards the clusters would be affected by the modifications to gravity. Therefore, if one would interpret these observations assuming GR, then one would infer dynamical masses, M_{dyn}, which are different from those estimated using lensing. A mismatch in the estimates of the lensing and dynamical masses would therefore be a smoking gun for modified gravity [105, 396, 397] (see, however, Ref. [398] for a discussion of how complications associated with assembly bias could affect these tests).

The merit of the test of gravity described above becomes less clear when applied to models that also modify the lensing potential. Consider, for simplicity, a model that boosts the dynamical and lensing potential by the same constant factor, $\alpha > 1$, i.e. $\Phi_{\mathrm{dyn}} = \Phi_{\mathrm{len}} \sim \alpha \Phi^{\mathrm{GR}}$. In such a model, the mass of a cluster inferred from the surrounding galaxy velocity field would be biased low w.r.t. GR. This is because, due to the enhanced gravitational strength felt by the galaxies, the cluster does not need to be as massive as in GR to accelerate the galaxies by the same amount. Following the same reasoning, the lensing mass estimates would also tend to be biased low compared to GR: due to the fifth force felt by the photons, the cluster can be less massive to induce lensing effects of the same magnitude. In such a

model, both M_{dyn} and M_{len} shift in the same direction. This therefore makes it harder to tell the two values apart and hence, harder to detect a signature of modified gravity.

The Galileon model also modifies the lensing potential, but adds complexity to the case described above in the sense that the modifications to gravity are scale dependent with screening inside the cluster radius. Just outside the cluster radius, the screening becomes less efficient and the fifth force significantly boosts the lensing convergence, as shown in Fig. 9. Although these larger scales are not accurately probed by the current cluster lensing data, they correspond roughly to the regions associated with galaxy infall, $2\mathrm{Mpc}/h \lesssim r \lesssim 20\mathrm{Mpc}/h$. For these radial scales, the right panel of Fig. 9 shows that the total force profile which surrounds the CLASH clusters in a Galileon cosmology can be up to $10\% - 40\%$ higher than in ΛCDM. As a result, galaxies located at these distances from the cluster center should feel the boost in the total force, which should translate into their velocity distribution. On these scales, both the lensing and dynamical masses would be different in a Galileon cosmology compared to ΛCDM. Inside the cluster radius, on the scales that are probed by the CLASH data, $\theta \lesssim 500 - 700$ arcsec, the left panel of Fig. 9 shows that the differences in the convergence profiles compared to those in ΛCDM are small enough for the mass estimates to be almost the same in the two models. Therefore, inside the cluster radius, this leaves us with a similar picture to that in $f(R)$ or DGP models: the lensing mass estimates are not affected by the modifications to gravity, but dynamical mass estimates using infalling galaxies are changed. We therefore conclude that, *despite it being a model that modifies the lensing potential, the fact that dynamical and lensing mass estimates are sensitive to radial scales of different screening efficiency allows the Cubic Galileon model to be tested by the methods proposed in Refs.* [125, 126, 394].

In the case of the Nonlocal model, although the lensing mass estimates are also practically the same as in ΛCDM, the enhancement of the force profile on scales $2\mathrm{Mpc}/h \lesssim r \lesssim 20\mathrm{Mpc}/h$ is kept below the $\sim 5\%$ level. This makes it more challenging for this model to be tested by these methods.

Galaxy-galaxy lensing

The left panel of Fig. 7.5 also shows that although the convergence profiles are very close in the three models for $R \lesssim R_{200}$, they can be visibly higher (by $\sim 20 - 80\%$) in the Galileon model on larger scales. The enhanced lensing signal outside dark matter haloes in Galileon-

like models has been analysed by Refs. [399, 400], but in the context of theories that emerge from massive gravity scenarios [353, 354, 355, 356, 357, 358]. In particular, the authors investigate the possibility of such a signal being detected in galaxy-galaxy lensing observations (see e.g. Ref. [401]). The latter can be measured by cross-correlating the position of foreground galaxies (the lenses) with their background shear field. Our results in Fig. 7.5 are in good qualitative agreement with the solutions explored in Refs. [399, 400]. For instance, we also find the appearence of a bump in the relative difference to ΛCDM, which we checked occurs at $\sim 10R_{200}$. Quantitatively, the comparisons become less straightforward. On the one hand, in this chapter we show the results for cluster mass scales between $\approx [0.5, 1.5] \times 10^{15} M_{\odot}/h$, which are higher than the galaxy group mass scales ($10^{13} - 10^{14} M_{\odot}/h$) probed in Refs. [399, 400]. Moreover, our models also differ at the level of the cosmological background, exact screening efficiency and time evolution of the linearized effective gravitational strength. Nevertheless, it seems reasonable to expect that the predictions of the Galileon model studied here are also likely to be scrutinized by galaxy-galaxy lensing observations. A more detailed investigation of the model predictions for galaxy-galaxy lensing is beyond the scope of the analysis here.

In the case of Nonlocal gravity, the modifications to the lensing convergence are small ($\lesssim 5\%$) on all scales, which makes it much harder to distinguish from standard ΛCDM with galaxy-galaxy lensing data.

Weak lensing on larger scales

The picture depicted in the left panel of Fig.7.5 that the lensing signal gets significantly enhanced on larger scales in the Galileon model should, in principle, also have an impact on the lensing of CMB photons. Indeed, in Chapters 2 and 3 we have seen that the amplitude of the CMB lensing potential angular power spectrum, $C_l^{\psi\psi}$, is very sensitive to the modifications to gravity in the Galileon model. To the best of our knowledge, the effect of the Nonlocal model on the CMB lensing potential power spectrum has never been investigated in detail. However, since the modifications to gravity on large scales are not as strong as in the Galileon model, then the effects on the amplitude of $C_l^{\psi\psi}$ should be less pronounced. By the same reasoning the weak lensing cosmic shear power spectrum should also be sensitive to the modifications to gravity in the Galileon model, but less so in the Nonlocal case. Again to the best of our knowledge, cosmic shear data, such as that gathered by the
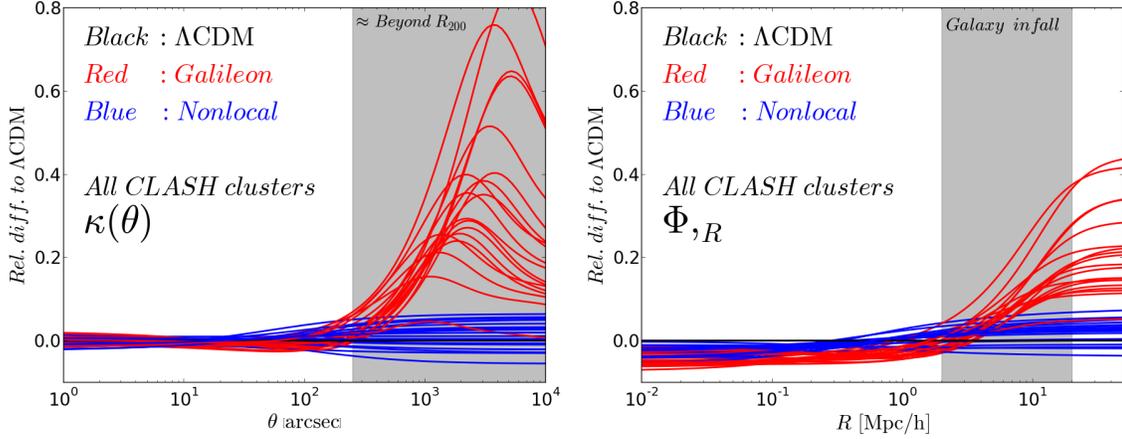
Figure 7.5: (Left) Best-fitting lensing convergence profiles, $\kappa(\theta) = \Upsilon\kappa_\infty$, for the all of the CLASH clusters in the Galileon (red) and Nonlocal (blue) gravity models, plotted as the difference relative to the best-fitting profiles in ΛCDM (black). To guide the eye, the shaded band represents approximately the regions that lie beyond R_{200} for all clusters. (Right) Same as the left panel, but for the total force profile $\Phi_{,R}$. The shaded band encloses the scales $2\mathrm{Mpc}/h \lesssim R \lesssim 20\mathrm{Mpc}/h$ which are approximately those associated with the infall of surrounding galaxies.

CFHTLens Survey [20], have never been used in direct tests of the models studied here, although Refs. [87, 97, 402] have used these data to constrain general parametrizations of modified gravity.

7.3 Weak-lensing by voids

We now turn to the discussion associated with the lensing signal caused by voids in the Cubic Galileon and Nonlocal gravity models. In this section, we make use of the following formula to describe the void density contrast profiles found in the simulations of these two models

$$\delta(R' = R/R_v) = \delta_v \frac{1 - (R'/s_1)^\alpha}{1 + (R'/s_2)^\beta}, \qquad (7.17)$$

were R_v is the void radius and δ_v, α, β, s_1 and s_2 are fitting parameters. Figure 7.6 shows the impact that each of the five parameters of Eq. (7.17) has on the density profiles and on the associated lensing signal (see Sec. 7.3.5 for the meaning of $\Delta\Sigma$ in Fig. 7.6). In Sec. 7.3.3, we shall see that this formula provides a very good fit to the void density profiles found in
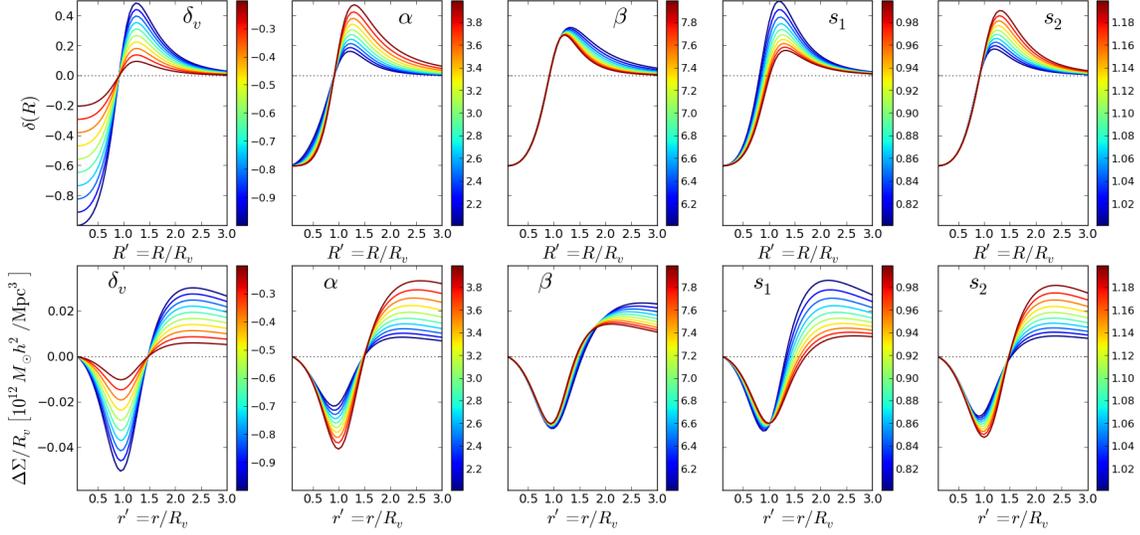
Figure 7.6: Impact of each of the parameters of the void density contrast formula of Eq. 7.17 (upper panels). The bottom panels show the respective lensing signal $\Delta\Sigma$. The curves are colored by the values of the parameter that is varying in each panel (from left to right, these are, δ_v, α, β, s_1 and s_2, respectively). The parameter values are indicated by the color bar at the right of each panel. When one parameter varies, the others are held fixed at their base values which are $(\delta_v, \alpha, \beta, s_1, s_2) = (-0.6, 3, 7, 0.9, 1.1)$. The calculation of the lensing signal was performed assuming GR.

the N-body simulations. The mass perturbation, $\delta M(< R) = 4\pi\bar{\rho}_m \int_0^R \delta(x) x^2 \mathrm{d}x$, admits a closed formula given by

$$\delta M(R) = 4\pi\bar{\rho}_m \frac{R^3}{3(\alpha+3)}\delta_v \left[(\alpha+3)\ {}_2F_1\left(1, \frac{3}{\beta}, \frac{\beta+3}{\beta}, -\left(\frac{R'}{s_2}\right)^\beta\right) \right.$$
$$\left. -3\left(\frac{R'}{s_1}\right)^\alpha {}_2F_1\left(1, \frac{\alpha+3}{\beta}, \frac{\alpha+\beta+3}{\beta}, -\left(\frac{R'}{s_2}\right)^\beta\right)\right],$$

$$(7.18)$$

where ${}_2F_1$ is the Gauss hypergeometric series function. The existence of this closed formula for $\delta M(R)$ facilitates straightforward calculation of the force and lensing profiles[6].

---

[6]In Sec. 7.2, we denoted $\delta M(R)$ by $M(R)$, but both correspond to the mass perturbation enclosed by radius R, and not to the total mass (i.e. including the contribution from the background matter distribution). In our void related discussions, we opt to use $\delta M(R)$ since close to the void center $\delta M < 0$, and this way we make it explicit that what is negative is the mass perturbation, and not the total mass.

7.3.1   Finding voids in the simulations

We make use of the N-body simulations of the variants of the Cubic Galileon and Non-local gravity models presented in Chapters 5 and 6, respectively. We show results from simulation boxes of side $400\mathrm{Mpc}/h$ for the Galileon (this is not the same box size analyzed in Chapter 5, but the results are convergent), and $200\mathrm{Mpc}/h$ for the Nonlocal model, both with 512^3 dark matter tracer particles.

We find voids using the Watershed Void Finder (WVF) method of Ref. [362]. Our code takes as input the discrete tracer distribution, which in our case are DM particles and/or DM haloes, to construct a continuous volume-weighted density field using a Delaunay Tessellation Field Estimator (DTFE) method [403, 404]. For computational convenience, the DTFE field is sampled onto a regular grid, whose cell size is of the order of the mean distance between tracers. The grid density field is smoothed with a Gaussian filter of size $2\ h^{-1}\mathrm{Mpc}$ to reduce small scale features that could lead to spurious voids [362]. In the language of the watershed technique, the resulting density field is viewed as a landscape that will be flooded by a rising level of water. The regions around every local minima of the density field are called *catchment basins* (where water collects) and will be identified as the voids. As the water level rises, the basins grow and, eventually, neighbouring basins meet at the higher-density ridges that separates them. These ridges mark the boundary of each basin/void, and are associated with the filaments and walls of the cosmic web [36, 405]. The process stops when the water level reaches the global maximum of the density field, by the end of which all basin/void boundaries have been identified. To overcome watershed over-segmentation[7], ridges whose density constrast is $\delta < -0.8$ are not classified as void boundaries, as such low density boundaries are indicative of subvoids that have merged [362, 406]. An appealing aspect of the watershed method is that it makes no *a priori* assumptions on the size, shape or mean underdensity of the voids (see Ref. [407] for a comparison study of different void finders).

Our halo catalogues were obtained as in Chapters 5 and 6. The number density of the haloes we consider is $n_{\mathrm{halo}} = 5 \times 10^{-4} h^3/\mathrm{Mpc}^3$ and $n_{\mathrm{halo}} = 5 \times 10^{-3} h^3/\mathrm{Mpc}^3$ for the Galileon and Nonlocal gravity simulations, respectively. This is roughly the number density of haloes after retaining only those haloes whose mass is at least 100 times the

---

[7]This refers to avoid finding too many small voids inside a large underdense region, where in fact the whole underdense region should be classified as a single void that resulted from the merging of smaller ones.

particle mass. This minimum mass is, $100 M_p \approx 4 \times 10^{12} M_\odot / h$ and $100 M_p \approx 5 \times 10^{11} M_\odot / h$, for the simulations of the Cubic Galileon and Nonlocal models, respectively [8].

As is customary in void studies, we define the effective void radius R_v as the radius of a sphere whose volume is the same as the volume of the watershed void. We take the center of the void to be the location of the barycenter which is defined as $\vec{r}_{\text{barycenter}} = \sum_i \vec{r}_i / N_{\text{cell}}$, where $\vec{r}_i$ is the position of each grid cell identified as part of the void and N_{cell} is the total number of grid cells associated with void. We evaluate the density profiles of the voids using the DM density field (for voids found in both the DM and halo density fields) since this is the mass distribution that determines the lensing signal. In what follows we limit ourselves to analysing the simulation results at $z = 0$.

7.3.2   Void size function

Figure 7.7 shows the cumulative size function of the voids found in the simulations of the Cubic Galileon (left panels) and Nonlocal (right panels) gravity models. For both models, the void population depends on the tracer type used. In particular, DM density field voids (circles) are smaller and, in total, are found in greater number than voids in the halo density field (squares). This follows straightforwardly from the fact that the distribution of collapsed haloes is sparser than that of the DM particles. It is also noteworthy that, for the same type of tracer, we find larger voids in the Cubic Galileon than in the Nonlocal gravity model. This is simply due to the fact that the box size used in the simulations of the Galileon model ($400 \text{Mpc}/h$) is larger than that used in the simulations of the Nonlocal one ($200 \text{Mpc}/h$). One should therefore bear this difference in the box size in mind when comparing the results between the two gravity models.

In terms of the relative difference to QCDM, the full and linear variants of the Galileon model predict an enhancement of order the $10-20\%$ for the larger DM field voids ($15 \text{Mpc}/h \lesssim R_v \lesssim 20 \text{Mpc}/h$). This is due to the enhanced gravity of these models which boosts the evacuation of matter from inside the voids and the formation of large scale structures. In other words, voids expand faster in the full and linear variants, which is why large voids are more abundant. By the same reasoning, one should also expect the number of smaller

---

[8]Note that due to the different growth of structure, the halo mass function differs between the different variants of the models. The halo catalogues of the different variants were cut at slightly different mass values to yield the same number density of haloes.
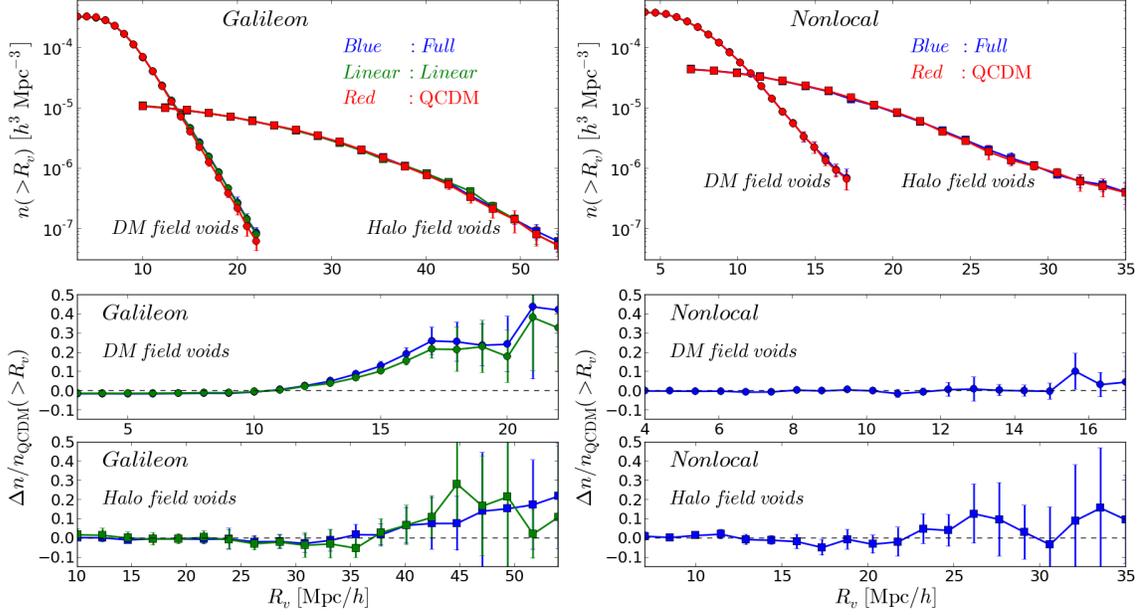
Figure 7.7: Cumulative void size function (number density of voids with radii above R_v) for the Cubic Galileon (left panels) and Nonlocal gravity (right panels) models. The upper panels show the number density of voids found in the DM (circles) and halo (squares) density fields for the full (blue), linear (green) and QCDM (red) variants of each model, as labelled. The lower panels show the difference relative to QCDM. The errorbars depict the variance across the five realizations of each variant.

voids to be suppressed in the linear and full variants, compared to QCDM. This is because the faster expansion of the voids makes it more likely for small neighbouring voids to merge into larger ones. In Fig. 7.7, this suppresion can be seen for $R_v \lesssim 10\mathrm{Mpc}/h$, although to a lesser extent than the enhancement seen for larger DM field voids. Another interesting aspect that is seen in the void abundances of the Galileon model is that the results of the full and linear variants are rather similar. This is very different from what is seen in the abundances of collapsed haloes, for which, due to the suppression effects of the screening mechanism, the full model has considerably fewer massive haloes than the linear variant (cf. Fig. 5.3). This illustrates that the effects of the screening mechanism are much weaker around underdense regions, as expected.

In the case of Nonlocal gravity, the number density of DM field voids is, within the errorbars, the same in the full and QCDM variants. Here, recall that the largest voids found in the Nonlocal simulations are smaller than those in the Galileon simulations due to the

smaller box size used. For instance, the largest DM field void found in the simulations of the Nonlocal model has $R_v \approx 17 \text{Mpc}/h$. This, together with the fact that in the Galileon model the enhancement is most noticeable for $R_v \gtrsim 15 \text{Mpc}/h$, suggests that the simulation box of the Nonlocal gravity model is not big enough to capture the impact of the fifth force on larger voids. Indeed, for large voids, there seems to be a trend for the full Nonlocal model to overpredict the number of voids with $R_v \gtrsim 15 \text{Mpc}/h$ relative to QCDM, although this is not significant due to the size of the errorbars. Nevertheless, for $R_v \sim 15 \text{Mpc}/h$, the enhancement in the full and linear variants of the Galileon model is already around $\sim 10\%$, whereas in the Nonlocal model it is still consistent with zero. This shows that the modifications to gravity in the Nonlocal model are, in general, weaker than those in the Cubic Galileon, which is also expected.

The results become noisier for voids found in the halo field due to the smaller number of tracers. For both the Galileon and Nonlocal gravity models, within the errorbars, the number density of voids is essentially the same in all model variants. However, as an exercise, if one ignores the size of the errorbars for a moment, then one notes that, at least qualitatively, the halo field voids show the same behaviour as their DM field counterparts. In the case of the Galileon, for instance, the largest halo field voids, $R_v \gtrsim 40 \text{Mpc}/h$, are $\sim 10 - 20\%$ more abundant in the full and linear variants, compared to QCDM. This qualitative trend, backed up by the expectation based on physical intuition, suggests that with improved halo field void statistics one should recover, at least to a certain degree, the same physical behavior seen for the DM field voids.

7.3.3 Void density profiles

Figure 7.8 shows the spherically averaged DM density field and halo density field void density profiles found in the simulations of the three variants of the Galileon model[9], with the void sample split to two size bins, as labelled. Figure 7.9 is the same as Fig. 7.8, but for the Nonlocal model. The void density profiles are characterized by a density increase from $R' = 0$ towards $R' \approx 1$; an overdense *ridge* at $R' \sim [1 - 1.5]$, which is associated with the filaments and walls that surround the void (the ridge is less pronounced for larger voids); and a steady decrease towards the cosmic mean, $\delta = 0$, at larger radii. In these

---

[9]The average density profile of all the voids in each bin should be spherical to a good approximation, even though each individual void is not.
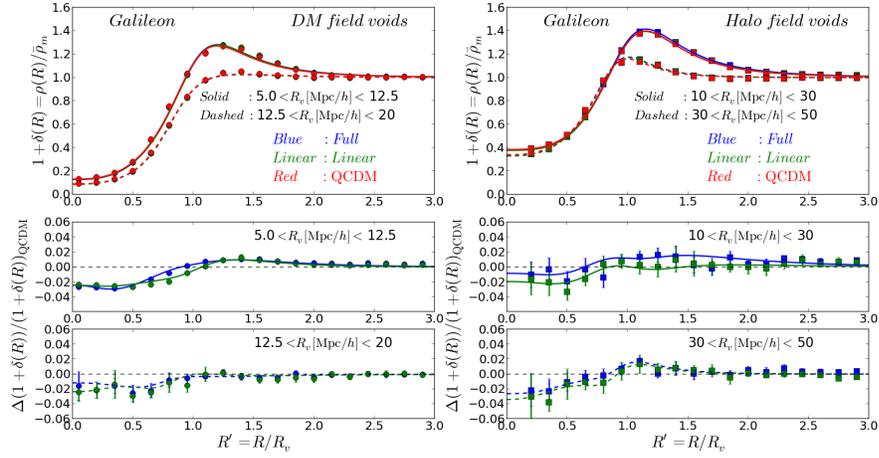
Figure 7.8: Void density profiles, $\rho_m/\bar{\rho}_m = 1 + \delta$, for the DM density field (circles, left panels) and halo density field (squares, right panels) voids found in the simulations of the three Galileon model variants (distinguished by the different colors, as labelled), plotted as function of the scaled radius $R' = R/R_v$. The solid (dashed) lines show the best-fitting density profiles, using the formula of Eq. (7.17), for the bin of smaller (larger) void sizes, as labelled. The choice of the two void size bins constitutes a compromise between having enough voids in each bin, whilst making sure that the void properties do not vary too much within a bin. The bottom panels show the relative difference to QCDM. The errorbars depict the variance accross the five realizations of each variant.
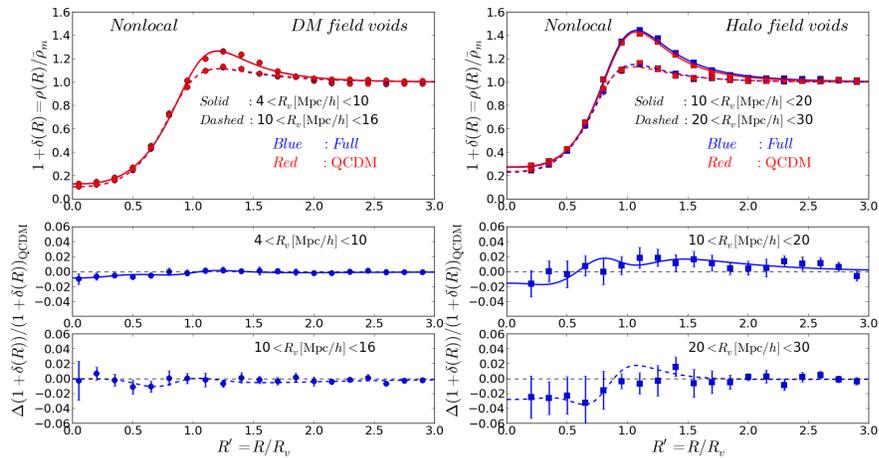
Figure 7.9: Same as Fig. 7.8 but for the Nonlocal gravity model.

figures, the curves show the best-fitting profiles obtained using the five-parameter formula of Eq. (7.17), which fits the simulation results very well. We note that it is not our goal here to determine if the voids found in our simulations are *self-similar* (i.e., independent of the void size) or *universal* (i.e., independent of tracer type and/or redshift). For the remainder of our analysis, what will be important is that the density profiles of the voids in the simulations are well matched by our formula of Eq. (7.17)[10], which can therefore be used in the calculation of the force profiles and lensing signal in the sections below.

The impact of the fifth force is better seen when comparing the difference relative to QCDM. In the case of the Galileon model (Fig. 7.8), compared to QCDM, the voids in the full and linear variants are $\approx 2 - 3\%$ emptier in the inner regions, i.e. $R' \lesssim 0.5$, for both the DM and halo voids (although the result is noisier for halo voids due to poorer statistics, specially for the smaller radius bin). Physically, this is because the enhanced gravity favours the piling up of matter in the outer regions, leaving less matter inside the void. The fact that the prediction from the linear and full variants are so close illustrates, once again, that the effects of the screening mechanism are weak around voids. In Ref. [117], similar results were found in the context of $f(R)$ gravity, using a spherical underdensity based void finder [408]. In particular, the authors of Ref. [117] found that the voids in $f(R)$ models can be up to $\approx 5\%$ emptier than in ΛCDM. In Fig. 7.8, it is also worth noting that for the smaller radius bin of DM field voids, at $R' \sim 0.5 - 1$, the voids are more underdense in the linear variant than in the full model. We shall present an explanation for this in the next subsection, when we look at the force profiles in the Galileon model.

The effects of the fifth force on the void profiles of the Nonlocal model (Fig. 7.9) are weaker than those seen in the Galileon case. In particular, for the DM field voids, the smaller void size bin in the full variant shows a decrement of only $\approx 1\%$, relative to QCDM; the difference becomes consistent with zero for the larger size bin. In the case of the halo field voids, there is a systematic trend for the voids in the full Nonlocal model to be $\approx 2-3\%$ emptier than in QCDM for $R' \lesssim 0.5$, but the poorer statistics make it hard to draw any decisive conclusions. Nevertheless, the result of Fig. 7.9 shows that, overall, the fifth force effects on the void density profiles in the Nonlocal model are weaker than in the Galileon model, which is expected.

---

[10]Even if one needs to fit the free parameters for different void sizes and for different density tracers.
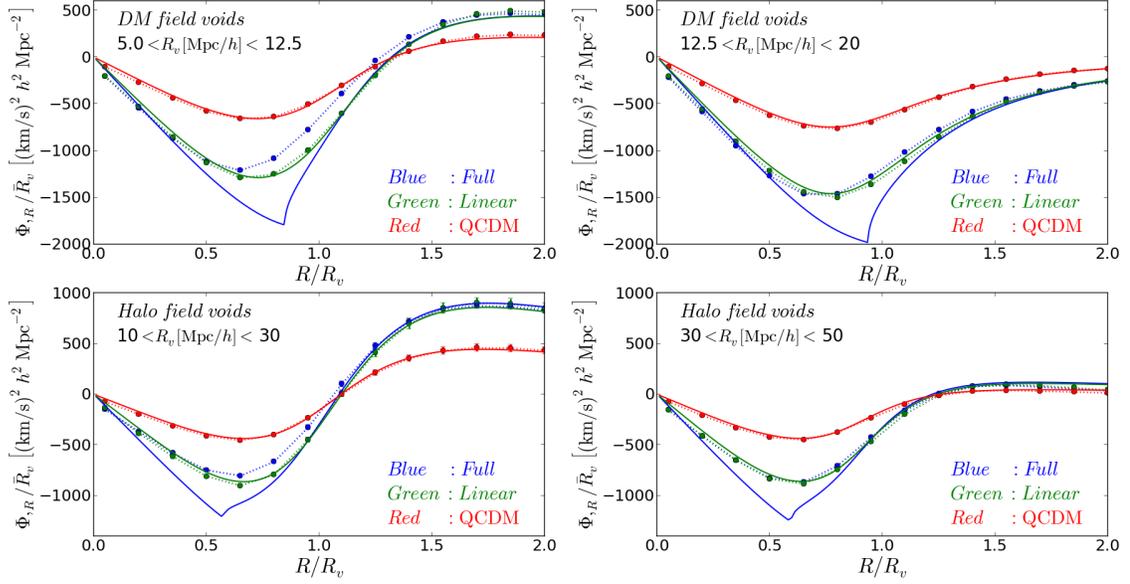
Figure 7.10: Radial force profiles around the DM field (upper panels) and halo field (lower panels) voids in the variants of the Galileon model (distinguished by the different colors, as labelled). The circles with errorbars (which are in most cases smaller than the circles), linked by the dotted lines, correspond to the spherically averaged radial force field in the simulations. The solid lines correspond to the analytical prediction computed using the corresponding best-fitting void density profiles of Eq. (7.17), shown in Fig. 7.8. The different panels show the result for the two void size bins, as labelled. What is actually plotted is the radial force scaled by the mean void size in each bin, $\Phi_{,R}/\bar{R}_v$. A negative sign for the force means that it points outwards.

7.3.4   Void force profiles in the Galileon model

Figure 7.10 shows the force profiles in the voids in the variants of the Galileon model. The circles, linked by the dotted lines, show the simulation results. These were obtained by spherically averaging the radial force field in the simulations, which was constructed by using the force information at the N-body particle positions. The solid curves show the analytical result computed using the best-fitting void density profiles of Eq. (7.17) (cf. Fig. 7.8). Figure 7.10 shows that, for the linear and QCDM variants, the analytical calculation is in very good agreement with the simulation results. However, the same is not true for the case of the full variant of the Galileon model. In this case, the analytical result differs from that of the simulations for $R' \lesssim 1.25$, for DM field voids, and for $R' \lesssim 1.0$ for halo

field voids. More specifically, for all cases shown, the analytical result of the full variant always predicts a stronger force (more negative) than the linear variant, inside the void. This follows directly from the equations of the model (cf. Sec. 5.1.2). On the other hand, in the simulations, the force inside the smaller voids (left panels) of the full variant is weaker than in the linear case. For larger voids (right panel), the full and linear variant simulations exhibit nearly the same force profiles.

The reason why the forces in the simulations of the full model are weaker (less negative) than those computed analytically using the spherically averaged density profiles can be linked to the effects of screening. The smooth void density profiles depicted in Fig. 7.8 correspond only to an average density field, which does not fully capture the detailed distribution of matter around the voids. A more realistic picture is that, inside the voids and at their edges, there are higher density peaks associated with dark matter haloes and their respective infall regions. Close to these higher density regions, the fifth force in the Galileon model is suppressed by the screening mechanism, which results in a weakening of the total force. Herein lies the explanation for the mismatch between the analytical result and the simulation force profiles. By averaging first the matter field, despite of the presence of higher density peaks, on average, one ends up with a smoother and lower density void profile. This profile, when used in the analytical calculation, gives a fifth force which is stronger in magnitude than the corresponding linear solution [11]. On the other hand, by averaging directly the forces at the particle positions, one is averaging a force field which is already affected by the suppression effects of the screening due to the existing higher density peaks. This is why the force profiles measured in the simulations are weaker (less negative), as seen in Fig. 7.10. In other words, since the force equation in the full model is nonlinear, it makes a difference whether one computes the force analytically from the averaged density field, or one computes the force by averaging directly the force field. In the case of the QCDM and linear variants, the force equation is linear, and as a result, the operations of averaging the density and the force field commute, which is why there is almost perfect agreement between the analytical and simulation results in these cases.

Figure 7.10 shows also that the suppression of the total force in the full variant relative

---

[11]The result that the total force in the full variant is stronger than in the linear variant inside voids using Eq. (7.17) is not shown explicitly, but it can be straightforwardly checked by working with the model equations displayed in Sec. 5.1.2.

to the linear one is more pronounced in smaller voids. This is because smaller voids are denser, and therefore contain more higher density peaks per volume inside them and in their surroundings, which enhances the suppresion effect of the screening. In particular, it is interesting to link this result with the differences between the linear and full model density profiles for the smaller size bin of the DM field haloes at $R' \sim 0.5 - 1$ in Fig. 7.8. As we noted in the previous section, on these radial scales the voids in the linear model are slightly emptier. This can be explained by the fact that, in the simulations, the force in the linear model is stronger (more negative), which favours the evacuation of matter from inside the void[12]. In principle, the same result should also be noticeable in the case of the smaller size bin of the halo field voids, for which the force in the full model is also weaker than in the linear one at $R' \sim 0.5 - 1$ (lower left panel of Fig. 7.10). This is not visible in Fig. 7.8 (lower left panel), possibly because of the noisier measurements.

For the Nonlocal gravity model, the force equations are linear, as in the cases of the QCDM and linear variants of the Cubic Galileon model. As a result, there is good agreement between force profiles computed from simulations and the analytical results.

Imaginary square-root problems

Before proceeding, we note that the visible "kinks" in the force profiles of the full variant in Fig. 7.10 are due to the *ad hoc* fixed described in Sec. 5.1.2 to overcome the imaginary square-root problems whenever the mass perturbation becomes negative. In Chapters 4 and 5, we were interested in the matter power spectrum and properties of haloes, for which this problem could be ignored. However, when studying voids, this problem becomes manifest and it becomes important to try to understand the implications of the existence of complex solutions for the fifth force. Recall that all our calculations for the nonlinear regime of structure formation are carried out assuming the quasi-static and weak-field limits. In the very low-density regions that characterize voids, one expects the weak-field approximation to still hold, but the quasi-static one may not (see Refs. [409, 410] for discussions about the quasi-static limit, and Refs. [130, 411] for work beyond this in N-body simulations). One

---

[12]It is worth noting that the relative differences in Fig. 7.8 correspond to different void populations, and as a result, some of the observed differences could arise from this. As a test, we have measured the density and force profiles in the full, linear and QCDM simulations, but at the spatial locations of the voids in the QCDM model. This increases the chances of comparing voids that evolved from the same initial underdense regions. From this test we found only small quantitative changes with no impact on our conclusions.
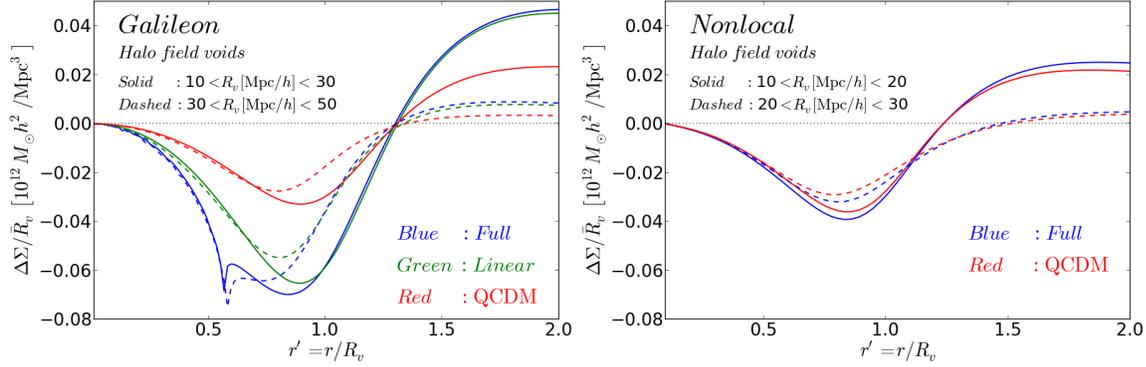
Figure 7.11: Lensing differential surface mass density, $\Delta\Sigma/\bar{R}_v$, for the best-fitting density profiles of the two void size bins (distinguished by the line styles, as labelled) for the halo density field voids found in the simulations of the different variants (distinguished by the colors, as labelled) of the Cubic Galileon (left panel) and Nonlocal (right panel) gravity models. The result is scaled by the inverse of the mean void radius in each size bin, $\bar{R}_v^{-1}$.

may therefore speculate that the terms that have been neglected by the quasi-static limit are such that, when present, keep the fifth force as a real number for all density values. Interestingly, however, the recent work of Ref. [412] has shown that the problem remains even after relaxing the quasi-static approximation. In particular, the authors find that the time derivative of the Galileon field perturbation becomes singular when the quasi-static solution becomes a complex number (see Ref. [412] for the details). This suggests that the breakdown of the quasi-static solutions may well be associated with a true instability of the Cubic Galileon model. Here, we shall keep these discussions in mind but proceed by retaining the *ad hoc* fix discussed in Sec. 5.1.2. Our treatment of the equations of the Cubic Galileon can be viewed as a toy model that we use to illustrate the effects of modified gravity in the properties of voids.

7.3.5 Void lensing signal

Figure 7.11 shows the lensing signal associated with the halo field voids found in the simulations of the Galileon (left panel) and Nonlocal (right panel) gravity models. What is shown are the profiles of the *differential surface mass density*, $\Delta\Sigma$, defined as $\Delta\Sigma = \Sigma_c \gamma_t$ (cf. Sec. 7.1). This was computed analytically using the best-fitting void density profiles of Figs. 7.8 and 7.9. For brevity, we show only the result for halo field voids. These are the
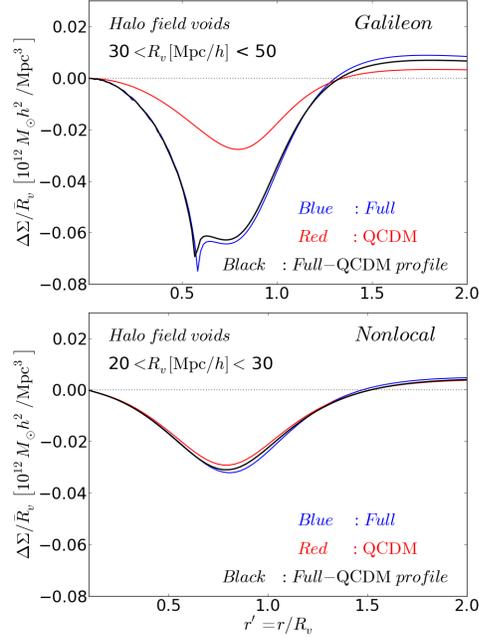
Figure 7.12: Relative impact of the fifth force and modified density profiles on the lensing signal of halo field voids in the Cubic Galileon (upper panel) and Nonlocal (lower panel) gravity. For both models, the red and blue lines have the same meaning at those in Fig. 7.11. The black curves are obtained by calculating the lensing signal with the full Galileon and full Nonlocal model force equations, but using the best-fitting void density profile of the QCDM voids.

ones that are more closely related to observations, where one first identifies voids using galaxy catalogues and then looks at the lensing signal at the void locations [413, 414]. Note also that the values of $\Delta\Sigma$ are scaled[13] by R_v^{-1}, which means that the voids in the larger size bin (dashed curves) have lensing effects of larger magnitude (i.e. one needs to multiply the result by R_v).

In the case of the Galileon model, the maximum of the lensing signal, which occurs at $r' \sim 0.75 - 1$, is approximately twice as strong in the full and linear variants, compared to QCDM. At $r' \lesssim 1$, the signal is slighlty stronger in the full than in the linear variant [14]. This follows from the stronger fifth force (more negative) in the full model, when computed

---

[13]It is straightforward to show that the lensing quantities are proportional to R_v, e.g., $\kappa(r) = R_v \kappa(r' = r/R_v)$, where $\kappa(r' = r/R_v)$ is the lensing convergence given in terms of the scaled radial coordinate $r' = r/R_v$.

[14]The "spikey" features seen in the blue curves follow from our *ad hoc* fix to the problem of complex fifth force solutions (cf. Sec. 7.3.4).

analytically (cf. Fig. 7.10). However, in Fig. 7.10, we have seen that, due to the screening mechanism, the force predictions of the full and linear variants measured in the simulations are actually closer than what is predicted by the analytical calculation using the best-fitting density profiles. For this reason, it is reasonable to assume that the lensing signal of the full model is actually closer to the prediction of the linear variant, compared to what is observed in Fig. 7.11. Nevertheless, given that the differences between the full and linear variants are smaller than their differences relative to QCDM, it remains safe to conclude, as we have seen in previous sections, that the effects of the fifth force in the Galileon model are quite pronounced in voids, where the screening is not very efficient.

In the case of the Nonlocal model, the effects of the fifth force are considerably weaker than in the Galileon model. In particular, for the cases shown in Fig. 7.10, the maximum amplitude in the value of $\Delta\Sigma$ (at $r' \sim 0.75 - 1$) is $\approx 10\%$ stronger in the full Nonlocal model, compared to its QCDM variant. This illustrates that the effect of the modifications to gravity in the Nonlocal model are more challenging to detect using the lensing signal from voids.

The modifications to gravity affect the lensing in voids in two main ways: (i) through the modifications to the average density profiles of voids; and (ii) directly through the modifications to the lensing potential. Figure 7.12 measures the relative impact of these two effects in the Galileon (upper panel) and Nonlocal gravity (lower panel). In the figure, the red and blue curves are the same as in Fig. 7.11. The black curves are computed using the lensing equations of the full variants of the Galileon and Nonlocal models, but using the density profile of the voids in the QCDM variants. As a result, comparing the red and black curves shows the effect of modifying the force law, whereas the difference between the black and blue lines shows the impact of the modified density profiles. In the case of the Galileon model, Fig. 7.12 shows that the dominant effect comes from the fifth force. This is seen by the large difference between the red and black curves. Fig. 7.12 shows the result for the larger size bin of the halo field voids, which are slightly emptier in the full variant of the Galileon model, compared to QCDM (cf. bottom right panel in Fig. 7.8). This helps to further suppress the amplitude of $\Delta\Sigma$, but by a much smaller amount. On the other hand, for Nonlocal gravity, the direct effect of the fifth force on lensing is comparable to the effect of having slightly emptier voids (cf. Fig.7.9).

7.3.6   The connection to observations

References [413] and [414] have recently detected the lensing signal associated with voids in the galaxy distribution (see also Refs. [415, 416, 417] for earlier forecast studies). In Ref. [413], the authors stacked the voids of the catalogue of Ref. [418], which were found using a watershed algorithm in the three-dimensional main galaxy and Luminous Red Galaxy (LRG) samples of the Sloan Digital Sky Survey-Data Release 7 [419] (SDSS-DR7). On the other hand, in Ref. [414], the authors used also the SDSS LRG catalogues, but the voids were found using a method that is specifically designed for lensing. In this method, emptier regions are found in projected two-dimensional slices of the survey volume, which seems to increase the significance of the lensing detection.

As we discuss below, a robust comparison between these observations and the results of Fig. 7.11 requires more detailed modelling of the theoretical predictions. Nevertheless, one can still compare some of our results to try to get a feeling about what these measurements imply for modified gravity. For instance, in Fig. 5 of Ref. [414], it is shown that for voids with size $R_v \in [15, 30]$ Mpc/h, the values of the differential surface mass density at its minimum are, approximately, within $\Delta\Sigma \in [-0.4, -0.7] \; 10^{12} M_\odot h/\mathrm{Mpc}^2$ (this estimate is based on the size of the errorbars there). From Fig. 7.11, for the case of the smaller size bin of the full Galileon model we have[15] $\min(\Delta\Sigma) \approx -0.065\bar{R}_v = -1.3 \times 10^{12} M_\odot h/\mathrm{Mpc}^2$. For the full Nonlocal model, we have $\min(\Delta\Sigma) \approx -0.032\bar{R}_v = -0.46 \times 10^{12} M_\odot h/\mathrm{Mpc}^2$ and $\min(\Delta\Sigma) \approx -0.039\bar{R}_v = -0.9 \times 10^{12} M_\odot h/\mathrm{Mpc}^2$, for the smaller and larger size bins, respectively. Hence, for both the Galileon and Nonlocal models of gravity, we get the same typical order of magnitude as in the observations. One notes that in the case of the Galileon model, the size of the effect is larger than the results presented in Ref. [414]. This suggests that, indeed, lensing by voids may have the potential to constrain models like the Galileon.

Before summarizing our results in the next section, we find it instructive to briefly comment on a number of aspects that should to be taken into account before properly confronting these (and other) models to lensing observations. These aspects include:

1. *Impact of Σ_c* In Fig. 7.11, we quote our results in terms of $\Delta\Sigma$, but in reality, what one measures directly from galaxy ellipticities is the shear, $g \approx \gamma_t = \Delta\Sigma/\Sigma_c$. The calculation of Σ_c depends on the cosmological background, which can be different between

---

[15]Here, $\bar{R}_v$ is the mean void radius in the void size bins

the Galileon, Nonlocal, and the standard ΛCDM models. Consequently, if in observational studies, one measures γ_t, but quotes the results in terms of $\Delta\Sigma$ by assuming a background cosmology to compute Σ_c, then this may introduce some bias that should be carefully addressed. Furthermore, Σ_c depends also on the redshift distribution of the source galaxy population, although this can always be set accordingly using the properties of the observed galaxies.

2. *Void redshift distribution* The lensing signal in Fig. 7.11 was obtained analytically using the density profiles of the voids in the simulations at $z = 0$. In the observations, however, the lensing signal is detected by stacking voids that span a given redshift distribution $z > 0$. In the particular case of the Galileon and Nonlocal gravity models, the fifth force is weaker at earlier times (see e.g. Fig. 3 of Ref. [6] and Fig. 2 fo Ref. [8]), which reduces the amplitude of the signal depicted in Fig. 7.11.

3. *Void stacking* The lensing signal associated with individual voids is too weak to be detected in current observations, which is why Refs. [413, 414] used stacked voids in their analyses. When interpreting such results in modified gravity, for a given stack, voids at different redshifts have different weights in the observed lensing signal because of the redshift dependence of the fifth force, Σ_c and also of the screening efficiency. Such effects should be taken into account if one, for instance, tries to use the lensing observations to reconstruct a mean density profile for the stack. Here, an interesting analysis would involve stacks of voids binned not only by size, but also by redshift.

4. *Systematic biases* The lensing calculations performed here assume that the density distribution in voids is perfectly smooth. In reality, however, voids contain substructure and its amount is expected to be different in models with different growth rates of structure. Given that the lensing signal from voids is relatively weak (compared to that induced by DM haloes) it may be interesting to investigate the extent to which void substructure can impact on the overall lensing signal. This can be studied by looking at the lensing signal using ray-tracing methods in the simulations, without modelling their profiles as a smooth distribution. Our lensing calculations also assume that the void is the only source of lensing. A ray-tracing analysis would also help to better quantify the contamination of the lensing signal coming from intervening matter along the line of sight.

5. *Screening effects* Related to the above point, a ray-tracing analysis is also able to capture

more accurately the effects of the nonlinear screening mechanism. In Sec. 7.3.4, we saw that, in the full variant of the Galileon model, it makes a difference whether one computes the force profiles analytically from the spherically averaged density profiles, or by spherically averaging the force field directly. Moreover, the efficiency of the Vainshtein mechanism depends also on the geometry of the mass distribution as investigated recently in Refs. [127, 128]. This means that calculations based on the mean spherical profile of a stack of voids may not fully capture the fifth force effects from each individual non-spherical void. These issues can be circumvented by directly integrating $\nabla^2\Phi$ along the line of sight for each void using ray-tracing and stacking the resulting signal. In this way, one probes directly the lensing potential distribution without introducing any bias that arises when one averages first the density field.

6. *Halo/galaxy bias* We have found voids using both DM particles and DM halos as tracers, with the latter case being that which is more relevant when comparing to observations. Due to halo bias, haloes cluster differently depending on their mass, and hence, the resulting void catalogues depend on the minimum halo mass cut used to identify them. This is turn has an impact on the abundances and profiles of voids [420, 421]. Since different types of galaxies populate haloes differently, a robust comparison with observations should ensure that the number density and bias of the tracers used in simulations matches those of the tracers used in observations. A first step torwards this goal could be to construct mock galaxy catalogues using halo occupation distribution modelling [422], as Ref. [421] has done for ΛCDM. Such an analysis can also inform on whether voids identified using certain types of density tracers are better suited for tests of modified gravity.

7. *Combining different void finders* The way voids are found in simulations and/or in real galaxy catalogues can also affect the resulting lensing signal. For instance, as we mentioned above, the authors of Ref. [414] optimize their analysis for lensing by finding the voids in projected two-dimensional slices of a spectroscopic galaxy survey. This may partly explain why the significance of their detection is higher than that found in Ref. [413], in which the voids are found in three dimensions. It would therefore be of great interest to find voids in the way of Ref. [414] in the N-body simulations as well. It is also well known that different void finding techniques yield different void profiles

[407], and hence, different lensing predictions. For instance, voids found with spherical underdensity (SU) methods have sharper transitions from the inside of the void to the surrounding ridge. This boosts the lensing effect, as can be checked in the α panel of Fig. 7.6, where α is the parameter of the formula of Eq. (7.17) that controls the slope of this transition. Moreover, the recent work of Ref. [423] has shown that it may be more natural to characterize the void profiles with respect to their boundaries (which is where most of the mass is), instead of with respect to the void center (which is devoid of tracers) [16]. This also results in steeper density profiles close to the void edge (see Fig. 7 of Ref. [423]). The differences in void profiles obtained with different void finding methods is generally portrayed as a source of uncertainty in void related work, but we note that some advantages may arise from it. For instance, since the fifth force acts to make voids emptier and the ridges denser, then methods like SU or that of Ref. [423] may be particularly suitable for modified gravity studies, as they may amplify the size of the fifth force effects (see e.g. Ref. [117], where the authors use SU methods to study voids in $f(R)$ gravity). Hence, we believe that the combination of the results from different void finding methods (provided they are consistently used in simulated and real data) is something to be explored with more detail when designing observational tests. These investigations are the subject of ongoing work [424].

7.4 Summary

In this chapter, we have studied the lensing signal associated with galaxy clusters and cosmic voids in Cubic Galileon and Nonlocal gravity cosmologies. In the part of this chapter devoted to galaxy clusters, we used the radially binned lensing convergence profiles obtained for 19 X-ray selected clusters from the CLASH survey [137, 360, 361] to determine the impact of the modifications to the lensing potential on estimates of the mass and concentration of the clusters from lensing. In our discussions, we paid particular attention to the compatibility of the data analysis with the modified gravity models we wished to test.

In the part of this chapter devoted to cosmic voids, we analysed the abundance and profiles of the density, force and lensing shear of the voids found in the DM and halo density

---

[16]In the approach of Ref. [423], one also circunvents the problem of assuming that voids are spherical, when in reality they are not.

fields of N-body simulations. The fifth force in the Cubic Galileon and Nonlocal gravity models has an impact on the lensing signal in and around voids through two main effects. First, the fifth force changes the density profiles of the voids, and second, it also modifies the lensing potential directly. This means that even for fixed mass distribution, the lensing signal in these theories of gravity is still modified w.r.t. GR. This is different from other popular models like $f(R)$ and/or DGP gravity, which practically do not directly modify the lensing potential. Hence, models that directly modify lensing are more amenable to being tested by lensing observations than those that do not.

Our main results can be summarized as follows:

• The M_{200} and c_{200} values obtained for the CLASH clusters using GR, Cubic Galileon and Nonlocal gravity agree to better than 5%, which is much smaller than the $\sim 50\% - 80\%$ accuracy allowed by the data at the 1σ level. In the case of the Galileon model, this is because the screening mechanism suppresses the modifications to gravity very efficiently on the scales probed by the lensing data, $R \lesssim R_{200}$. In the case of the Nonlocal gravity model, there are no systematic shifts in the values of M_{200} and c_{200} relative to those in ΛCDM because the boost in the gravitational strength is not strong enough at the redshift of the CLASH clusters, $z \sim 0.2 - 0.9$.

• The practically unmodified lensing masses in the Galileon model have interesting implications for tests of gravity that are designed to detect differences between lensing and dynamical mass estimates [125, 126, 394]. These tests were first put forward in the context of models like $f(R)$ and DGP that modify the dynamical potential (probed by, e.g., infalling galaxies outside R_{200}), but not the lensing potential. Our results show that, although the Galileon model also modifies the lensing potential, this does not translate into modified lensing masses because of the screening. However, outside R_{200}, the force profile of the CLASH clusters in the Galileon model can be $10 - 40\%$ higher than in ΛCDM (cf. Fig. 7.5), which can affect the velocity distribution of infalling galaxies, and hence, the dynamical mass estimates. The picture is therefore qualitatively similar to that of $f(R)$ and DGP gravity, and as a result, the techniques of Refs. [125, 126, 394] can also be applied to models like the Galileon model studied here.

• In the Galileon model, the fifth force boosts the abundance of the larger radius DM field voids ($R_v \gtrsim 15\mathrm{Mpc}/h$) by $\approx 10\% - 30\%$ (cf. Fig. 7.7). This is because the enhanced gravity causes voids to expand faster and also favours the merging of smaller voids into

larger ones. For the voids found in the halo density field, the same qualitative trend is also seen but is less pronounced due to poorer statistics. In the case of the Nonlocal model, the modifications to gravity are not strong enough to leave a clear signal on the abundances of the voids found in the simulations (cf. Fig. 7.7).

• The effects of the fifth force in the Galileon model can make the lensing signal in voids approximately twice as strong as in GR (cf. Fig. 7.11). This large difference comes predominantly from the modifications of the lensing potential *per se*, with the different void density profiles being of secondary importance (cf. Fig. 7.12). In the case of the Nonlocal gravity model, the fifth force also enhances the expected suppression of the lensing signal, but only by $\approx 10\%$ (cf. Fig. 7.11). In this model, the modifications to the density profiles and direct effects of the fifth force contribute equally to the difference relative to GR (cf. Fig. 7.12).

• For all our Galileon model results, the predictions from the full and linear variants are of comparable size. This is different from the case of predictions associated with dark matter haloes (like their abundances or concentration), for which the effects of the full variant are typically much smaller than those of the linear variant because of the screening (cf. Chapter 5). This illustrates that the suppression effects of the screening mechanism are not very strong around voids, which is why the latter can be regarded as potentially powerful probes of gravity on cosmological scales.

Overall, the results in this chapter show that observations of the lensing signal associated with voids have the potential to prove very valuable in constraining the gravitational law on large scales. In the future, we plan to use some of the results presented here to help to develop more robust observational tests, by following the steps outlined in Sec. 7.3.6. We believe that such investigations would be timely, specially when interpreted in light of future observational missions such as DESI [350], LSST [425] and Euclid [426].

Chapter 8

Summary, Conclusions and Future Work

8.1 Summary and Conclusions

The growing interest in modified gravity models is justified by their ability to explain the accelerated expansion of the Universe without requiring a cosmological constant and also because they help to pinpoint which observational methods have the best chances to test gravity on large scales. Models like $f(\mathcal{R})$, which uses chameleon screening, and DGP, which employs Vainshtein screening, have been and continue to be thoroughly studied in the nonlinear regime with N-body simulations. The study of their phenomenology allows us to build intuition about how we can constrain gravity on large scales using current and future data. For instance, chameleon models can be tightly constrained using unscreened dwarf galaxies [103], and studies of $f(\mathcal{R})$ and DGP have taught us that these models predict an offset between lensing and dynamical mass estimates [125, 126], which could be regarded as a smoking gun of modified gravity. Modified gravity models also change the growth rate of structure relative to GR, which has an impact on the clustering of matter on small scales, cluster/void properties, galaxy peculiar velocity field, etc.

The more models we study, then the greater our knowledge should be about the observational inprints of modified gravity, which can be used to design novel observational tests. Fortunately, over the past few years, *model builders* have been very productive in proposing interesting theories with new phenomenologies to study (as can be checked by the number of models described in the review of Ref. [42]). In this thesis, we took several steps forward in the analysis of two of the most recent classes of modified gravity models which are Galileon [56, 57] and Nonlocal [63, 136] gravity, by examining their predictions in the linear and nonlinear regimes of structure formation. This was the first time the CMB predictions for these models have been presented in the literature, as well as their predic-

tions for nonlinear structure formation using N-body simulations.

8.1.1   Linear theory constraints on the Galileon model

The analysis of Chapters 2 and 3 was devoted to the linear theory constraints on the co-variant Galileon model. We derived the covariant and gauge-invariant linearly perturbed equations, solved them by modifying the Einstein-Boltzmann code `CAMB` and used the parameter estimation code `CosmoMC` to obtain the constraints on the parameter space using data from the CMB, SNIa and BAO. In these chapters, we saw that the Galileon model (which can be divided into the so-called Cubic, Quartic and Quintic sectors) exhibits very different background dynamics (lower H at late times) and evolution of the linear density fluctuations (enhanced growth due to the fifth force) compared to ΛCDM. Nevertheless, the model can still provide a good fit to these data if neutrinos are sufficiently massive, $\Sigma m_\nu \sim 0.6\,\mathrm{eV}$ (cf. Tables 3.2 and 3.4). This constraint on neutrino masses is driven by (i) the impact that Σm_ν has on the late-time expansion rate, which reconciles the positions of the CMB and BAO peaks (see the discussion in Sec. 3.3.1); and (ii) by the suppression massive neutrinos induce on the amplitude of the CMB lensing potential power spectrum, which compensates for the boosting effects of the fifth force (cf. middle left panel of Fig. 3.8). *This tells us that one should be careful about making any ΛCDM-like assumptions, when constraining models which are not ΛCDM.* For instance, had we assumed in our constraints that $\Sigma m_\nu \approx 0$ (which is the ΛCDM result), then we would have ruled out the model prematurely. The analysis in these chapters provided us with the parameter values that were subsequently used in the studies of the nonlinear regime.

We saw that the lensing potential in the best-fitting Galileon models does not decay at late-times on sub-horizon scales. This is at odds with the observationally inferred positive sign of the ISW effect, which is likely to rule out these models. *Naturally, this tension with the sign of the ISW effect makes the covariant Galileon model less appealing, which means that it should no longer be seen as serious competitor to ΛCDM.* However, and as we have encountered throughout this thesis, the rich phenomenology of the model warrants its use as a working case in the illustration of the effects of modified gravity on various observables.

8.1.2 Nonlinear structure formation in the Galileon model

In Chapter 4, we analysed the predictions of the Quintic and Quartic Galileon models in the context of the analytical spherical collapse model and excursion set theory formalism. We saw that the spherically symmetric field equations in the quasi-static and weak-field limit in the Quintic model fail to admit real physical solutions for the fifth force if the density contrast becomes $\mathcal{O}(1)$ (cf. Sec. 4.2.1). Such a result could imply the break down of the quasi-static and weak-field assumptions, which would be an interesting and novel result since these assumptions are generally viewed as better approximations the larger the density contrast. The alternative could signify that the model is simply unphysical and therefore ruled out. These difficulties prevented us from studying nonlinear structure formation in this model. In the Quartic model, the modifications to the force law include terms that depend on the background evolution of the Galileon field, which cannot be suppressed by the Vainshtein mechanism. This results in $\dot{G}_{\mathrm{eff}} \neq 0$ and $G_{\mathrm{eff}}/G < 1$ on small scales, which leads to tensions with Solar System tests (cf. Fig. 3.11). The seriousness of these tensions is linked to the assumption that the time evolution of the Galileon field is felt locally, i.e., if one analyses the model predictions in perturbed Minkowskii space (as opposed to perturbed FRW) then the tension goes away. The new phenomenology encountered in this chapter for the Quartic and Quintic Galileon models *illustrates how much richer the analysis of modified gravity can become when one goes beyond the linear regime.*

In Chapter 5, we performed N-body simulations of the Quartic and Cubic Galileon models to study the properties of dark matter haloes such as their abundance, bias and concentration, and to build a halo model for the nonlinear matter power spectrum. In the Cubic model, the screening works very efficiently to suppress the fifth force inside haloes, a result that is manifest in the nearly unchanged halo concentrations (cf. Fig. 5.7) and amplitude of the nonlinear matter power spectrum on small scales (cf. Fig. 5.8), relative to GR. In the Quartic model, the weaker gravity felt on small scales suppresses the growth of structure (cf. Figs. 5.4, 5.7, 5.9). In Chapter 5, we also conducted a HOD analysis of LRGs to show that, in the Cubic and Quartic Galileon models, the relatively high amplitude of the linear matter power spectrum ($\sigma_8 \approx 1$) can be compensated by the modifications to halo abundances and bias to preserve the way in which LRGs populate those haloes, compared to ΛCDM (cf. Fig. 5.6). *This result highlights the importance of nonlinear studies with N-body simulations even when one is interested on scales typically associated with the linear regime*

($k \lesssim 0.1h/\mathrm{Mpc}$).

8.1.3 Linear and nonlinear structure formation in Nonlocal gravity

To study the cosmology of Nonlocal theories of gravity in Chapter 6, we took the recently proposed model of Ref. [136] (cf. Eq. (6.1)). This model is characterized by a term $\propto \mathcal{R}\Box^{-2}\mathcal{R}$ in the action (cf. Eqs. (1.14) and (6.1)) and has the same number of free parameters as ΛCDM. The equations of this model are simpler than those in the Galileon case, and as such, our analysis was not as extended. In this chapter, we saw that for fixed cosmological parameters, this model yields a CMB temperature spectrum that is already close to ΛCDM. Hence, this model should fit the CMB, BAO and SNIa data with only slightly different parameters such as Σm_ν, Ω_{m0} or H_0 (as confirmed later by Ref. [341]). In this chapter, most of the attention was devoted to studying nonlinear structure formation with excursion set theory and N-body simulation results. We have built a halo model that fits the simulation results well. In this model, the modifications to gravity operate on all scales with equal strength, and its impact on observables (cf. Figs. 6.4, 6.7, 6.8) is kept at the $10\% - 15\%$ level. Planned observational missions will be accurate enough to pinpoint these differences [348, 350, 351, 427]. The absence of a screening mechanism in this model puts it in tension with Solar System tests, in a way that is similar to the case of the Quartic Galileon model.

8.1.4 Cluster and void lensing in the Cubic Galileon and Nonlocal gravity models

Contrary to the popular cases of $f(R)$ and DGP gravity, the Galileon and Nonlocal gravity models also modify the gravitational lensing potential. Part of the analysis in Chapter 7 was devoted to the study of the lensing effects associated with galaxy clusters in these two models of gravity. In particular, our goal was to determine if the direct modifications to the lensing potential lead to any systematic bias in the observational determinations of cluster masses from lensing. We used the lensing convergence profiles of X-ray selected galaxy clusters from the CLASH survey. We paid attention to the role played by certain model dependent assumptions involving the background cosmology and non-parametric/parametric lensing reconstructions, which are made in the data analysis and could bias the interpretation of the results in alternative models. We have seen

that the mass and concentration estimates of the clusters remain unchanged w.r.t. ΛCDM (cf. Fig. 7.2). This is due to the relatively small size of the fifth force in the Nonlocal model at the cluster redshifts and to the strong efficiency of the screening in the Cubic Galileon model. In the Cubic Galileon model, however, the screening becomes less efficient outside of the cluster radius, which should impact the estimation of the dynamical mass of the cluster from the velocity distribution of surrouding galaxies. *This means that, despite the direct modifications to the lensing potential, tests of gravity based on comparisons of dynamical and lensing masses can still be applied to the Cubic Galileon model* (cf. Fig. 7.5).

Finally, in the second part of Chapter 7, we studied the lensing signal produced by cosmic voids found in the simulations of the Cubic Galileon and Nonlocal models. In these models, the modifications to the lensing signal are driven not only by the different void profiles (determined by the dynamical potential), but also by the intrinsic modifications to the lensing potential. In the Cubic Galileon and Nonlocal models, this results in a boost of the lensing signal of order 100% and 10%, respectively (cf. Fig. 7.11). The large effect in the Cubic Galileon is attributed to the fact that the fifth force is unscreened in voids, and hence, its effects are manifested very prominently. *Our results open prospects to use voids in tests of gravity, specially after the recent detection of the lensing signal in voids found in real galaxy catalogues [413, 414].*

8.2   Future research directions

Naturally, the work developed for this thesis could only cover a finite number of investigations of the phenomenology of the Galileon and Nonlocal gravity models. Next, and before we finish, we briefly outline what we believe are amongst the most interesting ways to extend our analysis, not only for these two models, but for modified gravity theories in general.

Tests of gravity in low density regions

Voids The picture depicted in Chapter 7 that the lensing signal inside voids can provide useful contraints on modified gravity models strongly motivates further studies. The steps to improve our analysis have already been outlined in Sec. 7.3.6.

Statistics of the log-density field Along the same lines to shift focus towards low density
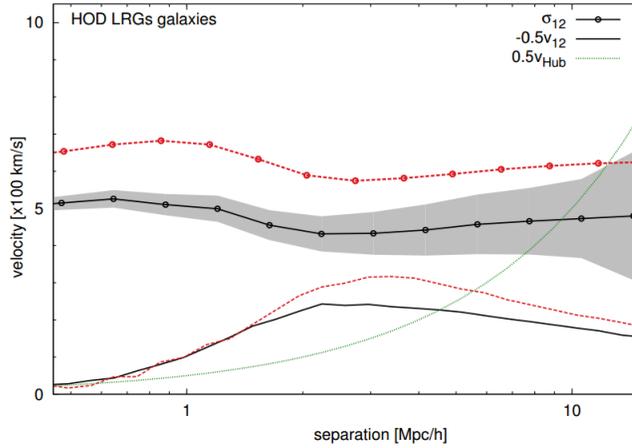
Figure 8.1: The scale dependence of the pairwise velocity moments extracted from HOD mock galaxy catalogues of $f(R)$ gravity (Hu-Sawicki model with $|f_{\mathcal{R}0}| = 10^{-4}$). The black lines show the GR case, while the red lines show the $f(R)$ model. The thin red and black lines show minus the mean streaming velocity, $-v_{12}(r)$, scaled down by a factor of 2 for clarity; the lines with filled circles show the dispersion, $\sigma_{12}(r)$; The shaded region represents an illustrative error as in Refs. [430, 431]. The dotted green line shows the Hubble velocity, $H_0 r$, also scaled by $1/2$. Figure taken from Ref. [11].

regions, it is also interesting to investigate whether different theories of gravity can be more easily distinguished by analysing the fluctuations in the logarithm of the density field, instead of the density field itself [428]. This *log-transform* transfers weight from the high-density to the low-density regions, which could potentially amplify the differences between different gravity models. Reference [429] has recently taken the first steps in this direction. There, the authors make use also of the *clipping* technique to suppress the contributions from high-density peaks.

Velocity statistics

Statistics of the peculiar velocity field The lines with circles in Figure 8.1 show the projected pairwise velocity dispersion, σ_{12}, of HOD galaxies as a function of galaxy separation for GR (black) and the Hu-Sawicki $f(R)$ model with $|f_{\mathcal{R}0}| = 10^{-4}$. The figure, which was obtained in Ref. [11], shows that there is a visible offset between GR and the modified gravity prediction, and that this occurs for a wide range of scales. The velocity field may be more sensitive than the density field to modified gravity because velocities are affected

since earlier times, i.e., the spatial distribution of the galaxies is only affected after their velocities are boosted. Currently, the most accurate peculiar velocity catalogues, such as the `Cosmicflows-2` compilation [432], are obtained by making use of the empirical Tully-Fisher (for late-type galaxies) and Fundamental Plane (for early-type galaxies). However, there are complications associated with some systematics in the determination of galaxy peculiar velocities [432]. These should be properly assessed before confronting theory and observations.

Scale-dependent measurements of $f\sigma_8$ As we discussed in Sec. 3.3.3, the assumption that the linear growth rate of structure is scale-independent in measurements of $f\sigma_8$ currently limits the constraining power of these data. A first step towards scale-dependent determinations of $f\sigma_8$ was recently taken in Ref. [433], where the authors use data from galaxy peculiar velocity catalogues to determine $f\sigma_8$ in a series of k-space bins. The results show no evidence for a scale-dependent growth, but the analysis is heavily model dependent as it assumes ΛCDM in the calculation of the velocity divergence power spectrum. A detection of a scale-dependent growth on large scales could be a sign of massive neutrinos and/or modifications to gravity, which motivates extensions to the analysis of Ref. [433] (see Ref. [89] for a recent work along these lines).

Similar studies for other modified gravity models

Judging from the theoretical developments in modified gravity over the past few years, it is reasonable to anticipate that novel models will keep being proposed in the literature. A recent example is the K-mouflage model studied in Refs. [12, 59, 60, 81, 82]. The analysis shown in this thesis for Galileon and Nonlocal gravity can therefore be repeated for this model, for which a few preliminary results have already been obtained. These are shown in Fig. 8.2 for the CMB lensing potential (upper panel) and linear matter (lower panel) power spectra. The results are shown for a model with the action of Eq. (1.13),

$$S = \int \mathrm{d}^4 x \sqrt{-g} \left[\frac{\mathcal{R}}{16\pi G} + \mathcal{L}_m \left(A(\varphi), g_{\mu\nu} \right) + K\left(\chi\right) \right], \tag{8.1}$$

with

$$K = -1 + \chi + K_0 \chi^m \; ; \qquad A(\varphi) = e^{\beta\varphi/M_{\mathrm{Pl}}}, \tag{8.2}$$
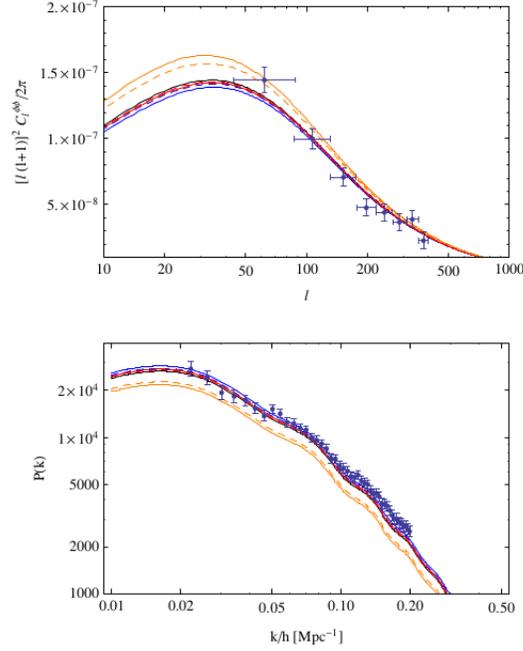
Figure 8.2: CMB lensing potential (upper panel) and linear matter (lower panel, in $\mathrm{Mpc}^3/\mathrm{h}^3$ units) power spectra for the K-mouflage model. The ΛCDM result is shown by the solid black line. The blue, red and orange lines correspond, respectively, to the choice of parameters $(K_0, \beta) = (100, 0.2), (100, 0.1), (-5, 0.2)$ in Eq. (8.2). The solid and dashed lines are for $m = 3$ and $m = 2$, respectively. The datapoints are the same as in Fig. 3.4. Figure taken from Ref. [12].

where $\chi = \nabla^\mu \varphi \nabla_\mu \varphi / 2\mathcal{M}^4$ and $\mathcal{M}$ is a mass scale. The model parameters are K_0, β and m. Reference [82] has recently shown that although this functional form for $K(\chi)$ is ruled out by Solar system tests, it is possible to construct viable models with similar cosmological predictions. The cosmology of this model has been discussed with great detail in Ref. [12] for a limited number of cosmological parameter values. Here we comment only on a particularly interesting result, which is that the same set of parameter choices can lead to opposite shifts in the amplitudes of the linear matter and CMB lensing potential power spectra. This is more readily apparent in the model of the orange lines, for which the amplitude of the lensing potential power spectrum is boosted, but the amplitude of the linear matter power spectrum is suppressed, relative to ΛCDM. This seems counterintuitive since both these spectra are generally portrayed as being proportional to the amount of matter clustering in the Universe. The origin of this result is linked to the different effects of the

coupling function $A(\varphi)$ on what determines exactly these two observables (see Ref. [12] for the details). In short, the coupling function scales the matter fluctuations, $\delta\rho_m$, by a factor of $A(\varphi)$. This affects the lensing potential, which is is proportional to $\delta\rho_m$. However, the coupling function also scales the background density, $\bar{\rho}_m$, by the same factor. Hence, the linear matter power spectrum, being sensitive to $\delta = \delta\rho_m/\bar{\rho}_m$, is not affected directly by $A(\varphi)$ because the dependence cancels out. Future work on this model could involve assessing the type of constraints that this interesting feature can leave on the parameter space of the model. The methods developed in Chapters 5 and 6 to study nonlinear structure formation in the Galileon and Nonlocal models can also be applied to this K-mouflage model, as well as other existing (and yet to be proposed) models.

Galaxy formation with modified gravity

The majority of the nonlinear studies in modified gravity are mostly based on dark matter only N-body simulations. However, in order to make a clearer connection between theory and observations, it is of interest to investigate how galaxies form and evolve in cosmologies with modified gravity. Some steps in this direction have already been taken by Ref. [434], where the authors coupled semi-analytical models of galaxy formation with results from (dark matter only) N-body simulations of the Hu-Sawicki $f(R)$ model. In principle, similar analysis can also be performed for other modified gravity models. The coupling of semi-analytical models to modified gravity simulations is not straightforward as care needs to be taken to ensure that the equations of the semi-analytical models are appropriately modified to take the effects of the screening mechanisms into account.

Instead of studying galaxy evolution with semi-analytical models, one can also solve for galaxy formation in the simulations directly. The majority of the current N-body algorithms for modified gravity [278, 435, 436] are built on top of numerical codes (RAMSES [291] and/or GADGET [437]) that have been used previously to run N-body simulations of galaxy formation. As a result, it would be interesting to couple the machinery developed for modified gravity simulations to that developed for galaxy formation in GR. One of the main current difficulties is that simulations of galaxy formation require high mass resolution, which would make the modified gravity algorithms very computationally expensive. One of the first steps towards modified gravity simulations of galaxy formation should then involve designing ways to speed up the modified gravity solvers for cases of high

mass resolution.

8.3 Concluding remarks

Modified gravity scenarios are one of the most popular theoretical alternatives to ΛCDM and will be tested by experiments like DESI [350], LSST [351] and Euclid [348]. These surveys will reach unprecedented statistical precision in measurements of the expansion rate and large-scale structure of the Universe. As a result, it is essential to ensure that we understand the physics of ΛCDM and competing models to the same extent. We therefore believe that the extensive analysis presented here for Galileon and Nonlocal gravity models is an example of what should be done for other existing (and also yet to be proposed) models. This should serve to improve current techniques in the theoretical modeling and data analysis to design new observational tests and avoid catastrophic systematic errors in the interpretation of these upcoming surveys. Some of the surveys listed above will have first light in a few years time, which makes investigations such as the ones presented in this thesis particularly timely.

Bibliography

[1] Alexandre Barreira, Baojiu Li, Carlton M. Baugh, and Silvia Pascoli. Linear perturbations in Galileon gravity models. *Phys.Rev.*, D86:124016, 2012, 1208.0600.

[2] Alexandre Barreira, Baojiu Li, Ariel Sanchez, Carlton M. Baugh, and Silvia Pascoli. The parameter space in Galileon gravity models. *Phys.Rev.*, D87:103511, 2013, 1302.6241.

[3] Alexandre Barreira, Baojiu Li, Carlton Baugh, and Silvia Pascoli. νGalileon: modified gravity with massive neutrinos as a testable alternative to ΛCDM. 2014, 1404.1365.

[4] Alexandre Barreira, Baojiu Li, Carlton Baugh, and Silvia Pascoli. The observational status of Galileon gravity after Planck. 2014, 1406.0485.

[5] Alexandre Barreira, Baojiu Li, Carlton M. Baugh, and Silvia Pascoli. Spherical collapse in Galileon gravity: fifth force solutions, halo mass function and halo bias. *JCAP*, 1311:056, 2013, 1308.3699.

[6] Alexandre Barreira, Baojiu Li, Wojciech A. Hellwing, Carlton M. Baugh, and Silvia Pascoli. Nonlinear structure formation in the Cubic Galileon gravity model. *JCAP*, 2013(10):027, 2013, 1306.3219.

[7] Alexandre Barreira, Baojiu Li, Wojciech A. Hellwing, Lucas Lombriser, Carlton M. Baugh, et al. Halo model and halo properties in Galileon gravity cosmologies. 2014, 1401.1497.

[8] Alexandre Barreira, Baojiu Li, Wojciech A. Hellwing, Carlton M. Baugh, and Silvia Pascoli. Nonlinear structure formation in Nonlocal Gravity. *JCAP*, 1409(09):031, 2014, 1408.1084.

[9] A. Barreira, B. Li, E. Jennings, J. Merten, L. King, C. Baugh, and S. Pascoli. Galaxy cluster lensing masses in modified lensing potentials. *ArXiv e-prints*, May 2015, 1505.03468.

[10] A. Barreira, M. Cautun, B. Li, C. Baugh, and S. Pascoli. Weak lensing by voids in modified lensing potentials. *ArXiv e-prints*, May 2015, 1505.05809.

[11] Wojciech A. Hellwing, Alexandre Barreira, Carlos S. Frenk, Baojiu Li, and Shaun Cole. A clear and measurable signature of modified gravity in the galaxy velocity field. 2014, 1401.0706.

[12] Alexandre Barreira, Philippe Brax, Sebastien Clesse, Baojiu Li, and Patrick Valageas. Linear perturbations in K-mouflage cosmologies with massive neutrinos. 2014, 1411.5965.

[13] P.A.R. Ade et al. Planck 2015 results. XIII. Cosmological parameters. 2015, 1502.01589.

[14] Adam G. Riess et al. Observational evidence from supernovae for an accelerating universe and a cosmological constant. *Astron.J.*, 116:1009–1038, 1998, astro-ph/9805201.

[15] S. Perlmutter et al. Measurements of Omega and Lambda from 42 high redshift supernovae. *Astrophys.J.*, 517:565–586, 1999, astro-ph/9812133.

[16] Shaun Cole et al. The 2dF Galaxy Redshift Survey: Power-spectrum analysis of the final dataset and cosmological implications. *Mon.Not.Roy.Astron.Soc.*, 362:505–534, 2005, astro-ph/0501174.

[17] Daniel J. Eisenstein et al. Detection of the baryon acoustic peak in the large-scale correlation function of SDSS luminous red galaxies. *Astrophys.J.*, 633:560–574, 2005, astro-ph/0501171.

[18] S. W. Allen, A. E. Evrard, and A. B. Mantz. Cosmological Parameters from Observations of Galaxy Clusters. *araa*, 49:409–470, September 2011, 1103.4829.

[19] P.A.R. Ade et al. Planck 2015 results. XXIV. Cosmology from Sunyaev-Zeldovich cluster counts. 2015, 1502.01597.

[20] C. Heymans, L. Van Waerbeke, L. Miller, T. Erben, H. Hildebrandt, H. Hoekstra, T. D. Kitching, Y. Mellier, P. Simon, C. Bonnett, J. Coupon, L. Fu, J. Harnois Déraps, M. J. Hudson, M. Kilbinger, K. Kuijken, B. Rowe, T. Schrabback, E. Semboloni, E. van Uitert, S. Vafaei, and M. Velander. CFHTLenS: the Canada-France-Hawaii Telescope Lensing Survey. *MNRAS*, 427:146–166, November 2012, 1210.0032.

[21] Catherine Heymans, Emma Grocutt, Alan Heavens, Martin Kilbinger, Thomas D. Kitching, et al. CFHTLenS tomographic weak lensing cosmological parameter constraints: Mitigating the impact of intrinsic galaxy alignments. 2013, 1303.1808.

[22] M.C. Gonzalez-Garcia, Michele Maltoni, Jordi Salvado, and Thomas Schwetz. Global fit to three neutrino mixing: critical look at present precision. *JHEP*, 1212:123, 2012, 1209.3023.

[23] Ch. Kraus, B. Bornschein, L. Bornschein, J. Bonn, B. Flatt, et al. Final results from phase II of the Mainz neutrino mass search in tritium beta decay. *Eur.Phys.J.*, C40: 447–468, 2005, hep-ex/0412056.

[24] V.N. Aseev et al. An upper limit on electron antineutrino mass from Troitsk experiment. *Phys.Rev.*, D84:112003, 2011, 1108.5034.

[25] Gianfranco Bertone, Dan Hooper, and Joseph Silk. Particle dark matter: Evidence, candidates and constraints. *Phys.Rept.*, 405:279–390, 2005, hep-ph/0404175.

[26] Manuel Drees and Gilles Gerbier. Mini-Review of Dark Matter: 2012. 2012, 1204.2373.

[27] J. Kormendy and G. R. Knapp, editors. *Dark matter in the universe; Proceedings of the IAU Symposium, Institute for Advanced Study and Princeton University, Princeton, NJ, June 24-28, 1985*, volume 117 of *IAU Symposium*, 1987.

[28] V. Trimble. Existence and nature of dark matter in the universe. *ARAA*, 25:425–472, 1987.

[29] K. G. Begeman, A. H. Broeils, and R. H. Sanders. Extended rotation curves of spiral galaxies - Dark haloes and modified dynamics. *MNRAS*, 249:523–537, April 1991.

[30] Neta A. Bahcall and Xiao-hui Fan. The Most massive distant clusters: Determining omega and σ_8. *Astrophys.J.*, 504:1, 1998, astro-ph/9803277.

[31] Douglas Clowe, Marusa Bradac, Anthony H. Gonzalez, Maxim Markevitch, Scott W. Randall, et al. A direct empirical proof of the existence of dark matter. *Astrophys.J.*, 648:L109–L113, 2006, astro-ph/0608407.

[32] C. S. Frenk, S. D. M. White, and M. Davis. Nonlinear evolution of large-scale structure in the universe. *APJ*, 271:417–430, August 1983.

[33] Matteo Viel, George D. Becker, James S. Bolton, and Martin G. Haehnelt. Warm dark matter as a solution to the small scale crisis: New constraints from high redshift Lyman- forest data. *Phys.Rev.*, D88:043502, 2013, 1306.2314.

[34] J. Richard Bond, Lev Kofman, and Dmitri Pogosyan. How filaments are woven into the cosmic web. *Nature*, 380:603–606, 1996, astro-ph/9512141.

[35] J.E. Forero-Romero, Y. Hoffman, S. Gottloeber, A. Klypin, and G. Yepes. A Dynamical Classification of the Cosmic Web. *Mon.Not.Roy.Astron.Soc.*, 396:1815–1824, 2009, 0809.4135.

[36] M. Cautun, R. van de Weygaert, and B. J. T. Jones. NEXUS: tracing the cosmic web connection. *Mon.Not.Roy.Astron.Soc.*, 429:1286–1308, February 2013, 1209.2043.

[37] G. Efstathiou. An anthropic argument for a cosmological constant. *MNRAS*, 274: L73–L76, June 1995.

[38] A. Barreira and P. P. Avelino. Anthropic versus cosmological solutions to the coincidence problem. *PRD*, 83(10):103001, May 2011, 1103.2401.

[39] J.A. Peacock. Testing anthropic predictions for Lambda and the CMB temperature. *Mon.Not.Roy.Astron.Soc.*, 379:1067–1074, 2007, 0705.0898.

[40] Clifford M. Will. The Confrontation between General Relativity and Experiment. 2014, 1403.7377.

[41] Austin Joyce, Bhuvnesh Jain, Justin Khoury, and Mark Trodden. Beyond the Cosmological Standard Model. 2014, 1407.0059.

[42] T. Clifton, P. G. Ferreira, A. Padilla, and C. Skordis. Modified gravity and cosmology. *PHYSREP*, 513:1–189, March 2012, 1106.2476.

[43] Kazuya Koyama. Cosmological Tests of Gravity. 2015, 1504.04623.

[44] Bhuvnesh Jain and Pengjie Zhang. Observational Tests of Modified Gravity. *Phys.Rev.*, D78:063503, 2008, 0709.2375.

[45] Bhuvnesh Jain, Austin Joyce, Rodger Thompson, Amol Upadhye, James Battat, et al. Novel Probes of Gravity and Dark Energy. 2013, 1309.5389.

[46] Emanuele Berti, Enrico Barausse, Vitor Cardoso, Leonardo Gualtieri, Paolo Pani, et al. Testing General Relativity with Present and Future Astrophysical Observations. 2015, 1501.07274.

[47] Gia Dvali, Stefan Hofmann, and Justin Khoury. Degravitation of the cosmological constant and graviton width. *Phys.Rev.*, D76:084006, 2007, hep-th/0703027.

[48] Kazuya Koyama. The cosmological constant and dark energy in braneworlds. *Gen.Rel.Grav.*, 40:421–450, 2008, 0706.1557.

[49] Ivaylo Zlatev, Li-Min Wang, and Paul J. Steinhardt. Quintessence, cosmic coincidence, and the cosmological constant. *Phys.Rev.Lett.*, 82:896–899, 1999, astro-ph/9807002.

[50] L. Amendola. Coupled quintessence. Phys. Rev. D, 62(4):043511, 2000, arXiv:astro-ph/9908023.

[51] Valeria Pettorino and Carlo Baccigalupi. Coupled and Extended Quintessence: theoretical differences and structure formation. *Phys.Rev.*, D77:103003, 2008, 0802.1086.

[52] Thomas P. Sotiriou and Valerio Faraoni. f(R) Theories Of Gravity. *Rev.Mod.Phys.*, 82: 451–497, 2010, 0805.1726.

[53] Antonio De Felice and Shinji Tsujikawa. f(R) theories. *Living Rev.Rel.*, 13:3, 2010, 1002.4928.

[54] Wayne Hu and Ignacy Sawicki. Models of f(R) Cosmic Acceleration that Evade Solar-System Tests. *Phys.Rev.*, D76:064004, 2007, 0705.1158.

[55] Philippe Brax, Carsten van de Bruck, Anne-Christine Davis, and Douglas J. Shaw. f(R) Gravity and Chameleon Theories. *Phys.Rev.*, D78:104021, 2008, 0806.3415.

[56] Alberto Nicolis, Riccardo Rattazzi, and Enrico Trincherini. Galileon as a local modification of gravity. *Phys. Rev. D*, 79:064036, 2009.

[57] C. Deffayet, G. Esposito-Farèse, and A. Vikman. Covariant galileon. *Phys. Rev. D*, 79: 084003, 2009.

[58] E. Babichev, C. Deffayet, and R. Ziour. k-Mouflage gravity. *Int.J.Mod.Phys.*, D18: 2147–2154, 2009, 0905.2943.

[59] Philippe Brax and Patrick Valageas. K-mouflage Cosmology: the Background Evolution. *Phys.Rev.*, D90(2):023507, 2014, 1403.5420.

[60] Philippe Brax and Patrick Valageas. K-mouflage Cosmology: Formation of Large-Scale Structures. 2014, 1403.5424.

[61] Stanley Deser and R.P. Woodard. Nonlocal Cosmology. *Phys.Rev.Lett.*, 99:111301, 2007, 0706.2151.

[62] S. Deser and R.P. Woodard. Observational Viability and Stability of Nonlocal Cosmology. *JCAP*, 1311:036, 2013, 1307.6639.

[63] R.P. Woodard. Nonlocal Models of Cosmic Acceleration. *Found.Phys.*, 44:213–233, 2014, 1401.0254.

[64] G. Dvali, G. Gabadadze, and M. Porrati. 4D gravity on a brane in 5D Minkowski space. *Phys. Lett. B*, 485:208–214, 2000, arXiv:hep-th/0005016.

[65] Markus A. Luty, Massimo Porrati, and Riccardo Rattazzi. Strong interactions and stability in the dgp model. *JHEP*, 2003(09):029, 2003.

[66] Alberto Nicolis and Riccardo Rattazzi. Classical and quantum consistency of the dgp model. *JHEP*, 2004(06):059, 2004.

[67] Dmitry Gorbunov, Kazuya Koyama, and Sergei Sibiryakov. More on ghosts in the dvali-gabadaze-porrati model. *Phys. Rev. D*, 73:044016, 2006.

[68] Ruth Gregory, Nemanja Kaloper, Robert C. Myers, and Antonio Padilla. A New perspective on DGP gravity. *JHEP*, 0710:069, 2007, 0707.2666.

[69] Wenjuan Fang, Sheng Wang, Wayne Hu, Zoltan Haiman, Lam Hui, et al. Challenges to the DGP Model from Horizon-Scale Growth and Geometry. *Phys.Rev.*, D78:103509, 2008, 0808.2208.

[70] Justin Khoury and Amanda Weltman. Chameleon cosmology. *Phys.Rev.*, D69:044026, 2004, astro-ph/0309411.

[71] Justin Khoury and Amanda Weltman. Chameleon fields: Awaiting surprises for tests of gravity in space. *Phys.Rev.Lett.*, 93:171104, 2004, astro-ph/0309300.

[72] Keith A. Olive and Maxim Pospelov. Environmental dependence of masses and coupling constants. *Phys.Rev.*, D77:043524, 2008, 0709.3825.

[73] Kurt Hinterbichler and Justin Khoury. Symmetron Fields: Screening Long-Range Forces Through Local Symmetry Restoration. *Phys.Rev.Lett.*, 104:231301, 2010, 1001.4525.

[74] Kurt Hinterbichler, Justin Khoury, Aaron Levy, and Andrew Matas. Symmetron Cosmology. *Phys.Rev.*, D84:103521, 2011, 1107.2112.

[75] T. Damour, G. W. Gibbons, and C. Gundlach. Dark matter, time-varying G, and a dilaton field. *Phys. Rev. Lett.*, 64:123–126, 1990.

[76] Philippe Brax, Carsten van de Bruck, Anne-Christine Davis, and Douglas Shaw. The Dilaton and Modified Gravity. *Phys.Rev.*, D82:063519, 2010, 1005.3735.

[77] Philippe Brax, Carsten van de Bruck, Anne-Christine Davis, Baojiu Li, and Douglas J. Shaw. Nonlinear Structure Formation with the Environmentally Dependent Dilaton. *Phys.Rev.*, D83:104026, 2011, 1102.3692.

[78] A.I. Vainshtein. To the problem of nonvanishing gravitation mass. *Phys. Lett. B*, 39 (3):393 – 394, 1972. ISSN 0370-2693.

[79] Eugeny Babichev and Cedric Deffayet. An introduction to the Vainshtein mechanism. 2013, 1304.7240.

[80] Kazuya Koyama, Gustavo Niz, and Gianmassimo Tasinato. Effective theory for Vainshtein mechanism from Horndeski action. 2013, 1305.0279.

[81] Philippe Brax and Patrick Valageas. Small-scale Nonlinear Dynamics of K-mouflage Theories. *Phys.Rev.*, D90(12):123521, 2014, 1408.0969.

[82] Alexandre Barreira, Philippe Brax, Sebastien Clesse, Baojiu Li, and Patrick Valageas. K-mouflage gravity models that pass Solar System and cosmological constraints. 2015, 1504.01493.

[83] Tessa Baker, Pedro G. Ferreira, Constantinos Skordis, and Joe Zuntz. Towards a fully consistent parameterization of modified gravity. *Phys.Rev.*, D84:124018, 2011, 1107.0491.

[84] Tessa Baker, Pedro G. Ferreira, and Constantinos Skordis. The Parameterized Post-Friedmann Framework for Theories of Modified Gravity: Concepts, Formalism and Examples. 2012, 1209.2117.

[85] Robert Caldwell, Asantha Cooray, and Alessandro Melchiorri. Constraints on a New Post-General Relativity Cosmological Parameter. *Phys.Rev.*, D76:023507, 2007, astro-ph/0703375.

[86] Luca Amendola, Martin Kunz, and Domenico Sapone. Measuring the dark side (with weak lensing). *JCAP*, 0804:013, 2008, 0704.2421.

[87] C. Danielle Leonard, Tessa Baker, and Pedro G. Ferreira. Exploring degeneracies in modified gravity with weak lensing. 2015, 1501.03509.

[88] Jason N. Dossett, Mustapha Ishak, David Parkinson, and Tamara Davis. Constraints and tensions in testing general relativity from Planck and CFHTLenS including intrinsic alignment systematics. 2015, 1501.03119.

[89] Andrew Johnson, Chris Blake, Jason Dossett, Jun Koda, David Parkinson, et al. Searching for Modified Gravity: Scale and Redshift Dependent Constraints from Galaxy Peculiar Velocities. 2015, 1504.06885.

[90] J. Bloomfield, É. É. Flanagan, M. Park, and S. Watson. Dark energy or modified gravity? An effective field theory approach. *JCAP*, 8:10, August 2013, 1211.7054.

[91] Giulia Gubitosi, Federico Piazza, and Filippo Vernizzi. The Effective Field Theory of Dark Energy. 2012, 1210.0201.

[92] Bin Hu, Marco Raveri, Noemi Frusciante, and Alessandra Silvestri. Effective Field Theory of Cosmic Acceleration: an implementation in CAMB. *Phys.Rev.*, D89(10): 103530, 2014, 1312.5742.

[93] Marco Raveri, Bin Hu, Noemi Frusciante, and Alessandra Silvestri. Effective Field Theory of Cosmic Acceleration: constraining dark energy with CMB data. *Phys.Rev.*, D90(4):043513, 2014, 1405.1022.

[94] Richard A. Battye and Jonathan A. Pearson. Effective action approach to cosmological perturbations in dark energy and modified gravity. *JCAP*, 1207:019, 2012, 1203.0398.

[95] Richard A. Battye and Jonathan A. Pearson. Parametrizing dark sector perturbations via equations of state. *Phys.Rev.*, D88(6):061301, 2013, 1306.1175.

[96] Richard A. Battye and Jonathan A. Pearson. Computing model independent perturbations in dark energy and modified gravity. *JCAP*, 1403:051, 2014, 1311.6737.

[97] P.A.R. Ade et al. Planck 2015 results. XIV. Dark energy and modified gravity. 2015, 1502.01590.

[98] Philippe Brax, Anne-Christine Davis, Baojiu Li, and Hans A. Winther. A Unified Description of Screened Modified Gravity. 2012, 1203.4812.

[99] Philippe Brax, Anne-Christine Davis, Baojiu Li, Hans A. Winther, and Gong-Bo Zhao. Systematic Simulations of Modified Gravity: Symmetron and Dilaton Models. 2012, 1206.3568.

[100] Philippe Brax, Anne-C. Davis, Baojiu Li, Hans A. Winther, and Gong-Bo Zhao. Systematic simulations of modified gravity: chameleon models. *JCAP*, 1304:029, 2013, 1303.0007.

[101] Bin Hu, Michele Liguori, Nicola Bartolo, and Sabino Matarrese. Parametrized modified gravity constraints after Planck. *Phys.Rev.*, D88(12):123514, 2013, 1307.5276.

[102] Andrea Marchini and Valentina Salvatelli. Updated constraints from the PLANCK experiment on modified gravity. *Phys.Rev.*, D88(2):027502, 2013, 1307.2002.

[103] B. Jain, V. Vikram, and J. Sakstein. Astrophysical Tests of Modified Gravity: Constraints from Distance Indicators in the Nearby Universe. *APJ*, 779:39, December 2013, 1204.6044.

[104] Vinu Vikram, Anna Cabr, Bhuvnesh Jain, and J.T. VanderPlas. Astrophysical Tests of Modified Gravity: the Morphology and Kinematics of Dwarf Galaxies. *JCAP*, 1308: 020, 2013, 1303.0295.

[105] G.-B. Zhao, B. Li, and K. Koyama. Testing Gravity Using the Environmental Dependence of Dark Matter Halos. *Physical Review Letters*, 107(7):071303, August 2011, 1105.0922.

[106] B. Li, G.-B. Zhao, and K. Koyama. Haloes and voids in f(R) gravity. *MNRAS*, 421: 3481–3487, April 2012, 1111.2602.

[107] A. Cabré, V. Vikram, G.-B. Zhao, B. Jain, and K. Koyama. Astrophysical tests of gravity: a screening map of the nearby universe. *JCAP*, 7:34, July 2012, 1204.6046.

[108] B. Li, W. A. Hellwing, K. Koyama, G.-B. Zhao, E. Jennings, and C. M. Baugh. The nonlinear matter and velocity power spectra in f(R) gravity. *Mon.Not.Roy.Astron.Soc.*, 428:743–755, January 2013, 1206.4317.

[109] W. A. Hellwing, B. Li, C. S. Frenk, and S. Cole. Hierarchical clustering in chameleon f(R) gravity. *Mon.Not.Roy.Astron.Soc.*, 435:2806–2821, November 2013, 1305.7486.

[110] Atsushi Taruya, Takahiro Nishimichi, Francis Bernardeau, Takashi Hiramatsu, and Kazuya Koyama. Regularized cosmological power spectrum and correlation function in modified gravity models. *Phys.Rev.*, D90(12):123515, 2014, 1408.4232.

[111] Difu Shi, Baojiu Li, Jiaxin Han, Liang Gao, and Wojciech A. Hellwing. Exploring the liminality: properties of haloes and subhaloes in borderline $f(R)$ gravity. 2015, 1503.01109.

[112] Lucas Lombriser, Kazuya Koyama, and Baojiu Li. Halo modelling in chameleon theories. 2013, 1312.1292.

[113] Max Gronke, Claudio Llinares, David F. Mota, and Hans A. Winther. Halo velocity profiles in screened modified gravity theories. *Mon.Not.Roy.Astron.Soc.*, 449:2837, 2015, 1412.0066.

[114] Matteo Cataneo, David Rapetti, Fabian Schmidt, Adam B. Mantz, Steven W. Allen, et al. New constraints on $f(R)$ gravity from clusters of galaxies. 2014, 1412.0133.

[115] Elise Jennings, Carlton M. Baugh, Baojiu Li, Gong-Bo Zhao, and Kazuya Koyama. Redshift space distortions in f(R) gravity. 2012, 1205.2698.

[116] J. Clampitt, Y.-C. Cai, and B. Li. Voids in modified gravity: excursion set predictions. *MNRAS*, 431:749–766, May 2013, 1212.2216.

[117] Yan-Chuan Cai, Nelson Padilla, and Baojiu Li. Testing Gravity using Cosmic Voids. 2014, 1410.1510.

[118] Yan-Chuan Cai, Baojiu Li, Shaun Cole, Carlos S. Frenk, and Mark Neyrinck. The Integrated Sachs-Wolfe effect in $f(R)$ gravity. 2013, 1310.6986.

[119] Christian Arnold, Ewald Puchwein, and Volker Springel. Scaling relations and mass bias in hydrodynamical f(R) gravity simulations of galaxy clusters. *Mon.Not.Roy.Astron.Soc.*, 440(1):833–842, 2014, 1311.5560.

[120] Christian Arnold, Ewald Puchwein, and Volker Springel. The Lyman-alpha forest in f(R) modified gravity. *Mon.Not.Roy.Astron.Soc.*, 448:2275, 2015, 1411.2600.

[121] Lucas Lombriser. Constraining chameleon models with cosmology. *Annalen Phys.*, 526:259–282, 2014, 1403.4268.

[122] L. Lombriser, W. Hu, W. Fang, and U. Seljak. Cosmological constraints on DGP braneworld gravity with brane tension. *PRD*, 80(6):063536, September 2009, 0905.1112.

[123] F. Schmidt. Cosmological simulations of normal-branch braneworld gravity. *prd*, 80 (12):123003, December 2009, 0910.0235.

[124] Baojiu Li, Gong-Bo Zhao, and Kazuya Koyama. Exploring Vainshtein mechanism on adaptively refined meshes. *JCAP*, 1305:023, 2013, 1303.0008.

[125] T. Y. Lam, T. Nishimichi, F. Schmidt, and M. Takada. Testing Gravity with the Stacked Phase Space around Galaxy Clusters. *Physical Review Letters*, 109(5):051301, August 2012, 1202.4501.

[126] Ying Zu, D.H. Weinberg, Elise Jennings, Baojiu Li, and Mark Wyman. Galaxy Infall Kinematics as a Test of Modified Gravity. 2013, 1310.6768.

[127] Bridget Falck, Kazuya Koyama, Gong-bo Zhao, and Baojiu Li. The Vainshtein Mechanism in the Cosmic Web. *JCAP*, 1407:058, 2014, 1404.2206.

[128] Bridget Falck, Kazuya Koyama, and Gong-bo Zhao. Cosmic Web and Environmental Dependence of Screening: Vainshtein vs. Chameleon. 2015, 1503.06673.

[129] A.-C. Davis, B. Li, D. F. Mota, and H. A. Winther. Structure Formation in the Symmetron Model. *APJ*, 748:61, March 2012, 1108.3081.

[130] Claudio Llinares and David F. Mota. Cosmological simulations of screened modified gravity out of the static approximation: effects on matter distribution. 2013, 1312.6016.

[131] Baojiu Li and John D. Barrow. N-Body Simulations for Coupled Scalar Field Cosmology. *Phys.Rev.*, D83:024007, 2011, 1005.4231.

[132] B. Li, D. F. Mota, and J. D. Barrow. N-body Simulations for Extended Quintessence Models. *APJ*, 728:109, February 2011, 1009.1400.

[133] Marco Baldi, Valeria Pettorino, Georg Robbers, and Volker Springel. Hydrodynamical N-body simulations of coupled dark energy cosmologies. *Mon.Not.Roy.Astron.Soc.*, 403:1684–1702, 2010, 0812.3901.

[134] Andrea V. Maccio, Claudia Quercellini, Roberto Mainini, Luca Amendola, and Silvio A. Bonometto. N-body simulations for coupled dark energy: Halo mass function and density profiles. *Phys.Rev.*, D69:123516, 2004, astro-ph/0309671.

[135] Camilla Penzo, Andrea V. Macci, Marco Baldi, Luciano Casarini, and Jose Oorbe. Effects of Coupled Dark Energy on the Milky Way and its Satellites. 2015, 1504.07243.

[136] M. Maggiore and M. Mancarella. Non-local gravity and dark energy. *Phys.Rev.*, D90: 023005, 2014, 1402.0448.

[137] J. Merten, M. Meneghetti, M. Postman, K. Umetsu, A. Zitrin, et al. CLASH: The Concentration-Mass Relation of Galaxy Clusters. 2014, 1404.1376.

[138] M. A. Luty, M. Porrati, and R. Rattazzi. Strong interactions and stability in the DGP model. *JHEP*, 9:29, 2003, arXiv:hep-th/0303116.

[139] A. Nicolis and R. Rattazzi. Classical and Quantum Consistency of the DGP Model. *JHEP*, 6:59, 2004, arXiv:hep-th/0404159.

[140] Richard P. Woodard. Avoiding dark energy with 1/r modifications of gravity. *Lect.Notes Phys.*, 720:403–433, 2007, astro-ph/0601672.

[141] Kurt Hinterbichler, Mark Trodden, and Daniel Wesley. Multi-field galileons and higher co-dimension branes. *Phys.Rev.*, D82:124018, 2010, 1008.1305.

[142] C. Deffayet, S. Deser, and G. Esposito-Farese. Generalized Galileons: All scalar models whose curved background extensions maintain second-order field equations and stress-tensors. *Phys.Rev.*, D80:064015, 2009, 0906.1967.

[143] Jrme Gleyzes, David Langlois, Federico Piazza, and Filippo Vernizzi. Healthy theories beyond Horndeski. 2014, 1404.6495.

[144] Gregory Walter Horndeski. Second-order scalar-tensor field equations in a four-dimensional space. *Int.J.Theor.Phys.*, 10:363–384, 1974.

[145] C. Deffayet, Xian Gao, D.A. Steer, and G. Zahariade. From k-essence to generalised Galileons. *Phys.Rev.*, D84:064039, 2011, 1103.3260.

[146] Tsutomu Kobayashi, Masahide Yamaguchi, and Jun'ichi Yokoyama. Generalized G-inflation: Inflation with the most general second-order field equations. *Prog.Theor.Phys.*, 126:511–529, 2011, 1105.5723.

[147] Cedric Deffayet, Oriol Pujolas, Ignacy Sawicki, and Alexander Vikman. Imperfect Dark Energy from Kinetic Gravity Braiding. *JCAP*, 1010:026, 2010, 1008.0048.

[148] Oriol Pujolas, Ignacy Sawicki, and Alexander Vikman. The Imperfect Fluid behind Kinetic Gravity Braiding. *JHEP*, 1111:156, 2011, 1103.5360.

[149] Rampei Kimura, Tsutomu Kobayashi, and Kazuhiro Yamamoto. Observational Constraints on Kinetic Gravity Braiding from the Integrated Sachs-Wolfe Effect. *Phys.Rev.*, D85:123503, 2012, 1110.3598.

[150] Christos Charmousis, Edmund J. Copeland, Antonio Padilla, and Paul M. Saffin. General second order scalar-tensor theory, self tuning, and the Fab Four. *Phys.Rev.Lett.*, 108:051101, 2012, 1106.2000.

[151] Christos Charmousis, Edmund J. Copeland, Antonio Padilla, and Paul M. Saffin. Self-tuning and the derivation of a class of scalar-tensor theories. *Phys.Rev.*, D85: 104040, 2012, 1112.4866.

[152] Jean-Philippe Bruneton, Massimiliano Rinaldi, Antonin Kanfon, Aurelien Hees, Sandrine Schlogel, et al. Fab Four: When John and George play gravitation and cosmology. 2012, 1203.4446.

[153] Edmund J. Copeland, Antonio Padilla, and Paul M. Saffin. The cosmology of the Fab-Four. 2012, 1208.3373.

[154] Stephen A. Appleby, Antonio De Felice, and Eric V. Linder. Fab 5: Noncanonical Kinetic Gravity, Self Tuning, and Cosmic Acceleration. *JCAP*, 1210:060, 2012, 1208.4163.

[155] Tsutomu Kobayashi, Hiroyuki Tashiro, and Daichi Suzuki. Evolution of linear cosmological perturbations and its observational implications in Galileon-type modified gravity. *Phys.Rev.*, D81:063513, 2010, 0912.4641.

[156] Tsutomu Kobayashi. Cosmic expansion and growth histories in Galileon scalar-tensor models of dark energy. *Phys.Rev.*, D81:103533, 2010, 1003.3281.

[157] Genly Leon and Emmanuel N. Saridakis. Dynamical analysis of generalized Galileon cosmology. 2012, 1211.3088.

[158] Clare Burrage, Nemanja Kaloper, and Antonio Padilla. Strong Coupling and Bounds on the Graviton Mass in Massive Gravity. 2012, 1211.6001.

[159] Stephen A. Appleby and Eric V. Linder. The Paths of Gravity in Galileon Cosmology. *JCAP*, 1203:043, 2012, 1112.1981.

[160] Sergey V. Sushkov. Exact cosmological solutions with nonminimal derivative coupling. *Phys.Rev.*, D80:103505, 2009, 0910.0980.

[161] Giulia Gubitosi and Eric V. Linder. Purely Kinetic Coupled Gravity. *Phys.Lett.*, B703: 113–118, 2011, 1106.2815.

[162] Claudia de Rham and Lavinia Heisenberg. Cosmology of the Galileon from Massive Gravity. *Phys.Rev.*, D84:043503, 2011, 1106.3312.

[163] Karel Van Acoleyen and Jos Van Doorsselaere. Galileons from Lovelock actions. *Phys.Rev.*, D83:084025, 2011, 1102.0487.

[164] Miguel Zumalacarregui, Tomi S. Koivisto, and David F. Mota. DBI Galileons in the Einstein Frame: Local Gravity and Cosmology. 2012, 1210.8016.

[165] Luca Amendola. Cosmology with nonminimal derivative couplings. *Phys.Lett.*, B301: 175–182, 1993, gr-qc/9302010.

[166] Anthony Challinor and Anthony Lasenby. Cosmic microwave background anisotropies in the CDM model: A Covariant and gauge invariant approach. *Astrophys.J.*, 513:1–22, 1999, astro-ph/9804301.

[167] Chung-Pei Ma and Edmund Bertschinger. Cosmological perturbation theory in the synchronous versus conformal Newtonian gauge. *Astrophys. J.*, 1994, astro-ph/9401007.

[168] Antonio De Felice and Shinji Tsujikawa. Cosmology of a covariant Galileon field. *Phys.Rev.Lett.*, 105:111301, 2010, 1007.2700.

[169] Antonio De Felice and Shinji Tsujikawa. Generalized Galileon cosmology. *Phys.Rev.*, D84:124029, 2011, 1008.4236.

[170] Antonio De Felice and Shinji Tsujikawa. Conditions for the cosmological viability of the most general scalar-tensor theories and their applications to extended Galileon dark energy models. *JCAP*, 1202:007, 2012, 1110.3878.

[171] Eugeny Babichev, Viatcheslav Mukhanov, and Alexander Vikman. k-Essence, superluminal propagation, causality and emergent geometry. *JHEP*, 0802:101, 2008, 0708.0561.

[172] Antony Lewis. `http://camb.info/`.

[173] D. Larson, J. Dunkley, G. Hinshaw, E. Komatsu, M.R. Nolta, et al. Seven-Year Wilkinson Microwave Anisotropy Probe (WMAP) Observations: Power Spectra and WMAP-Derived Parameters. *Astrophys.J.Suppl.*, 192:16, 2011, 1001.4635.

[174] A. G. Sánchez, M. Crocce, A. Cabré, C. M. Baugh, and E. Gaztañaga. Cosmological parameter constraints from SDSS luminous red galaxies: a new treatment of large-scale clustering. *MNRAS*, 400:1643–1664, December 2009, 0901.2570.

[175] Radouane Gannouji and M. Sami. Galileon gravity and its relevance to late time cosmic acceleration. *Phys.Rev.*, D82:024011, 2010, 1004.2808.

[176] Nathan Chow and Justin Khoury. Galileon cosmology. *Phys. Rev. D*, 80:024037, 2009.

[177] Savvas Nesseris, Antonio De Felice, and Shinji Tsujikawa. Observational constraints on Galileon cosmology. *Phys.Rev.*, D82:124054, 2010, 1010.0407.

[178] Amna Ali, Radouane Gannouji, and M. Sami. Modified gravity *à la* galileon: Late time cosmic acceleration and observational constraints. *Phys. Rev. D*, 82:103015, 2010.

[179] Ignacy Sawicki, Ippocratis D. Saltas, Luca Amendola, and Martin Kunz. Consistent perturbations in an imperfect fluid. 2012, 1208.4855.

[180] Stephen A. Appleby and Eric V. Linder. Galileons on Trial. 2012, 1204.4314.

[181] E. Komatsu et al. Seven-Year Wilkinson Microwave Anisotropy Probe (WMAP) Observations: Cosmological Interpretation. *Astrophys. J. Supp.*, 192:18, 2011.

[182] J. Dunkley, R. Hlozek, J. Sievers, V. Acquaviva, P.A.R. Ade, et al. The Atacama Cosmology Telescope: Cosmological Parameters from the 2008 Power Spectra. *Astrophys.J.*, 739:52, 2011, 1009.0866.

[183] Antonio De Felice, Ryotaro Kase, and Shinji Tsujikawa. Matter perturbations in Galileon cosmology. *Phys.Rev.*, D83:043515, 2011, 1011.6132.

[184] Antonio De Felice, Tsutomu Kobayashi, and Shinji Tsujikawa. Effective gravitational couplings for cosmological perturbations in the most general scalar-tensor theories with second-order field equations. *Phys.Lett.*, B706:123–133, 2011, 1108.4242.

[185] Antony Lewis and Anthony Challinor. Weak gravitational lensing of the cmb. *Phys.Rept.*, 429:1–65, 2006, astro-ph/0601594.

[186] Gong-Bo Zhao, Levon Pogosian, Alessandra Silvestri, and Joel Zylberberg. Searching for modified growth patterns with tomographic surveys. *Phys.Rev.*, D79:083513, 2009, 0809.3791.

[187] Beth A. Reid et al. Cosmological Constraints from the Clustering of the Sloan Digital Sky Survey DR7 Luminous Red Galaxies. *Mon. Not. Roy. Astron. Soc.*, 404:60–85, 2010, 0907.1659.

[188] Beth A. Reid et al. Erratum: Cosmological constraints from the clustering of the sloan digital sky survey dr7 luminous red galaxies. *Monthly Notices of the Royal Astronomical Society*, 417(4):3103–3104, 2011.

[189] D. J. Eisenstein, J. Annis, J. E. Gunn, A. S. Szalay, A. J. Connolly, R. C. Nichol, N. A. Bahcall, M. Bernardi, and et al. Spectroscopic Target Selection for the Sloan Digital Sky Survey: The Luminous Red Galaxy Sample. *Ap J*, 122:2267–2280, November 2001, arXiv:astro-ph/0108153.

[190] R. E. Angulo, C. M. Baugh, C. S. Frenk, and C. G. Lacey. The detectability of baryonic acoustic oscillations in future galaxy surveys. *MNRAS*, 383:755–776, January 2008, arXiv:astro-ph/0702543.

[191] E. Jennings, C. M. Baugh, and S. Pascoli. Modelling redshift space distortions in hierarchical cosmologies. *MNRAS*, 410:2081–2094, January 2011, 1003.4282.

[192] Hiroyuki Okada, Tomonori Totani, and Shinji Tsujikawa. Constraints on f(R) theory and Galileons from the latest data of galaxy redshift surveys. 2012, 1208.4681.

[193] P.A.R. Ade et al. Planck 2013 results. XV. CMB power spectra and likelihood. 2013, 1303.5075.

[194] P.A.R. Ade et al. Planck 2013 results. XVI. Cosmological parameters. 2013, 1303.5076.

[195] Antony Lewis and Sarah Bridle. Cosmological parameters from CMB and other data: A Monte Carlo approach. *Phys.Rev.*, D66:103511, 2002, astro-ph/0205436.

[196] Lm An, Stephen Brooks, and Andrew Gelman. Stephen brooks and andrew gelman. *Journal of Computational and Graphical Statistics*, 7:434–455, 1998.

[197] J. Neveu, V. Ruhlmann-Kleider, A. Conley, N. Palanque-Delabrouille, P. Astier, et al. Experimental constraints on the uncoupled Galileon model from SNLS3 data and other cosmological probes. 2013, 1302.2786.

[198] Jian-hua He. Weighing Neutrinos in $f(R)$ gravity. *Phys. Rev. D 88,*, 103523:103523, 2013, 1307.4876.

[199] Hayato Motohashi, Alexei A. Starobinsky, and Jun'ichi Yokoyama. Cosmology Based on f(R) Gravity Admits 1 eV Sterile Neutrinos. *Phys.Rev.Lett.*, 110(12):121302, 2013, 1203.6828.

[200] Marco Baldi, Francisco Villaescusa-Navarro, Matteo Viel, Ewald Puchwein, Volker Springel, et al. Cosmic Degeneracies I: Joint N-body Simulations of Modified Gravity and Massive Neutrinos. 2013, 1311.2588.

[201] G. Hinshaw, D. Larson, E. Komatsu, D.N. Spergel, C.L. Bennett, et al. Nine-Year Wilkinson Microwave Anisotropy Probe (WMAP) Observations: Cosmological Parameter Results. 2012, 1212.5226.

[202] J. Guy, M. Sullivan, A. Conley, N. Regnault, P. Astier, et al. The Supernova Legacy Survey 3-year sample: Type Ia Supernovae photometric distances and cosmological constraints. *Astron.Astrophys.*, 523:A7, 2010, 1010.4743.

[203] Florian Beutler, Chris Blake, Matthew Colless, D. Heath Jones, Lister Staveley-Smith, et al. The 6dF Galaxy Survey: Baryon Acoustic Oscillations and the Local Hubble Constant. *Mon.Not.Roy.Astron.Soc.*, 416:3017–3032, 2011, 1106.3366.

[204] Beth A. Reid, Lado Samushia, Martin White, Will J. Percival, Marc Manera, et al. The clustering of galaxies in the SDSS-III Baryon Oscillation Spectroscopic Survey: measurements of the growth of structure and expansion rate at z=0.57 from anisotropic clustering. 2012, 1203.6641.

[205] Beth A. Reid et al. Cosmological Constraints from the Clustering of the Sloan Digital Sky Survey DR7 Luminous Red Galaxies. *Mon. Not. Roy. Astron. Soc.*, 404:60–85, 2010, 0907.1659.

[206] P.A.R. Ade et al. Planck 2013 results. XVII. Gravitational lensing by large-scale structure. 2013, 1303.5077.

[207] Nikhil Padmanabhan, Xiaoying Xu, Daniel J. Eisenstein, Richard Scalzo, Antonio J. Cuesta, et al. A 2 per cent distance to z=0.35 by reconstructing baryon

acoustic oscillations - I. Methods and application to the Sloan Digital Sky Survey. *Mon.Not.Roy.Astron.Soc.*, 427(3):2132–2145, 2012, 1202.0090.

[208] Lauren Anderson, Eric Aubourg, Stephen Bailey, Dmitry Bizyaev, Michael Blanton, et al. The clustering of galaxies in the SDSS-III Baryon Oscillation Spectroscopic Survey: Baryon Acoustic Oscillations in the Data Release 9 Spectroscopic Galaxy Sample. *Mon.Not.Roy.Astron.Soc.*, 427(4):3435–3467, 2013, 1203.6594.

[209] Chris Blake, Eyal Kazin, Florian Beutler, Tamara Davis, David Parkinson, et al. The WiggleZ Dark Energy Survey: mapping the distance-redshift relation with baryon acoustic oscillations. *Mon.Not.Roy.Astron.Soc.*, 418:1707–1724, 2011, 1108.2635.

[210] Baojiu Li, Wojciech A. Hellwing, Kazuya Koyama, Gong-Bo Zhao, Elise Jennings, et al. The nonlinear matter and velocity power spectra in f(R) gravity. 2012, 1206.4317.

[211] C. Alcock and B. Paczynski. An evolution free test for non-zero cosmological constant. Nature, 281:358, October 1979.

[212] Chris Blake, Sarah Brough, Matthew Colless, Carlos Contreras, Warrick Couch, et al. The WiggleZ Dark Energy Survey: the growth rate of cosmic structure since redshift z=0.9. *Mon.Not.Roy.Astron.Soc.*, 415:2876, 2011, 1104.2948.

[213] J. Neveu, V. Ruhlmann-Kleider, P. Astier, M. Besanon, A. Conley, et al. First experimental constraints on the disformally-coupled Galileon model. 2014, 1403.0854.

[214] Adam G. Riess, Lucas Macri, Stefano Casertano, Hubert Lampeitl, Henry C. Ferguson, et al. A 3Space Telescope and Wide Field Camera 3. *Astrophys.J.*, 730:119, 2011, 1103.2976.

[215] E.M.L. Humphreys, Mark J. Reid, Jim M. Moran, Lincoln J. Greenhill, and Alice L. Argon. Toward a New Geometric Distance to the Active Galaxy NGC 4258. III. Final Results and the Hubble Constant. *Astrophys.J.*, 775:13, 2013, 1307.6031.

[216] Yong-Seon Song and Will J. Percival. Reconstructing the history of structure formation using redshift distortions. *Journal of Cosmology and Astroparticle Physics*, 2009(10): 004, 2009, 0807.0810.

[217] Florian Beutler, Chris Blake, Matthew Colless, D. Heath Jones, Lister Staveley-Smith, et al. The 6dF Galaxy Survey: $z \approx 0$ measurement of the growth rate and σ_8. *Mon.Not.Roy.Astron.Soc.*, 423:3430–3444, 2012, 1204.4725.

[218] L. Samushia, W. J. Percival, and A. Raccanelli. Interpreting large-scale redshift-space distortion measurements. *Monthly Notices of the Royal Astronomical Society*, 420(3): 2102–2119, 2012, 1102.1014.

[219] Chris Blake, Karl Glazebrook, Tamara Davis, Sarah Brough, Matthew Colless, et al. The WiggleZ Dark Energy Survey: measuring the cosmic expansion history using the Alcock-Paczynski test and distant supernovae. *Mon.Not.Roy.Astron.Soc.*, 418:1725–1735, 2011, 1108.2637.

[220] P.A.R. Ade et al. Planck 2013 results. XIX. The integrated Sachs-Wolfe effect. 2013, 1303.5079.

[221] Benjamin R. Granett, Mark C. Neyrinck, and Istvan Szapudi. An Imprint of Super-Structures on the Microwave Background due to the Integrated Sachs-Wolfe Effect. *Astrophys.J.*, 683:L99–L102, 2008, 0805.3695.

[222] B. R. Granett, M. C. Neyrinck, and I. Szapudi. Dark Energy Detected with Supervoids and Superclusters. *ArXiv e-prints*, May 2008, 0805.2974.

[223] P.M. Sutter, Guilhem Lavaux, Benjamin D. Wandelt, and David H. Weinberg. A public void catalog from the SDSS DR7 Galaxy Redshift Surveys based on the watershed transform. *Astrophys.J.*, 761:44, 2012, 1207.2524.

[224] Danny C. Pan, Michael S. Vogeley, Fiona Hoyle, Yun-Young Choi, and Chang-bom Park. Cosmic Voids in Sloan Digital Sky Survey Data Release 7. *Mon.Not.Roy.Astron.Soc.*, 421:926–934, 2012, 1103.4156.

[225] Carlos Hernandez-Monteagudo and Robert E. Smith. On the signature of nearby superclusters and voids in the Integrated Sachs-Wolfe effect. 2012, 1212.1174.

[226] Yan-Chuan Cai, Mark C. Neyrinck, Istvan Szapudi, Shaun Cole, and Carlos S. Frenk. A Possible Cold Imprint of Voids on the Microwave Background Radiation. *Astrophys.J.*, 786:110, 2014, 1301.6136.

[227] Fabio Finelli, Juan Garcia-Bellido, Andras Kovacs, Francesco Paci, and Istvan Sza-pudi. A Supervoid Imprinting the Cold Spot in the Cosmic Microwave Background. 2014, 1405.1555.

[228] Istvn Szapudi, Andrs Kovcs, Benjamin R. Granett, Zsolt Frei, Joseph Silk, et al. De-tection of a Supervoid Aligned with the Cold Spot of the Cosmic Microwave Back-ground. 2014, 1405.1566.

[229] S. Boughn and R. Crittenden. A correlation between the cosmic microwave back-ground and large-scale structure in the Universe. Nature, 427:45–47, January 2004, astro-ph/0305001.

[230] S. Ho, C. Hirata, N. Padmanabhan, U. Seljak, and N. Bahcall. Correlation of CMB with large-scale structure. I. Integrated Sachs-Wolfe tomography and cosmological implications. Phys. Rev. D, 78(4):043519, August 2008, 0801.0642.

[231] Tommaso Giannantonio, Robert Crittenden, Robert Nichol, and Ashley J. Ross. The significance of the integrated Sachs-Wolfe effect revisited. *Mon.Not.Roy.Astron.Soc.*, 426:2581–2599, 2012, 1209.2125.

[232] Yong-Seon Song, Hiranya Peiris, and Wayne Hu. Cosmological Constraints on f(R) Acceleration Models. *Phys.Rev.*, D76:063517, 2007, 0706.2399.

[233] Tommaso Giannantonio, Yong-Seon Song, and Kazuya Koyama. Detectability of a phantom-like braneworld model with the integrated Sachs-Wolfe effect. *Phys.Rev.*, D78:044017, 2008, 0803.2238.

[234] C.L. Francis and J.A. Peacock. An estimate of the local ISW signal, and its impact on CMB anomalies. *Mon.Not.Roy.Astron.Soc.*, 406:14, 2010, 0909.2495.

[235] C.L. Francis and J.A. Peacock. ISW measurements with photometric redshift surveys: 2MASS results and future prospects. *Mon.Not.Roy.Astron.Soc.*, 406:2, 2010, 0909.2494.

[236] Carlos Hernandez-Monteagudo. Revisiting the WMAP - NVSS angular cross corre-lation. A skeptic view. 2009, 0909.4294.

[237] U. Sawangwit, T. Shanks, R.D. Cannon, S.M. Croom, Nicholas P. Ross, et al. Cross-correlating WMAP5 with 1.5 million LRGs: a new test for the ISW effect. *Mon.Not.Roy.Astron.Soc.*, 402:2228, 2010, 0911.1352.

[238] M. Lopez-Corredoira, F. Sylos Labini, and J. Betancort-Rijo. Absence of significant cross-correlation between WMAP and SDSS. *Astron.Astrophys.*, 513:A3, 2010, 1001.4000.

[239] George Efstathiou. H0 Revisited. 2013, 1311.3461.

[240] P.A.R. Ade et al. Planck 2013 results. XX. Cosmology from Sunyaev-Zeldovich cluster counts. 2013, 1303.5080.

[241] Mark Wyman, Douglas H. Rudd, R. Ali Vanderveld, and Wayne Hu. $\nu\Lambda$CDM: Neutrinos help reconcile Planck with the Local Universe. *Phys.Rev.Lett.*, 112:051302, 2014, 1307.7715.

[242] Richard A. Battye and Adam Moss. Evidence for massive neutrinos from CMB and lensing observations. *Phys.Rev.Lett.*, 112:051303, 2014, 1308.5870.

[243] G. Drexlin, V. Hannen, S. Mertens, and C. Weinheimer. Current direct neutrino mass experiments. *Adv.High Energy Phys.*, 2013:293986, 2013, 1307.0101.

[244] http://www.katrin.kit.edu/.

[245] J.D. Vergados, H. Ejiri, and F. Simkovic. Theory of Neutrinoless Double Beta Decay. *Rept.Prog.Phys.*, 75:106301, 2012, 1205.0649.

[246] E. Jennings, C. M. Baugh, and S. Pascoli. Modelling redshift space distortions in hierarchical cosmologies. *MNRAS*, 410:2081–2094, January 2011, 1003.4282.

[247] Mark Wyman, Elise Jennings, and Marcos Lima. Simulations of Galileon modified gravity: Clustering statistics in real and redshift space. *Phys.Rev.*, D88:084029, 2013, 1303.6630.

[248] Eugeny Babichev, Cedric Deffayet, and Gilles Esposito-Farese. Constraints on Shift-Symmetric Scalar-Tensor Theories with a Vainshtein Mechanism from Bounds on the Time Variation of G. *Phys.Rev.Lett.*, 107:251102, 2011, 1107.1569.

[249] Rampei Kimura, Tsutomu Kobayashi, and Kazuhiro Yamamoto. Vainshtein screening in a cosmological background in the most general second-order scalar-tensor theory. *Phys.Rev.*, D85:024023, 2012, 1111.6749.

[250] James G. Williams, Slava G. Turyshev, and Dale H. Boggs. Progress in lunar laser ranging tests of relativistic gravity. *Phys.Rev.Lett.*, 93:261101, 2004, gr-qc/0411113.

[251] Anthony Challinor. Microwave background anisotropies from gravitational waves: The (1+3) covariant approach. *Class.Quant.Grav.*, 17:871–889, 2000, astro-ph/9906474.

[252] Anthony Challinor. Microwave background polarization in cosmological models. *Phys.Rev.*, D62:043004, 2000, astro-ph/9911481.

[253] P.A.R. Ade et al. Detection of B-Mode Polarization at Degree Angular Scales by BICEP2. *Phys.Rev.Lett.*, 112:241101, 2014, 1403.3985.

[254] J. R. Bond, S. Cole, G. Efstathiou, and N. Kaiser. Excursion set mass functions for hierarchical Gaussian fluctuations. ApJ, 379:440–460, October 1991.

[255] Emilio Bellini, Nicola Bartolo, and Sabino Matarrese. Spherical Collapse in covariant Galileon theory. *JCAP*, 1206:019, 2012, 1202.2712.

[256] Hans A. Winther and Pedro G. Ferreira. *in preparation*.

[257] Andrew R. Zentner. The Excursion Set Theory of Halo Mass Functions, Halo Clustering, and Halo Growth. *Int.J.Mod.Phys.*, D16:763–816, 2007, astro-ph/0611454.

[258] Enrique Gaztanaga and J. Alberto Lobo. Nonlinear gravitational growth of large scale structures inside and outside standard cosmology. *Astrophys.J.*, 548:47–59, 2001, astro-ph/0003129.

[259] Bjoern Malte Schaefer and Kazuya Koyama. Spherical collapse in modified gravity with the Birkhoff-theorem. *Mon.Not.Roy.Astron.Soc.*, 385:411–422, 2008, 0711.3129.

[260] Matthew C. Martino, Hans F. Stabenau, and Ravi K. Sheth. Spherical Collapse and Modified Gravity. *Phys.Rev.*, D79:084013, 2009, 0812.0200.

[261] Baojiu Li and George Efstathiou. An Extended Excursion Set Approach to Structure Formation in Chameleon Models. *Mon.Not.Roy.Astron.Soc.*, 421:1431, 2012, 1110.6440.

[262] Alexander Borisov, Bhuvnesh Jain, and Pengjie Zhang. Spherical Collapse in f(R) Gravity. *Phys.Rev.*, D85:063518, 2012, 1102.4839.

[263] Tsz Yan Lam and Baojiu Li. Excursion set theory for modified gravity: correlated steps, mass functions and halo bias. *Mon.Not.Roy.Astron.Soc.*, 426:3260–3270, 2012, 1205.0059.

[264] Baojiu Li and Tsz Yan Lam. Excursion set theory for modified gravity: Eulerian versus Lagrangian environments. *MNRAS, 425,*, 730, 2012, 1205.0058.

[265] Joseph Clampitt and Yan-Chuan Cai. Voids in Modified Gravity: Excursion Set Predictions. *2013*, 431:749C, MNRAS, 1212.2216.

[266] Lucas Lombriser, Baojiu Li, Kazuya Koyama, and Gong-Bo Zhao. Modeling halo mass functions in chameleon f(R) gravity. *Phys. Rev. D 87,*, 123511, 2013, 1304.6395.

[267] Michael Kopp, Stephen A. Appleby, Ixandra Achitouv, and Jochen Weller. Spherical collapse and halo mass function in f(R) theories. 2013, 1306.3233.

[268] James M. Bardeen, J.R. Bond, Nick Kaiser, and A.S. Szalay. The Statistics of Peaks of Gaussian Random Fields. *Astrophys.J.*, 304:15–61, 1986.

[269] W. H. Press and P. Schechter. Formation of Galaxies and Clusters of Galaxies by Self-Similar Gravitational Condensation. ApJ, 187:425–438, February 1974.

[270] Kyle Parfrey, Lam Hui, and Ravi K. Sheth. Scale-dependent halo bias from scale-dependent growth. *Phys.Rev.*, D83:063511, 2011, 1012.1335.

[271] H.J. Mo and Simon D.M. White. An Analytic model for the spatial clustering of dark matter halos. *Mon.Not.Roy.Astron.Soc.*, 282:347, 1996, astro-ph/9512127.

[272] James N. Fry and Enrique Gaztanaga. Biasing and hierarchical statistics in large scale structure. *Astrophys.J.*, 413:447–452, 1993, astro-ph/9302009.

[273] Ravi K. Sheth and Giuseppe Tormen. Large scale bias and the peak background split. *Mon.Not.Roy.Astron.Soc.*, 308:119, 1999, astro-ph/9901122.

[274] Ravi K. Sheth, H.J. Mo, and Giuseppe Tormen. Ellipsoidal collapse and an improved model for the number and spatial distribution of dark matter haloes. *Mon.Not.Roy.Astron.Soc.*, 323:1, 2001, astro-ph/9907024.

[275] Ravi K. Sheth and Giuseppe Tormen. An Excursion set model of hierarchical clustering : Ellipsoidal collapse and the moving barrier. *Mon.Not.Roy.Astron.Soc.*, 329:61, 2002, astro-ph/0105113.

[276] Baojiu Li, Alexandre Barreira, Carlton M. Baugh, Wojciech A. Hellwing, Kazuya Koyama, et al. Simulating the quartic Galileon gravity model on adaptively refined meshes. *JCAP*, 1311:012, 2013, 1308.3491.

[277] Asantha Cooray and Ravi K. Sheth. Halo models of large scale structure. *Phys.Rept.*, 372:1–129, 2002, astro-ph/0206508.

[278] Baojiu Li, Gong-Bo Zhao, Romain Teyssier, and Kazuya Koyama. ECOSMOG: An Efficient Code for Simulating Modified Gravity. *JCAP*, 1201:051, 2012, 1110.1379.

[279] Claudia de Rham. Galileons in the Sky. *Comptes Rendus Physique*, 13:666–681, 2012, 1204.5492.

[280] Fabian Schmidt. Self-Consistent Cosmological Simulations of DGP Braneworld Gravity. *Phys.Rev.*, D80:043001, 2009, 0905.0858.

[281] Fabian Schmidt. Cosmological Simulations of Normal-Branch Braneworld Gravity. *Phys.Rev.*, D80:123003, 2009, 0910.0235.

[282] K.C. Chan and Roman Scoccimarro. Large-Scale Structure in Brane-Induced Gravity II. Numerical Simulations. *Phys.Rev.*, D80:104005, 2009, 0906.4548.

[283] Justin Khoury and Mark Wyman. N-Body Simulations of DGP and Degravitation Theories. *Phys.Rev.*, D80:064023, 2009, 0903.1292.

[284] Fabian Schmidt, Wayne Hu, and Marcos Lima. Spherical Collapse and the Halo Model in Braneworld Gravity. *Phys.Rev.*, D81:063005, 2010, 0911.5178.

[285] Kazuya Koyama and Fabio P. Silva. Non-linear interactions in a cosmological background in the DGP braneworld. *Phys.Rev.*, D75:084040, 2007, hep-th/0702169.

[286] Julio F. Navarro, Carlos S. Frenk, and Simon D.M. White. A Universal density profile from hierarchical clustering. *Astrophys.J.*, 490:493–508, 1997, astro-ph/9611107.

[287] James S. Bullock, Tsafrir S. Kolatt, Yair Sigad, Rachel S. Somerville, Andrey V. Kravtsov, et al. Profiles of dark haloes. Evolution, scatter, and environment. *Mon.Not.Roy.Astron.Soc.*, 321:559–575, 2001, astro-ph/9908159.

[288] Angelo F. Neto, Liang Gao, Philip Bett, Shaun Cole, Julio F. Navarro, et al. The statistics of lambda CDM Halo Concentrations. *Mon.Not.Roy.Astron.Soc.*, 381:1450–1462, 2007, 0706.2919.

[289] Andrea V. Maccio', Aaron A. Dutton, and Frank C.van den Bosch. Concentration, Spin and Shape of Dark Matter Haloes as a Function of the Cosmological Model: WMAP1, WMAP3 and WMAP5 results. 2008, 0805.1926.

[290] Francisco Prada, Anatoly A. Klypin, Antonio J. Cuesta, Juan E. Betancort-Rijo, and Joel Primack. Halo concentrations in the standard LCDM cosmology. 2011, 1104.5130.

[291] Romain Teyssier. Cosmological hydrodynamics with adaptive mesh refinement: a new high resolution code called ramses. *Astron.Astrophys.*, 385:337–364, 2002, astro-ph/0111367.

[292] Peter S. Behroozi, Risa H. Wechsler, and Hao-Yi Wu. The Rockstar Phase-Space Temporal Halo Finder and the Velocity Offsets of Cluster Cores. *Astrophys.J.*, 762:109, 2013, 1110.4372.

[293] M. C. Cautun and R. van de Weygaert. The DTFE public software - The Delaunay Tessellation Field Estimator code. *ArXiv e-prints*, May 2011, 1105.0370.

[294] W. E. Schaap and R. van de Weygaert. Continuous fields and discrete samples: reconstruction through Delaunay tessellations. *A&A*, 363:L29–L32, November 2000, arXiv:astro-ph/0011007.

[295] Andrey V. Kravtsov, Andreas A. Berlind, Risa H. Wechsler, Anatoly A. Klypin, Stefan Gottloeber, et al. The Dark side of the halo occupation distribution. *Astrophys.J.*, 609: 35–49, 2004, astro-ph/0308519.

[296] David A. Wake, Ravi K. Sheth, Robert C. Nichol, Carlton M. Baugh, Joss Bland-Hawthorn, et al. The 2dF-SDSS LRG and QSO survey: Evolution of the clustering of

Luminous Red Galaxies since z = 0.6. *Mon.Not.Roy.Astron.Soc.*, 387:1045–1062, 2008, 0802.4288.

[297] Zheng Zheng, Idit Zehavi, Daniel J. Eisenstein, David H. Weinberg, and Yipeng Jing. Halo Occupation Distribution Modeling of Clustering of Luminous Red Galaxies. *Astrophys.J.*, 707:554–572, 2009, 0809.1868.

[298] U. Sawangwit, T. Shanks, F.B. Abdalla, R.D. Cannon, S.M. Croom, et al. Angular correlation function of 1.5 million LRGs: clustering evolution and a search for BAO. *Mon.Not.Roy.Astron.Soc.*, 416:3033–3056, 2011, 0912.0511.

[299] C. Almeida, C.M. Baugh, D.A. Wake, C.G. Lacey, A.J. Benson, et al. Luminous Red Galaxies in hierarchical cosmologies. *: Mon.Not.Roy.Astron.Soc.*, 2007, 0710.3557.

[300] Manda Banerji, Ignacio Ferreras, Filipe B. Abdalla, Paul Hewett, and Ofer Lahav. Exploring the Luminosity Evolution and Stellar Mass Assembly of 2SLAQ Luminous Red Galaxies Between Redshift 0.4 and 0.8. *Mon.Not.Roy.Astron.Soc.*, 402:2264–2278, 2010, 0910.5372.

[301] Carlton M. Baugh. A primer on hierarchical galaxy formation: The semi-analytical approach. *Rept.Prog.Phys.*, 69:3101–3156, 2006, astro-ph/0610031.

[302] Andrea V. Maccio', Aaron A. Dutton, and Frank C.van den Bosch. Concentration, Spin and Shape of Dark Matter Haloes as a Function of the Cosmological Model: WMAP1, WMAP3 and WMAP5 results. 2008, 0805.1926.

[303] E. Komatsu et al. Five-Year Wilkinson Microwave Anisotropy Probe (WMAP) Observations: Cosmological Interpretation. *Astrophys.J.Suppl.*, 180:330–376, 2009, 0803.0547.

[304] J.C. Munoz-Cuartas, A.V. Maccio, S. Gottlober, and A.A. Dutton. The Redshift Evolution of LCDM Halo Parameters: Concentration, Spin, and Shape. 2010, 1007.0438.

[305] Aaron D. Ludlow, Julio F. Navarro, Raul E. Angulo, Michael Boylan-Kolchin, Volker Springel, et al. The Mass-Concentration-Redshift Relation of Cold Dark Matter Halos. 2013, 1312.0945.

[306] W. A. Hellwing. Galactic halos in cosmology with long-range scalar DM interaction. *Annalen der Physik*, 522:351–354, March 2010, 0911.0573.

[307] Wojciech A. Hellwing and Roman Juszkiewicz. Dark Matter Gravitational Clustering With a Long-Range Scalar Interaction. *Phys.Rev.*, D80:083522, 2009, 0809.1976.

[308] Jeremy Sakstein. Stellar Oscillations in Modified Gravity. 2013, 1309.0495.

[309] David F. Mota and Douglas J. Shaw. Evading Equivalence Principle Violations, Cosmological and other Experimental Constraints in Scalar Field Theories with a Strong Coupling to Matter. *Phys.Rev.*, D75:063501, 2007, hep-ph/0608078.

[310] Stephane Colombi, Andrew H. Jaffe, Dmitri Novikov, and Christophe Pichon. Accurate estimators of power spectra in N-body simulations. 2008, 0811.0313.

[311] H.J. Mo, Y.P. Jing, and S.D.M. White. High-order correlations of peaks and halos: A Step toward understanding galaxy biasing. 1996, astro-ph/9603039.

[312] Roman Scoccimarro, Ravi K. Sheth, Lam Hui, and Bhuvnesh Jain. How many galaxies fit in a halo? Constraints on galaxy formation efficiency from spatial clustering. *Astrophys.J.*, 546:20–34, 2001, astro-ph/0006319.

[313] R.E. Smith et al. Stable clustering, the halo model and nonlinear cosmological power spectra. *Mon.Not.Roy.Astron.Soc.*, 341:1311, 2003, astro-ph/0207664.

[314] Ryuichi Takahashi, Masanori Sato, Takahiro Nishimichi, Atsushi Taruya, and Masamune Oguri. Revising the Halofit Model for the Nonlinear Matter Power Spectrum. *Astrophys.J.*, 761:152, 2012, 1208.2701.

[315] Gong-Bo Zhao. Modeling the nonlinear clustering in modified gravity models I: A fitting formula for matter power spectrum of f(R) gravity. 2013, 1312.1291.

[316] Fabian Schmidt, Marcos Vinicius Lima, Hiroaki Oyaizu, and Wayne Hu. Nonlinear Evolution of f(R) Cosmologies III: Halo Statistics. *Phys.Rev.*, D79:083518, 2009, 0812.0545.

[317] Laura Taddei, Riccardo Catena, and Massimo Pietroni. Spherical collapse and halo mass function in the symmetron model. 2013, 1310.6175.

[318] C. Deffayet and R.P. Woodard. Reconstructing the Distortion Function for Nonlocal Cosmology. *JCAP*, 0908:023, 2009, 0904.0961.

[319] Shin'ichi Nojiri and Sergei D. Odintsov. Modified non-local-F(R) gravity as the key for the inflation and dark energy. *Phys.Lett.*, B659:821–826, 2008, 0708.0924.

[320] S. Jhingan, S. Nojiri, S.D. Odintsov, M. Sami, I Thongkool, et al. Phantom and non-phantom dark energy: The Cosmological relevance of non-locally corrected gravity. *Phys.Lett.*, B663:424–428, 2008, 0803.2613.

[321] Tomi Koivisto. Dynamics of Nonlocal Cosmology. *Phys.Rev.*, D77:123513, 2008, 0803.3399.

[322] Tomi S. Koivisto. Newtonian limit of nonlocal cosmology. *Phys.Rev.*, D78:123505, 2008, 0807.3778.

[323] E. Elizalde, E. O. Pozdeeva, and S. Y. Vernov. De Sitter universe in nonlocal gravity. Phys. Rev. D, 85(4):044002, February 2012, 1110.5806.

[324] E. Elizalde, E. O. Pozdeeva, and S. Y. Vernov. Reconstruction procedure in nonlocal cosmological models. *Classical and Quantum Gravity*, 30(3):035002, February 2013, 1209.5957.

[325] S. Park and S. Dodelson. Structure formation in a nonlocally modified gravity model. Phys. Rev. D, 87(2):024003, January 2013, 1209.0836.

[326] Scott Dodelson and Sohyun Park. Nonlocal Gravity and Structure in the Universe. 2013, 1310.4329.

[327] Michele Maggiore. Phantom dark energy from non-local infrared modifications of General Relativity. *Phys.Rev.*, D89:043008, 2014, 1307.3898.

[328] S. Foffa, M. Maggiore, and E. Mitsou. Cosmological dynamics and dark energy from non-local infrared modifications of gravity. *Int.J.Mod.Phys. A, to appear*, 2014, 1311.3435.

[329] A. Kehagias and M. Maggiore. Spherically symmetric static solutions in a non-local infrared modification of General Relativity. *JHEP, to appear*, 2014, 1401.8289.

[330] Savvas Nesseris and Shinji Tsujikawa. Cosmological perturbations and observational constraints on non-local massive gravity. 2014, 1402.4613.

[331] Maud Jaccard, Michele Maggiore, and Ermis Mitsou. Nonlocal theory of massive gravity. *Phys.Rev.*, D88(4):044033, 2013, 1305.3034.

[332] Stefano Foffa, Michele Maggiore, and Ermis Mitsou. Apparent ghosts and spurious degrees of freedom in non-local theories. *Phys.Lett.*, B733:76–83, 2014, 1311.3421.

[333] Leonardo Modesto and Shinji Tsujikawa. Non-local massive gravity. *Phys.Lett.*, B727:48–56, 2013, 1307.6968.

[334] Pedro G. Ferreira and Antonio L. Maroto. A few cosmological implications of tensor nonlocalities. *Phys.Rev.*, D88(12):123502, 2013, 1310.1238.

[335] Yves Dirian, Stefano Foffa, Nima Khosravi, Martin Kunz, and Michele Maggiore. Cosmological perturbations and structure formation in nonlocal infrared modifications of general relativity. *JCAP*, 1406:033, 2014, 1403.6068.

[336] Salvatore Capozziello, Emilio Elizalde, Shin'ichi Nojiri, and Sergei D. Odintsov. Accelerating cosmologies from non-local higher-derivative gravity. *Phys.Lett.*, B671:193–198, 2009, 0809.1535.

[337] N.A. Koshelev. Comments on scalar-tensor representation of nonlocally corrected gravity. *Grav.Cosmol.*, 15:220–223, 2009, 0809.4927.

[338] Tomi S. Koivisto. Cosmology of modified (but second order) gravity. *AIP Conf.Proc.*, 1206:79–96, 2010, 0910.4097.

[339] Andrei O. Barvinsky. Serendipitous discoveries in nonlocal gravity theory. *Phys.Rev.*, D85:104018, 2012, 1112.4340.

[340] R. Kimura, T. Kobayashi, and K. Yamamoto. Vainshtein screening in a cosmological background in the most general second-order scalar-tensor theory. Phys. Rev. D, 85(2):024023, January 2012, 1111.6749.

[341] Yves Dirian, Stefano Foffa, Martin Kunz, Michele Maggiore, and Valeria Pettorino. Non-local gravity and comparison with observational datasets. 2014, 1411.7692.

[342] W. A. Hellwing and R. Juszkiewicz. Dark matter gravitational clustering with a long-range scalar interaction. *Phys. Rev. D*, 80(8):083522–+, October 2009, 0809.1976.

[343] W. A. Hellwing, S. R. Knollmann, and A. Knebe. Boosting hierarchical structure formation with scalar-interacting dark matter. *MNRAS*, 408:L104–L108, October 2010, 1004.2929.

[344] W. A. Hellwing, M. Cautun, A. Knebe, R. Juszkiewicz, and S. Knollmann. DM haloes in the fifth-force cosmology. *J. Cosmology Astropart. Phys.*, 10:12, October 2013, 1111.7257.

[345] M. Cautun, R. van de Weygaert, B. J. T. Jones, and C. S. Frenk. Evolution of the cosmic web. *Mon.Not.Roy.Astron.Soc.*, 441:2923–2973, July 2014, 1401.7866.

[346] N. I. Libeskind, Y. Hoffman, and S. Gottlöber. The velocity shear and vorticity across redshifts and non-linear scales. *Mon.Not.Roy.Astron.Soc.*, 441:1974–1983, July 2014, 1310.5706.

[347] Junsup Shim, Jounghun Lee, and Marco Baldi. Breaking the Cosmic Degeneracy between Modified Gravity and Massive Neutrinos with the Cosmic Web. 2014, 1404.3639.

[348] R. Laureijs et al. Euclid Definition Study Report. 2011, 1110.3193.

[349] Luca Amendola et al. Cosmology and fundamental physics with the Euclid satellite. 2012, 1206.1225.

[350] Michael Levi et al. The DESI Experiment, a whitepaper for Snowmass 2013. 2013, 1308.0847.

[351] LSST Dark Energy Science Collaboration. Large Synoptic Survey Telescope: Dark Energy Science Collaboration. *ArXiv e-prints*, November 2012, 1211.0310.

[352] G.R. Dvali, Gregory Gabadadze, and Massimo Porrati. 4-D gravity on a brane in 5-D Minkowski space. *Phys.Lett.*, B485:208–214, 2000, hep-th/0005016.

[353] Gregory Gabadadze. General Relativity With An Auxiliary Dimension. *Phys.Lett.*, B681:89–95, 2009, 0908.1112.

[354] Claudia de Rham. Massive gravity from Dirichlet boundary conditions. *Phys.Lett.*, B688:137–141, 2010, 0910.5474.

[355] Claudia de Rham, Gregory Gabadadze, and Andrew J. Tolley. Resummation of Massive Gravity. *Phys.Rev.Lett.*, 106:231101, 2011, 1011.1232.

[356] Claudia de Rham and Gregory Gabadadze. Selftuned Massive Spin-2. *Phys.Lett.*, B693:334–338, 2010, 1006.4367.

[357] Claudia de Rham and Gregory Gabadadze. Generalization of the Fierz-Pauli Action. *Phys.Rev.*, D82:044020, 2010, 1007.0443.

[358] Claudia de Rham, Gregory Gabadadze, Lavinia Heisenberg, and David Pirtskhalava. Cosmic Acceleration and the Helicity-0 Graviton. *Phys.Rev.*, D83:103516, 2011, 1010.1780.

[359] S.F. Hassan and Rachel A. Rosen. Bimetric Gravity from Ghost-free Massive Gravity. *JHEP*, 1202:126, 2012, 1109.3515.

[360] M. Postman and et al. The Cluster Lensing and Supernova Survey with Hubble: An Overview. *APJS*, 199:25, April 2012, 1106.3328.

[361] Keiichi Umetsu, Elinor Medezinski, Mario Nonino, Julian Merten, Marc Postman, et al. CLASH: Weak-Lensing Shear-and-Magnification Analysis of 20 Galaxy Clusters. *Astrophys.J.*, 795(2):163, 2014, 1404.1375.

[362] Erwin Platen, Rien van de Weygaert, and Bernard J.T. Jones. A Cosmic Watershed: The WVF Void Detection Technique. *Mon.Not.Roy.Astron.Soc.*, 380:551–570, 2007, 0706.2788.

[363] K. Umetsu. Cluster Weak Gravitational Lensing. *ArXiv e-prints*, February 2010, 1002.3952.

[364] Matthias Bartelmann and Peter Schneider. Weak gravitational lensing. *Phys.Rept.*, 340:291–472, 2001, astro-ph/9912508.

[365] M. Bartelmann. TOPICAL REVIEW Gravitational lensing. *Classical and Quantum Gravity*, 27(23):233001, December 2010, 1010.3829.

[366] C. Oaxaca Wright and T. G. Brainerd. Gravitational Lensing by NFW Halos. *ArXiv Astrophysics e-prints*, August 1999, astro-ph/9908213.

[367] T. D. Kitching, J. Rhodes, C. Heymans, R. Massey, Q. Liu, M. Cobzarenco, B. L. Cragin, A. Hassaine, D. Kirkby, E. J. Lok, D. Margala, J. Moser, M. O'Leary, A. M. Pires, and S. Yurgenson. Image Analysis for Cosmology: Shape Measurement Challenge Review AMP Results from the Mapping Dark Matter Challenge. *ArXiv e-prints*, April 2012, 1204.4096.

[368] R. Massey, H. Hoekstra, T. Kitching, J. Rhodes, M. Cropper, J. Amiaux, D. Harvey, Y. Mellier, M. Meneghetti, L. Miller, S. Paulin-Henriksson, S. Pires, R. Scaramella, and T. Schrabback. Origins of weak lensing systematics, and requirements on future instrumentation (or knowledge of instrumentation). *MNRAS*, 429:661–678, February 2013, 1210.7690.

[369] Matthias Bartelmann. Arcs from a universal dark matter halo profile. *Astron.Astrophys.*, 313:697–702, 1996, astro-ph/9602053.

[370] J. Merten, M. Cacciato, M. Meneghetti, C. Mignone, and M. Bartelmann. Combining weak and strong cluster lensing: Applications to simulations and MS 2137. *Astron.Astrophys.*, 500:681, 2009, 0806.1967.

[371] J. Merten, D. Coe, R. Dupke, R. Massey, A. Zitrin, E. S. Cypriano, N. Okabe, B. Frye, F. G. Braglia, Y. Jiménez-Teja, N. Benítez, T. Broadhurst, J. Rhodes, M. Meneghetti, L. A. Moustakas, L. Sodré, Jr., J. Krick, and J. N. Bregman. Creation of cosmic structure in the complex galaxy cluster merger Abell 2744. *MNRAS*, 417:333–347, October 2011, 1103.2772.

[372] J.P. Kneib, R.S. Ellis, I. Smail, W.J. Couch, and R.M. Sharples. Hubble space telescope observations of the lensing cluster abell 2218. *Astrophys.J.*, 471:643, 1996, astro-ph/9511015.

[373] Thomas J. Broadhurst et al. Strong lensing analysis of A1689 from deep Advanced Camera images. *Astrophys.J.*, 621:53–88, 2005, astro-ph/0409132.

[374] Graham P. Smith, Jean-Paul Kneib, Ian Smail, Pasquale Mazzotta, Harald Ebeling, et al. A Hubble Space Telescope lensing survey of x-ray luminous galaxy clusters: 4. Mass, structure and thermodynamics of cluster cores at z = 0.2. *Mon.Not.Roy.Astron.Soc.*, 359:417–446, 2005, astro-ph/0403588.

[375] Aleksi Halkola, S. Seitz, and M. Pannella. Parametric Strong Gravitational Lensing Analysis of Abell 1689. *Mon.Not.Roy.Astron.Soc.*, 372:1425–1462, 2006, astro-ph/0605470.

[376] Eric Jullo, Jean-Paul Kneib, Marceau Limousin, Ardis Eliasdottir, Phil Marshall, et al. A Bayesian approach to strong lensing modelling of galaxy clusters. *New J.Phys.*, 9: 447, 2007, 0706.0048.

[377] A. Zitrin, T. Broadhurst, K. Umetsu, D. Coe, N. Benítez, B. Ascaso, L. Bradley, H. Ford, J. Jee, E. Medezinski, Y. Rephaeli, and W. Zheng. New multiply-lensed galaxies identified in ACS/NIC3 observations of Cl0024+1654 using an improved mass model. *MNRAS*, 396:1985–2002, July 2009, 0902.3971.

[378] M. Oguri. The Mass Distribution of SDSS J1004+4112 Revisited. *PASJ*, 62:1017–, August 2010, 1005.3103.

[379] A. B. Newman, T. Treu, R. S. Ellis, D. J. Sand, C. Nipoti, J. Richard, and E. Jullo. The Density Profiles of Massive, Relaxed Galaxy Clusters. I. The Total Density Over Three Decades in Radius. *APJ*, 765:24, March 2013, 1209.1391.

[380] Eric Jullo, Sandrine Pires, Mathilde Jauzac, and Jean-Paul Kneib. Weak Lensing Galaxy Cluster Field Reconstruction. *Mon.Not.Roy.Astron.Soc.*, 437:3969, 2014, 1309.5718.

[381] Traci L. Johnson, Keren Sharon, Matthew B. Bayliss, Michael D. Gladders, Dan Coe, et al. Lens models and magnification maps of the six Hubble Frontier Fields clusters. *Astrophys.J.*, 797(1):48, 2014, 1405.0222.

[382] A. Monna, S. Seitz, N. Greisel, T. Eichner, N. Drory, et al. CLASH: z 6 young galaxy candidate quintuply lensed by the frontier field cluster RXC J2248.7-4431. *Mon.Not.Roy.Astron.Soc.*, 438:1417, 2014, 1308.6280.

[383] K. Umetsu, T. Broadhurst, A. Zitrin, E. Medezinski, D. Coe, and M. Postman. A Precise Cluster Mass Profile Averaged from the Highest-quality Lensing Data. *APJ*, 738:41, September 2011, 1105.0444.

[384] M. Oguri, M. B. Bayliss, H. Dahle, K. Sharon, M. D. Gladders, P. Natarajan, J. F. Hennawi, and B. P. Koester. Combined strong and weak lensing analysis of 28 clusters from the Sloan Giant Arcs Survey. *MNRAS*, 420:3213–3239, March 2012, 1109.2594.

[385] M. Jauzac, B. Clment, M. Limousin, J. Richard, E. Jullo, et al. Hubble Frontier Fields: a high-precision strong-lensing analysis of galaxy cluster MACSJ0416.1-2403 using 200 multiple images. *Mon.Not.Roy.Astron.Soc.*, 443(2):1549–1554, 2014, 1405.3582.

[386] Mathilde Jauzac, Eric Jullo, Dominique Eckert, Harald Ebeling, Johan Richard, et al. Hubble Frontier Fields: the geometry and dynamics of the massive galaxy cluster merger MACSJ0416.12403. *Mon.Not.Roy.Astron.Soc.*, 446(4):4132–4147, 2015, 1406.3011.

[387] Mathilde Jauzac, Johan Richard, Eric Jullo, Benjamin Clment, Marceau Limousin, et al. Hubble Frontier Fields : A High-Precision Strong-Lensing Mass Model of the Massive Galaxy Cluster Abell 2744 using 150 Multiple Images. 2014, 1409.8663.

[388] K. Umetsu, T. Broadhurst, A. Zitrin, E. Medezinski, and L.-Y. Hsu. Cluster Mass Profiles from a Bayesian Analysis of Weak-lensing Distortion and Magnification Measurements: Applications to Subaru Data. *APJ*, 729:127, March 2011, 1011.3044.

[389] Alan R. Duffy, Joop Schaye, Scott T. Kay, and Claudio Dalla Vecchia. Dark matter halo concentrations in the Wilkinson Microwave Anisotropy Probe year 5 cosmology. *Mon.Not.Roy.Astron.Soc.*, 390:L64, 2008, 0804.2486.

[390] M. Oguri and T. Hamana. Detailed cluster lensing profiles at large radii and the impact on cluster weak lensing studies. *MNRAS*, 414:1851–1861, July 2011, 1101.0650.

[391] Matthieu Schaller, Carlos S. Frenk, Richard G. Bower, Tom Theuns, Adrian Jenkins, et al. The masses and density profiles of halos in a LCDM galaxy formation simulation. 2014, 1409.8617.

[392] Matthieu Schaller, Carlos S. Frenk, Richard G. Bower, Tom Theuns, James Trayford, et al. The effect of baryons on the inner density profiles of rich clusters. 2014, 1409.8297.

[393] M. Meneghetti, E. Rasia, J. Vega, J. Merten, M. Postman, et al. The MUSIC of

CLASH: predictions on the concentration-mass relation. *Astrophys.J.*, 797(1):34, 2014, 1404.1384.

[394] Tsz Yan Lam, Fabian Schmidt, Takahiro Nishimichi, and Masahiro Takada. Modeling the Phase-Space Distribution around Massive Halos. *Phys.Rev.*, D88:023012, 2013, 1305.5548.

[395] Harry Wilcox, David Bacon, Robert C. Nichol, Philip J. Rooney, Ayumu Terukina, et al. The XMM Cluster Survey: Testing chameleon gravity using the profiles of clusters. 2015, 1504.03937.

[396] T. L. Smith. Testing gravity on kiloparsec scales with strong gravitational lenses. *ArXiv e-prints*, July 2009, 0907.4829.

[397] F. Schmidt. Dynamical masses in modified gravity. *PRD*, 81(10):103002, May 2010, 1003.0409.

[398] Andrew P. Hearin. Assembly Bias and Redshift-Space Distortions: Impact on cluster dynamics tests of general relativity. 2015, 1501.02798.

[399] M. Wyman. Galilean-Invariant Scalar Fields Can Strengthen Gravitational Lensing. *Physical Review Letters*, 106(20):201102, May 2011, 1101.1295.

[400] Youngsoo Park and Mark Wyman. Detectability of Weak Lensing Modifications under Galileon Theories. 2014, 1408.4773.

[401] R. Mandelbaum, A. Slosar, T. Baldauf, U. Seljak, C. M. Hirata, R. Nakajima, R. Reyes, and R. E. Smith. Cosmological parameter constraints from galaxy-galaxy lensing and galaxy clustering with the SDSS DR7. *MNRAS*, 432:1544–1575, June 2013, 1207.1120.

[402] Richard A. Battye, Adam Moss, and Jonathan A. Pearson. Constraining dark sector perturbations I: cosmic shear and CMB lensing. 2014, 1409.4650.

[403] W.E. Schaap and R. van de Weygaert. Continuous fields and discrete samples: reconstruction through delaunay tessellations. *Astron.Astrophys.*, 363:L29, 2000, astro-ph/0011007.

[404] R. van de Weygaert and W. Schaap. The Cosmic Web: Geometric Analysis. In V. J. Martínez, E. Saar, E. Martínez-González, and M.-J. Pons-Bordería, editors, *Data Analysis in Cosmology*, volume 665 of *Lecture Notes in Physics, Berlin Springer Verlag*, pages 291–413, 2009.

[405] Marius Cautun, Rien van de Weygaert, Bernard J. T. Jones, and Carlos S. Frenk. Evolution of the cosmic web. *Mon.Not.Roy.Astron.Soc.*, 441(4):2923–2973, 2014, 1401.7866.

[406] Ravi K. Sheth and Rien van de Weygaert. A Hierarchy of voids: Much ado about nothing. *Mon.Not.Roy.Astron.Soc.*, 350:517, 2004, astro-ph/0311260.

[407] Joerg M. Colberg, Frazer Pearce, Caroline Foster, Erwin Platen, Riccardo Brunino, et al. The Aspen–Amsterdam Void Finder Comparison Project. *Mon.Not.Roy.Astron.Soc.*, 387:933, 2008, 0803.0918.

[408] Nelson David Padilla, L. Ceccarelli, and D.G. Lambas. Spatial and dynamical properties of voids in a lambda-CDM Universe. *Mon.Not.Roy.Astron.Soc.*, 363:977–990, 2005, astro-ph/0508297.

[409] Johannes Noller, Francesca von Braun-Bates, and Pedro G. Ferreira. Relativistic scalar fields and the quasistatic approximation in theories of modified gravity. *Phys.Rev.*, D89(2):023521, 2014, 1310.3266.

[410] Ignacy Sawicki and Emilio Bellini. Limits of Quasi-Static Approximation in Modified-Gravity Cosmologies. 2015, 1503.06831.

[411] Sownak Bose, Wojciech A. Hellwing, and Baojiu Li. Testing the quasi-static approximation in $f(R)$ gravity simulations. *JCAP*, 1502(02):034, 2015, 1411.6128.

[412] Hans A. Winther and Pedro G. Ferreira. The Vainshtein mechanism beyond the quasi-static approximation. 2015, 1505.03539.

[413] Peter Melchior, P.M. Sutter, Erin S. Sheldon, Elisabeth Krause, and Benjamin D. Wandelt. First measurement of gravitational lensing by cosmic voids in SDSS. *Mon.Not.Roy.Astron.Soc.*, (440):2922–2927, 2014, 1309.2045.

[414] Joseph Clampitt and Bhuvnesh Jain. Lensing Measurements of the Mass Distribution in SDSS Voids. 2014, 1404.1834.

[415] Luca Amendola, Joshua A. Frieman, and Ioav Waga. Weak Gravitational lensing by voids. *Mon.Not.Roy.Astron.Soc.*, 309:465, 1999, astro-ph/9811458.

[416] E. Krause, T.-C. Chang, O. Doré, and K. Umetsu. The Weight of Emptiness: The Gravitational Lensing Signal of Stacked Voids. *APJL*, 762:L20, January 2013, 1210.2446.

[417] Y. Higuchi, M. Oguri, and T. Hamana. Measuring the mass distribution of voids with stacked weak lensing. *MNRAS*, 432:1021–1031, June 2013, 1211.5966.

[418] P. M. Sutter, G. Lavaux, B. D. Wandelt, and D. H. Weinberg. A Public Void Catalog from the SDSS DR7 Galaxy Redshift Surveys Based on the Watershed Transform. *APJ*, 761:44, December 2012, 1207.2524.

[419] Kevork N. Abazajian et al. The Seventh Data Release of the Sloan Digital Sky Survey. *Astrophys.J.Suppl.*, 182:543–558, 2009, 0812.0649.

[420] G. Pollina, M. Baldi, F. Marulli, and L. Moscardini. Cosmic voids in coupled dark energy cosmologies: the impact of halo bias. *ArXiv e-prints*, June 2015, 1506.08831.

[421] S. Nadathur and S. Hotchkiss. The nature of voids: II. Tracing underdensities with biased galaxies. *ArXiv e-prints*, July 2015, 1507.00197.

[422] A. V. Kravtsov, A. A. Berlind, R. H. Wechsler, A. A. Klypin, S. Gottlöber, B. Allgood, and J. R. Primack. The Dark Side of the Halo Occupation Distribution. *APJ*, 609: 35–49, July 2004, astro-ph/0308519.

[423] Marius Cautun, Rien van de Weygaert, Bernard J. T. Jones, and Carlos S. Frenk. Understanding the cosmic web. 2015, 1501.01306.

[424] Marius Cautun. *et al; in preparation*.

[425] Paul A. Abell et al. LSST Science Book, Version 2.0. 2009, 0912.0201.

[426] R. Laureijs, J. Amiaux, S. Arduini, J. . Auguères, J. Brinchmann, R. Cole, M. Cropper, C. Dabin, L. Duvet, A. Ealet, and et al. Euclid Definition Study Report. *arXiv:1110.3193L*, October 2011, 1110.3193.

[427] Andreas Albrecht, Gary Bernstein, Robert Cahn, Wendy L. Freedman, Jacqueline Hewitt, et al. Report of the Dark Energy Task Force. 2006, astro-ph/0609591.

[428] M. C. Neyrinck, I. Szapudi, and A. S. Szalay. Rejuvenating the Matter Power Spectrum: Restoring Information with a Logarithmic Density Mapping. *APJL*, 698:L90–L93, June 2009, 0903.4693.

[429] Lucas Lombriser, Fergus Simpson, and Alexander Mead. Unscreening modified gravity in the matter power spectrum. 2015, 1501.04961.

[430] I. Zehavi et al. Galaxy clustering in early SDSS redshift data. *Astrophys.J.*, 571:172–190, 2002, astro-ph/0106476.

[431] Ed Hawkins, Steve Maddox, Shaun Cole, Darren Madgwick, Peder Norberg, et al. The 2dF Galaxy Redshift Survey: Correlation functions, peculiar velocities and the matter density of the universe. *Mon.Not.Roy.Astron.Soc.*, 346:78, 2003, astro-ph/0212375.

[432] R. Brent Tully, Helene M. Courtois, Andrew E. Dolphin, J. Richard Fisher, Philippe Heraudeau, et al. Cosmicflows-2: The Data. *Astron.J.*, 146:86, 2013, 1307.7213.

[433] Andrew Johnson, Chris Blake, Jun Koda, Yin-Zhe Ma, Matthew Colless, et al. The 6dF Galaxy Velocity Survey: Cosmological constraints from the velocity power spectrum. *Mon.Not.Roy.Astron.Soc.*, 444:3926, 2014, 1404.3799.

[434] Davide Bianchi. Semi-analytic galaxy formation in f(R)-gravity cosmologies. *Mon.Not.Roy.Astron.Soc.*, 436:2672, 2013, 1307.5065.

[435] Claudio Llinares, David F. Mota, and Hans A. Winther. ISIS: a new N-body cosmological code with scalar fields based on RAMSES. 2013, 1307.6748.

[436] Ewald Puchwein, Marco Baldi, and Volker Springel. Modified Gravity-GADGET: A new code for cosmological hydrodynamical simulations of modified gravity models. 2013, 1305.2418.

[437] Volker Springel. The Cosmological simulation code GADGET-2. *Mon.Not.Roy.Astron.Soc.*, 364:1105–1134, 2005, astro-ph/0505010.